

UNIVERSITY OF CALIFORNIA, SAN DIEGO

Particle size/ grain size correlation and mechanical properties of spark plasma sintered  
8Y-ZrO<sub>2</sub>, MgAl<sub>2</sub>O<sub>4</sub>, and Al<sub>2</sub>O<sub>3</sub> based composites

A dissertation submitted in partial satisfaction of the  
requirements for the degree of Doctor of Philosophy

in

Engineering Science (Mechanical Engineering)

by

Keyur Kashinath Karandikar

Committee in charge:

Professor Olivia Graeve, Chair  
Professor Shengqiang Cai  
Professor Robert Continetti  
Professor Joanna McKittrick  
Professor Martha Mecartney

2018

Copyright

Keyur Kashinath Karandikar, 2018

All rights reserved.

The Dissertation of Keyur Kashinath Karandikar as it is listed on UCSD Academic Records is approved, and it is acceptable in quality and form for publication on microfilm and electronically:

---

---

---

---

---

Chair

University of California, San Diego

2018

## TABLE OF CONTENTS

SIGNATURE PAGE.....	iii
TABLE OF CONTENTS.....	iv
LIST OF FIGURES.....	vii
LIST OF TABLES.....	xii
ACKNOWLEDGEMENTS.....	xiv
VITA.....	xvi
ABSTRACT OF DISSERTATION.....	xvii
CHAPTER 1: INTRODUCTION AND MOTIVATION.....	
1.1 Ceramic oxide materials.....	1
1.2 Oxide ceramics surrogate for nuclear project.....	2
1.3 Significance of particle size and grain size.....	4
CHAPTER 2: PARTICLE SIZE DISTRIBUTION.....	
2.1 Motivation for particle size distribution studies.....	8
2.2 Powder information and properties.....	9
2.3 Powder characterization methods and experiments.....	12
2.4 Particle size distribution results.....	21
2.5 Effect of milling in particle size distribution.....	24
2.6 Particle size measurements and milling of multiphase powder mixtures.....	30
2.7 Conclusion.....	33
CHAPTER 3: SINTERING RESULTS & PARTICLE-GRAIN SIZE CORRELATION.....	
3.1 Spark Plasma Sintering: Background and motivation.....	34
3.2 Experimental setup and sintering load diagrams.....	37

3.3 Post-sintering characterization: Density, X-ray diffraction, Polishing, Imaging.....	43
3.4 Sintering results: Grain size distribution in single/multiphase composites.....	47
3.5 Sintering results: Densification tendency in single/multiphase composites.....	50
3.6 Results: particle size/grain size correlation – “size ratio” .....	51
3.7 Discussion of sintering results: Grain growth/Densification.....	60
3.8 Sintering of ceramic oxides of two different powder sizes.....	70
3.9 Discussion: Sintering of ceramic oxides of two different powder sizes.....	75
3.10 Significance of current study as compared to previous literature.....	82
3.11 Conclusion.....	91
<b>CHAPTER 4: MECHANICAL PROPERTIES AND MICROSTRUCTURAL CHARACTERIZATION.....</b>	
4.1 Motivation and Background.....	93
4.2 Experimental Setup.....	95
4.3 Results: Hardness of single/multiphase composites.....	99
4.4 Results: Fracture toughness of single/multiphase composites.....	105
4.5 Results: Fracture surface characterization of single/multiphase oxides.....	109
4.6 Discussion of hardness results in Single phase ceramic oxides.....	113
4.7 Comparisons of mechanical properties among single phase materials.....	115
4.8 Fracture toughness vs. grain size tendency.....	117
4.9 Fractal Micrography discussion studies.....	119
4.10 Comparative studies between single and multiphase composites.....	121
4.11 Significance of the present study.....	124
4.12 Conclusion.....	129

CHAPTER 5: HEATING RATE AND MASTER SINTERING CURVE.....	
5.1 Experimental Set-up, Results, and Discussion.....	131
5.2 Master Sintering Curve: Theory and Procedure.....	141
5.3 Conclusion .....	153
REFERENCES.....	153

## LIST OF FIGURES

Figure 1.1 Model multiphase fine-grained ceramic oxide surrogate material for advance inert matrix fuel .....	4
Figure 1.2 Schematics of ceramic sintering process .....	5
Figure 2.1 Dynamic light characterizing technique used for particle size distribution.34, 35	
Figure A highlights the schematics of laser diffraction system with laser pulse scattered by resulting particles and collected by a detector at an angle $\Theta$ .....	12
Figure 2.2 Change in zeta potential concerning to pH in solution and respective stability of the suspension. The isoelectric point is the point where zeta potential is 0mV, i.e., the solution undergoes maximum deagglomeration. ....	14
Figure 2.3 Zeta potential (mV) vs. pH values for increasing concentrations of YSZ-3Y or 3Y-ZrO <sub>2</sub> by volume % .....	18
Figure 2.4 Zeta potential (mV) vs. pH values at various concentrations (vol %) of YSZ-8Y or 8Y-ZrO <sub>2</sub> .....	18
Figure 2.5 Zeta potential (mV) vs. pH values at various concentrations of monoclinic ZrO <sub>2</sub> .19	
Figure 2.6A Particle size distribution by DLS of individual sample powder of (Al <sub>2</sub> O <sub>3</sub> ) <sub>3</sub> (Fig. E, F) single phase ceramic size powders. The results about change in particle sizes before and after milling are highlighted.....	27
Figure 2.7 SEM micrographs of as received(left) and milled powder(right) of single-phase ceramic oxides of 8Y-ZrO <sub>2</sub> (in the previous page), MgAl <sub>2</sub> O <sub>4</sub> and Al <sub>2</sub> O <sub>3</sub> (present page).....	29
Figure 2.8 Particle size distribution results obtained by DLS of binary sample powder of (8Y-ZrO <sub>2</sub> ) <sub>1</sub> /(MgAl <sub>2</sub> O <sub>4</sub> ) <sub>1</sub> , (8Y-ZrO <sub>2</sub> ) <sub>2</sub> /(Al <sub>2</sub> O <sub>3</sub> ) <sub>3</sub> , and (8Y-ZrO <sub>2</sub> ) <sub>2</sub> /(MgAl <sub>2</sub> O <sub>4</sub> ) <sub>1</sub> /(Al <sub>2</sub> O <sub>3</sub> ) <sub>2</sub> ternary phase ceramic size powders. ....	32
Figure 3.1 Timeline diagram regarding the background and the history of spark plasma sintering process. 61, 62.....	34
Figure 3.2 Publication history and trends related to use of spark plasma sintering to process potential advanced engineering materials.63 .....	34
Figure 3.3 Principle set up for spark plasma sintering furnace.....	36
Figure 3.4 Photograph of spark plasma sintering furnace at Alfred University, New York. The graphite die-cone arrangement along with the sample inside the die is shown in the inset picture to the right. ....	37

Figure 3.5 Loading diagram for $(Al_2O_3)_2$ single phase partially sintered composite (left plot) and fully sintered composite (right plot) with the respective temperature, displacement, and velocity profiles of the piston.....	40
Figure 3.6 Loading diagram for single phase $(MgAl_2O_4)_1$ partially sintered composite (left plot) and fully sintered composite (right plot) with the respective temperature, displacement, and velocity profiles of the piston.....	41
Figure 3.7 Loading diagram for single phase $(8Y-ZrO_2)_2$ partially sintered composite (left plot) and fully sintered composite (right plot) with the respective temperature, displacement, and velocity profiles of the piston.....	41
Figure 3.8 Loading diagram for single phase $(8Y-ZrO_2)_2/(Al_2O_3)_3$ partially sintered composite (left plot) and fully sintered composite (right plot) with the respective temperature, displacement, and velocity profiles of the piston.....	42
Figure 3.9 Loading diagram for three-phase $(8Y-ZrO_2)_2/(MgAl_2O_4)_1/(Al_2O_3)_3$ partially sintered composite (left plot) and fully sintered composite (right plot) with the respective temperature, displacement, and velocity profiles of the piston.....	42
Figure 3.10 X-ray diffraction spectra representative example of ceramic powder- as received $(Al_2O_3)_4$ (A) and milled binary powder $(8Y-ZrO_2)_1/(MgAl_2O_4)_1$ (B), and SPS sintered ternary phase $(8Y-ZrO_2)_2/(MgAl_2O_4)_1/(Al_2O_3)_3$ (C) specimens.....	44
Figure 3.11. Graphical results indicating the overall effect of sintering temperature on grain size of single phase ceramics (Fig. 2A) and multiphase ceramic oxides (Fig. 2B) of $8Y-ZrO_2$ , $MgAl_2O_4$ , and $Al_2O_3$ .....	47
Figure 3.12 Bulk densification tendency of single phase ceramic oxides as compared to three phase oxide (dash line) at different sintering temperature; % density is the theoretical density of the sample obtained from Archimedes measurements .....	50
Figure 3.13 Bulk densification tendency of multiphase ceramic oxides at different sintering temperature; % density is the theoretical density of the sample obtained from Archimedes measurements.....	50
Figure 3.14 Plot of Grain size (G.S)/Particle size (P.S) ratio indicating the overall effect of sintering temperature on grain growth tendency of single phase ceramic oxides. Details of the curve fits of the empirical data have been provided in the table above. ....	56
Figure 3.15 Plot of Grain size (G.S)/Particle size (P.S) ratio indicating the overall effect of sintering temperature on grain growth tendency of equal proportional binary and ternary phase composites of $8Y-ZrO_2$ , $MgAl_2O_4$ , and $Al_2O_3$ .....	57



Figure 3.16 Arrhenius plot of natural logarithm of G.S/P.S ratio versus sintering temperature (1000/K). The respective slope of the lines gives activation energy values for grain growth for 8Y-ZrO <sub>2</sub> in Fig.A, Al <sub>2</sub> O <sub>3</sub> in Fig B. and MgAl <sub>2</sub> O <sub>4</sub> , in Fig.C. ....	58
Figure 3.17 Arrhenius plot of natural logarithm of G.S/P.S ratio versus sintering temperature (1000/K) for multiphase composites. The respective slopes of the lines give activation energy values for grain growth for 8Y-ZrO <sub>2</sub> /MgAl <sub>2</sub> O <sub>4</sub> in Fig. A,.....	59
Figure 3.18 SEM micrographs of the representative fracture surface of sintered (8Y-ZrO <sub>2</sub> )v ceramic composites with average grain size information at different sintering temperatures ..	66
Figure 3.19 SEM micrographs of representative fracture surfaces of sintered (MgAl <sub>2</sub> O <sub>4</sub> ) <sub>1</sub> (top) and (Al <sub>2</sub> O <sub>3</sub> ) <sub>2</sub> (bottom) ceramic composites with average grain size information at different sintering temperatures. ....	67
Figure 3.20 SEM micrographs of representative fracture surfaces of binary sintered composites of 8Y-ZrO <sub>2</sub> /Al <sub>2</sub> O <sub>3</sub> (top) and Al <sub>2</sub> O <sub>3</sub> /MgAl <sub>2</sub> O <sub>4</sub> (bottom) ceramic composites with average grain size information at different sintering temperatures.....	68
Figure 3.21 SEM micrographs of representative fracture surfaces of binary composite of 8Y-ZrO <sub>2</sub> /MgAl <sub>2</sub> O <sub>4</sub> (top) and 8Y-ZrO <sub>2</sub> /MgAl <sub>2</sub> O <sub>4</sub> /Al <sub>2</sub> O <sub>3</sub> three phase sintered (bottom) ceramic composites with average grain size information at different sintering temperatures.....	69
Figure 3.22 Graphical results are indicating the effect of sintering temperature on grain size and size ratio in single phase ceramic oxides of 8Y-ZrO <sub>2</sub> (A), Al <sub>2</sub> O <sub>3</sub> (B) and MgAl <sub>2</sub> O <sub>4</sub> (C). Black and grey colored lines highlight the two different powder sizes. ....	71
Figure 3.23 Graphical results indicating the effect of sintering temperature on grain size and size ratio in binary composites of 8Y-ZrO <sub>2</sub> /MgAl <sub>2</sub> O <sub>4</sub> (fig. A), Al <sub>2</sub> O <sub>3</sub> /MgAl <sub>2</sub> O <sub>4</sub> (fig. B), 8Y-ZrO <sub>2</sub> /Al <sub>2</sub> O <sub>3</sub> (fig. C) and ternary phases.....	73
Figure 3.24 SEM micrographs of alumina sintered specimens fabricated from two different particles sized powders (Al <sub>2</sub> O <sub>3</sub> ) <sub>2</sub> (Left) and (Al <sub>2</sub> O <sub>3</sub> ) <sub>3</sub> (Right) sintered at 1300°C. This representative image highlights.....	79
Figure 3.25 SEM micrographs of alumina-spinel binary composite (top) and three phase 8Y-ZrO <sub>2</sub> /MgAl <sub>2</sub> O <sub>4</sub> /Al <sub>2</sub> O <sub>3</sub> composite. The ceramic oxides are fabricated from two different particles sized powders sintered.....	80
Figure 3.26 SEM micrographs of polished surfaces of three-phase composites obtained by sintering of various powder mixtures at 1150°C. The different powder mixture used are labeled according to their designations. ....	81

Figure 4.1 Fig.A shows respective densified SPS pellet (19mm Ø) before fracture. Fig.1B shows sketch depicting hardness and fracture toughness measurements using Vickers indentation method. D1&D2 diagonal measurements for hardness.....97

Figure 4.2 Hardness tester LM 810-AT model manufactured by LECO Corporation135. ....98

Figure 4.3 Microhardness of single-phase ceramics (3A-3C) plotted as inversely proportional to the square root of grain size to validate the Hall-Petch relationship. The linear intercept (red dashed line) indicates this relationship. ....99

Figure 4.4 Microhardness of binary phase 8Y-ZrO<sub>2</sub>/Al<sub>2</sub>O<sub>3</sub> (4A) and Al<sub>2</sub>O<sub>3</sub>/MgAl<sub>2</sub>O<sub>4</sub> (4B) ceramic oxides plotted as inversely proportional to the square root of grain size to evaluate Hall-Petch relationship.....100

Figure 4.5 Microhardness of binary phase 8Y-ZrO<sub>2</sub>/MgAl<sub>2</sub>O<sub>4</sub> (4C) and 8Y-ZrO<sub>2</sub>/MgAl<sub>2</sub>O<sub>4</sub>/Al<sub>2</sub>O<sub>3</sub> (4D) ceramic oxides plotted as inversely proportional to the square root of grain size to evaluate Hall-Petch relationship. ....101

Figure 4.6 Fracture toughness of single phase 8Y-ZrO<sub>2</sub> (A), Al<sub>2</sub>O<sub>3</sub>(B) and MgAl<sub>2</sub>O<sub>4</sub> (C) ceramic oxides plotted against various grain sizes of the given composites. The logarithmic tendency (if applicable) is highlighted by the trend line in red.....106

Figure 4.7 Fracture toughness results for the different types of binary and ternary composites of 8Y-ZrO<sub>2</sub>, Al<sub>2</sub>O<sub>3</sub>, and MgAl<sub>2</sub>O<sub>4</sub> ceramic oxides have been plotted against various grain sizes of the given composites.....**Error! Bookmark not defined.**

Figure 4.8 SEM micrographs of fracture surfaces of single phase ceramics of Al<sub>2</sub>O<sub>3</sub> (A), 8Y-ZrO<sub>2</sub> (B) and MgAl<sub>2</sub>O<sub>4</sub> (C). Two different modes of fracture Intergranular (IGF) and Transgranular (TGF) are highlighted in. ....110

Figure 4.9 SEM micrographs of fracture surfaces in binary phase ceramics of Al<sub>2</sub>O<sub>3</sub>/MgAl<sub>2</sub>O<sub>4</sub> (A), 8Y-ZrO<sub>2</sub>/Al<sub>2</sub>O<sub>3</sub> (B), 8Y-ZrO<sub>2</sub>/MgAl<sub>2</sub>O<sub>4</sub> (C) and ternary phase composite (D). Intergranular (IGF) and Transgranular (TGF) modes.....111

Figure 4.10 Crack interaction and the resulting mobility due to microstructural grains. In case of single-phase ceramics (A), the crack can either propagate or deflect thereby affecting according to their interactions with grain boundaries between larger or finer grains.....116

Figure 5.1 SEM micrographs of the fracture surface of the (8Y-ZrO<sub>2</sub>)<sub>1</sub> sintered composite at different heating rates of 10,50, and 100°C/min. The sintering temperature at 1000°C while other parameters were kept constant. Powder particle size was 82±31nm. ....134

Figure 5.2 SEM micrographs of the fracture surface of the (MgAl<sub>2</sub>O<sub>4</sub>)<sub>1</sub> sintered composite at different heating rates of 10, 50, and 100 °C/min. The sintering temperature was constant at 1030 °C. The powder particle size was measured as 84±15 nm .....134

Figure 5.3 SEM micrographs of the fracture surface of  $(Al_2O_3)_3$  sintered composite at different heating rates of 10, 50, and 100 °C/min. The sintering temperature was constant at 1030°C. The powder particle size was measured as  $149\pm 28$  nm. ....135

Figure 5.4 SEM micrographs of the fracture surface of  $(Al_2O_3)_3/(MgAl_2O_4)_1$  sintered composite at different heating rates of 10,50 and 100 °C/min. The sintering temperature was constant at 1100°C. The powder particle size was measured as  $147\pm 22$  nm. ....135

Figure 5.5 SEM micrographs of the fracture surface of the  $(8Y-ZrO_2)_2/(Al_2O_3)_1$  sintered composite at different heating rates of 10,50 and 100°C/min. The sintering temperature was constant at 1100°C. The powder particle size was measured as  $197\pm 31$  nm.....136

Figure 5.6 SEM micrographs of the fracture surface of the  $(8Y-ZrO_2)_2/(MgAl_2O_4)_1$  sintered composite at different heating rates of 10 and 100°C/min. The sintering temperature was constant at 1100°C. The powder particle size was measured as  $91\pm 15$ nm.....136

Figure 5.7 SEM micrographs of the fracture surface of the  $(8Y-ZrO_2)_2/(MgAl_2O_4)_1/(Al_2O_3)_2$  sintered composite at different heating rates of 10 and 100°C/min. The sintering temperature was constant at 1100°C. The powder particle size was measured as  $214\pm 30$ nm.....137

Figure 5.8 Master sintering curves of relative density vs work of sintering calculations for single phase  $Al_2O_3$  at different empirical values of activation energy. Data sets of sintering profile at three different heating rates is used for this purpose.. ....147

Figure 5.9 Fig.B portrays Linearization of master sintering curve model for calculation of activation energy for  $Al_2O_3$ . The linearization is performed using an initial estimate of  $Q=1000$  kJ/mol that is used to plot the sigmoid curves in Figure A.....148

Figure 5.10 Master sintering curves of relative density vs. work of sintering plotted for binary phase composites of 8Y-ZrO<sub>2</sub>,  $Al_2O_3$ , and  $MgAl_2O_4$ . The resulting apparent activation energy of the sintering process for each ceramic is provided. Three sintering rates are used for plotting of MSC curves. ....149

## LIST OF TABLES

Table 1.1 Novel engineering applications for advanced ceramic oxides 3–6.....	1
Table 1.2 Literature study information regarding importance of particle size and grain size distribution in ceramic material properties .....	6
Table 2.1 Material properties of Ceramic oxides of Cubic Zirconia, Spinel and $\alpha$ -Alumina.27,32-35 .....	10
Table 2.2 Information related to particle size, impurities and characterization method regarding ceramic oxide commercial powders obtained from different vendors .....	11
Table 2.3 Example of experimental matrix highlighting the effect of changes in four different factors (highlighted in italics) to affect the stability of the solution. The respective particle size is provided along with.....	20
Table 2.4 Particle sizes of single-phase commercial ceramic oxide powders indicating the difference in particle sizes as provided by powder manufacturers and measured by dynamic light scattering.....	21
Table 2.5 Specifications of the planetary milling machine and the dry milling conditions.....	24
Table 2.6 Experimental results obtained for different batches of ball-milling of few ceramic powders in increasing amounts of milling time and the effects on particle size distribution. Note that the respective size distributions were carried out at stable zeta. ....	25
Table 2.7 Particle size distribution measurements of binary and ternary phase powder mixtures of 8Y-ZrO <sub>2</sub> , MgAl <sub>2</sub> O <sub>4</sub> , and Al <sub>2</sub> O <sub>3</sub> -based ceramic oxides. The mixtures are in equal proportion by volume, i.e., 50-50 in case of binary mixtures.. ....	30
Table 3.1 Range of sintering parameters used to obtain variable grain sized and dense ceramic composites.....	38
Table 3.2 Particle size information of the single-phase powders sintered in the current study	46
Table 3.3 Particle size information of the binary/ternary phase powders sintered in the current study .....	46
Table 3.4 Size ratios of representative specimens of single phase ceramic oxides at variable sintering temperatures .....	52
Table 3.5 Size ratios of representative specimens of multiphase ceramic oxides at variable sintering temperatures .....	53

Table 3.6 Bulk density of the sintered composites of single phase powders in Figure 3.18 as obtained from Archimedes method.....	77
Table 3.7 Bulk density of the sintered composites of binary and ternary-phase powders in Figure 3.19, as obtained from Archimedes method. ....	78
Table 3.8. Summary of studies performed on grain growth of single phase ceramic oxides. Information is provided regarding powder sizes, grain sizes of sintered specimens, sintering parameters, and key observations for comparisons with the present study. ....	82
Table 3.9 Summary of literature studies performed on grain growth of binary/ternary phase ceramic oxides. Information is provided regarding powder sizes with mixture proportions, respective grain sizes,.....	86
Table 4.1 Information regarding the range of sintering temperatures used to obtain variable grain sized single/multiphase composites. Lowest density values of the samples calculated by Archimedes' method are tabulated .....	95
Table 4.2 Equation parameters of the linear fit obtained for the hardness vs. grain size results for individual ceramic oxide specimens as plotted in figure 2-3. ....	104
Table 4.3 Performance matrix of multiphase composites versus single phase ceramic oxides in terms of % change (% $\Delta$ ) in hardness and fracture toughness .....	121
Table 4.4 Summary of relevant studies performed regarding mechanical properties of sintered single-phase ceramic oxides in past literature. Information is provided regarding hardness, and fracture toughness for respective grain sizes. ....	124
Table 4.5 Summary of literature studies performed regarding mechanical properties of sintered multiphase ceramic oxides .....	127
Table 5.1 Results highlighting grain size values for single phase 8Y-ZrO <sub>2</sub> , MgAl <sub>2</sub> O <sub>4</sub> and Al <sub>2</sub> O <sub>3</sub> powders at different heating rates at a sintering temperature. Density % is the bulk density of the samples calculated by Archimedes principle.. ....	131
Table 5.2 Results highlighting grain size values for multiphase 8Y-ZrO <sub>2</sub> , MgAl <sub>2</sub> O <sub>4</sub> and Al <sub>2</sub> O <sub>3</sub> powders at different heating rates at a particular sintering temperature. Density % is the bulk density of the samples calculated by Archimedes principle .....	132
Table 5.3 Dataset for one of the three heating rates (10°C/min) used for generation of master sintering curve of single phase Al <sub>2</sub> O <sub>3</sub> composite. Density was obtained using green density, final density from Archimedes principle and ram displacement.. ....	146

## ACKNOWLEDGEMENTS

It is with immense gratitude that I acknowledge the support and the help of my adviser, Prof. Olivia Graeve for giving me an opportunity to pursue my doctoral research in her lab. I cannot find words to express my gratitude to my advisor for her patience, motivation, enthusiasm, and guidance during this journey. I am grateful to the rest of my dissertation committee: Prof. Joanna Mckittrick, Prof. Robert Continetti, Prof. Shengqiang Cai and Prof. Martha Mecartney for their encouragement, insightful comments, and guidance.

I am lucky to have amazing fellow lab-mates in the Xtreme Materials Laboratory at UC San Diego. Special thanks to Kira Cummings, Luz Zavala, Dr. Ekaterina Novitskaya, Dr. James Kelly, Shuang Qiao, Robyn Ridley, Carson Cheung, Ivan Torres, Jason Mayeda, Jordan Furlong, Rocio Pena, and Christopher Pisano for helping me immensely in my doctoral work. The ceramic processing work would not have been possible without the help of all the staff and research colleagues at Alfred University in New York. I am very grateful for the NEUP project collaborators namely, Prof. Martha Mecartney, Kenta Ohtaki, Austin Travis, Kara Philips, Andy Nelson and Maulik Patel for their inputs during the project meetings. The current doctoral work was funded by the Department of Energy (Grant no). I am forever grateful to Prof. Joanna Mckittrick and Dr. Michael Frank who gave me a wonderful opportunity to contribute my research ideas and work on their freeze casting project. My graduate friends and researchers in UCSD, UNAM (Ensenada, Mexico), Team SLFU along with KCB, and my undergraduate friends in India for their constant encouragement, guidance that made the past six years of graduate school memorable.

I would like to take this opportunity to bow down to my parents Kashinath Karandikar, Dr. Sunanda Karandikar, my brother Kedar, and sister-in-law Ketki, who have made immense

sacrifices for me throughout my life. I am forever grateful to Maria Mladenik for tolerating for the past two difficult years. Finally, I would like to dedicate my doctoral thesis in the memory of my late grandmother and my late uncle who introduced me to this beautiful field of science.

Chapters 2 and 3, in part are currently being prepared for submission for publication of the material. Karandikar, Keyur; Graeve, Olivia A.; Mecartney, Martha L.; Ohtaki Kenta; Travis, Austin; Evokodimiko Ekaterina; Cummings, Kira. The dissertation/thesis author was the primary investigator and author of this material under the title “Correlation between powder particle size and sintered grain size distributions in ceramic oxides: A spark plasma sintering study.” The thesis author was responsible for extensive particle characterization, ball milling, sintering, and grain growth analysis of ceramic oxide single/multiphase composites.

Chapter 4, in part is currently being prepared for submission for publication of the material. Karandikar, Keyur; Graeve, Olivia A.; Mecartney, Martha L.; Ohtaki Kenta; Travis, Austin; Evokodimiko Ekaterina; Cummings, Kira. The thesis author was the primary investigator and author of this material under the title “Mechanical properties of 8Y-ZrO<sub>2</sub>, MgAl<sub>2</sub>O<sub>4</sub>, and Al<sub>2</sub>O<sub>3</sub> based single/multiphase ceramic composites produced by spark plasma sintering.” The thesis author was responsible for testing hardness and toughness mechanical properties and fractography of the single/multiphase phase composites.

Chapter 5, in part is currently being prepared for submission for publication of the material. Karandikar, Keyur; Graeve, Olivia A.; Mecartney, Martha L.; Ohtaki Kenta; Travis, Austin. The thesis author was the primary investigator and author of this material under the title “Effect of heating rate on microstructure and properties of spark plasma sintered ceramic oxides.” The thesis author was responsible for heating rate effects on sintering condition of ceramic oxide composites

## VITA

- 2011 Bachelor of Production Engineering, University of Mumbai, Mumbai, India
- 2013 Master of Science, University of California, San Diego
- 2016-2017 Associate Lecturer, ENG 10, University of California, San Diego
- 2018 Doctor of Philosophy, University of California, San Diego

## PUBLICATIONS

Correlation of particle size and grain size in ceramic oxide: a spark plasma sintering study, in preparation, 2018

Master thesis titled “Modeling of Brittle to Ductile Transition in BCC metals : Strain Rate and Temperature dependence in  $\alpha$ -Iron and Tantalum monocrystals, UC San Diego, 2013

## FIELDS OF STUDY

Major Field: Engineering Sciences-Mechanical Engineering

Studies in Ceramic processing, material science

Professor Olivia Graeve

Studies in Dynamic behavior of Materials, solid mechanics

Professor Marc Meyers

Studies in Fluid Mechanics

Professor Eric Lauga



## ABSTRACT OF THE DISSERTATION

Particle size/ grain size correlation and mechanical properties of spark plasma sintered  
8Y-ZrO<sub>2</sub>, MgAl<sub>2</sub>O<sub>4</sub>, and Al<sub>2</sub>O<sub>3</sub> based composites

by

Keyur Kashinath Karandikar

Doctor of Philosophy in Engineering Sciences (Mechanical Engineering)

University of California, San Diego, 2018

Professor Olivia Graeve, Chair

The primary goal of this dissertation is to obtain relationship between the two fundamental ceramic processing parameters of particle size and grain size distribution in order to describe grain growth in ceramic oxides. Commercial powders of cubic zirconia (8Y-ZrO<sub>2</sub>), Spinel (MgAl<sub>2</sub>O<sub>4</sub>), and Alumina (Al<sub>2</sub>O<sub>3</sub>) were characterized for particle sizes by using dynamic light scattering. Agglomeration of powder particles was avoided using surface chemistry and planetary ball milling. Lower average sizes by as much as 50% along with narrower distribution were obtained as compared to the as-received information.

Using the advanced technique of Spark plasma sintering highly dense fine-grained commercial ceramic oxides were fabricated grain sizes varying from 150 nm to >10 μm. Average grain size and size ratio calculated using powder particle sizes were used to empirically model grain growth tendencies among ceramic oxides at different sintering temperatures (950-

1300°C). Activation energy of grain growth was also calculated for all the sintered composites. Spinel sintered composites exhibited slowest grain growth (range of grain size = 1.7-2.3  $\mu\text{m}$ ) amongst the single-phase ceramics while  $\alpha$ -Alumina specimens exhibited grains in the range of 10.5-16  $\mu\text{m}$ . For multiphase ceramics, 8Y-ZrO<sub>2</sub>/Al<sub>2</sub>O<sub>3</sub> exhibited uniform grain size compared to spinel-based binary composites while the novel three-phase composite were also studied. It was concluded that multiphase composites exhibit limited grain growth tendency, as indicated by a 10x smaller size ratio when compared to single phase composites. For each ceramic oxide, sintering experiments were performed using powders with two different particle sizes (~100 and ~200 nm). Results indicate that larger-sized powders result in slower grain growth but eventually achieve higher grain size at temperatures >1200°C.

An extensive analysis of hardness properties was analyzed by plotting Hall-Petch relationship for the sintered single/multiphase ceramic oxides. A strong correlation of hardness-grain size relationship was observed for single phase ceramic oxides and ternary composite ( $R^2 \sim 0.8$ ). On the other hand, fracture toughness values for most of the ceramic oxide samples sintered contained a scatter of results for microstructures with different grain sizes; thereby no correlation was obtained. Fractal micrography study of sintered single/multiphase composites highlighted the presence of primary inter-granular/trans-granular or mix modes of failure. The effects of different heating rates on the microstructure and sintering kinetics via master sintering curves of single, binary and ternary phase composites were also studied

# CHAPTER 1: INTRODUCTION AND MOTIVATION

## 1.1 Ceramic oxides materials

Oxide-based ceramics are a part of advanced materials that are being favored over metal-based systems for today's engineering applications<sup>1</sup>. They possess various material properties like resistance to abrasion, chemical inertness, high melting point, favorable mechanical properties of hardness and toughness, that are responsible for better performance at lower costs<sup>2</sup>.

Consequently, these ceramics in their single/multiphase mixtures have shown promising potential for various modern applications, few of which are summarized below in **Table 1.1**

**Table 1.1 Novel engineering applications for advanced ceramic oxides**<sup>3-6</sup>

Ceramic materials	Application
Hydroxyapatite, Tricalcium phosphate	Bio-ceramics used in Medicine for stents, bone tissue.
Aluminum, Zirconium, Magnesium oxides	Petroleum waste, drinking water purification, treatment of gases.
Corundum +eutectic additions	Sealing/Insulation in valves, spark plug, ceramic substrates for electrical/electronic components.
Zirconium dioxide (PZSD),	Metal cutting tools, wear- resistant applications.
Nanostructured oxides like RuO <sub>2</sub>	Supercapacitors for high electrical charge storage
Rare earth oxide, yttria stabilized zirconia	Thermal barrier coatings for heat engines, turbine blades

## 1.2 Oxide ceramics surrogate for nuclear project

Ceramics are playing an important role in the field of nuclear power as they find their usability in for fission/fusion reactor fuels, moderators, control rods, radioactive waste disposal. Uranium( $\text{UO}_2$ ), plutonium ((U, Pu)  $\text{O}_2$ ) and thorium ( $\text{ThO}_2$ ) oxide-based fuels are currently being used as ceramic fuels for generating nuclear power. They have been noted to have many benefits that include high melting point, corrosion resistance, stability to irradiation, fewer difficulties in manufacturing and so on. Simultaneously, respective carbide and nitride of these radioactive elements are also being tested for future radiation experiments. Besides the commonly used boron carbide, europium hexaboride and oxides are studied for their use in control rods in nuclear reactors. These rods play an important part in controlling the fission reaction through absorption of by-product neutrons. Lastly, Borosilicates, single phase zircon-based systems are also considered for the purpose of permanent disposal of radioactive waste products.

Thus, based on the current scenario, it can be believed that ceramics are increasingly going to play an essential role in the development of nuclear power energy in the future. A significant area of growth is actual nuclear fuel itself, as oxide-based fuels that are most common in existing nuclear reactors exhibit substantial limitations. Firstly, they show low thermal conductivity, ( $\text{UO}_2$  fuel: 2.9 W/mK at 1273°C which drops down to 1.8 W/mK at 2273°C)<sup>7</sup> resulting in large temperature gradients between the center and surface of the fuel pellets causing them to crack. Lastly, they exhibit poor thermal shock resistance thereby observing brittle behavior at low temperatures (<1200°C) and low fuel density.

The present doctoral research work was a part of a multiple institute collaboration project<sup>8</sup> that aims to overcome the limitations of conventional nuclear fuels through the concept

of advanced inert matrix oxide fuel. The primary goal of the project is to develop nanocrystalline inert matrix multiphase nuclear fuel with higher efficiency, longer lifetimes, and better tolerance to accidents for future nuclear reactors. The use of fine/nanostructured ceramic oxides is explored to fabricate an advanced material that will act as surrogates for the nuclear fuel. The ceramics are expected to add following advantages to the advanced fuel:

- Use of finer grain sized ceramics will lead to improvements in overall mechanical strength thereby thermal shock resistance.
- Solve the problem of melting and cracking of fuel pellets by increasing the effective thermal conductivity of  $\text{UO}_2$  matrix.
- Ceramics having submicron/nano-grain sizes are found to be more ductile and even show superplasticity;<sup>9</sup> This enhanced plasticity will be helpful especially at higher temperatures to make the fuel more, safer in case of overheating.

Accordingly, it was decided that Ytria-stabilized cubic zirconia ( $8\text{Y-ZrO}_2$ ) be a suitable candidate material as non-radioactive surrogates along with depleted  $\text{UO}_2$ .  $8\text{Y-ZrO}_2$  with its cubic structure is isostructural with  $\text{UO}_2$  and possesses similar properties, i.e., low thermal conductivity, poor ductility and rapid oxygen diffusion.<sup>10</sup> The stable phases of Spinel ( $\text{MgAl}_2\text{O}_4$ ) and alumina ( $\alpha\text{-Al}_2\text{O}_3$ ) are chosen additional phases primarily for imparting higher thermal conductivity after radiation damage to the matrix fuel. Besides, the presence of multiphases plays a big part in retention of fine grain sized microstructure of the overall matrix, which is beneficial as shown previously. The respective model of advanced inert matrix oxide fuel is shown in **Figure 1.1**

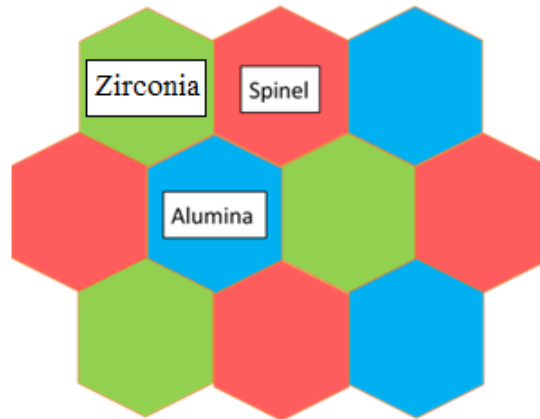


**Figure 1.1 Model multiphase fine-grained ceramic oxide surrogate material for advance inert matrix fuel**

Thus, the selection of ceramic oxides for the present thesis topic was based upon the suitability of these materials for the inert multi-matrix fuel project. The current doctoral research has been expected to play an essential part of for actual sintering of single /binary and multiphase ceramic composite samples of fine grain sizes (~100nm) and high sample density (> 90%).

### **1.3 Particle size, sintering, and grain size distribution**

The given ceramic oxides are fabricated using advanced methods to obtain fine/ultrafine microstructures which then affect the bulk properties of the respective material. It is known that fine-grained structures can either enhance the given material properties or introduce novel properties respectively. According to Maier,<sup>11, 12</sup> these factors can be classified as “trivial” size effects or “real” effects in properties due to size. For example, mass transport, bulk density, or mechanical properties of ceramic oxides like zirconia, alumina improve as the average grain size decreases.<sup>11</sup> On the other hand, ultra-fine spinel (grain size <40nm) exhibits unique optical

transparency, ferrites ( $AB_2O_4$ ) exhibit novel superparamagnetic behavior at grain sizes between 10-60 nm.

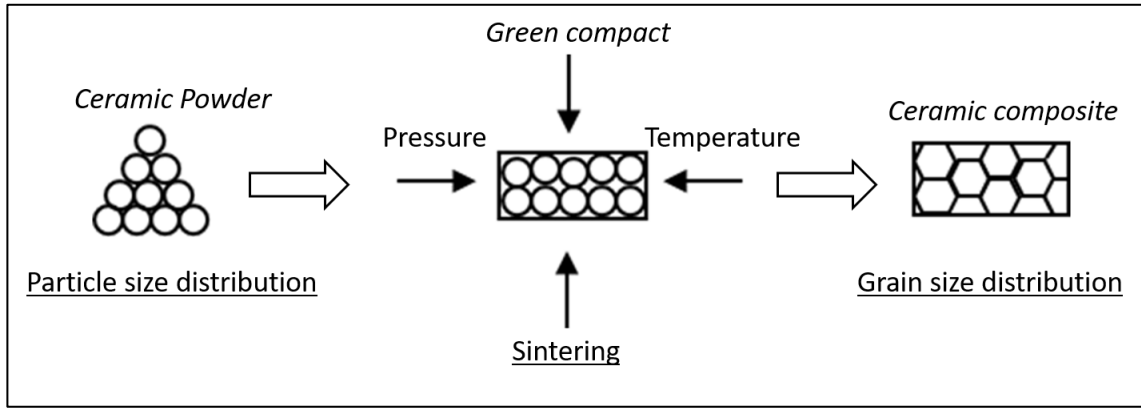


**Figure 1.2 Schematics of ceramic sintering process**

To obtain these advanced fine/nano-structured composites, it is necessary for a deeper understanding of fundamental factors that govern the ceramic powder processing technique itself. As shown in **Figure 1.2**, the two primary elements, i.e., the particle size of the powders that affect the green compact and the sintering parameters that exist at different stages of processing are responsible for optimizing resulting compacts with a specific grain size. The particle size distribution of the powder itself is a reliable indicator of the extent of agglomeration, homogenous nature of particles, and their densification tendency when they form solid compacts. On the other hand, the actual stage of densification or “sintering” is also controlled by single or combination of multiple factors namely, magnitude and duration of pressure applied, the temperature during sintering of powders, the rate of heating/cooling, microwave or electrical parameters and the actual type of sintering itself. The combination of these two factors results in a unique grain sized microstructural composite which is responsible for its material properties – mechanical, electrical, optical, magnetic and so on. A summary of

few literature studies is provided in **Table 1.2** below as a reference to highlight the impacts of powder processing parameters on material properties of different ceramic oxides.

**Table 1.2 Literature study information regarding importance of particle size and grain size distribution in ceramic material properties**

Author	Year	Properties affected by particle/grain size distribution
Bojesen <i>et al.</i> <sup>13</sup>	2012	Different <b>particle sized powders</b> affect the <b>thermal conductivity</b> of ZnO at low temperatures.
Huang <i>et al.</i> <sup>14</sup>	2012	<b>Particle size</b> affects the <b>magnetic properties</b> of single-phased NdFeB magnets.
Eilers <i>et al.</i> <sup>15</sup>	2009	Small <b>particle sizes</b> affect the <b>optical properties</b> in Y <sub>2</sub> O <sub>3</sub> : Er, Yb oxides used for making solid-state lasers.
Gao <i>et al.</i> <sup>16</sup>	1999	Use of different <b>sintering parameters</b> (heating rate, temperature) in spark plasma sintering to obtain SiC-ZrO <sub>2</sub> -Al <sub>2</sub> O <sub>3</sub> composites of high <b>bending strength</b> .
Wu <i>et al.</i> <sup>17</sup>	2013	<b>Sintering parameters</b> affect the <b>thermoelectric properties</b> of CaCO <sub>4</sub> O <sub>9+δ</sub> .
An <i>et al.</i> <sup>18</sup>	2012	Increasing the <b>sintering temperature</b> improves the <b>transparency</b> and <b>hardness</b> of Lutetium aluminum garnet.



Overall, it is found that literature studies performed by researchers mainly focuses on the effects sintering parameters on the final microstructures and resulting material properties. The present doctoral research emphasized the importance of powder morphology and specifically of particle size on the subsequent ceramic processing (sintering). The goal was achieved by studying the impact of particle size distribution on grain sizes of several single/binary or ternary phase composites. The respective chapters 2-5 thus focus on accurate characterization of commercial powders for their particle sizes, sintering of these powders to obtain composites with variable grain sizes, the mechanical strength of respective composites and lastly analyze the role played by the heating rate of sintering via master sintering curves.

## **CHAPTER 2: PARTICLE SIZE DISTRIBUTION**

### **2.1 Motivation for particle size distribution studies**

The role of particle size on material properties has been presented in literature summary in the previous chapter 1. Concerning sintering of ceramics, particle size has been known to impact the green density of the compact. This density is affected by the extent of packing uniformity<sup>19, 20</sup> as well as packing density<sup>21, 22</sup> (how loosely or tightly particles are packed) inside the die. As a result, amount of porosity present in the final sintered sample can vary. Secondly, during sintering with the increase in temperature, powder particles start undergoing surface diffusion and combine to undergo grain growth expansion.<sup>23</sup> If the powder has agglomerated particles, it results variability to the extent of surface diffusion. Smaller particles will undergo rapid diffusion with temperature as compared to larger particles and thereby combine with each other to form large grains (surrounded by finer ones) to results in overall abnormal grain growth.<sup>24</sup> This non-uniformity can also cause pores, defects, and thereby leading to internal density fluctuations that affect sintering thereby affecting the overall performance of the specimen. Accurate particle size information of powders is thereby essential to obtain homogeneous, dense ceramic compact.

Previous research includes various advanced synthesis techniques like colloidal processing,<sup>25</sup> spray pyrolysis<sup>26</sup> that have produced fine ceramic oxide powders. These controlled processing techniques result in particles which are more homogenous in size, to synthesize a powder with narrow particle distribution. However, in general, the commercial powders of ceramic oxides are obtained by bulk traditional manufacturing processes that have less control over particle morphology leading to potentially wide distribution in particle sizes. Furthermore, a low emphasis is placed on powder characterization and treatment due to economic factors in case of large-scale industrial production.<sup>27</sup> Hence the typical procedure

followed by vendors to provide particle size information of a commercial powder as a single value (median size of the particles) as shown in **Table 1.1** labeled as “vendors size” lacks accuracy. This inaccurate information is critical for comprehending the validity post-experimental results obtained in many cases, this fact is explored in literature. For example, Zemetsova *et al.*<sup>28</sup> concluded that increase in alumina powder particle size (40 nm to 200 µm) synthesized by sol-gel method lead to decrease in overall flexural strength of the sintered composites. Instead of synthesized powders if commercial submicron and nano-powders of alumina are used without sufficient characterization processes, any unreliability in case of powder size measurements can affect the respective mechanical strength of sintered composites thereby leading to further errors in post-processing data of the respective specimens.

Thus, the current chapter primarily focuses on in-depth characterization of commercial powders in their respective individual phases as well as in their binary and ternary mixtures. Using the advanced experimental technique of dynamic light scattering (DLS) along with surface chemistry concepts (Zeta-potential) and high energy ball milling the aim of the present research was to obtain an entire distribution of particle size (30+/- 5 nm instead of just mentioning size as 30 nm) with minimum agglomeration. These results are essential to check the quality and homogeneity of powder purchased and to use further the accurate data obtained in next step of ceramic powder processing, i.e., sintering.

## **2.2 Powder information and properties**

The ceramic oxides used in the present research study are polycrystalline powders of Yttria-Stabilized Zirconia (8Y-ZrO<sub>2</sub>), Spinel (MgAl<sub>2</sub>O<sub>4</sub>), and Alumina (Al<sub>2</sub>O<sub>3</sub>). In general, these materials are used for diverse engineering applications precisely due to their optical/mechanical properties.

Polycrystalline 8Y-ZrO<sub>2</sub> due to its high refractive index of 2.2 and sizeable dielectric constant is an excellent candidate for an optical material.<sup>29</sup> Additionally, a high ionic conductivity of this material (due to yttria-doping) also makes it an excellent electrolyte for solid oxide fuel applications.<sup>30</sup> On the other hand, spinel exhibits high strength, and transparent properties in the mid-infrared region (4.5-5.5  $\mu\text{m}$ ).<sup>29</sup> It is commonly used in lenses, infrared-windows, and protective windshields in defense industry.<sup>31</sup> Lastly,  $\alpha$ -alumina or corundum ( $\alpha$ -Al<sub>2</sub>O<sub>3</sub>) is known for its corrosive resistance, hardness, and insulating properties; thus, its application is mostly in abrasives and polishing slurries.<sup>29</sup> It is important to note that the presence of a nano-/submicron-grained microstructure has also been observed to be a key reason for their superior mechanical strength,<sup>32</sup> optical transparency, thermal conductivity, and superplasticity.<sup>33</sup> Additional essential material properties of respected ceramics are listed in **Table 2.1** Furthermore, all the ceramic vendors were contacted for additional powder information that includes impurity analysis, results and method of particle size characterization, this information is summarized in **Table 2.2**.

**Table 2.1** Material properties of Ceramic oxides of Cubic Zirconia, Spinel and  $\alpha$ -Alumina.<sup>27,32-35</sup>

<b>Parameters</b>	<b>Cubic Zirconia (8Y-ZrO<sub>2</sub>)</b>	<b>Spinel (MgAl<sub>2</sub>O<sub>4</sub>)</b>	<b>Alumina (<math>\alpha</math>-Al<sub>2</sub>O<sub>3</sub>)</b>
Theoretical Density (g/cc)	6.010	3.579	3.987
Crystal structure	Cubic (Fm3m)	Cubic (Fd3m)	Trigonal (R3c)
Melting point (K)	2345	2408	2345
Elastic modulus (GPa)	218	277	215

**Table 2.2 Information related to particle size, impurities and characterization method regarding ceramic oxide commercial powders obtained from different vendors**

Powder/ Vendor	Size information	Method	Impurity analysis
8Y-ZrO <sub>2</sub> Tosoh Corp.	0.6 μm (D <sub>50</sub> size)	BET/Sieving	Purity: ZrO <sub>2</sub> + HfO <sub>2</sub> + Y <sub>2</sub> O <sub>3</sub> = >99.7 wt% Impurities: Al <sub>2</sub> O <sub>3</sub> , SiO <sub>2</sub> , Fe <sub>2</sub> O <sub>3</sub> = 0.01-0.1 wt%
8Y-ZrO <sub>2</sub> Skyspring.	0.3-0.5 μm (particle size)	SEM/TEM	Purity: 99.9% Impurities: Sm, Gd, Eu, B, Cd = ≤ 10ppm, Hf ≤ 300ppm
8Y-ZrO <sub>2</sub> Skyspring.	20 nm (Particle size)	SEM/TEM	ZrO <sub>2</sub> + HfO <sub>2</sub> = 86%, Y <sub>2</sub> O <sub>3</sub> = 13.5% Impurity: Fe <sub>2</sub> O <sub>3</sub> , Na <sub>2</sub> O, SiO <sub>2</sub> , TiO <sub>2</sub> , Al <sub>2</sub> O <sub>3</sub> = 0.002-0.03 wt%
α-alumina Skyspring.	40nm (Particle size)	TEM	Purity: > 98%, Fe <sub>2</sub> O <sub>3</sub> : 0.26%, MgO: 0.005%, SiO <sub>2</sub> : 0.033%
α-alumina Skyspring.	150nm (Particle size)	TEM	Purity: 97.26%, Impurity: H <sub>2</sub> O: 0.25% Ca, Fe, K, Na= 5-16 ppm
α-alumina Taimei.*	0.05-0.2 μm (particle size)	Sedigraph	Purity: 99.99% Impurity: K, Ca, Fe, Ti, Na, Mg, So, Cu < 25ppm
α-alumina Baikowski.	500 nm (Particle size)	TEM	Purity: N/A Impurity: Fe, Na, Si, Ca, K, Mg, = 5-23 ppm Ti, Cr, Mn, Ni, Cu, Zn ≤ 1ppm
Spinel Baikowski	0.2 μm (Particle size)	BET/TEM	Purity: ≥ 99% MgAl <sub>2</sub> O <sub>4</sub> Impurity: Fe, Na, Si, Ca = 6 - 41 ppm, S = 700 ppm
Spinel Sigma Aldr.	< 50nm	Sieving	-----N/A-----

\* Powder was obtained from Pred materials, USA

### 2.3 Powder characterization methods and experiments

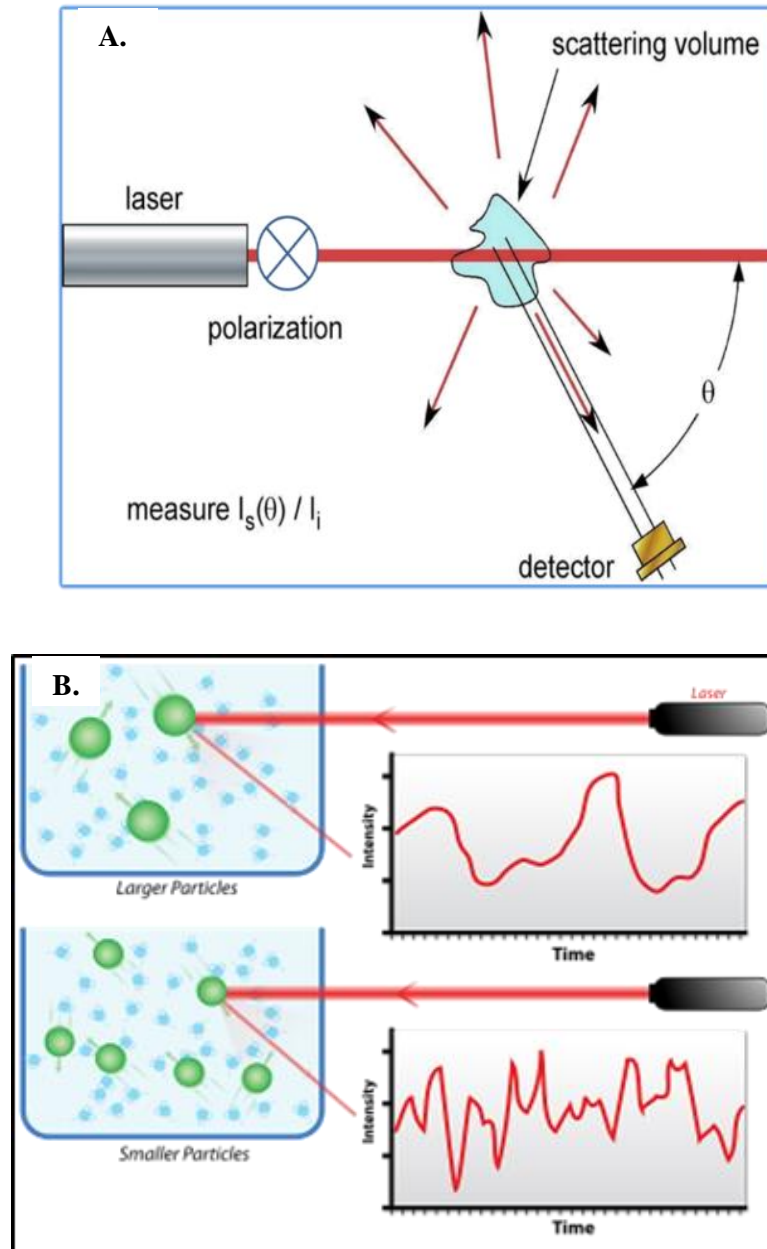
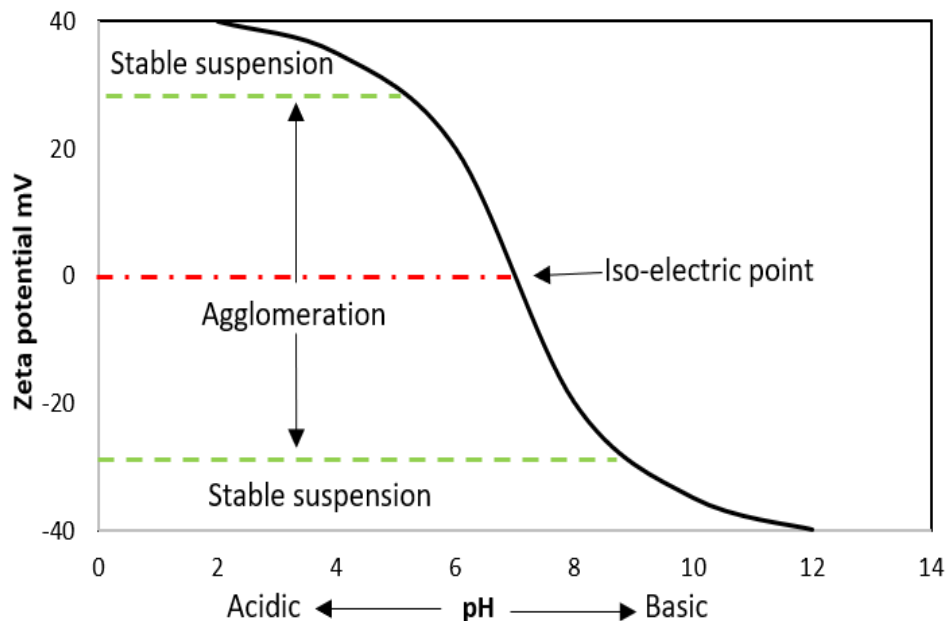


Figure 2.1 Dynamic light characterizing technique used for particle size distribution.<sup>34, 35</sup> Figure A highlights the schematics of laser diffraction system with laser pulse scattered by resulting particles and collected by a detector at an angle  $\Theta$ . Figure B indicates the variations in resulting scattering as a function of intensity over time by smaller and larger powder particles as they undergo Brownian motion in the dispersion solution.

Dynamic light scattering (DLS) is a well-known technique used to determine average particle size or diameter ( $D_{50}$ ) of particles over a broad range of powder sizes between 0.1 nm to  $<5 \mu\text{m}$ .<sup>36,37</sup> According to the literature,<sup>38-40</sup> the  $D_{50}$  measurement called as the hydrodynamic diameter is related to particle diffusion when immersed in a liquid and is considered to be the equivalent diameter of a spherically shaped body having same translational diffusion coefficient as the particle. Thus, for our purpose of powder measurements, this diametrical measurement was obtained by assuming the powder particles and their agglomerates being assumed having a spherical shape. It is cheap, easy to operate, and a non-destructive method used to measure a large number of particles thereby giving a size distribution profile of the resulting powder. The target powder is first suspended in a non-polar solvent, and a small batch is placed inside the load cell of the DLS equipment. It uses a laser source to illuminate the mobile powder particles governed by Brownian motion, that scatter light in all directions (**Figure 2.1A**). Depending upon the particle morphology, the intensity of scattering light fluctuates is measured which is related to particle size by Stokes-Einstein equation<sup>41</sup> (**Figure 2.1B**).

A fundamental requirement for sample preparation for DLS characterization is that the stability of the dispersion containing respective powder and the solvent.<sup>42, 43</sup> The accuracy of the particle size distribution results depends upon if the powder particles in the colloidal dispersion remain suspended throughout the measurement process. This problem arises because if the solution is unstable, then agglomeration of powder particles occurs, thereby resulting in considerable particles settling down. The resulting laser scattering only occurs for the small powder particles that remain suspended in the solution thereby leading to an error in overall particle size.



**Figure 2.2 Change in zeta potential concerning to pH in solution and respective stability of the suspension. The isoelectric point is the point where zeta potential is 0mV, i.e., the solution undergoes maximum deagglomeration.**

A known popular indicator of dispersion stability is surface chemistry concept of “Zeta potential.” Zeta potential is the charge associated with individual particle when it is suspended in a liquid also defined as the potential of the boundary layer, i.e., stern layer according to double layer theory.<sup>40, 44</sup> In case of submicron/nano-powder based dispersion, powder particles tend to stick each other either forming soft agglomerate due to weak Vander Waals forces of attraction when undergoing collision due to Brownian motion or either exist as hard aggregates held by strong chemical bond.<sup>45</sup> Zeta potential is vital to avoid as higher surface charge results in greater electrostatic repulsive forces among the particles to consequently remain suspended in the solution and thus, can be useful in reducing soft agglomeration. Information relating to suspension stability and zeta potential values has been presented in various studies<sup>46-49</sup> and summarized in **Figure 2.2** which indicates that zeta potential greater than  $\pm 30$  mV is a good indicator of a stable deagglomerated dispersion/suspension.



Since the current project involves characterizing commercial ceramic oxide powders of various particle size range, optimum sample preparation conditions are necessary to obtain a given stable suspension. Soft agglomerates in powders need to be removed so that the actual size represents the hard-aggregate particle size only. Thus, for this purpose we established following four factors that can be modified to eventually achieve high zeta potential values for the powder based dispersion:


1. As concluded from **Figure 2.2**, pH value and tendency (acidic /basic) of the solution affects the stability of the suspension. For the current study, for most of the dispersions, the pH is adjusted to acidic behavior (pH 3-4) by adding varying concentrations (0.1-0.001 N) of hydrochloric acid. A short experiment has been described to explain the pH effects on suspension stability in case of zirconia powders in the next section.
2. The choice of dispersion medium affects the surface charge of the particles thereby affecting the zeta potential. Therefore, it should be important to select a specific dispersion liquid that does not chemically affect the powder particles<sup>50</sup>; Common polar/non-polar solvents like water, ethanol, isopropanol were different candidates, and each has different dielectric constant and isoelectric point. For the current research DI water (dielectric constant =79) as dispersion liquid since it is found out to give the highest potential and thereby appropriate particle size.
3. The type and duration of dispersion/stirring method used to mix particles in the liquid also govern the agglomeration tendency and thereby zeta potential of the system. Various literature studies have highlighted the effects of type of ultrasonication and the duration on agglomeration of powders.<sup>51</sup> Thus, according to

empirical data for current ceramic oxide powder based dispersions, 15 minutes of stirring time followed by 15 minutes of ultrasonication bath was deemed sufficient to obtain stable dispersion conditions.

4. The stability of the dispersion is also determined according to dilution/concentration of the solution. For this purpose, the DLS system has powder loading limits for a given dispersion;<sup>39</sup> as highly diluted solution contains a low amount of particles which will lead to less scattering and thereby resulting in a less accurate sample size for particle size distribution. On the other hand, the concentrated solution will have more collisions among the mobile particles in the liquid leading to agglomeration and eventually sedimentation of the powder at the bottom. Furthermore, the solution will be more viscous and affect the parameters in Stoke's equation, thereby causing measurement errors.<sup>52</sup> For the current study, concentrations of ceramic oxide dispersions were adjusted between 0.05-0.1 vol% of the solution depending on theoretical powder density.

It is important to note that for obtaining particle size results in the present study, five different sample runs of the same solution were measured, and for every individual run, five readings for particle size were obtained regarding mean number distribution (mN). Mean number distribution(mN) is a statistical count of a given number of particles of the powder belonging to particular size range. To ensure the repeatability of results, another solution was made with same dispersion condition to get additional readings. It is important to note that particle size results in each powder in this study are an average of at least 50 size distribution readings necessary for accuracy and reliability purposes. Similarly, for zeta potential value of every powder is an average of a minimum of 5 different values from two solutions that are

prepared separately. Additionally, the specifications and the model image of the current machine are tabulated as follows:

<b>Machine details</b>	Nanotrac Wave 2	
<b>Manufacturer info</b>	Microtrac Inc., Montgomeryville, PA	
<b>Standard deviation</b>	$\pm 7$ nm	
<b>Instrument precision</b>	1.1% (20 runs)	
<b>Zeta potential</b>	$\pm 5$ mV	

Further preliminary experiments were performed to explore the effects of changes in pH and thereby resulting variations in zeta-potential values that are responsible for particle size distribution. These “Zeta potential mapping” experiments were performed on three different types of commercial zirconia powders ( $ZrO_2$ ). These commercial powders were pure monoclinic  $ZrO_2$ , yttria-stabilized tetragonal  $ZrO_2$ , and cubic  $ZrO_2$  or 8Y- $ZrO_2$  obtained from different vendors (sky spring. and Tosoh Corporation). Suspensions with different concentrations of powders ranging from 0.01 to 0.2 volume% in water were prepared and treated with 15min with stirring and ultrasonication (ultrasonication bath). The resulting solutions prepared were modified to different pH values between 3-11 using concentrated solutions of HCl and NaOH (0.1-0.001 N). DLS was used to measure the zeta potential and particle size of the resulting dispersions to obtain a curve like one shown in **Figure 2.2**.

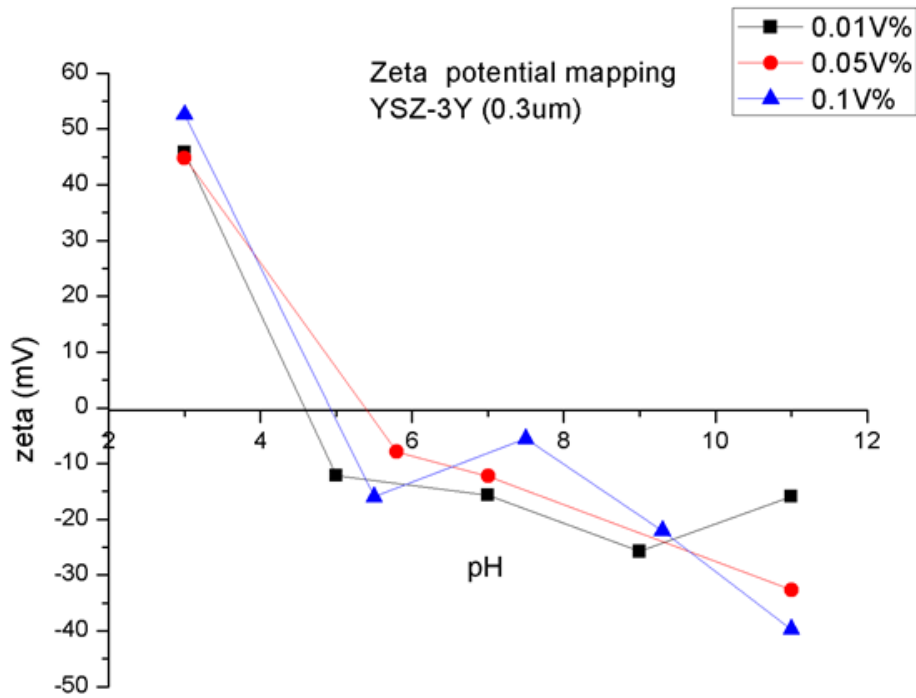


Figure 2.3 Zeta potential (mV) vs. pH values for increasing concentrations of YSZ-3Y or 3Y-ZrO<sub>2</sub> by volume %

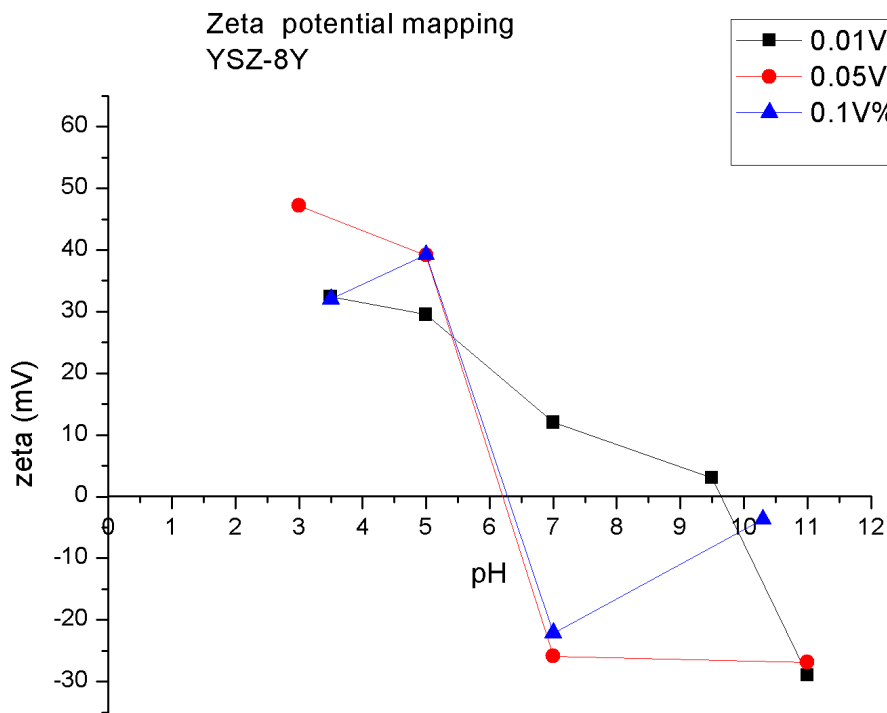
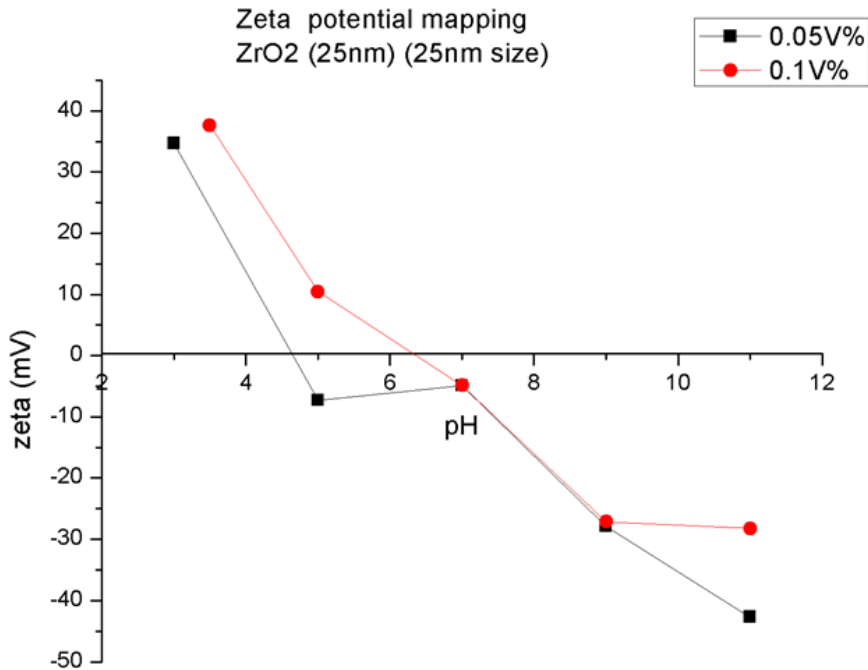


Figure 2.4 Zeta potential (mV) vs. pH values at various concentrations (vol %) of YSZ-8Y or 8Y-ZrO<sub>2</sub>



**Figure 2.5 Zeta potential (mV) vs. pH values at various concentrations of monoclinic ZrO<sub>2</sub>**

The results in **Figure 2.3**, **Figure 2.4** and **Figure 2.5** exhibit the changes in zeta potential values with variations in pH of the solution for given three zirconia powders. The isoelectric point or the point of complete deagglomeration (potential = 0 mV) was found to be in the acidic range of pH, i.e., 4-6 and was similar for monoclinic, tetragonal cubic zirconia commercial powders. The given results for isoelectric point for commercial powders of zirconia agree within the limits with respect to those obtained in literature for ZrO<sub>2</sub>,<sup>48</sup> 8Y-ZrO<sub>2</sub>, and 3Y-ZrO<sub>2</sub>,<sup>53</sup> thereby proving the validity of the experiments. Furthermore, we can also conclude that for different powder concentrations, we obtain the highest zeta value of >40 mV, i.e., indicating the most stable suspension was obtained for a pH value of 3. This result shows that the zirconia powder should be stabilized using acidic solutions for obtaining stable solution rather than in higher pH or basic range. We can assume that the negative charge of O<sub>2</sub><sup>-</sup> ions are attracted to positive H<sup>+</sup> anions that could form a stable stern layer which is responsible for higher zeta

potential values at lower pH. Thus, the given approach was used to optimize the other powders of cubic zirconia as well as spinel,  $\alpha$ -alumina to obtain maximum suspension stability. Reliable and accurate particle size distribution measurements could be then achieved for the given powders. An example of this methodology is provided in **Table 2.3** below, where stable solutions with particle size results of a representative 8Y-ZrO<sub>2</sub> powder were obtained by carefully optimizing parameters that vary the zeta potential, one at a time

**Table 2.3 Example of experimental matrix highlighting the effect of changes in four different factors (highlighted in italics) to affect the stability of the solution. The respective particle size is provided along with zeta potential results in the comment column for the given powder of 8Y-ZrO<sub>2</sub>(0.3-0.5  $\mu$ m). This approach was used to obtain the accurate size distribution of respective ceramic oxide powders. \*st= stirring time, Ul=ultrasonication time.**

<b>Ceramic powder</b>	<i><u>Conc.</u></i>	<i><u>Mixing condition</u></i>	<i><u>pH</u></i>	<i><u>Dispersant</u></i>	<b>Particle size (nm)</b>	<b>Comments</b>
8Y-ZrO <sub>2</sub> (0.3-0.5 $\mu$ m)	0.32g/25ml (0.13M)	St.:15min Ul: 5 min	~7	Water	103.2 $\pm$ 23.8	Zeta pot. = +55.0 mV  Excellent stability
8Y-ZrO <sub>2</sub> (0.3-0.5 $\mu$ m)	0.32g/25ml (0.13M)	St.:15min Ul: 5 min	~7	Ethanol	185.7 $\pm$ 0.3	Zeta pot. = 28.1 mV  Less stable more particle size than #1
8Y-ZrO <sub>2</sub> (0.3-0.5 $\mu$ m)	0.32g/25ml (0.13M)	St.:15min Ul: 5 min	~7	Isopropanol	51.1 $\pm$ 18.8	Less particle size than #1, but zeta potential is out of bounds

## 2.4 Particle size distribution results

**Table 2.4 Particle sizes of single-phase commercial ceramic oxide powders indicating the difference in particle sizes as provided by powder manufacturers and measured by dynamic light scattering.**

Powder	Vendor size (nm)	Designation	Initial size (D <sub>50</sub> ) by DLS (nm)
8Y-ZrO <sub>2</sub> (Sky spring)	300-500	(8Y-ZrO <sub>2</sub> ) <sub>1</sub>	97.5 ± 12
	20	(8Y-ZrO <sub>2</sub> ) <sub>3</sub>	120 ± 18
8Y-ZrO <sub>2</sub> (Tosoh)	600	(8Y-ZrO <sub>2</sub> ) <sub>2</sub>	240 ± 36
MgAl <sub>2</sub> O <sub>4</sub> (Baikalox)	200	(MgAl <sub>2</sub> O <sub>4</sub> ) <sub>1</sub>	242 ± 24
MgAl <sub>2</sub> O <sub>4</sub> (Sigma)	<50	(MgAl <sub>2</sub> O <sub>4</sub> ) <sub>2</sub>	295 ± 89
Al <sub>2</sub> O <sub>3</sub> (Sky Spring.)	40	(Al <sub>2</sub> O <sub>3</sub> ) <sub>1</sub>	160 ± 90
Al <sub>2</sub> O <sub>3</sub> (Baikowski.)	500	(Al <sub>2</sub> O <sub>3</sub> ) <sub>2</sub>	482 ± 130
Al <sub>2</sub> O <sub>3</sub> (Taimei)	100-300	(Al <sub>2</sub> O <sub>3</sub> ) <sub>3</sub>	155 ± 52
Al <sub>2</sub> O <sub>3</sub> (Skyspring)	150	(Al <sub>2</sub> O <sub>3</sub> ) <sub>4</sub>	274 ± 70

The column in **Table 2.4** is labeled as “vendor size” which indicates the size information provided by the powder manufacturers and while the size results obtained from our dynamic light scattering (DLS) experiments labeled as “initial D<sub>50</sub> size”. Comparing the results from these two sub-columns, we find considerable differences in values in almost 6 out of the whole nine powders characterized. In some cases, measured particle sizes of powders are greater than

twice the vendor size (example-(8Y-ZrO<sub>2</sub>)<sub>3</sub>, (Al<sub>2</sub>O<sub>3</sub>)<sub>1</sub>) while in other cases their D<sub>50</sub> sizes are smaller (8Y-ZrO<sub>2</sub>)<sub>1</sub>, (8Y-ZrO<sub>2</sub>)<sub>2</sub>, (MgAl<sub>2</sub>O<sub>4</sub>)<sub>1</sub>) than size provided.

A major factor in these differences lies in the accuracy of the data of vendor sizes which was emphasized in the motivation **section 1.1** before. These inconsistencies are primarily due to the measurement techniques used by vendors for displaying their size information. After confirming with respected powder manufacturers, it was found out that the techniques used for particle size characterization by commercial powder vendors were mainly from sieving of powders or analyzing images obtained from microscopy techniques of SEM and moreover TEM; as represented in **Table 2.2**. The sample size in these measurements can be minimal, i.e., regarding few particles. Therefore, for accurate particle size distribution of entire powder, since commercial powders are rarely of single shape and size, large sampling is required, and imaging techniques prove to be expensive and time-consuming. Furthermore, it is hard to incorporate the presence of hard/soft particle agglomerates into one single reading of particle size result. This limitation is also observed when powder size is assumed to be less than the size of the sieve through which it is passed. On the other hand, the stable powder dispersions in DLS contains a large sample size (thousands of particles), and hence we could map the entire distribution of the powder by giving the upper, and the lower limit of particles present through standard deviation values. This method was proved to be further helpful if the powder is bimodal as it can display the values of the two-particle size peak value in the powder (discussed in multiphase powder characterization section). Further, pursuing dynamic light scattering that involves the concept of Brownian motion can be more favorable for characterizing non-spherical shaped particles rather than manually selecting the largest dimension of the resulting particles for from SEM images. Thus, as pointed out before in the motivation section 1.1, the



DLS results are more helpful in case of experiments which requires multiple nano- or submicron ceramic powders with minimal difference in sizes.

These observations are found to be coherent with a similar study performed by Souza *et al.*<sup>54</sup> although the literature data obtained for a single powder of TiO<sub>2</sub> instead of the extensive nature of the present study. The given researchers concluded that readings from the DLS method (stated as mN in the present study, DLS-number in corresponding literature) gave a better approximation of the size of the commercial Titania powder than the respective TEM measurements. Hence for the given study, characterization of the necessary ceramic oxide powders of 8Y-ZrO<sub>2</sub>, alumina, and spinel by dynamic light scattering method was considered to be more accurate and reliable than using size information obtained from vendors. This method was significant for the sake of current particle-grain size research and the nuclear fuel project since different nano/submicron grain-sized and high-density composites must be obtained with the primary availability of fine powders being of utmost importance before sintering.


A secondary application use of present particle size processing technique using zeta potential can be found in Frank *et al.*<sup>55</sup> where the individual alumina particles were characterized before they were fabricated into solid compacts by using freeze casting process through magnetization. The author observed a discrepancy between DLS measured and supplier provided particle sizes for submicron alumina powders. The measured particle sizes were 195nm, 225nm and 350nm as compared to supplier estimations of 150nm, 300nm, and 500nm respectively. The resulting entire size distribution data of powders allowed calculation of extent of surface magnetization per particle size that occurs during freeze casting for individual powders. This calculation allowed to analyze the extent of adsorption of super-paramagnetic

magnetite particles on individual alumina powders and thereby optimize the efficiency of the given method. The variations in surface magnetized powder also affected the tendency of growth of lamellar microstructure in the respective sintered scaffolds which were thereby responsible for improvements in the respective mechanical properties notably, Young's modulus and strength.

## **2.5 Effect of milling in particle size distribution**

The previous section emphasized on accurate particle size distribution of ceramic oxide powders especially for a current research study that is related to fine sintering composites. The accuracy is achieved mainly by reducing the amount of particle size agglomeration or in other terms soft agglomerates. The suspension stability studies cannot alone be sufficient to eliminate the presence of soft agglomerates. This fact can be more prominent in especially nano/-submicron-sized powders where Van der Waal's adhesive forces between particles are strong enough to resist the four factors. Hence additional mechanical treatments of the powder itself have been carried out by using high energy planetary ball milling. The milling conditions were optimized for preferred dry milling of the powders. Wet milling method was not used to avoid the presence of organic residues/solvents and effects on particle sizes/agglomeration from heat treatment during powder drying. Since this process is performed without any solvents, short runs of high-speed milling were performed for dry mixing. Due to the hard nature of  $\text{Al}_2\text{O}_3$ , 8Y-ZrO<sub>2</sub> and MgAl<sub>2</sub>O<sub>4</sub> powder particles, tungsten-carbide milling bowls and vials are used. Further information on the planetary ball mill used as well as regarding the dry milling method in the current research is stated accordingly in **Table 2.5**

**Table 2.5 Specifications of the planetary milling machine and the dry milling conditions.**

<b>Machine details</b>	Frtisch Pulverisette 5 planetary ball mill	
<b>Manufacturer info</b>	Fritsch GmbH, Germany	
<b>Milling cycle/Batch</b>	12 cycles per batch, 3 batches of milling	
<b>Cycle time/speed</b>	3 min at 220rpm	
<b>Total milling time</b>	36 minutes	
<b>Milling media</b>	WC-bowl (50ml volume), WC-balls (10mm)	

**Table 2.6 Experimental results obtained for different batches of ball-milling of few ceramic powders in increasing amounts of milling time and the effects on particle size distribution. Note that the respective size distributions were carried out at stable zeta potential suspensions (>30mV) Batch 1 is 12 cycles, Batch 2 is 24 cycles, and Batch 3 is 36 cycles respectively.**

<b>Powder</b>	<b>Vendor size (nm)</b>	<b>Initial size (nm)</b>	<b>Milled Size Batch 1(nm)</b>	<b>Milled Size Batch 2(nm)</b>	<b>Milled Size Batch 3(nm)</b>
(8Y-ZrO <sub>2</sub> ) <sub>1</sub>	0.3-0.5 μm	97.5 ± 12	83 ± 6	80 ± 14	82 ± 14
(8Y-ZrO <sub>2</sub> ) <sub>3</sub>	20 nm	120 ± 18	121 ± 27	81 ± 14	96 ± 23
(8Y-ZrO <sub>2</sub> ) <sub>2</sub>	90 nm	240 ± 36	209 ± 52	168 ± 39	178 ± 17
(MgAl <sub>2</sub> O <sub>4</sub> ) <sub>2</sub>	<50 nm	295.5 ± 80	208 ± 48	182 ± 42	150 ± 41
(MgAl <sub>2</sub> O <sub>4</sub> ) <sub>1</sub>	300 nm	242 ± 24	108 ± 15	98 ± 17	84 ± 15
(Al <sub>2</sub> O <sub>3</sub> ) <sub>1</sub>	40 nm	160 ± 90	107 ± 72	N/A	N/A
(Al <sub>2</sub> O <sub>3</sub> ) <sub>2</sub>	500 nm	482 ± 130	274 ± 53		
(Al <sub>2</sub> O <sub>3</sub> ) <sub>3</sub>	100-300nm	155 ± 52	149 ± 21		
(Al <sub>2</sub> O <sub>3</sub> ) <sub>4</sub>	150 nm	274 ± 70	231 ± 54	N/A	N/A

The results of multiple planetary ball milling run on commercial ceramic powders is shown in **Table 2.6**. it can be concluded in almost all the powders of zirconia and spinel in the table; the use of ball milling helps in powder characterization by eliminating agglomerates; as indicated by lower average particle size results with narrower standard deviation. In case of Spinel ( $\text{MgAl}_2\text{O}_4$ )<sub>1</sub> (Baikalox) powder, the initial particle size measured by DLS are reduced by as much as 50% as indicated after milling (as shown by values in batch 1-3 milling). Thus, the results corroborate with literature studies highlighting the refinement in particle size due to milling by other researchers.<sup>56-59</sup> Additionally, it was observed that the first run of ball milling, i.e., batch one milled particle size results showed maximum reductions in data when compared to initial readings. Other batches 2 and 3 of the powder obtained by additional ball milling lowers the particle size significantly (considering standard deviation of values) only in Spinel 150nm powder. Especially in case of alumina powders, the particle sizes were not affected significantly by standard deviations and hence no further batch 2&3 milling results have been noted in **Table 2.7**. In fact, in some instances, additional planetary milling of powders caused a slight increase in average size in  $(8\text{Y-ZrO}_2)_2$  and  $(8\text{Y-ZrO}_2)_3$  powders. Thus, overall planetary milling was efficient in breaking up soft agglomerates, but over milling the powder could also potentially result in re-agglomeration by the increased electrostatic attraction between particles; a phenomenon which has also been observed in the literature.<sup>60</sup>

To summarize, we can conclude that planetary ball milling and accurate particle size results with stable dispersions help to determine optimum milling conditions to obtain a uniform, deagglomerated single-phase powders. For additional supplemental information, average size distribution plots of one of  $(8\text{Y-ZrO}_2)_2$ ,  $(\text{Al}_2\text{O}_3)_4$  and  $(\text{MgAl}_2\text{O}_4)_1$  powders have been provided in **Figure 2.6A&B**. Furthermore, SEM micrographs have also been provided in

figure **Figure 2.7** that shows the powder morphology of as-received powders (left figures) and respective powders after milling(right) for additional information.

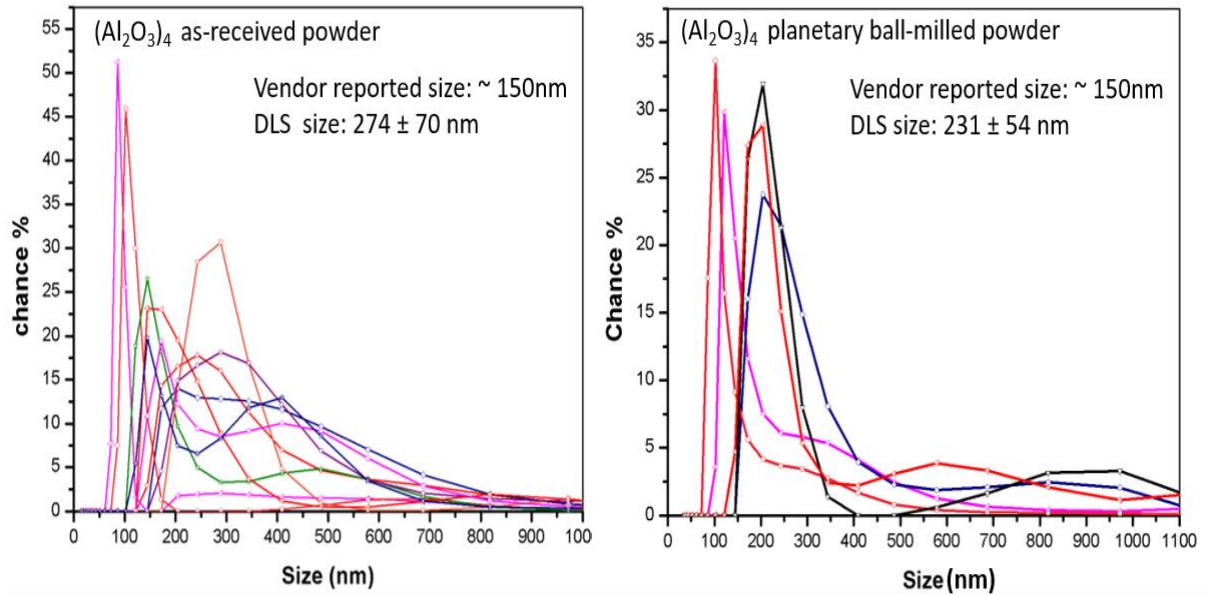


**Figure 2.6A Particle size distribution by DLS of individual sample powder of (Al<sub>2</sub>O<sub>3</sub>)<sub>3</sub> (Fig. E, F) single phase ceramic size powders. The results about change in particle sizes before and after milling are highlighted.**

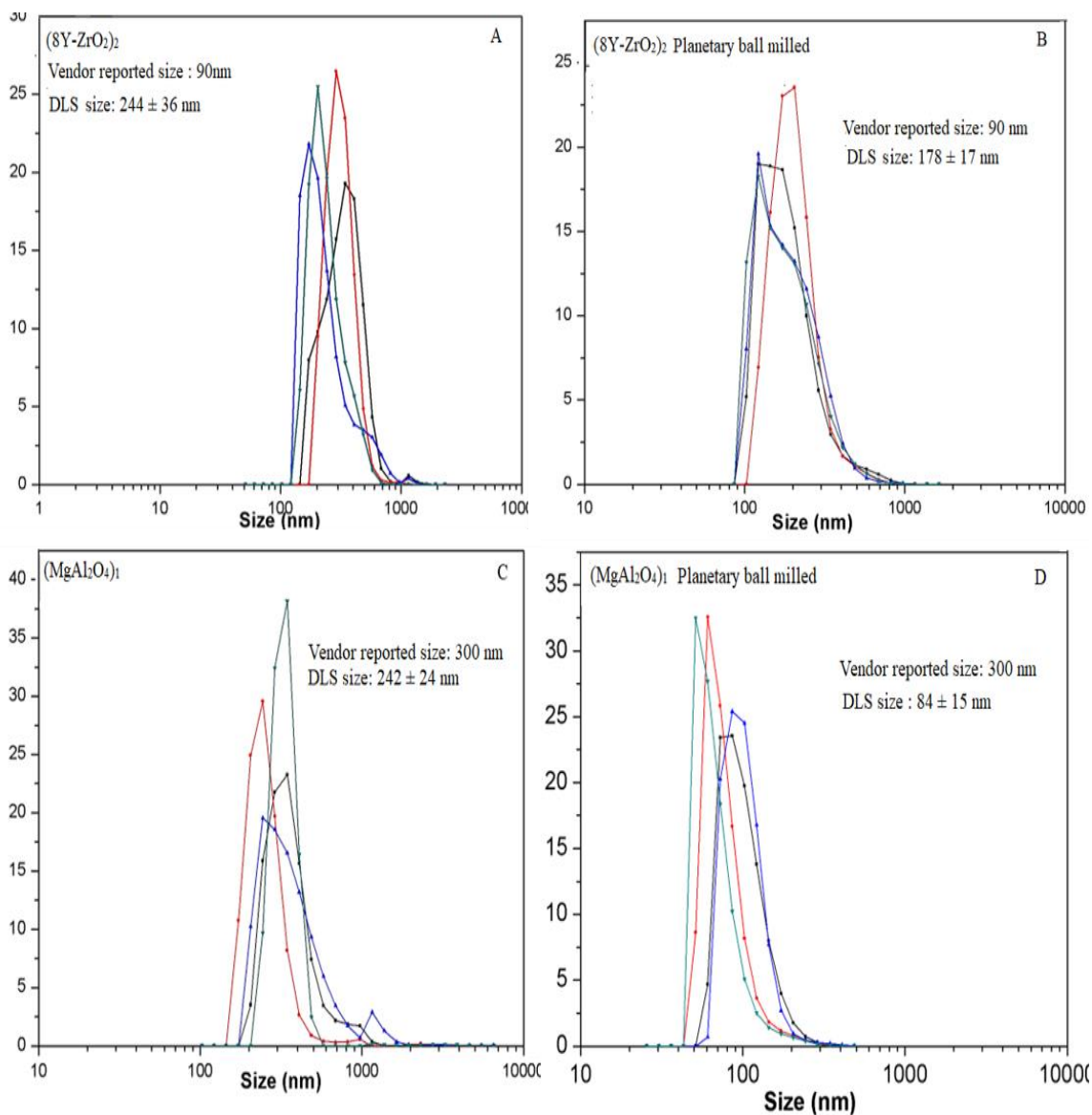


**Figure 2.6B Particle size measurements by DLS of commercial powders of  $(8Y-ZrO_2)_2$  as-received from the vendor in fig. A,  $(8Y-ZrO_2)_2$  after ball milling in fig. B,  $(MgAl_2O_4)_1$  as-received from the vendor in fig. C, and  $(MgAl_2O_4)_1$  in Fig. D after undergoing planetary milling. Each measurement curve is an average of 5 runs.**

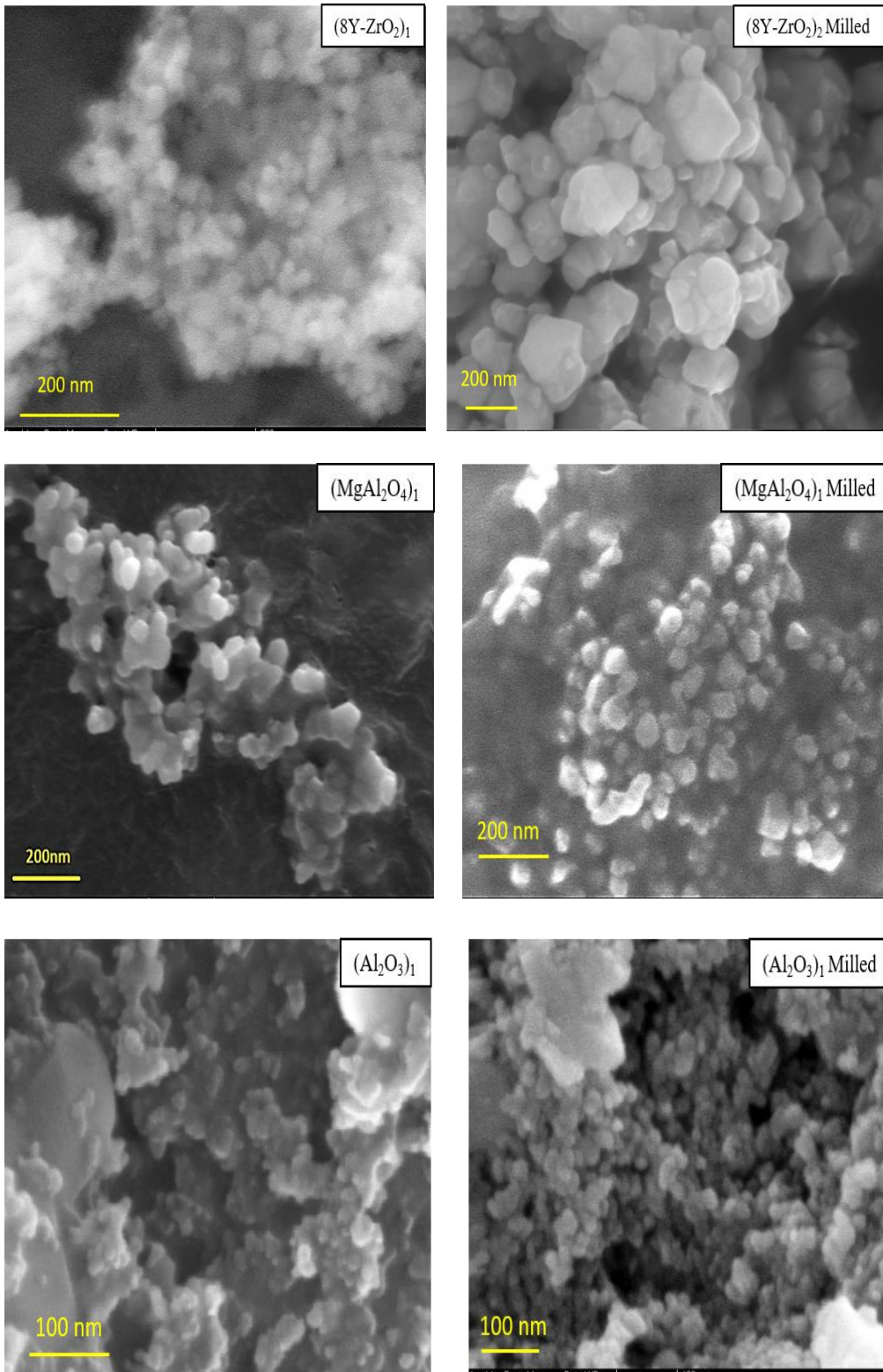


**Figure 2.7 SEM micrographs of as received(left) and milled powder(right) of single-phase ceramic oxides of 8Y-ZrO<sub>2</sub> (in the previous page), MgAl<sub>2</sub>O<sub>4</sub> and Al<sub>2</sub>O<sub>3</sub> (present page)**

## 2.6 Particle size measurements and milling of multiphase powder mixtures

**Table 2.7 Particle size distribution measurements of binary and ternary phase powder mixtures of 8Y-ZrO<sub>2</sub>, MgAl<sub>2</sub>O<sub>4</sub>, and Al<sub>2</sub>O<sub>3</sub>-based ceramic oxides. The mixtures are in equal proportion by volume, i.e., 50-50 in case of binary mixtures and 1/3-1/3-1/3 in case of ternary phase. The last column indicates the high zeta potential values of stable dispersions necessary to characterize these powders.**

	<b>Powder</b>	<b>Particle size DLS (nm)</b>	<b>Zeta Potential (mV)</b>
1	(8Y-ZrO <sub>2</sub> ) <sub>1</sub> /(MgAl <sub>2</sub> O <sub>4</sub> ) <sub>1</sub>	91 ± 15	47 ± 3
2	(8Y-ZrO <sub>2</sub> ) <sub>2</sub> /(MgAl <sub>2</sub> O <sub>4</sub> ) <sub>1</sub>	204 ± 38	56 ± 2
3	(8Y-ZrO <sub>2</sub> ) <sub>1</sub> /(Al <sub>2</sub> O <sub>3</sub> ) <sub>1</sub>	98 ± 17	50 ± 8
4	(8Y-ZrO <sub>2</sub> ) <sub>2</sub> /(Al <sub>2</sub> O <sub>3</sub> ) <sub>3</sub>	173 ± 43	40 ± 8
5	(8Y-ZrO <sub>2</sub> ) <sub>1</sub> /(Al <sub>2</sub> O <sub>3</sub> ) <sub>3</sub>	92 ± 14	48 ± 4
6	(8Y-ZrO <sub>2</sub> ) <sub>2</sub> /(Al <sub>2</sub> O <sub>3</sub> ) <sub>2</sub>	207 ± 33	56 ± 4
7	(Al <sub>2</sub> O <sub>3</sub> ) <sub>1</sub> /(MgAl <sub>2</sub> O <sub>4</sub> ) <sub>1</sub>	143 ± 25	53 ± 3
8	(Al <sub>2</sub> O <sub>3</sub> ) <sub>2</sub> /(MgAl <sub>2</sub> O <sub>4</sub> ) <sub>1</sub>	201 ± 38	61 ± 3
9	(Al <sub>2</sub> O <sub>3</sub> ) <sub>3</sub> /(MgAl <sub>2</sub> O <sub>4</sub> ) <sub>1</sub>	147 ± 22	55 ± 3
10	(8Y-ZrO <sub>2</sub> ) <sub>1</sub> /(MgAl <sub>2</sub> O <sub>4</sub> ) <sub>1</sub> /(Al <sub>2</sub> O <sub>3</sub> ) <sub>1</sub>	100 ± 26	40 ± 3
11	(8Y-ZrO <sub>2</sub> ) <sub>2</sub> /(MgAl <sub>2</sub> O <sub>4</sub> ) <sub>1</sub> /(Al <sub>2</sub> O <sub>3</sub> ) <sub>2</sub>	204 ± 43	56 ± 6
12	(8Y-ZrO <sub>2</sub> ) <sub>2</sub> /(MgAl <sub>2</sub> O <sub>4</sub> ) <sub>1</sub> /(Al <sub>2</sub> O <sub>3</sub> ) <sub>3</sub>	197 ± 52	56 ± 4
13	(8Y-ZrO <sub>2</sub> ) <sub>1</sub> /(MgAl <sub>2</sub> O <sub>4</sub> ) <sub>1</sub> /(Al <sub>2</sub> O <sub>3</sub> ) <sub>3</sub>	118 ± 27	46 ± 8



One of the primary goals of current doctoral research is to sinter binary and ternary phase ceramic oxides composites with grain sizes varying between nano to submicron grain sizes. For this purpose, it is necessary to obtain an accurate characterization of mixed powders for resulting multiphase composites. This characterization is also necessary to study effects of respective “particle size of mixtures on respective grain size.” Thus, the commercial powders of 8Y-ZrO<sub>2</sub>, MgAl<sub>2</sub>O<sub>4</sub>, and Al<sub>2</sub>O<sub>3</sub> were mixed in equal proportions by volume to obtain different multiphase powders; these powders are designated accordingly in **Table 2.7**. Planetary ball milling was again used to performing mixing using the same dry milling conditions as noted in **Table 2.5**

A significant aspect of this research study is the obtain accurate DLS characterization of multiphase powders by mixing different single-phase powders. These size results for several binary phases and ternary phases powder results are presented in **Table 2.5**. The results for binary mixtures indicates most of the particle size of binary powders are in the range of 100-200nm. These values are consistent with the milled results individual powder particle sizes discussed in **Table 2.6** without significant aggregation. The mixture powders with average particle sizes closed to 200nm have higher-standard deviations and thus are also validated as the corresponding individual phased powders ((8Y-ZrO<sub>2</sub>)<sub>2</sub>, (Al<sub>2</sub>O<sub>3</sub>)<sub>2</sub>) have higher particle sizes. Particle size results tabulated for the different ternary phase mixtures characterized in **Table 2.6** and are observed in the same range between 100-200nm. Thus, the current experimental particle size methods are more reliable than just using an analytical method of the rule of mixtures that outputs a single average size of the multiphase powder mixture. DLS plots of milled binary/ternary phase powders are provided as a supplemental data in **Figure 2.8**.

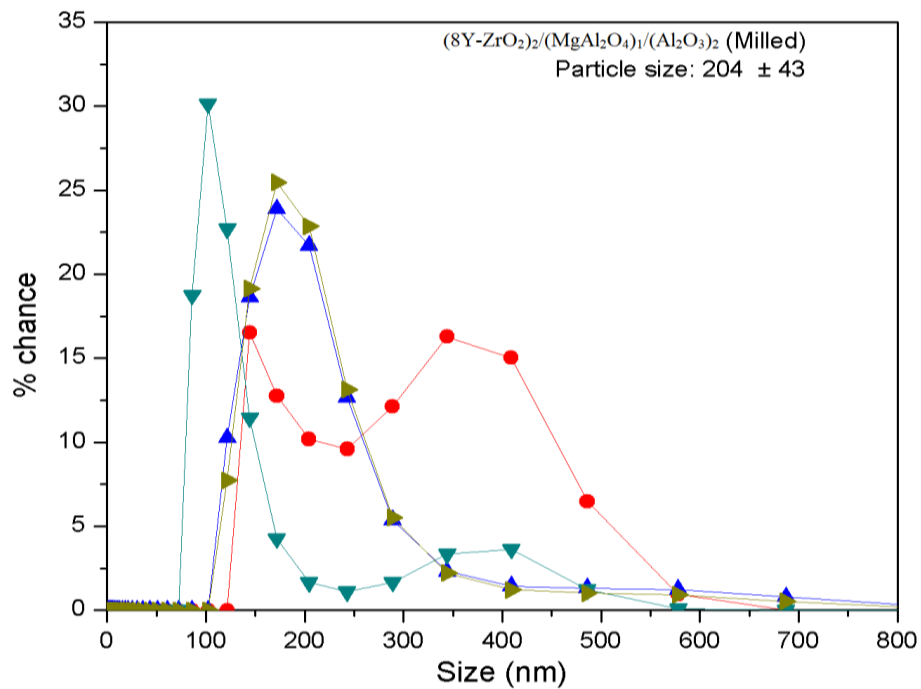
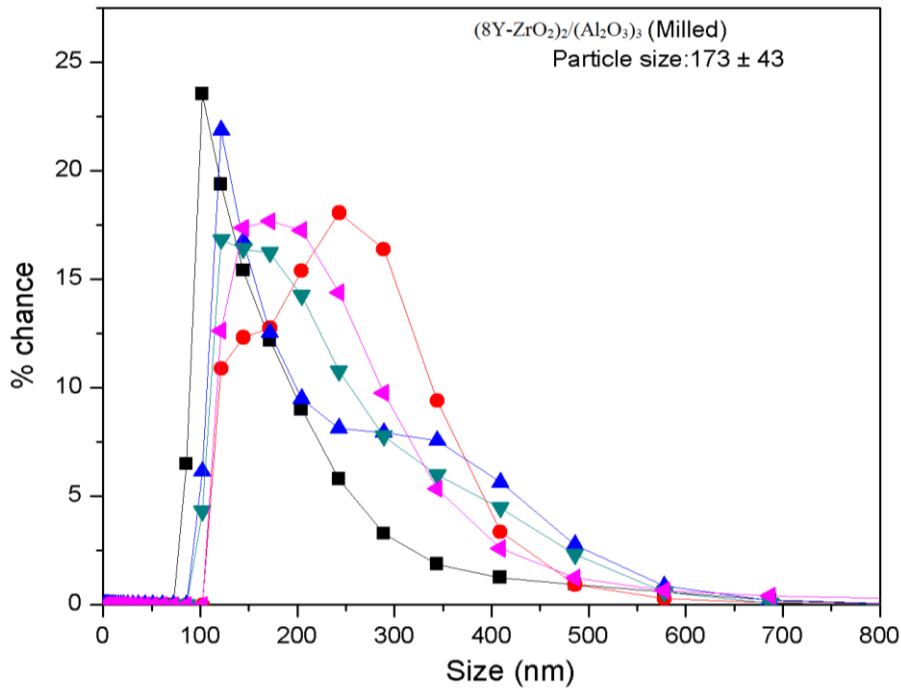


**Figure 2.8** Particle size distribution results obtained by DLS of binary sample powder of (8Y-ZrO<sub>2</sub>)<sub>2</sub>/(Al<sub>2</sub>O<sub>3</sub>)<sub>3</sub>, and (8Y-ZrO<sub>2</sub>)<sub>2</sub>/(MgAl<sub>2</sub>O<sub>4</sub>)<sub>1</sub>/(Al<sub>2</sub>O<sub>3</sub>)<sub>2</sub> ternary phase ceramic size powders.

## 2.7 Conclusion

The motivation, results, and discussion in chapter 2 have highlighted the significance of characterizing commercial ceramic oxide powders using the advanced and reliable technique of dynamic light scattering of resulting powder based stable suspensions over traditional powder information provided by vendors. The respective powder refining to further attain accurate particle size by planetary ball milling is also summarized. The binary and ternary equal volume mixtures of powders have also been obtained and efficiently characterized. This information played an essential part in sintering of these powders to obtain different grain size composites as described in the next chapter 3.

Chapters 2, in part, are currently being prepared for submission for publication of the material. Karandikar, Keyur; Graeve, Olivia A.; Mecartney, Martha L.; Ohtaki Kenta; Travis, Austin; Evokodimiko Ekaterina; Cummings, Kira. The dissertation/thesis author was the primary investigator and author of this material under the title “Correlation between powder particle size and sintered grain size distributions in ceramic oxides: A spark plasma sintering study.” The thesis author was responsible for extensive particle characterization, ball milling, sintering, and grain growth analysis of ceramic oxide single/multiphase composites.

## CHAPTER 3: SINTERING RESULTS & PARTICLE-GRAIN SIZE CORRELATION

### 3.1 Spark Plasma Sintering: Background and motivation

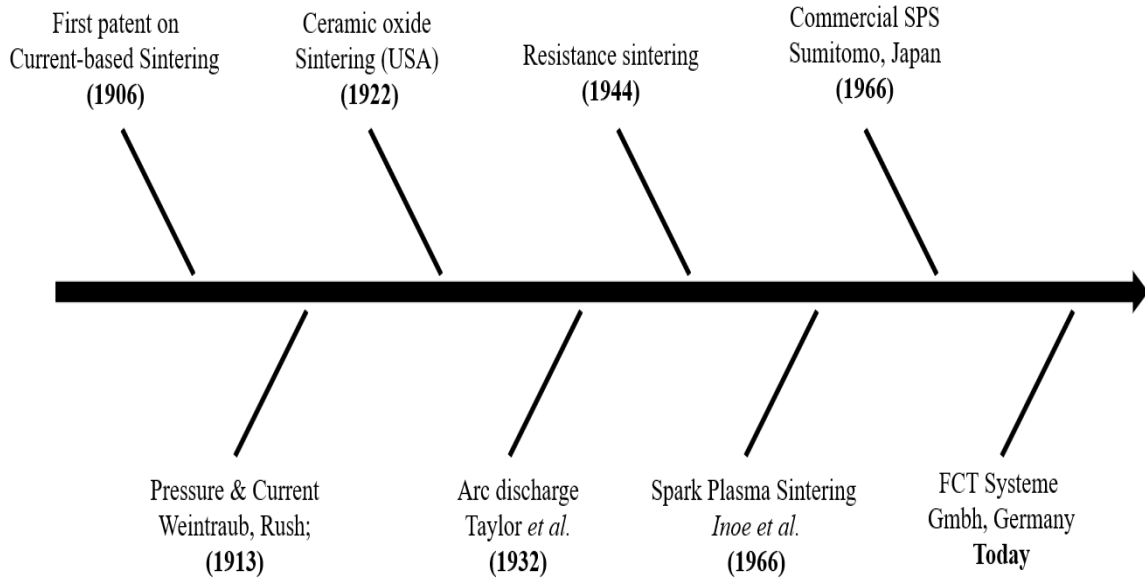


**Figure 3.1** Timeline diagram regarding the background and the history of spark plasma sintering process.<sup>61, 62</sup>

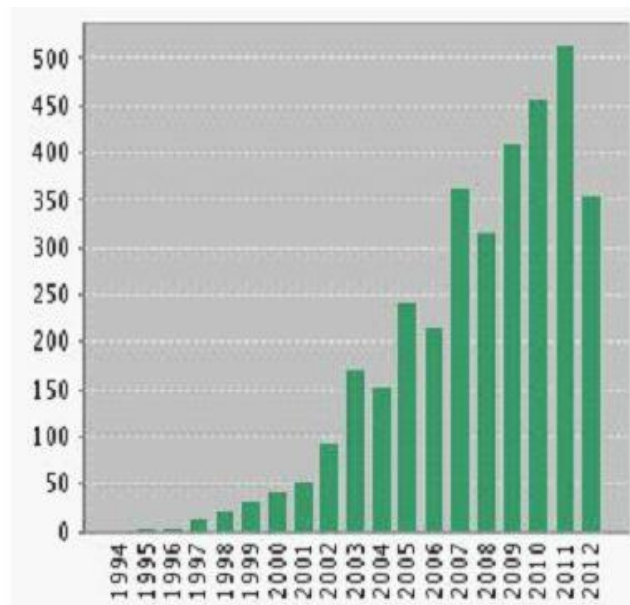


**Figure 3.2** Publication history and trends related to use of spark plasma sintering to process potential advanced engineering materials.<sup>63</sup>

The use of advanced ceramic processing technique of Spark Plasma Sintering (SPS) has played a key part in the current research to obtain various nano- to micron grain sized single and multiphase composites. These composites were sintered from commercial ceramic oxide powders as characterized in **chapter 2**. Spark plasma sintering (SPS) has found wide application in the processing of advanced materials especially for the variety of ceramics<sup>64-66</sup> and metals/glasses.<sup>67-69</sup> The technique offers numerous advantages, which include high heating rates (in some cases greater than 500 °C/min), fast sintering times (generally <10 minutes), resulting in highly dense compacts (>99% theoretical density) and fine grain sizes. Further, as compared to other sintering techniques like hot-pressing, conventional sintering, SPS includes additional advantages like ease of operation, reliability, and safety. Lastly, the efficient sintering of commercial powders is achieved with fewer or no additives to the fabrication process.<sup>70</sup>

A summary of the history of spark plasma sintering technique is illustrated in the timeline in **Figure 3**. While the impact of electric current in sintering was studied in 1906, pressure-based and electric discharge sintering was experimented by researchers in the later years. Spark Plasma Sintering was first researched and patented in the USA by Inou *et al.*<sup>71</sup> in 1966, while it took almost 25 years before this process was commercially made available in 1990 in Japan by Sumitomo Heavy industries limited. Since then for the past three decades, the popularity of SPS has grown at an exponential rate as indicated by the number of published papers in **Figure 3.2** due to its contribution in obtaining novel property based materials. It has also led to a large material processing based patents and has thus played a key role in making progress to obtain materials modern engineering applications.

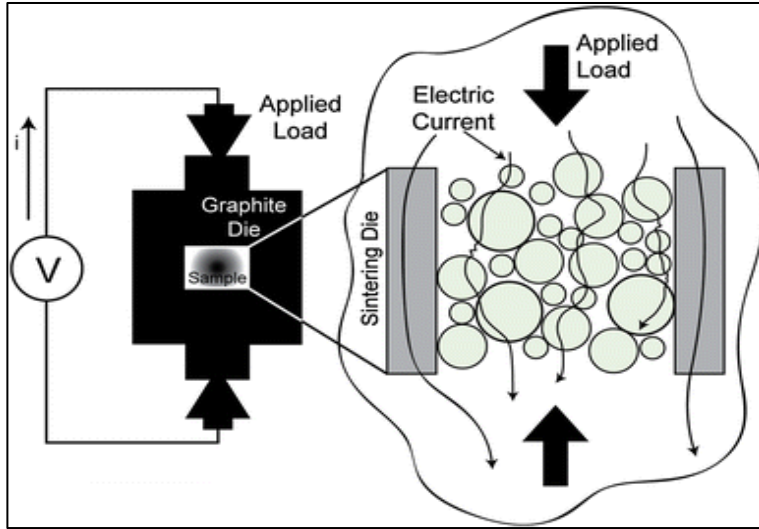


**Figure 3.3 Principle set up for spark plasma sintering furnace**

The principle mechanism behind spark plasma sintering is the application of uniaxial pressure and direct current pulses along with temperature profile under vacuum/low atmospheric conditions directly thereby aiding rapid consolidation of powders as exhibited in **Figure 3.3**. During the sintering process by SPS, various densification mechanisms play an important role in obtaining a uniform and fine microstructure.<sup>61, 72</sup> As observed in conventional sintering, different transport mechanisms of the surface, grain boundary, and lattice diffusion are involved in the sintering and densification process during SPS.<sup>63</sup> In addition to these factors, the presence of high current (kA) small electric pulses applied to the powder compact between the dies leads to the formation of localized heating due to “Joule’s heating” occurring at the surface of the particles which further helps in rapid densification of powder. Furthermore, as described in literature<sup>70, 73, 74</sup>, the densification tendency of ceramic powders during SPS is governed by two processes that are opposite. On the one hand, plastic deformation is primarily responsible for this compaction, when applied pressure during sintering is higher than the yield stress of the densified ceramic powder material. Alternatively, the electric pulse effect results in the creation of high surface charged particles of the powder (ceramic powders are mainly

non-conductive). The excess charge leads to ionization of gases presents in pockets between two particles of loosely packed powder in the die, thereby causing melting of the powder due to localized heating at its surface; resulting in a homogenous microstructure and a solid compact with less porosity. Depending on powder properties (electrical, mechanical) and morphology, the densification tendency can be primarily due to plastic deformation or surface melting of particles.

### 3.2 Experimental setup and sintering load diagrams



**Figure 3.4** Photograph of spark plasma sintering furnace at Alfred University, New York. The graphite die-cone arrangement along with the sample inside the die is shown in the inset picture to the right.

The ceramic oxide powders were loaded and pre-pressed into a graphite punch die setup ( $\text{Ø} = 18.75 \text{ mm}$ ) using a 3-ton hydraulic press at 3MPa. High purity and density graphite die obtained from were used for this purpose. They were then placed inside the chamber of a spark plasma sintering (SPS) furnace (Model HP D25, FCT Systeme, Frankenblick, Germany) in the

given die-cone setup (onset picture in **Figure 3.4**) and subjected to a continuous vacuum atmosphere during the sintering process. The die was wrapped around a graphite jacket that helps in maintaining a uniform temperature between the center of the sample and outside die surface. This setup helped to avoid the temperature gradients across the radius of the sample pellet thereby aiding uniform sintering of the powder. The sintering temperatures were measured using an optical pyrometer (effective at temperatures  $>450^{\circ}\text{C}$ ) aimed at the surface of the die at the center of the sample. The sintered pellets obtained were 19 mm in diameter and about 5 mm in thickness with varying densities depending on sintering parameters. The range of different sintering parameters used in the present research is tabulated in **Table 3.1** given below.

**Table 3.1 Range of sintering parameters used to obtain variable grain sized and dense ceramic composites.**

Ceramic oxide	Press. MPa	Sintering temperature	Hold time	Heating rate $^{\circ}\text{C}/\text{min}$	Cooling rate $^{\circ}\text{C}/\text{min}$	%Theoretical density range
8Y-ZrO <sub>2</sub>	100	950°C-1300°C	5	10	10	88.0% to > 99%
MgAl <sub>2</sub> O <sub>4</sub>	100	940°C-1300°C	5	10	50	78% to > 99%
Al <sub>2</sub> O <sub>3</sub>	100	900°C-1300°C	5	10	50	81% to > 99%
8Y-ZrO <sub>2</sub> / MgAl <sub>2</sub> O <sub>4</sub>	100	1000°C-1300°C	5	100	50	91% to >99%
Al <sub>2</sub> O <sub>3</sub> / MgAl <sub>2</sub> O <sub>4</sub>	100	1000°C-1300°C	5	100	50	81% to >99%
8Y-ZrO <sub>2</sub> / /Al <sub>2</sub> O <sub>3</sub>	100	1000°C-1300°C	5	100	50	80% to >99%
8Y-ZrO <sub>2</sub> / MgAl <sub>2</sub> O <sub>4</sub> / Al <sub>2</sub> O <sub>3</sub>	100	950°C-1300°C	5	100	50	63% to >99%

As discussed in the introduction to fulfill the main goals of this doctoral research we needed to obtain single/multiphase ceramic composites of variable grain sizes along with high



density (>90% theoretical density). Apart from using ceramic powders with different particle size, sintering temperature was the key SPS parameter that was optimized to obtain these compacts. As a starting point, an important experimentally obtained plots, i.e., load diagrams were used to predict resulting density of sintered composite for a given set of sintering parameters. These loading diagrams are graphical plots of sintering temperature, the displacement of the top and bottom pistons/electrodes, piston speed (rate of piston displacement) on Y-axis as a function of sintering time on X-axis. The broad spike or “hump” in the speed profile simultaneously sharp increase in the displacement curve indicated the start of sintering activity normally known as initial sintering stage in literature. Most of the work in densifying the sample is done in the initial stage of sintering, and hence sintering temperature (temperature at which sample is held before cooling down) plays an important part in optimizing the final theoretical density of the sample.

This concept is further elaborated by providing graphical illustrations in the **Figures 3.5-3.9** between the loading diagrams of each of representative single, binary, and ternary ceramic oxides. The resulting plots in **Figures 3.5-3.9** exhibit completion of sintering process in the plots on the right side, specifically at higher sintering temperatures. This completion was found to be indicated by the presence of a spike in the velocity profile, and the location of the spike can be extrapolated vertically on the temperature profile (blue curve) to obtain a specific temperature range. For example, in case of  $(8Y-ZrO_2)_2$ , the primary work of sintering activity/densification begins at 850°C and ends around 1000°C. The spike in velocity curve also corresponds to increase in displacement curve (green curve). Thus, the overall density of the sample can be optimized by heating the sample at a specific temperature in this range (or sintering temperature); furthermore, heating the sample beyond sintering temperature leads to

not only complete densification but also grain growth; this is discussed in the subsequent results section. Thus, using load diagram variable densified samples were obtained for single/binary and ternary phase composites as summarized in **Table 3.1**. An important point to note that during initial stages of load diagram, the sensitivity of optical pyrometer, the pressure applied, affects the velocity/displacement curves and hence are not an indicator of sintering activity. Also during the cooling stages of sintering cycle, the resulting curves are rather an indicator of the cooling activity of piston/electrodes rather than actual densification of the sample. Thus, the velocity and the displacement profiles in the initial heating and final cooling stages were not considered in our analysis.

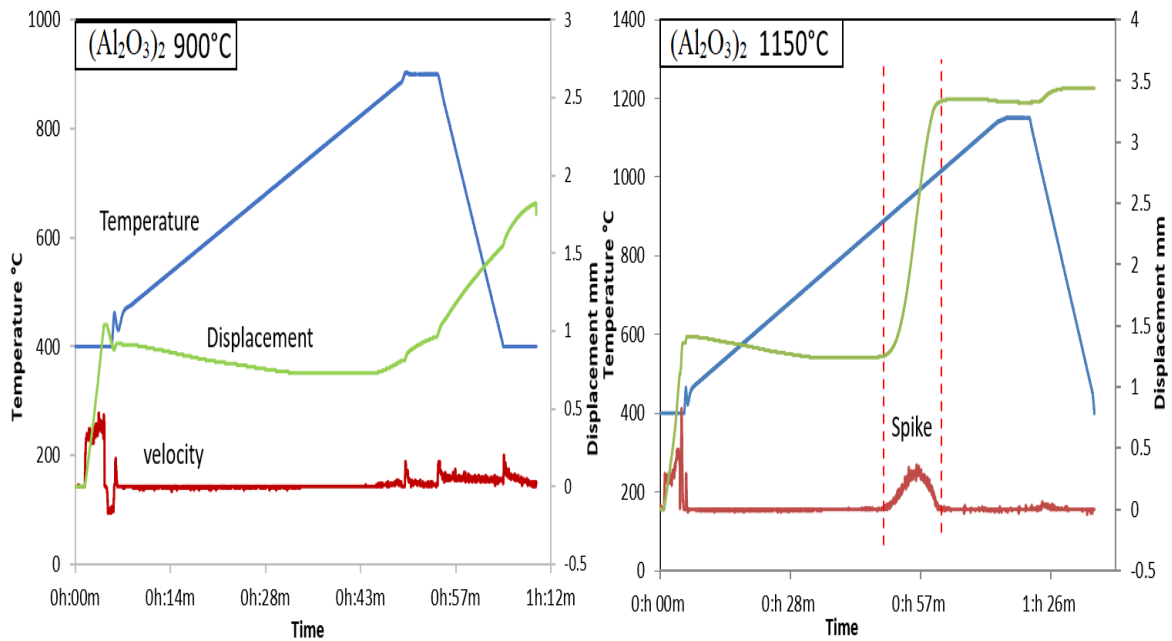


**Figure 3.5** Loading diagram for  $(Al_2O_3)_2$  single phase partial sintered composite (left plot) and fully sintered composite (right plot) with the respective temperature, displacement, and velocity profiles of the piston. The spike on the velocity of the full sintered composite indicates densification tendency; its position is extrapolated on the temperature curve which indicates that the primary work of sintering occurs between  $>900^\circ C$  to  $\sim 1000^\circ C$ .

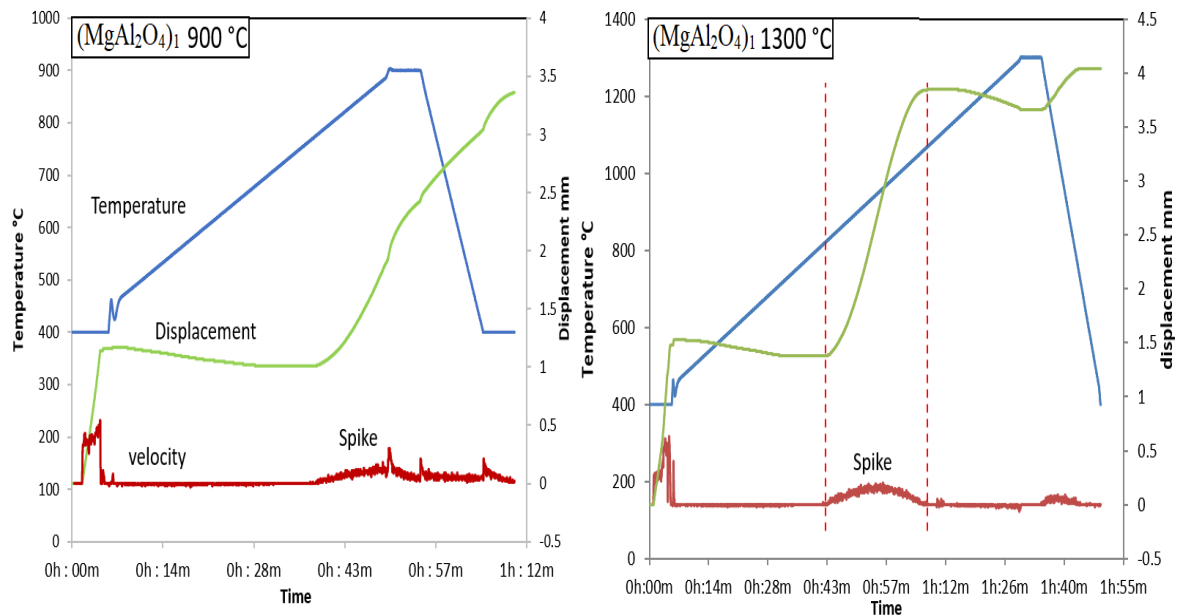


**Figure 3.6** Loading diagram for single phase (MgAl<sub>2</sub>O<sub>4</sub>)<sub>1</sub> partially sintered composite (left plot) and fully sintered composite (right plot) with the respective temperature, displacement, and velocity profiles of the piston. The spike on the velocity of the full sintered composite indicates densification tendency; its position is extrapolated on the temperature curve which indicates that the primary work of sintering occurs between >800°C to ~1050°C. Hence partial sintering is observed by small spike on the 900°C loading diagram on the left.

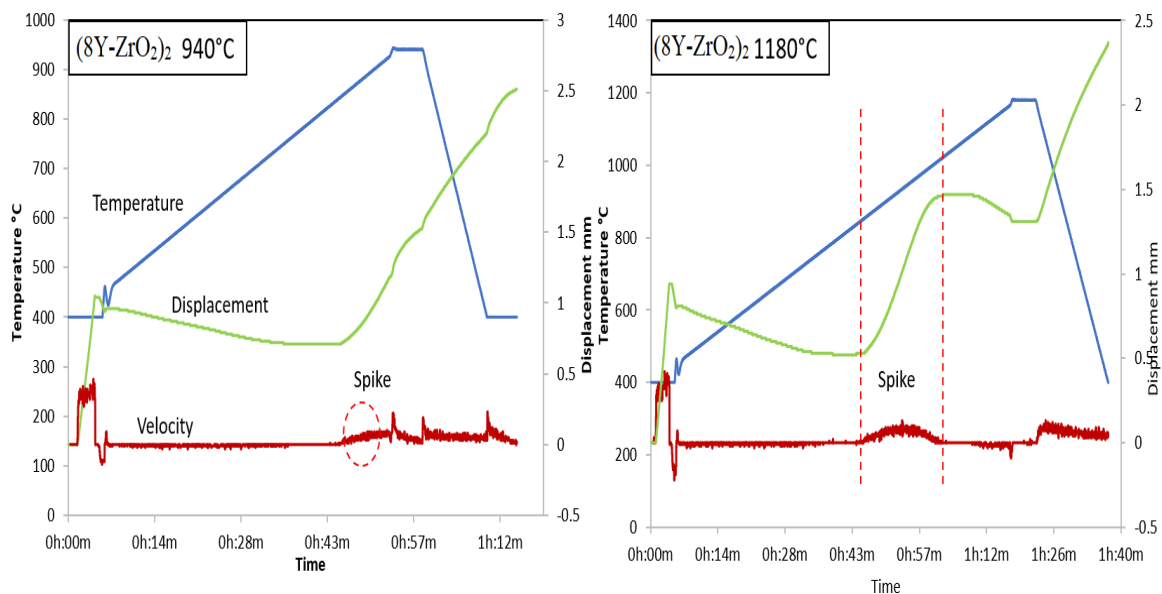


**Figure 3.7** Loading diagram for single phase (8Y-ZrO<sub>2</sub>)<sub>2</sub> partially sintered composite (left plot) and fully sintered composite (right plot) with the respective temperature, displacement, and velocity profiles of the piston. The spike on the velocity of the full sintered composite indicates densification tendency; its position is extrapolated on the temperature curve which indicates that the primary work of sintering occurs between >820°C to ~1030°C. Hence partial sintering is observed by small spike on the 940°C loading diagram on the left.

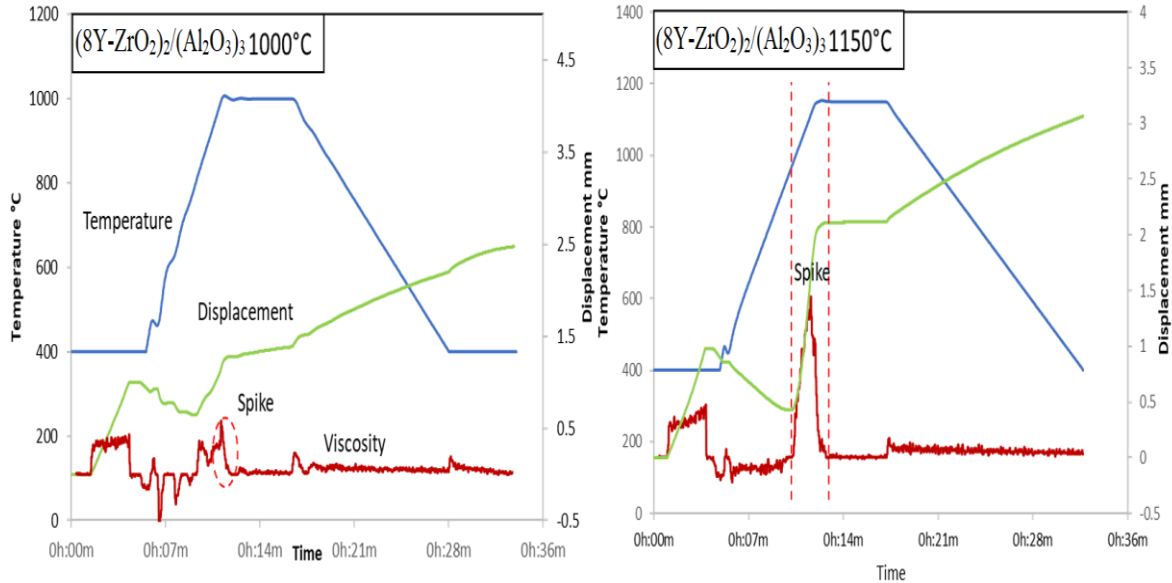


**Figure 3.8** Loading diagram for single phase  $(8Y-ZrO_2)_2/(Al_2O_3)_3$  partially sintered composite (left plot) and fully sintered composite (right plot) with the respective temperature, displacement, and velocity profiles of the piston. The spike on the velocity of the full sintered composite indicates densification tendency; its position is extrapolated on the temperature curve which indicates that the primary work of sintering occurs between  $>920^\circ C$  to  $\sim 1200^\circ C$ . Hence partial sintering is observed by small spike on the  $1000^\circ C$  loading diagram on the left.

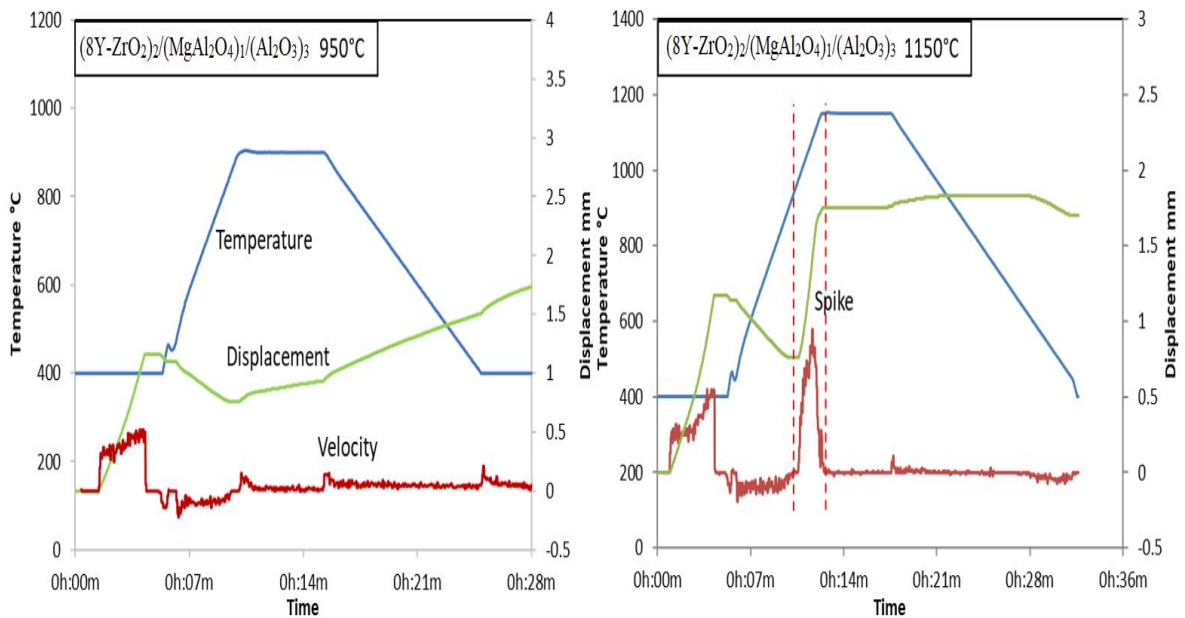


**Figure 3.9** Loading diagram for three-phase  $(8Y-ZrO_2)_2/(MgAl_2O_4)_1/(Al_2O_3)_3$  partially sintered composite (left plot) and fully sintered composite (right plot) with the respective temperature, displacement, and velocity profiles of the piston. The spike on the velocity of the full sintered composite indicates densification tendency; its position is extrapolated on the temperature curve which indicates that the primary work of sintering occurs between  $>950^\circ C$  to  $\sim 1150^\circ C$ . Hence partial sintering is observed by small spike on the  $1000^\circ C$  loading diagram on the left.

### 3.3 Post-sintering characterization: Density, X-ray diffraction, Polishing, Imaging

All the samples summarized in were characterized by density analysis and surface porosity using Archimedes principle (**Table 3.1**). The procedure as stated in ASTM C373<sup>75</sup> involves calculations concerning dry weight, saturated weight, and suspended weight under vacuum in water. Formulas for calculating % theoretical density are as follows:

$$\text{Sintered Density} = \frac{\text{Saturated weight} - \text{Suspended weight}}{\text{Dry weight}}$$

$$\% \text{ theoretical density (sample)} = \frac{\text{Theoretical powder density} - \text{Sintered density}}{\text{Theoretical powder density}}$$

The values for theoretical powder density were taken from table **2.1** for single phase; while for binary phase and ternary phase it was calculated using the rule of mixtures with respective individual powder density values. The resulting data is primarily important to generate densification curves for sintered ceramic oxides; these are described in the latter sections.

Fracture surfaces of the specimens were obtained using ultra high-resolution mode of scanning electron microscope (FEI XL30 SFEG, 5 kV Philips). For imaging purposes, the samples were coated with an iridium coating for better charging of electrons during SEM. For grain size analysis, more than 300 grains were analyzed using the linear intercept method using Image-J software to obtain average grain size distribution as per ASTM E112-12.<sup>76</sup>

The fracture surfaces were further embedded in a fast curing epoxy made by mixing resin and hardener in 1:2 ratio. Grinding was performed using silicon carbide (SiC) lapping discs (TED Pella, USA) of 60, 80, 120, 240, 600, 800 grit roughness in successive steps on a benchtop manual polishing machine (XP 8 Grinder/Polisher, TED Pella, USA). In order to obtain a finer surface roughness and smooth/mirror finish of the sample cross-section, polishing

was also performed using water-based diamond suspensions in A-4 alpha polishing cloths (TED Pella, USA) in the decreasing steps of surface roughness, i.e., 6 $\mu$ m, 3 $\mu$ m, 1 $\mu$ m, 0.5  $\mu$ m and 0.25 $\mu$ m with increasing amounts of polishing times.<sup>77</sup>

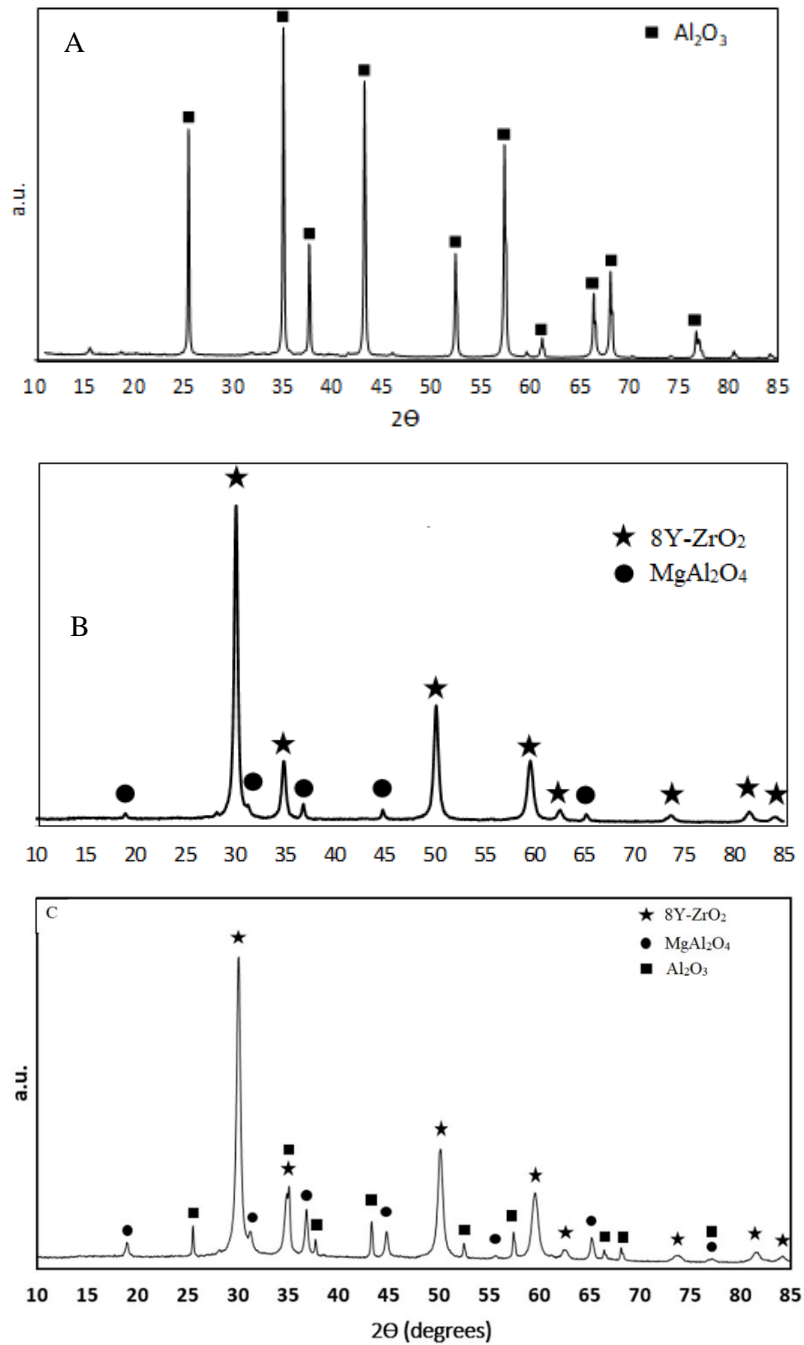


**Figure 3.10** X-ray diffraction spectra representative example of ceramic powder- as received  $(\text{Al}_2\text{O}_3)_4$  (A) and milled binary powder  $(8\text{Y-ZrO}_2)_1/(\text{MgAl}_2\text{O}_4)_1$  (B), and SPS sintered ternary phase  $(8\text{Y-ZrO}_2)_2/(\text{MgAl}_2\text{O}_4)_1/(\text{Al}_2\text{O}_3)_3$  (C) specimens.

X-ray diffraction studies were performed at different stages of the current research before and after sintering. Firstly, as received powders from vendors were characterized as received for secondary phases or impurities along with crystallite size **Figure 3.10A**. If impurities were present, then heat treatment was carried out appropriately. Out of all the powders used in present study, Alumina 40nm ( $\text{Al}_2\text{O}_3$ )<sub>1</sub> from sky spring was found to contain substantial impurities as observed from SEM images of the powder as well as the sintered composite. This powder, when characterized by XRD, was found to have substantial quantities of sulfates. As a result, the powder was treated at 1000C for 1.5 hours in the atmosphere and resulting XRD showed primary peaks of alpha alumina with no significant impurities. Secondly, XRD was also used to characterize binary and ternary mixtures. The resulting characterization was important to make sure all the individual phases were present, i.e., unwanted phase transformation of stable cubic zirconia, spinel and Alumina were avoided. Furthermore, the milled single/multiphase powders were also characterized to make sure no significant impurities (Tungsten, Carbon) were present from milled media as shown in binary powder namely (8Y-ZrO<sub>2</sub>)<sub>1</sub>/(MgAl<sub>2</sub>O<sub>4</sub>)<sub>1</sub> (**Figure 3.10B**). Lastly, XRD- spectra of all the SPS samples indicated no additional impurities from the sintering process except Carbon as shown in ternary phase specimen of (8Y-ZrO<sub>2</sub>)<sub>2</sub>/(MgAl<sub>2</sub>O<sub>4</sub>)<sub>1</sub>/(Al<sub>2</sub>O<sub>3</sub>)<sub>3</sub> in (**Figure 3.10C**). The carbon contamination which is typically common in SPS samples is assumed to be derived from the graphite foil and dies used during ceramic processing.<sup>78</sup> In general, the samples underwent heat-treatment for removal of this impurity, but since the current research deals with grain size, heat treatment post sintering was expected to affect the grain growth/microstructure of the sample; Hence no carbon removal processes were applied as it was deemed less significant for the scope of present research.

**Table 3.2 Particle size information of the single-phase powders sintered in the current study**

<b>Powder</b>	<b>Designation</b>	<b>Vendor</b>	<b>Milled particle size (nm)</b>
8Y-ZrO <sub>2</sub>	(8Y-ZrO <sub>2</sub> ) <sub>1</sub>	Skyspring	82 ± 14
	(8Y-ZrO <sub>2</sub> ) <sub>3</sub>	Skyspring	81 ± 14
	(8Y-ZrO <sub>2</sub> ) <sub>2</sub>	Tosoh	178 ± 17
MgAl <sub>2</sub> O <sub>4</sub>	(MgAl <sub>2</sub> O <sub>4</sub> ) <sub>1</sub>	Baikalox	84 ± 15
	(MgAl <sub>2</sub> O <sub>4</sub> ) <sub>2</sub>	Sigma Aldrich	150 ± 41
Al <sub>2</sub> O <sub>3</sub>	(Al <sub>2</sub> O <sub>3</sub> ) <sub>1</sub>	Skyspring	165 ± 50
	(Al <sub>2</sub> O <sub>3</sub> ) <sub>2</sub>	Baikowski	273 ± 54
	(Al <sub>2</sub> O <sub>3</sub> ) <sub>3</sub>	Taimei*	149 ± 22

\* Supplied by Pred Materials International Corp.

**Table 3.3 Particle size information of the binary/ternary phase powders sintered in the current study**

<b>Mixture</b>	<b>Mixture quantities (vol. %)</b>	<b>Mixture particle size (nm)</b>
(8Y-ZrO <sub>2</sub> ) <sub>1</sub> -(MgAl <sub>2</sub> O <sub>4</sub> ) <sub>1</sub>	50-50	91 ± 15
(8Y-ZrO <sub>2</sub> ) <sub>2</sub> -(MgAl <sub>2</sub> O <sub>4</sub> ) <sub>1</sub>	50-50	204 ± 38
(8Y-ZrO <sub>2</sub> ) <sub>2</sub> -(Al <sub>2</sub> O <sub>3</sub> ) <sub>3</sub>	50-50	173 ± 43
(8Y-ZrO <sub>2</sub> ) <sub>2</sub> -(Al <sub>2</sub> O <sub>3</sub> ) <sub>2</sub>	50-50	219 ± 25
(8Y-ZrO <sub>2</sub> ) <sub>1</sub> -(Al <sub>2</sub> O <sub>3</sub> ) <sub>1</sub>	50-50	98 ± 17
(Al <sub>2</sub> O <sub>3</sub> ) <sub>2</sub> -(MgAl <sub>2</sub> O <sub>4</sub> ) <sub>1</sub>	50-50	202 ± 38
(Al <sub>2</sub> O <sub>3</sub> ) <sub>3</sub> -(MgAl <sub>2</sub> O <sub>4</sub> ) <sub>1</sub>	50-50	147 ± 22
(8Y-ZrO <sub>2</sub> ) <sub>2</sub> -(MgAl <sub>2</sub> O <sub>4</sub> ) <sub>1</sub> -(Al <sub>2</sub> O <sub>3</sub> ) <sub>3</sub>	33-33-33	167 ± 32
(8Y-ZrO <sub>2</sub> ) <sub>2</sub> -(MgAl <sub>2</sub> O <sub>4</sub> ) <sub>1</sub> -(Al <sub>2</sub> O <sub>3</sub> ) <sub>2</sub>	33-33-33	214 ± 31
(8Y-ZrO <sub>2</sub> ) <sub>1</sub> -(MgAl <sub>2</sub> O <sub>4</sub> ) <sub>1</sub> -(Al <sub>2</sub> O <sub>3</sub> ) <sub>3</sub>	33-33-33	117 ± 27



### 3.4 Sintering results: Grain size distribution in single/multiphase composites

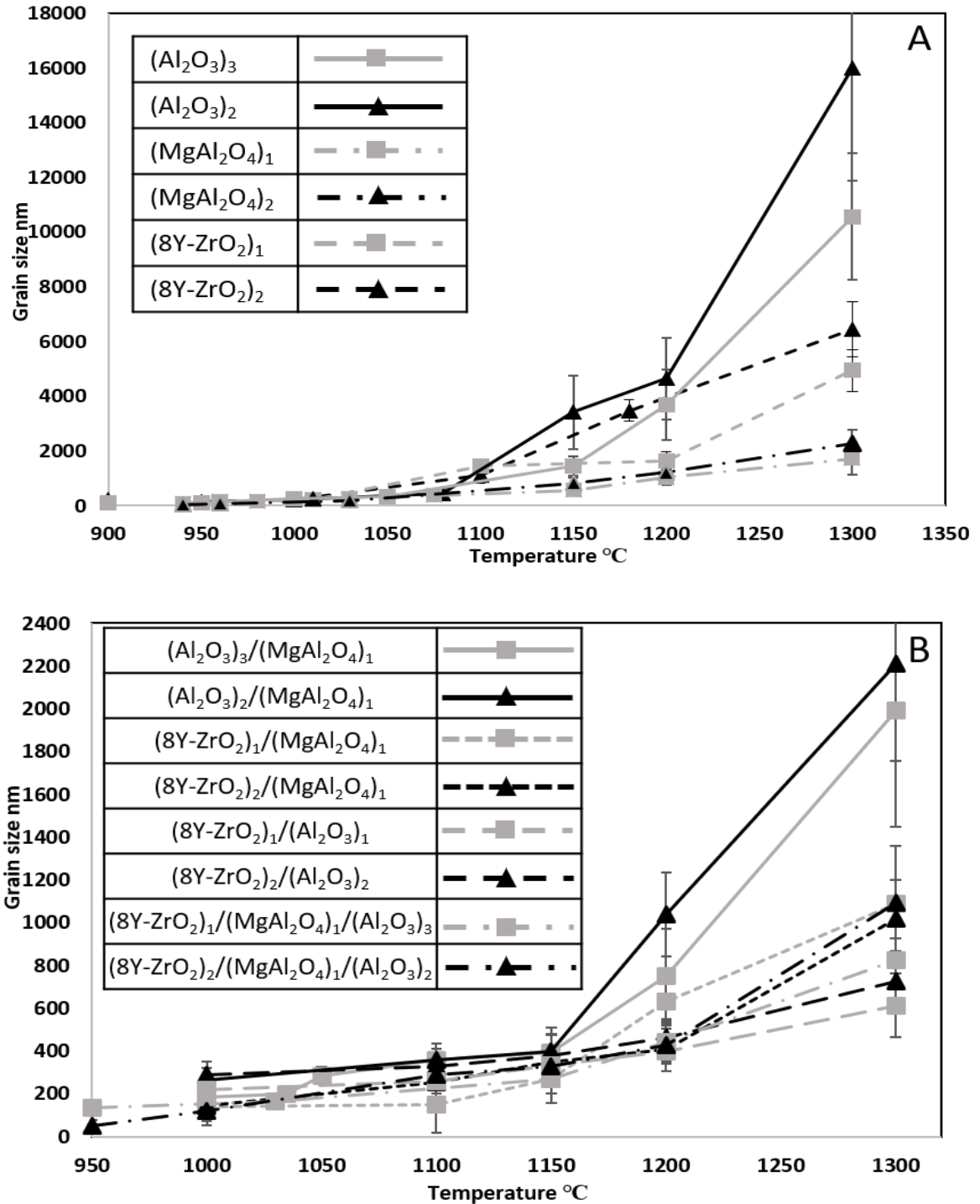


Figure 3.11 Graphical results indicating the overall effect of sintering temperature on grain size of single phase ceramics (Fig. 2A) and multiphase ceramic oxides (Fig. 2B) of 8Y-ZrO<sub>2</sub>, MgAl<sub>2</sub>O<sub>4</sub>, and Al<sub>2</sub>O<sub>3</sub>. Two samples of different particle sizes have been sintered for every ceramic oxide, with the gray colored lines indicating the smaller powder sized composites. For details of particle sizes and powder designations refer to table 1.

The average grain size results distribution versus sintering temperature of all the single/binary and ternary phase composites of ceramic oxide powders sintered are plotted as shown in **Figure 3.11 A-B**. Firstly, the average grain size of specimens of single phase composites of 8Y-ZrO<sub>2</sub>, MgAl<sub>2</sub>O<sub>4</sub> and Al<sub>2</sub>O<sub>3</sub> range from sub-nanometer to greater than 10 μm as the sintering temperatures is increased till 1300°C. Two samples of different particle sizes have been sintered for every ceramic oxide, with the gray colored lines indicating the smaller powder sized composites . Furthermore, the standard deviation of the result values, i.e., indicated by Y-axis error bars is found to be larger especially at high-temperatures (>1150°C) which indicates the presence of a broad distribution of grain sizes in the composite. Furthermore, the net increase in average grain size with temperature was found to be varied for all the single phases specifically at higher temperatures. For example, as the average grain size in both (Al<sub>2</sub>O<sub>3</sub>)<sub>3</sub> and (Al<sub>2</sub>O<sub>3</sub>)<sub>2</sub> increases exponentially between 1100-1300 °C to achieve results >10 μm (10000 nm) at the maximum temperature. Also, the standard deviations of grain size results (Y-error bars) at these temperatures are larger, indicating a more non-uniform and anisotropic morphology of the grains present in the microstructure. The maximum grain size achieved among the single-phase composites is by (Al<sub>2</sub>O<sub>3</sub>)<sub>2</sub> which is 15.99 ± 4.1 μm while (MgAl<sub>2</sub>O<sub>4</sub>)<sub>1</sub> has the least size of 1.73 ± 0.6 μm at 1300 °C.

Similarly, the grain size results for different specimens of binary phase composites 8Y-ZrO<sub>2</sub>/MgAl<sub>2</sub>O<sub>4</sub>, Al<sub>2</sub>O<sub>3</sub>/MgAl<sub>2</sub>O<sub>4</sub>, 8Y-ZrO<sub>2</sub>/Al<sub>2</sub>O<sub>3</sub>, and ternary composite 8Y-ZrO<sub>2</sub>/MgAl<sub>2</sub>O<sub>4</sub>/Al<sub>2</sub>O<sub>3</sub> composite with increasing sintering temperature up to 1300°C are highlighted by the inset plot in **Figure 3.11B**. Two samples of different particle sizes have been sintered for every ceramic oxide, with the gray colored lines indicating the smaller powder sized composites. The grain growth with temperature follows a similar trend as compared to

single phase ceramics. Among binary phase composites, the grain size distribution of  $(8\text{Y-ZrO}_2)_2/(\text{Al}_2\text{O}_3)_2$  is limited to  $612 \pm 148$  nm ( $\sim 0.6$   $\mu\text{m}$ ) while all specimens of  $8\text{Y-ZrO}_2/\text{MgAl}_2\text{O}_4$  and  $\text{Al}_2\text{O}_3/\text{MgAl}_2\text{O}_4$  fabricated microstructures tend to sinter to a higher grain size ( $>1$   $\mu\text{m}$ ) at a maximum sintering temperature of  $1300$   $^\circ\text{C}$ . For example, in case of  $(\text{Al}_2\text{O}_3)_2/(\text{MgAl}_2\text{O}_4)_1$ , the grain size increased exponentially with temperature to achieve a maximum size of  $2210 \pm 450$  nm at  $1300$   $^\circ\text{C}$ ; the broad standard deviation value highlighted the variations among different grains in the given microstructure. The average grain sizes of the two specimens of novel sintered three-phase composites plotted in **Figure 3.11B** (maximum size  $<1000$  nm) with the respective error values at different temperatures.

From **Figure 3.11** grain size distribution of  $(8\text{Y-ZrO}_2)_2/(\text{Al}_2\text{O}_3)_2$  is the highest among the multiphase, i.e., around  $2\mu\text{m}$  at  $1300^\circ\text{C}$  with large Y-error bars than other two binary compositions of  $8\text{Y-ZrO}_2/\text{MgAl}_2\text{O}_4$  and  $\text{Al}_2\text{O}_3/\text{MgAl}_2\text{O}_4$ . In case of  $8\text{Y-ZrO}_2/\text{MgAl}_2\text{O}_4/\text{Al}_2\text{O}_3$  ternary composite, the resulting grain sizes at different temperatures are found to similar within standard deviation with  $8\text{Y-ZrO}_2/\text{Al}_2\text{O}_3$ ,  $8\text{Y-ZrO}_2/\text{MgAl}_2\text{O}_4$  for most of the sintering temperatures, with average grain size limited to  $1\mu\text{m}$  at a sintering temperature of  $1300^\circ\text{C}$ .

### 3.5 Sintering results: Densification tendency in single/multiphase composites

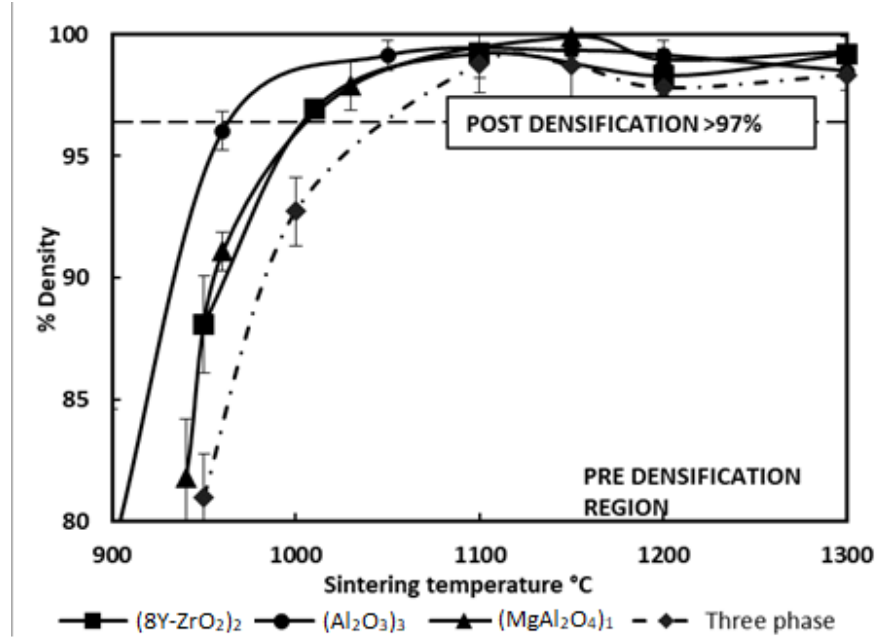


Figure 3.12 Bulk densification tendency of single phase ceramic oxides as compared to three phase oxide (dash line) at different sintering temperature; % density is the theoretical density of the sample obtained from Archimedes measurements

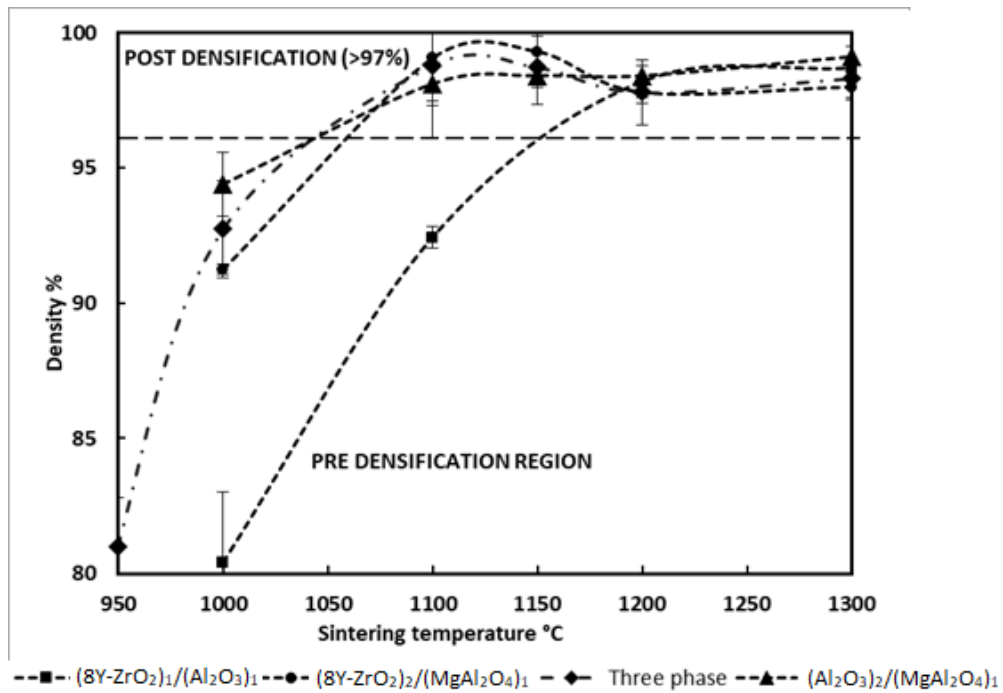


Figure 3.13 Bulk densification tendency of multiphase ceramic oxides at different sintering temperature; % density is the theoretical density of the sample obtained from Archimedes measurements.

**Figure 3.12** depicts the densification curves obtained for representative sintered oxides of  $\text{MgAl}_2\text{O}_4$ ,  $\text{Al}_2\text{O}_3$ , and 8Y-ZrO<sub>2</sub>, as well as their corresponding multiphase composites, **Figure 3.13** concerning sintering temperature. It is important to note that due to inherent deviations in measurements arising from Archimedes method and experimental setup samples, samples with density >97% are considered to fully sintered especially those obtained at higher temperatures. Hence for simplicity purposes, the pre-densification region is assumed to be for bulk density values until 90%, while samples with higher density (>97%) lie in the post-densification region. For the current sintered specimens to be viable as candidates for surrogate nuclear fuel project, minimum 90% density is required. Thus, from **Figure 3.12**, we can conclude that single phase ceramic materials achieve these results when sintered beyond temperatures <950°C, similar to ternary phase composites (950°C -1000°C). On the other hand, binary phase composites achieve 90% of their theoretical density at higher temperatures (1000°C -1100°C). Lastly, the post-densification region is achieved at lower temperatures for single phases samples (~1050°C) as compared to multiphase composites (~1150°C). These densification curves were useful as they affected the grain growth behavior among the given ceramic oxides at different sintering temperatures.

### **3.6 Results: particle size/grain size correlation – “size ratio”**

For the purpose to obtain a significant correlation between the grain size results obtained after sintering with the particle size of the powders, we have formulated a dimensionless ratio called a size ratio in the present research study. This dimensionless “size ratio or grain growth ratio” is obtained by normalizing the average grain sizes of the sintered specimens concerning particle size of the powder mixtures measured previously

**Table 3.2-Table 3.3).** It is an empirical quantity that can correlate the two relevant fundamental distributions involved in powder processing. This ratio was expected to be helpful to quantify the magnitude of an average size change that occurs in a powder particle as it undergoes diffusion due to a spark plasma sintering process to form resulting microstructural grains. The resulting data can then provide a further understanding of the phenomenon of grain growth and densification quantitatively during sintering specifically due to powder parameters, *i.e.*, particle size rather than the sintering parameters (*i.e.*, temperature). We have provided an example of the size ratio calculations for  $(8\text{Y-ZrO}_2)_2$  presented in **Table 3.4** and **Table 3.5**.

Particle size of powder  $(8\text{Y-ZrO}_2)_2 = 178 \pm 17$  nm.

The grain size of the sintered sample at  $1200^\circ\text{C} = 3473 \pm 389$  nm.

Average size ratio = Average grain size/ Particle size = 19.5.

Maximum size ratio = Maximum of grain size/ Minimum of particle size = 23.9.

Minimum size ratio = Minimum of grain size/ Maximum of particle size = 15.8.

Size ratio with an average deviation of  $(8\text{Y-ZrO}_2)_2$  at  $1200^\circ\text{C} = 19.5 \pm 4.0$ .

**Table 3.4 Size ratios of representative specimens of single phase ceramic oxides at variable sintering temperatures**

Temperature ( $^\circ\text{C}$ )	Size ratio		
	$(8\text{Y-ZrO}_2)_2$	$(\text{MgAl}_2\text{O}_4)_1$	$(\text{Al}_2\text{O}_3)_3$
950	$0.8 \pm 0.2$	$0.4 \pm 0.2$	$1.1 \pm 0.4$
1000	$1.2 \pm 0.4$	$1.3 \pm 0.7$	$1.7 \pm 0.8$
1150	$6.2 \pm 2.3$	$5.5 \pm 3.0$	$9.8 \pm 4.4$
1200	$19.5 \pm 4.0$	$8.1 \pm 5.1$	$24.7 \pm 13.8$
1300	$36.2 \pm 16.1$	$15.2 \pm 8.1$	$71.0 \pm 30.1$

**Table 3.5 Size ratios of representative specimens of multiphase ceramic oxides at variable sintering temperatures**

Temperature (°C)	Size ratio			
	(8Y-ZrO <sub>2</sub> ) <sub>2</sub> / (Al <sub>2</sub> O <sub>3</sub> ) <sub>2</sub>	(8Y-ZrO <sub>2</sub> ) <sub>2</sub> / (MgAl <sub>2</sub> O <sub>4</sub> ) <sub>1</sub>	(Al <sub>2</sub> O <sub>3</sub> ) <sub>3</sub> / (MgAl <sub>2</sub> O <sub>4</sub> ) <sub>1</sub>	(8Y-ZrO <sub>2</sub> ) <sub>2</sub> / (MgAl <sub>2</sub> O <sub>4</sub> ) <sub>1</sub> / (Al <sub>2</sub> O <sub>3</sub> ) <sub>2</sub>
1000	1.3 ± 0.6	0.7 ± 0.2	1.2 ± 0.5	0.2 ± 0.4
1100	1.5 ± 0.7	1.3 ± 0.3	2.4 ± 0.8	0.3 ± 0.1
1150	1.9 ± 0.9	1.7 ± 0.3	2.7 ± 1.0	1.3 ± 0.8
1200	2.3 ± 1.0	2.0 ± 0.6	5.1 ± 2.3	2.0 ± 1.1
1300	3.5 ± 1.9	5.0 ± 1.0	13.5 ± 5.9	5.0 ± 1.6

The size ratios of different ceramic oxides with increasing sintering temperatures are provided in **Table 3.4** (single phase) and **Table 3.5** (multiphase). The grain ratio results quantitatively validate the variations in increasing grain growth tendency among the single-phase ceramic oxides as described in the previous section. It is found out that single-phase (Al<sub>2</sub>O<sub>3</sub>)<sub>3</sub> composite has the highest grain growth with average grain size almost 71 times powder particle size (size ratio = 71.0 ± 30.1) as compared to spinel whose size ratio is 15.2 at 1300 °C. Similarly, both specimens of (Al<sub>2</sub>O<sub>3</sub>)/(MgAl<sub>2</sub>O<sub>4</sub>) powder exhibits a double-digit grain growth (>10), maximum among the binary phase oxides with (8Y-ZrO<sub>2</sub>)<sub>2</sub>/ (Al<sub>2</sub>O<sub>3</sub>)<sub>2</sub> (ratio = 3.5) has the least net expansion of grains. The three-phase (8Y-ZrO<sub>2</sub>)<sub>2</sub>/ (MgAl<sub>2</sub>O<sub>4</sub>)<sub>1</sub>/ (Al<sub>2</sub>O<sub>3</sub>)<sub>2</sub> (size ratio = 4.9) shows restricted grain growth as compared to single phase ceramics and lower than most of the binary phase mixtures. Thus, it can be said that multiphase oxide powders exhibit limited

grain growth with highest size ratio values less than as much ten times as compared to respective results for individual 8Y-ZrO<sub>2</sub>, MgAl<sub>2</sub>O<sub>4</sub> and Al<sub>2</sub>O<sub>3</sub> ceramics. Lastly, specifically in single-phase ceramics, the higher standard deviation values of size ratio at a higher temperature (>1200°C) indicates the higher presence of larger or smaller grains or broader distribution in the granular microstructure of sintered SPS sample.

These size ratios are plotted for different samples of individual single-phase ceramic oxides in **Figure 2.14** whereas **Figure 2.15** portrays ratios of respective binary and ternary-phase specimens. An empirical fit based on the results is also obtained in the plots for all the samples. In general, an exponential correlation is determined between the average grain size and sintering temperature and its accuracy supported by the high correlation factor, i.e.,  $R^2 \geq 0.9$  for most of the curve fittings. The resulting equations in the form  $y=e^{ax}$  have also been tabulated for single/multiphase composites in **Figure 2.14 and 2.15**. The resulting trends agree with the previous literature regarding the kinetic grain growth that defines the increase in grain size with higher sintering temperatures in solid-state sintering<sup>79</sup>. Thus, the resulting Arrhenius law can be obtained for the current sintering study which incorporates both particle size (P.S), grain size (G.S), i.e., size ratio and temperature in the following equation (1),

$$\frac{G.S}{P.S} = \exp\left[-\frac{Q}{RT}\right] \quad (1)$$

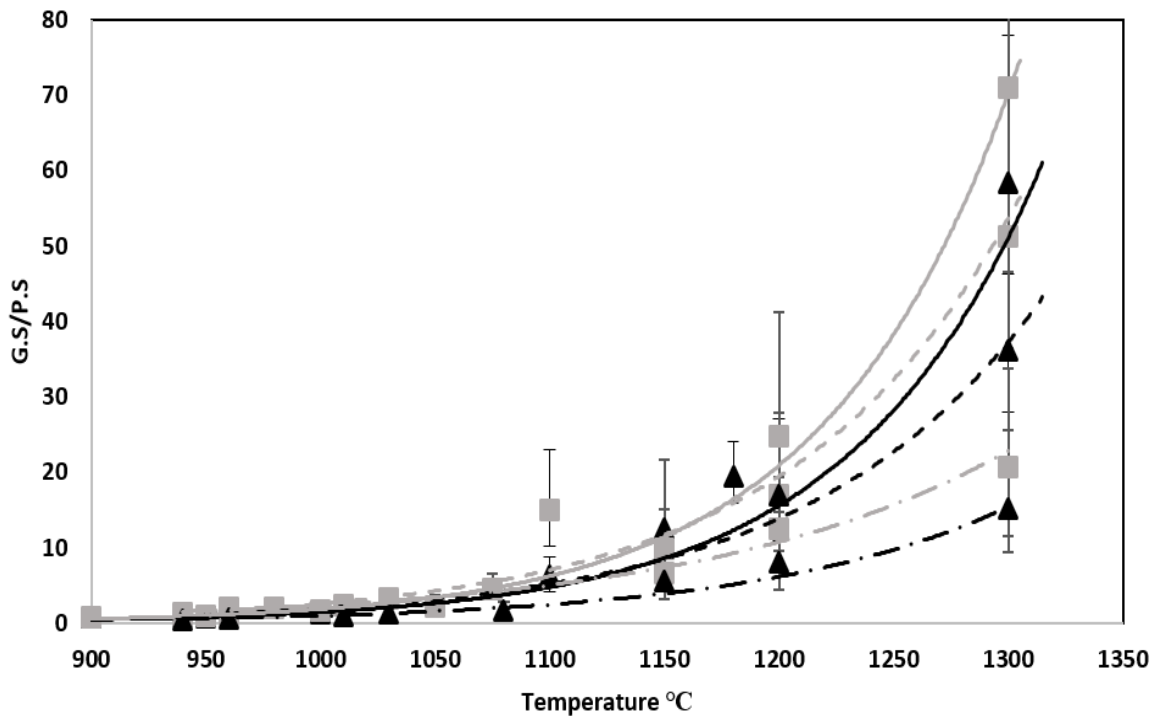
Where G.S/P.S is the average size ratio at a particular sintering temperature T in Kelvin (K), Q is the activation energy for grain growth, and R denote ideal gas constant (8.312 kJ/mol.K).

Taking natural logarithms on both sides versus reciprocal of sintering temperature (1000/T) gives a linear fit for the above equation (1). Thus, for all the sintered ceramic oxide specimens the slope of the linear fit gives empirical values of activation energies of grain growth











during the SPS sintering cycle, these are calculated for single phase in **Figure 2.16 (A-C)** and binary/ternary phase in **Figure 2.17(A-D)**. Since spark plasma sintering involves rapid diffusion process, the sintering occurs at lower temperatures and thereby the activation energies for all the composites are on the low, i.e.,  $\leq 200$  kJ/mol as compared to another sintering process like co-precipitation.<sup>79</sup> Thus the present activation energy values for grain growth in case of alumina (192-202 kJ/mol) and also for spinel (110-152 kJ/mol) are well within the range of values obtained in literature<sup>80-82</sup>. In the case of 8Y-ZrO<sub>2</sub>, the energy values (161-191 kJ/mol) are closer to the value reported by similar 8Y-ZrO<sub>2</sub> sintering studies performed by Quach for nanocrystalline (226 kJ/mol) samples. No comparable values from the past literature were found for resulting activation energy of grain growth for the given equal-proportional binary and ternary phase ceramic oxides-based composites as shown in **Figure 2.17**. The use of size ratio and the activation energy in the present study is mainly used for comparing the grain growth tendencies among ceramic oxides which is more elaborated later.

Composite		Equation	R <sup>2</sup>
(Al <sub>2</sub> O <sub>3</sub> ) <sub>3</sub>	—■—	$y = 1E-05e^{0.0121x}$	0.98
(Al <sub>2</sub> O <sub>3</sub> ) <sub>2</sub>	—▲—	$y = 1E-05e^{0.0119x}$	0.92
(MgAl <sub>2</sub> O <sub>4</sub> ) <sub>1</sub>	- - ■ - -	$y = 2E-05e^{0.0108x}$	0.98
(MgAl <sub>2</sub> O <sub>4</sub> ) <sub>2</sub>	- - ▲ - -	$y = 0.0001e^{0.0092x}$	0.95
(8Y-ZrO <sub>2</sub> ) <sub>1</sub>	- - ■ - -	$y = 0.0001e^{0.0101x}$	0.92
(8Y-ZrO <sub>2</sub> ) <sub>2</sub>	- - ▲ - -	$Y = 0.0001e^{0.0099x}$	0.94



**Figure 3.14** Plot of Grain size (G.S)/Particle size (P.S) ratio indicating the overall effect of sintering temperature on grain growth tendency of single phase ceramic oxides. Details of the curve fits of the empirical data have been provided in the table above. Two samples of different particle sizes have been sintered for every ceramic oxide, with the gray colored lines indicating the smaller powder sized composites. For details of particle sizes and powder designations refer to table 1.

Composite		Equation	R <sup>2</sup>
(Al <sub>2</sub> O <sub>3</sub> ) <sub>3</sub> /(MgAl <sub>2</sub> O <sub>4</sub> ) <sub>1</sub>		$y = 0.0002e^{0.0085x}$	0.95
(Al <sub>2</sub> O <sub>3</sub> ) <sub>2</sub> /(MgAl <sub>2</sub> O <sub>4</sub> ) <sub>1</sub>		$y = 0.0002e^{0.0082x}$	0.89
(8Y-ZrO <sub>2</sub> ) <sub>1</sub> /(MgAl <sub>2</sub> O <sub>4</sub> ) <sub>1</sub>		$y = 0.0005e^{0.0077x}$	0.89
(8Y-ZrO <sub>2</sub> ) <sub>2</sub> /(MgAl <sub>2</sub> O <sub>4</sub> ) <sub>1</sub>		$y = 0.0012e^{0.0063x}$	0.98
(8Y-ZrO <sub>2</sub> ) <sub>1</sub> /(Al <sub>2</sub> O <sub>3</sub> ) <sub>1</sub>		$y = 0.0588e^{0.0035x}$	0.97
(8Y-ZrO <sub>2</sub> ) <sub>2</sub> /(Al <sub>2</sub> O <sub>3</sub> ) <sub>2</sub>		$y = 0.053e^{0.0031x}$	0.93
(8Y-ZrO <sub>2</sub> ) <sub>1</sub> /(MgAl <sub>2</sub> O <sub>4</sub> ) <sub>1</sub> /(Al <sub>2</sub> O <sub>3</sub> ) <sub>3</sub>		$y = 0.003e^{0.006x}$	0.95
(8Y-ZrO <sub>2</sub> ) <sub>2</sub> /(MgAl <sub>2</sub> O <sub>4</sub> ) <sub>1</sub> /(Al <sub>2</sub> O <sub>3</sub> ) <sub>2</sub>		$y = 0.0001e^{0.0084x}$	0.96

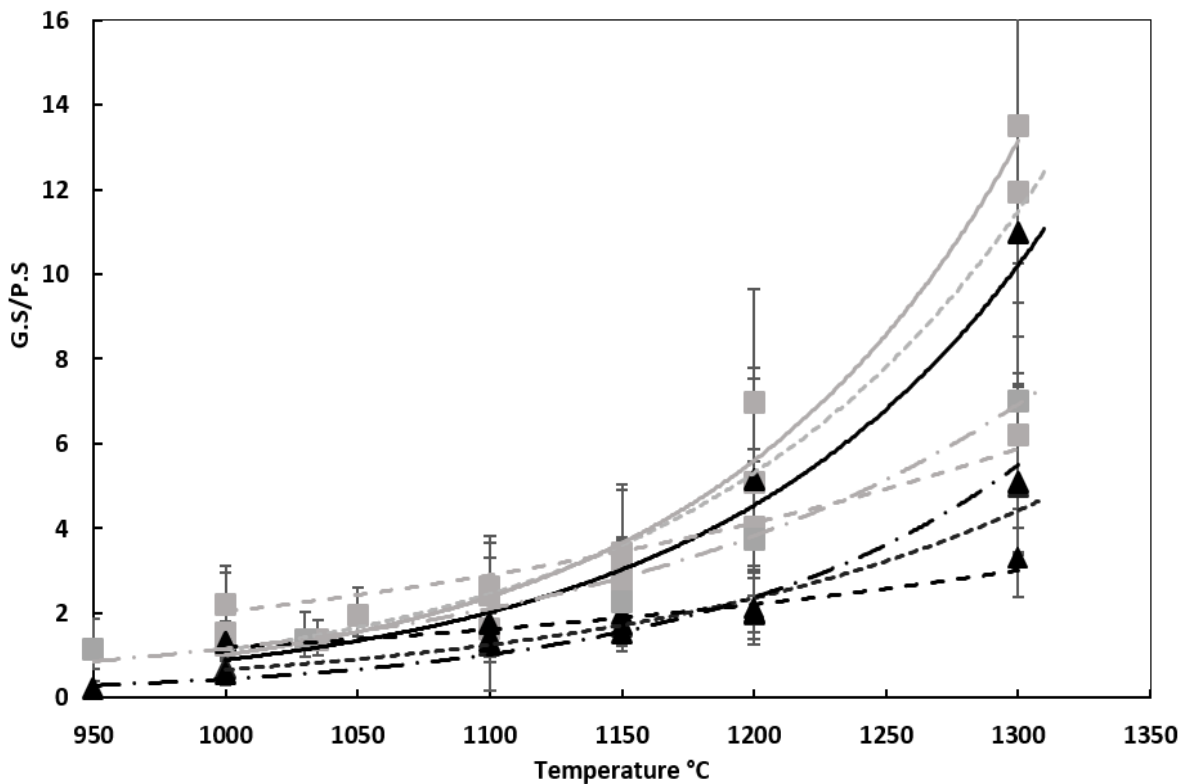


**Figure 3.15** Plot of Grain size (G.S)/Particle size (P.S) ratio indicating the overall effect of sintering temperature on grain growth tendency of equal proportional binary and ternary phase composites of 8Y-ZrO<sub>2</sub>, MgAl<sub>2</sub>O<sub>4</sub>, and Al<sub>2</sub>O<sub>3</sub>. Details of the curve fits of the empirical data have been provided in the table above. Two samples of different particle sizes have been sintered for every ceramic oxide, with the gray colored lines indicating the smaller powder sized composites. For details of particle sizes and powder designations refer to table 1.

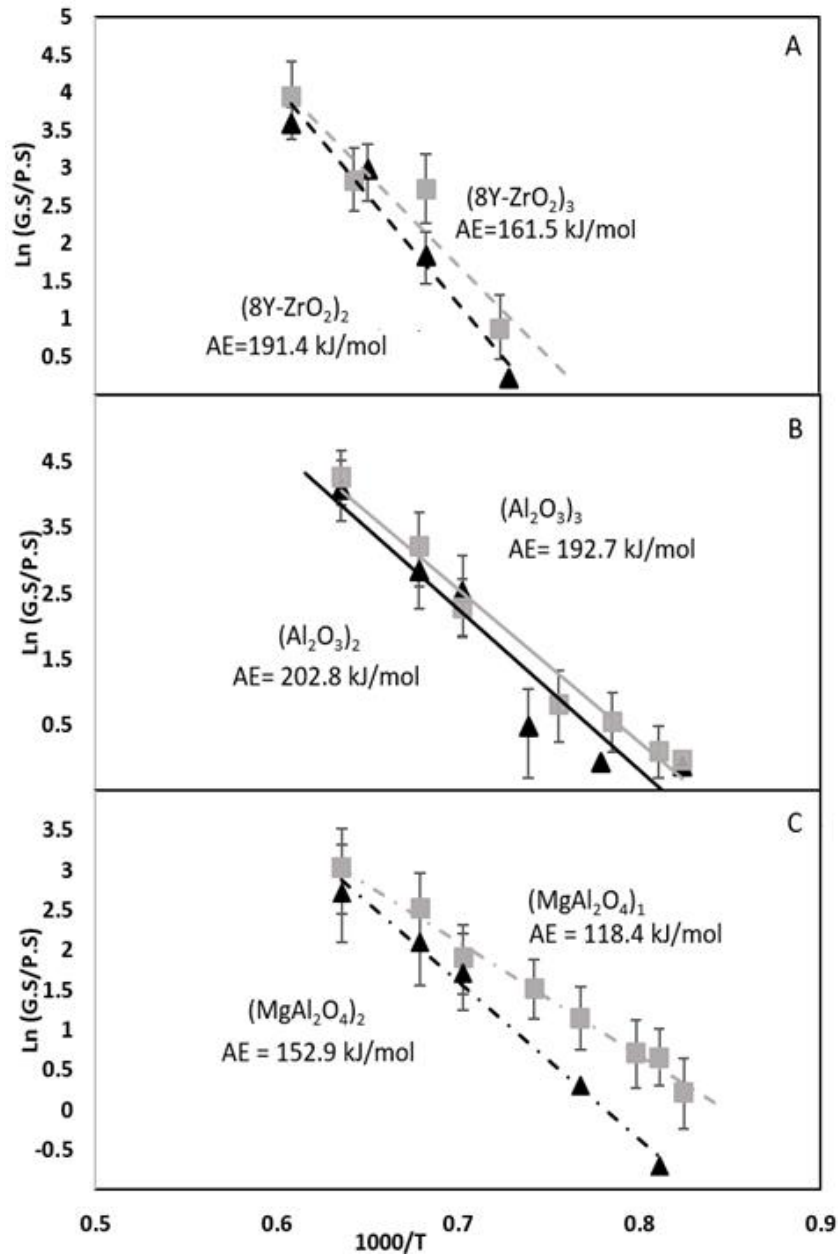
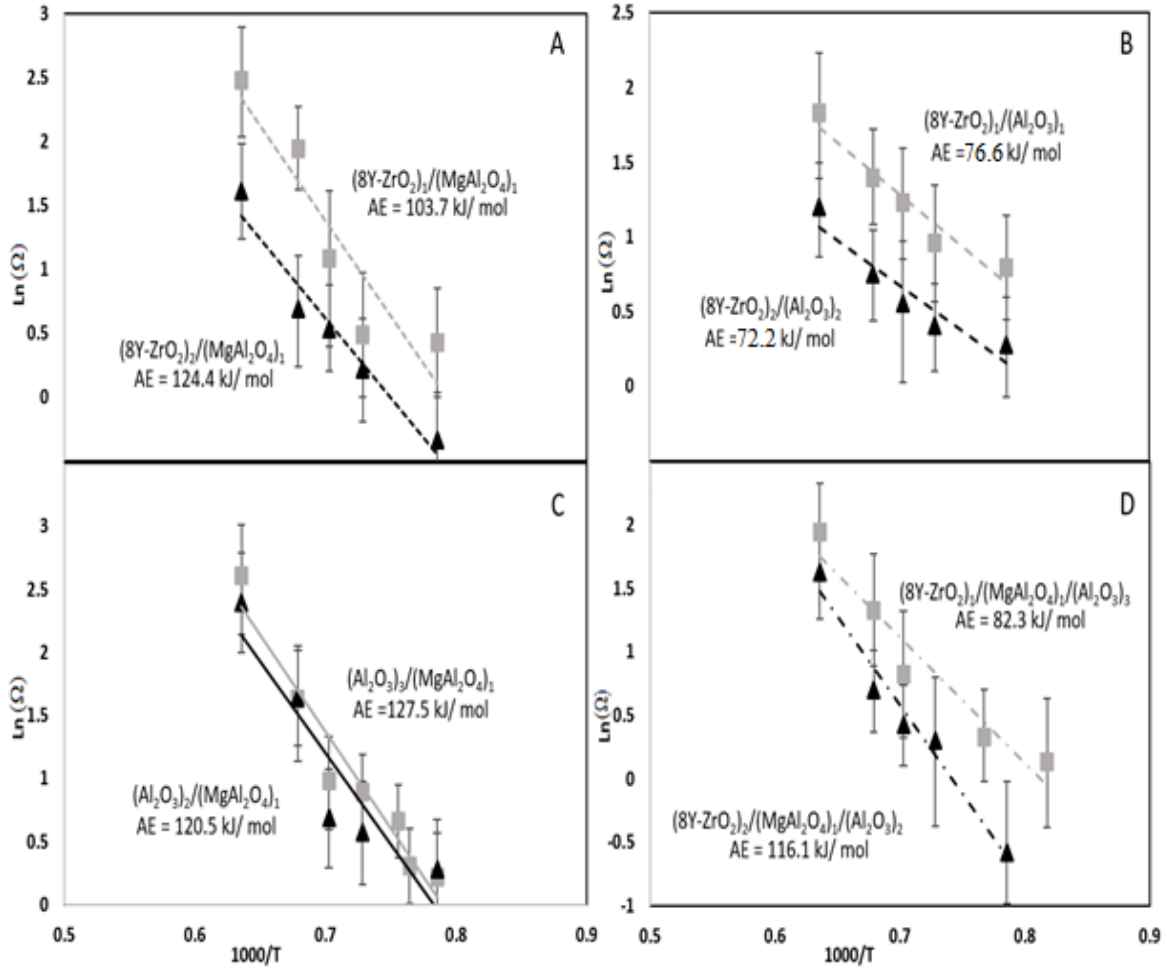


Figure 3.16 Arrhenius plot of natural logarithm of G.S/P.S ratio versus sintering temperature (1000/K). The respective slope of the lines gives activation energy values for grain growth for 8Y-ZrO<sub>2</sub> in Fig.A, Al<sub>2</sub>O<sub>3</sub> in Fig B. and MgAl<sub>2</sub>O<sub>4</sub>, in Fig.C. Two samples of different particle sizes have been sintered for every ceramic oxide, with the gray colored lines indicating the smaller powder sized composites. For details of particle sizes and powder designations refer to table 1.



**Figure 3.17** Arrhenius plot of natural logarithm of G.S/P.S ratio versus sintering temperature (1000/K) for multiphase composites. The respective slopes of the lines give activation energy values for grain growth for 8Y-ZrO<sub>2</sub>/MgAl<sub>2</sub>O<sub>4</sub> in Fig. A, 8Y-ZrO<sub>2</sub>/Al<sub>2</sub>O<sub>3</sub> in Fig. B, Al<sub>2</sub>O<sub>3</sub>/MgAl<sub>2</sub>O<sub>4</sub>, in Fig. C and 8Y-ZrO<sub>2</sub>/MgAl<sub>2</sub>O<sub>4</sub>/Al<sub>2</sub>O<sub>3</sub> in Fig. D. Two samples of different particle sizes have been sintered for every ceramic oxide, with the gray colored lines indicating the smaller powder sized composites. For details of particle sizes and powder designations refer to table 1.

### 3.7 Discussion of sintering results: Grain growth/Densification

The use of individual grain size plots in **Figures 3.11A-B** and size ratio plots in **Figure 3.14 and 3.15** assisted in developing an exponential based Arrhenius model of grain growth versus sintering temperature by empirically fitting the data points. As a result, the activation energy for grain growth was obtained for all sintered single/binary and ternary based composites of  $\text{MgAl}_2\text{O}_4$ ,  $\text{Al}_2\text{O}_3$ , and  $8\text{Y-ZrO}_2$  as enumerated in **Figures 3.16 and 3.17**. The results thus enabled us to make a novel comparative study of sintering tendencies of ceramic oxide composites among themselves and between their multiphase mixtures. Thus, comparing the activation energy values of the sintered specimens, the grain growth of single-phase composites shows the following trend:  $\text{Al}_2\text{O}_3 > 8\text{Y-ZrO}_2 > \text{MgAl}_2\text{O}_4$ . Since limited comparison studies exist regarding grain growth among the given ceramic oxides, few probable reasons were documented for this behavior from literature studies. The low grain growth in polycrystalline spinel can be explained by the fact that it was found to be hard to sinter by Morita *et al.*<sup>84, 85</sup> The study also corroborates by the slower, delayed densification curve shown in **Figure 3.12**. As a result, it can be concluded that densification and grain growth tendency both played a part in the finer spinel microstructures. Saylor *et al.*<sup>86</sup> further discuss this by observing that the adjoining boundaries between two grains in dense polycrystalline  $\text{MgAl}_2\text{O}_4$  have more internal planes oriented in  $\langle 111 \rangle$  direction rather than  $\langle 100 \rangle$  that possess low surface energy; as a result, the grain growth is more inhibited in nature. On the other hand, researchers related the grain growth of  $8\text{Y-ZrO}_2$  and  $\text{Al}_2\text{O}_3$ <sup>87</sup> based sintered composites to various inherent material factors that include crystal structure of ceramics, type of bonding which affect the resulting microstructures. The sintered cubic grains of  $8\text{Y-ZrO}_2$  have high grain boundary energy leading large dihedral angles between them ( $\sim 135^\circ$ ); this is favorable for high

grain growth<sup>88</sup>. Additionally, as compared to cubic zirconia, alumina possesses hexagonal crystal structure which is found to be anisotropic. The resulting dihedral angles are even higher than  $\text{Al}_2\text{O}_3$ ; this leaves alumina prone to unstable and large grain growth.<sup>89-91</sup> This fact is supported by high grain growth of  $(\text{Al}_2\text{O}_3)_2$  composite ( $>10\mu\text{m}$  and size ratio  $> 50$ ) beyond  $1200^\circ\text{C}$  in the present study. The experimental results obtained in our current study are helpful in supporting the different assumptions attributed to varied grain growth in the given ceramic oxides.

The variable grain growth tendencies among individual ceramic oxides themselves as observed from the activation energy values in **Figure 3.17** aid in discussing the respective phenomenon among the binary/ternary based ceramic oxide composites. This trend as stated in the results section is as follows:  $\text{Al}_2\text{O}_3/\text{MgAl}_2\text{O}_4$  (127.5 kJ/mol)  $>$   $8\text{Y-ZrO}_2/\text{MgAl}_2\text{O}_4$  (124.4 kJ/mol)  $>$   $8\text{Y-ZrO}_2/\text{Al}_2\text{O}_3$  (58.1 kJ/mol). Primarily, the results in  $\text{Al}_2\text{O}_3/\text{MgAl}_2\text{O}_4$  and  $8\text{Y-ZrO}_2/\text{MgAl}_2\text{O}_4$  binary composites with anisotropic grain growth are indicated by a high average grain size ( $>2\ \mu\text{m}$ ) and grain growth at  $>10$  times the particle size, at  $1300^\circ\text{C}$  and large standard deviation of resulting values as observed in **Figure 3.15**. On the other hand,  $8\text{Y-ZrO}_2$  and  $\text{Al}_2\text{O}_3$  particles both thermally expand at a similar rate during sintering which leads to limited maximum grain size of  $723 \pm 142.6\ \text{nm}$  ( $(8\text{Y-ZrO}_2)_2/(\text{Al}_2\text{O}_3)_2$ ) and size ratio of 6.2 ( $(8\text{Y-ZrO}_2)_1/(\text{Al}_2\text{O}_3)_1$ ) for respective sintered binary specimens at  $1300^\circ\text{C}$ . Thus, the grain growth tendency of individual ceramic oxides themselves affects the sintering behavior of multiphase composites. Hence both the samples of the  $8\text{Y-ZrO}_2/\text{Al}_2\text{O}_3$  powder achieves a more homogenous sintering as indicated by resulting lower grain size ( $\sim 1\mu\text{m}$ ). This observation is corroborated by other research studies, which labels this phenomenon as the "pinning effect" in  $8\text{Y-ZrO}_2/\text{Al}_2\text{O}_3$  composites.<sup>92-94</sup> Zhou *et al.*<sup>95</sup> also observed similar results to the present

research in this study aimed at exploring super-plasticity in these ceramics regarding variations in grain sizes/shapes of binary and ternary composites of 3Y-ZrO<sub>2</sub>/Al<sub>2</sub>O<sub>3</sub> and spinel ceramic oxide material. Composites of the ternary phase and the binary 3Y-ZrO<sub>2</sub>/Al<sub>2</sub>O<sub>3</sub> show smallest grain sizes as compared to spinel-based binaries (alumina-spinel possesses largest grains). For the case of present novel ternary phase composites, the proportion of slow-growing MgAl<sub>2</sub>O<sub>4</sub> and rapidly growing Al<sub>2</sub>O<sub>3</sub> phase is lower than the binary samples, (*i.e.*, at 1/3rd volume %). Hence the overall nonuniform growth, compared to 8Y-ZrO<sub>2</sub>/Al<sub>2</sub>O<sub>3</sub> and 8Y-ZrO<sub>2</sub>/MgAl<sub>2</sub>O<sub>4</sub>, is much lower with sintering temperature as shown by size ratio values in **Figure 3.15**. The activation energies of two samples of 8Y ZrO<sub>2</sub>/MgAl<sub>2</sub>O<sub>4</sub>/Al<sub>2</sub>O<sub>3</sub> ceramic oxides is between ~ 80-115 kJ/ mol.

Furthermore, most of the multiphase composites exhibit a lower grain growth when compared to the single-phase ceramics, as represented by average grain size <2 μm and respective size ratio <10. For example, from plots in **Figures 3 & 4**, the size ratio of (8Y-ZrO<sub>2</sub>)<sub>2</sub> ~40 reduces to (8Y-ZrO<sub>2</sub>)<sub>2</sub>/(MgAl<sub>2</sub>O<sub>4</sub>)<sub>1</sub> ~7, and ternary to (8Y-ZrO<sub>2</sub>)<sub>2</sub>/(MgAl<sub>2</sub>O<sub>4</sub>)<sub>1</sub>/(Al<sub>2</sub>O<sub>3</sub>)<sub>2</sub> ~4 at a sintering temperature of 1300 °C. Thus comparing the results of the multiphase composite with their single-phase sintered compacts, we can conclude that there is a significant decrease in grain sizes. The presence of secondary and ternary phases proves to be effective in inhibiting grain growth mechanisms in single-phase ceramics during spark plasma sintering. The respective grain refinement is mainly due to previously mentioned phenomenon called “grain boundary pinning,” this is explained in most of the studies highlighted in the later sections in **Table 3.8**. We can conclude that there is a significant decrease in grain sizes due to the addition of phases to single-phase powders based on results obtained in **Figure 3.11 & Table 3.5**. The respective grain refinement is mainly due to previously mentioned phenonmen called “grain



boundary pinning” in these materials. For example, as pointed out by Yalamac *et al.*,<sup>96</sup> the pure alumina sample has nearly twice the grain size (6.2  $\mu\text{m}$ ) as compared to its binary alumina-spinel (3.3  $\mu\text{m}$ ) for similar sintering conditions. In the case of addition of secondary phase alumina in 8Y-ZrO<sub>2</sub> matrix phase (as observed by Chen *et al.*<sup>87</sup>) or the subsequent increase in the spinel content from 10% to 20% in alumina-zirconia-magnesia composites as experimented by Khoskalam *et al.*<sup>97</sup> The net result in both the studies is the reduction of overall grain size of primary matrix phase of the composite. The change in size was concluded to be due to the secondary phase grains that pin or hinder the grain boundary motion of primary phase grains which limits the grain growth as the sintering temperature increases. Meng *et al.*<sup>98</sup> further observed pinning due to the secondary phase zirconia grains exerting a dragging force on the primary phase alumina grain boundaries in Alumina-Zirconia composites. In case of both the sintered composites of three-phase 8Y-ZrO<sub>2</sub>/MgAl<sub>2</sub>O<sub>4</sub>/Al<sub>2</sub>O<sub>3</sub> ceramic oxides in **Figure 4**, it can be estimated that grain sizes or size ratio results are lower by as much as a factor of 10 when compared to their single phase ceramic oxides as plotted in **Figure 3**. Additionally, the presence of the third phase in the ternary phased sintered specimens efficiently reduces the non-uniform growth that is observed in 8Y-ZrO<sub>2</sub>/Al<sub>2</sub>O<sub>3</sub> and 8Y-ZrO<sub>2</sub>/MgAl<sub>2</sub>O<sub>4</sub> binary phase composites. Thus, the present study through its empirical model of size ratio versus temperature provides is unique as it quantifies the effect of the grain boundary pinning effect in the present multiphase ceramics. In the present study, the different temperature-dependent grain growth tendencies of individual ceramic phases give rise slower grain growth ceramic acting as secondary phases thereby causing grain growth pinning and reducing the overall grain size of the sample. reduction in grain size due to phase additions, a concept that is well known but not effectively characterized quantitatively in ceramic literature.

Lastly, scanning electron micrographs of fracture surfaces of the representative sintered ceramic oxide samples have been provided in the figure for additional graphical information. The micrographs in **Figure 3.18** shows the fine-grained microstructures for single phase zirconia [(8Y-ZrO<sub>2</sub>)<sub>3</sub>] at low and high sintering temperatures. **Figures 3.20 and 3.21** summarize the fracture surfaces for the representative binary [(8Y-ZrO<sub>2</sub>)<sub>1</sub>/(MgAl<sub>2</sub>O<sub>4</sub>)<sub>1</sub>] and ternary phase composites [(8Y-ZrO<sub>2</sub>)<sub>2</sub>/(MgAl<sub>2</sub>O<sub>4</sub>)<sub>1</sub>/(Al<sub>2</sub>O<sub>3</sub>)<sub>3</sub>].

The densification curves for MgAl<sub>2</sub>O<sub>4</sub>, Al<sub>2</sub>O<sub>3</sub>, and 8Y-ZrO<sub>2</sub> single-phase ceramics are plotted in **Figure 3.12** and for their corresponding multiphase composites in **Figure 3.13** concerning sintering temperature. These densification curves are useful in explaining the grain growth in ceramic oxides at different sintering temperatures. As explained by Shen *et al.*,<sup>89</sup> at lower sintering temperatures or during initial stages, most of the work during sintering is spent on densification of green compacts rather than grain growth; this is exhibited by the sharp increase in graphical plots for respective single and multiphase samples in the pre-densification in **Figure 3.12-3.13**. In post-densification stage, thermally activated mechanisms during sintering play an important role in the rapid expansion of grains since most of the pores/vacancies between powder compacts are eliminated, and hence the sintered ceramics achieved a higher grain growth.<sup>89, 99, 100</sup> The growth was observed with significant changes in average grain size and size ratio values for single/multiphase ceramics at higher temperatures. Specifically, the transition from densification to grain growth is more prominent for single phase as the sintering temperature goes up to 1050°C. This post-densification region was found to be at lower temperatures for single phases (1050°C) as compared to multiphase composites (1150°C). This delayed densification in binary/ternary phases was mainly attributed to lower grain growth at higher temperatures, i.e., >1200°C. Further, the single-phase samples reached

90% density when sintered temperatures are around 950°C, while most multiphase samples became dense only beyond 1000 °C. This delay can be attributed to varying individual densifying tendencies of MgAl<sub>2</sub>O<sub>4</sub>, Al<sub>2</sub>O<sub>3</sub>, and 8Y-ZrO<sub>2</sub> phases<sup>101</sup> as observed previously. We observed that the variable nature of the thermal expansion of ceramic phases makes it more complex to establish the role of densification of composite on average grain size. Hence the densification tendency in single/multiphase composites was different from grain growth tendency. It can thus be concluded that single-phase samples sintered faster as compared to multiphase composites (**Figure 3.12-3.13**). The given conclusion was especially significant as obtaining 90% theoretical dense multiphase composites is one of the key requirements for these ceramic oxides to be candidate surrogate materials for the nanocrystalline nuclear fuel project.

Lastly, it is important to note that the heating rate of 10°C/min was selected for single phase samples; while we obtained multiphase composites with large standard deviation in average grain size values when sintered at the same rate. Hence, binary, and ternary phase mixtures were sintered at a higher heating rate of 100°C/min leading to more uniform grain sized composites that are better suited for the current study. The heating rate for the single-phase samples was chosen based on studies (refer to chapter 5) which highlight that while moderate changes in heating rates do not significantly affect grain size and density,<sup>102-104</sup> higher heating rates in sintering of monolithic samples (especially spinel) causes porosity, thereby degrading its optical properties.

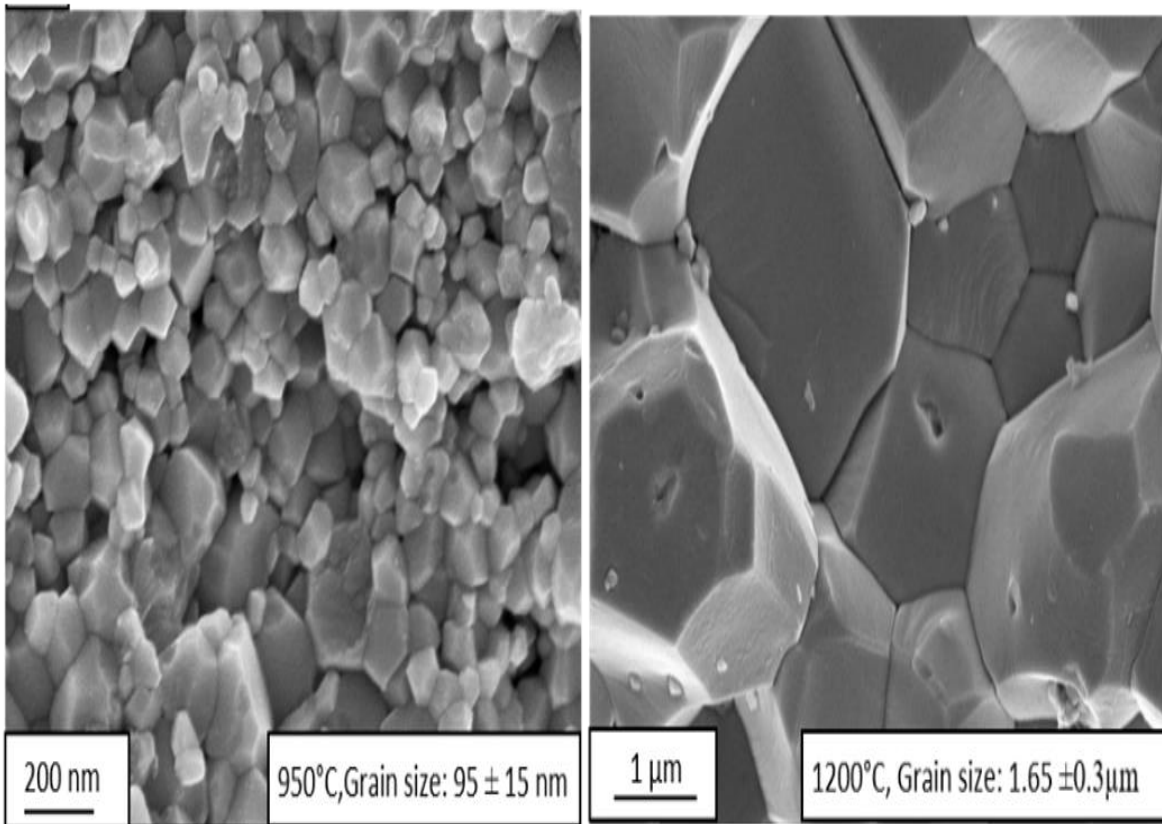


**Figure 3.18 SEM micrographs of the representative fracture surface of sintered  $(8\text{Y-ZrO}_2)_3$  ceramic composites with average grain size information at different sintering temperatures**

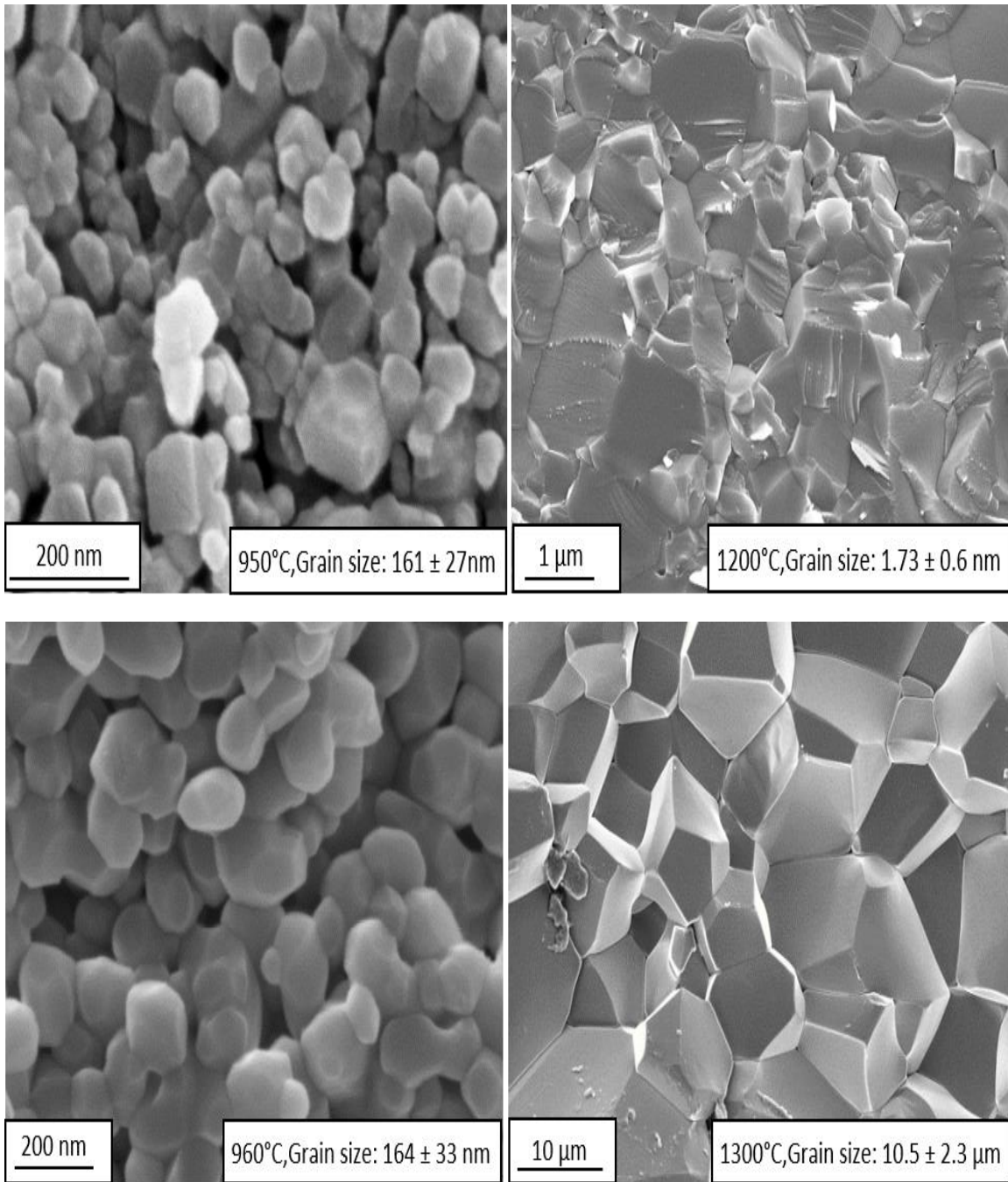


**Figure 3.19 SEM micrographs of representative fracture surfaces of sintered  $(\text{MgAl}_2\text{O}_4)_1$  (top) and  $(\text{Al}_2\text{O}_3)_2$  (bottom) ceramic composites with average grain size information at different sintering temperatures.**

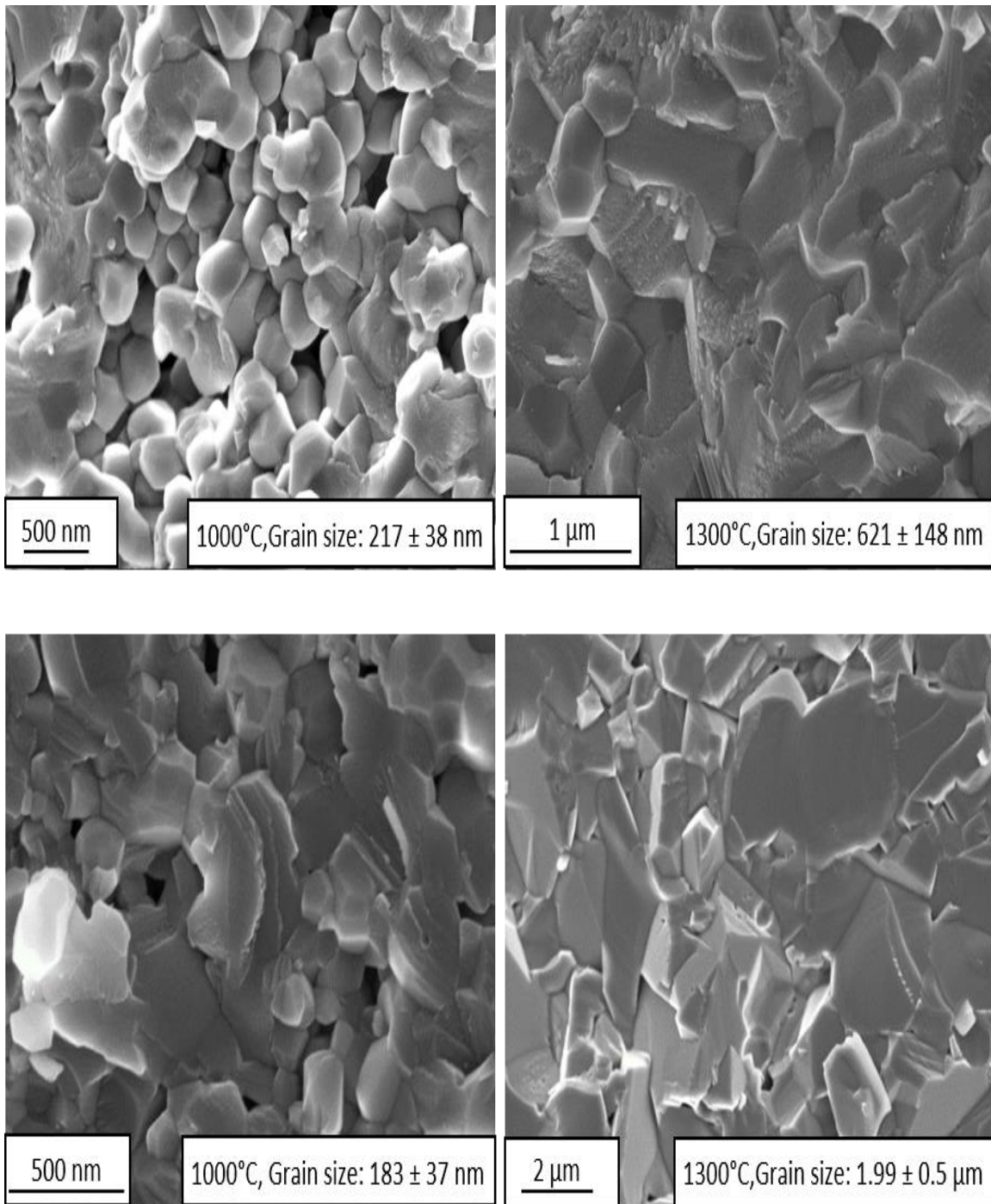


**Figure 3.20 SEM micrographs of representative fracture surfaces of binary sintered composites of 8Y-ZrO<sub>2</sub>/Al<sub>2</sub>O<sub>3</sub>(top) and Al<sub>2</sub>O<sub>3</sub>/MgAl<sub>2</sub>O<sub>4</sub>(bottom) ceramic composites with average grain size information at different sintering temperatures**

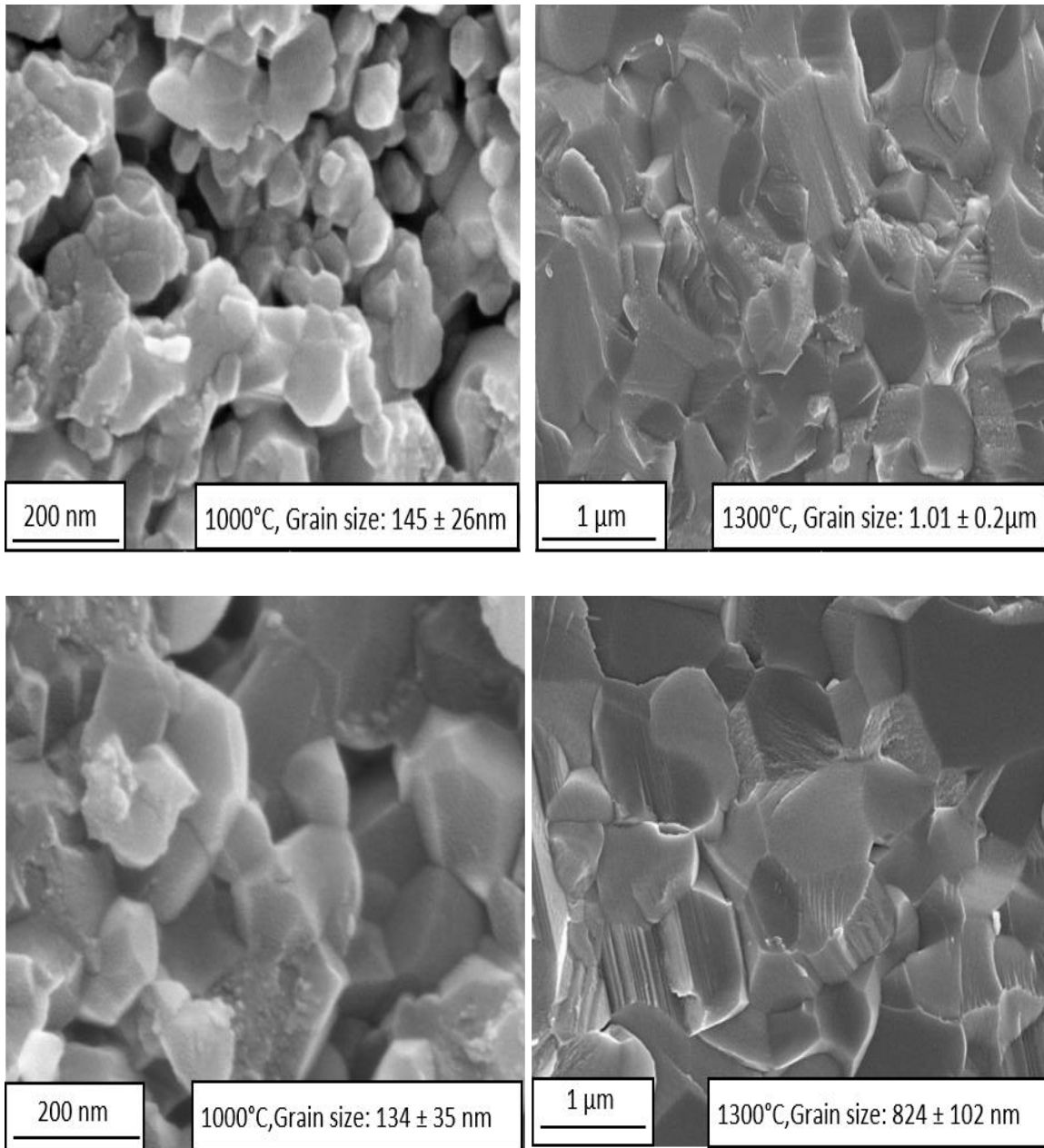


**Figure 3.21 SEM micrographs of representative fracture surfaces of binary composite of 8Y-ZrO<sub>2</sub>/MgAl<sub>2</sub>O<sub>4</sub> (top) and 8Y-ZrO<sub>2</sub>/MgAl<sub>2</sub>O<sub>4</sub>/Al<sub>2</sub>O<sub>3</sub> three phase sintered (bottom) ceramic composites with average grain size information at different sintering temperatures**

### 3.8 Results: Sintering of ceramic oxides of two different powder sizes

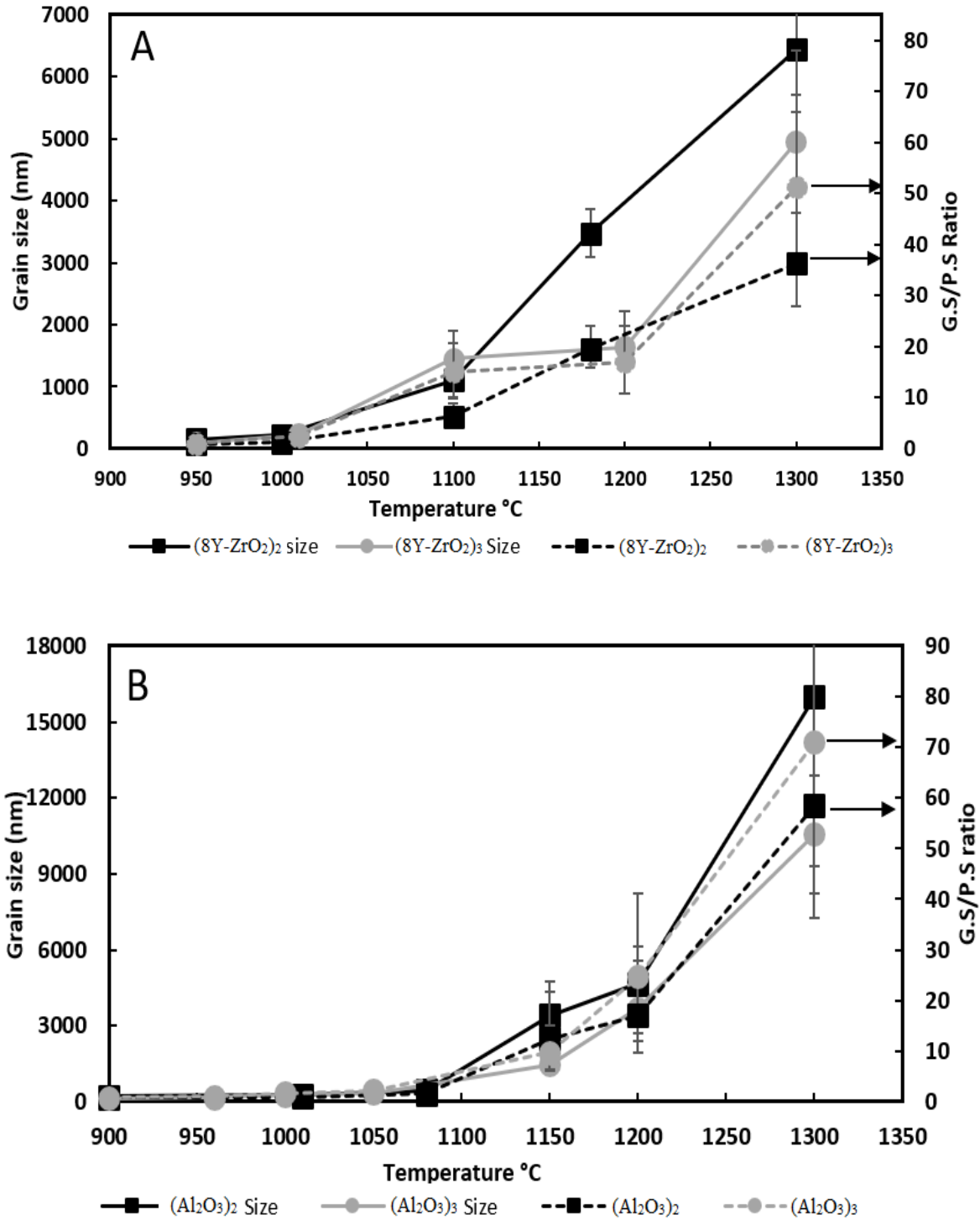


Figure 3.22 Graphical results are indicating the effect of sintering temperature on grain size and size ratio in single phase ceramic oxides of 8Y-ZrO<sub>2</sub> (A), Al<sub>2</sub>O<sub>3</sub> (B) and MgAl<sub>2</sub>O<sub>4</sub> (C). Black and grey colored lines highlight the two different powder sizes.



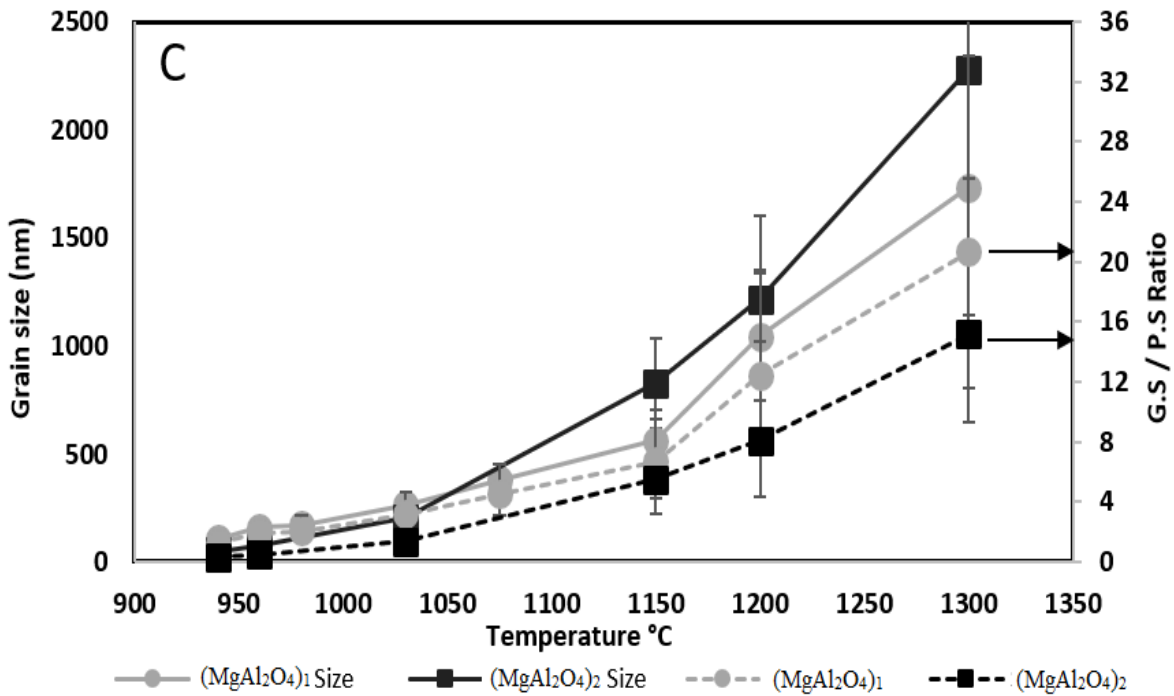


Figure 3.22 continued

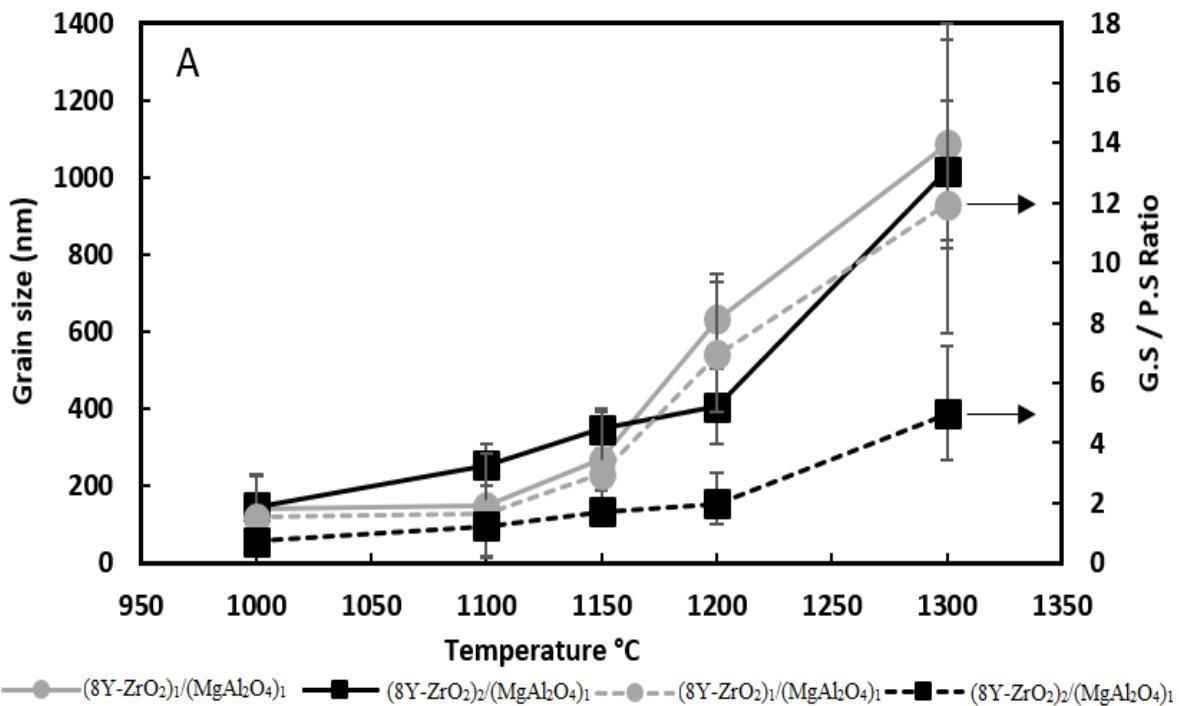


Figure 3.23 Graphical results indicating the effect of sintering temperature on grain size and size ratio in binary composites of 8Y-ZrO<sub>2</sub>/MgAl<sub>2</sub>O<sub>4</sub> (fig. A), Al<sub>2</sub>O<sub>3</sub>/MgAl<sub>2</sub>O<sub>4</sub> (fig. B), 8Y-ZrO<sub>2</sub>/Al<sub>2</sub>O<sub>3</sub> (fig. C) and ternary phase ceramic composites 8Y-ZrO<sub>2</sub>/MgAl<sub>2</sub>O<sub>4</sub>/Al<sub>2</sub>O<sub>3</sub> (fig.D) with two different particle sizes.

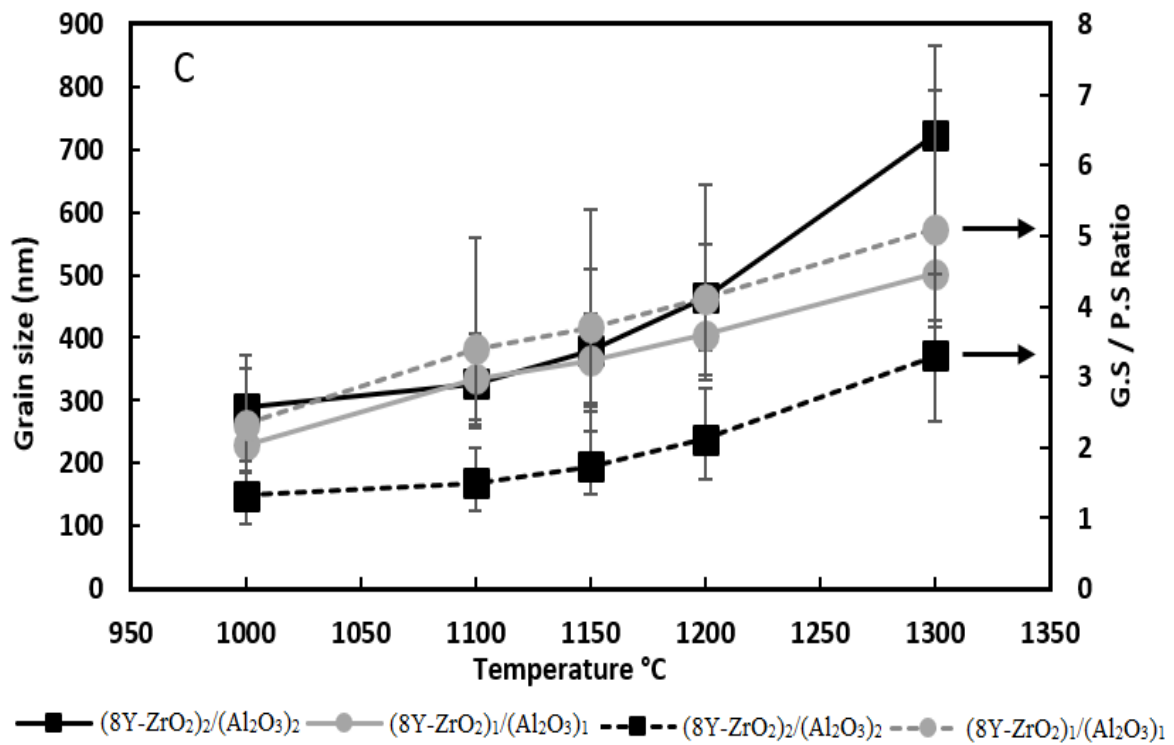
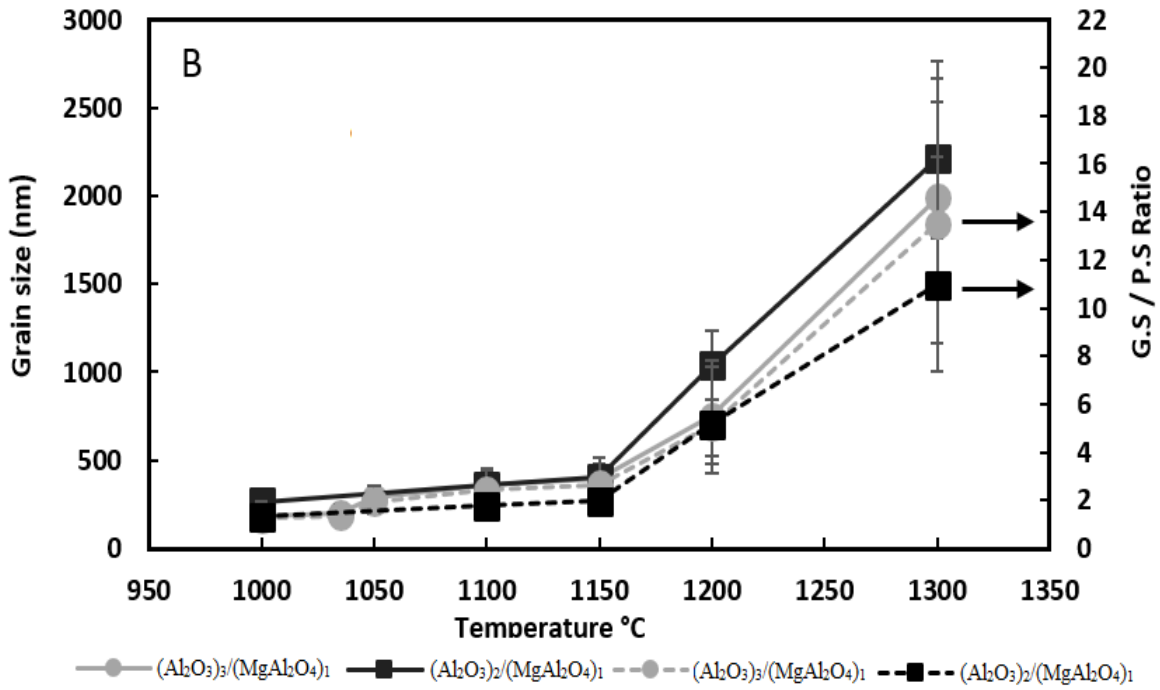
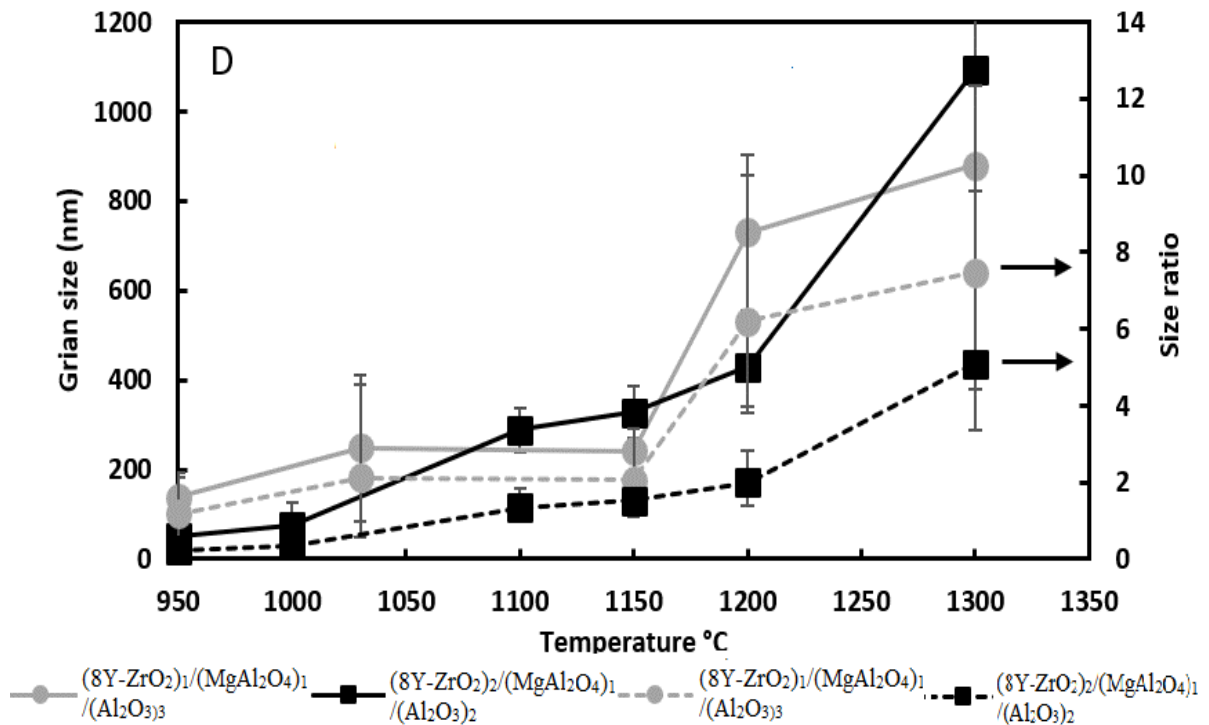


Figure 3.23 Continued.



**Figure 3.23 continued.**

Sintering experiments were carried out on ceramic oxide powders with two different particle size ranges: one closer to 100 nm, while the other powder ~200 nm at a range of temperatures between 950-1300°C, this is shown in **Table 3.3 and 3.4**. These experiments were performed to further analyze the role of particle size of the powders on grain sizes of the final sintered compacts, The respective trends in average grain sizes and size ratios are plotted previously for single phase in Figure 3.22 and binary/ternary phase in Figure 3.23 previously. Further detailed graphs are plotted for single phase ceramics in **Figure 3.22(A-C)** and multiphase ceramics in **Figure 3.23(A-D)** for the two different size powders for each ceramic composite. The graphs consist of two Y axes, one for average grain size and the other for size ratio, plotted versus sintering temperature. For each plot, the grain growth results, i.e., grain size and size ratio of two individual sintered powders are highlighted by black/grey colored lines, with the smaller particle sized powder being designated by the grey color. The dotted

lines with circle markers correspond to size ratio values (with arrows pointing towards Y-axis of size ratio), while solid lines with square markers relate to grain size distribution.

From **Figure 3.22A** it can be observed that at higher sintering temperatures, the larger particle sized powder  $(8Y-ZrO_2)_2$  (particle size  $\sim 180$  nm) contains a higher grain size than the smaller sized  $(8Y-ZrO_2)_3$  (particle size  $\sim 80$  nm). For example, the average grain size of  $(8Y-ZrO_2)_2$  is  $6.44 \pm 2.2$   $\mu\text{m}$  at  $1300^\circ\text{C}$  when compared to that of  $(8Y-ZrO_2)_3$  which is  $3.44 \pm 0.69$   $\mu\text{m}$  (**Figure 3.22A**). Similar significant higher grain sizes are obtained for larger spinel (**Figure 3.22B**)  $((MgAl_2O_4)_1 > (MgAl_2O_4)_2)$  and  $Al_2O_3$  (**Figure 3.22C**)  $((Al_2O_3)_2 > (Al_2O_3)_3)$  powders during densification stage at lower temperatures and post densification (sintering temperature  $> 1200^\circ\text{C}$ ) as observed in diagrams (**Figure 3.12**). However, in case of the size ratio, especially during post densification stage finer powder shows higher values as compared to larger particle sized powder. For example, as observed from **Figure 3.22A**, at  $1300^\circ\text{C}$ , larger  $(8Y-ZrO_2)_2$  powder shows of ratio, i.e.,  $\sim 36$  which was much lower than for the  $(8Y-ZrO_2)_3$  powder (ratio = 52). A similar trend in ratios was also observed for  $(MgAl_2O_4)_1$  (**Figure 3.22B**) and Alumina powders  $((Al_2O_3)_2$  and  $(Al_2O_3)_3)$  in **Figure 3.22C**, indicating that the larger sized powders result in a slower rate of grain growth. The activation energy of grain growth for different powders of given single phase ceramics obtained in **Figure 3.16** also follow similar trend as size ratio. For example the size ratio and activation energy of grain growth for the  $(8Y-ZrO_2)_3$  powder (Activation energy = 161.5 kJ/mol ) was much smaller than that of the  $(8Y-ZrO_2)_2$  powder (191.4 kJ/mol).

On a similar note, sintering experiments were performed for binary and ternary phase mixtures of  $8Y-ZrO_2$ ,  $MgAl_2O_4$ , and  $Al_2O_3$  ceramic oxide powders for two different size ranges similar those of single-phase powders (refer to table for particle size information of mixed

powders). **Figure 3.30A-C** show resulting plots for binary phase oxides while **Figure 3.30D** portrays the respective data for ternary phase composites. The changes in average grain size distribution (solid line) and size ratio (dashed lines) are plotted versus sintering temperature. The nomenclature behind choosing the type of lines (solid/dash) and color (black/grey) for respective larger/smaller particle powders is similar as described for single phase composites. For multiphase composites of 8Y-ZrO<sub>2</sub>/Al<sub>2</sub>O<sub>3</sub>(**Figure 3.30C**), three phase 8Y-ZrO<sub>2</sub>/MgAl<sub>2</sub>O<sub>4</sub>/Al<sub>2</sub>O<sub>3</sub> (**Figure 3.30D**), larger particle size led to a higher grain size, but lower size ratio at the higher temperatures. However, in the case of Al<sub>2</sub>O<sub>3</sub>/MgAl<sub>2</sub>O<sub>4</sub>(**Figure 3.30B**), and 8Y-ZrO<sub>2</sub>/MgAl<sub>2</sub>O<sub>4</sub>(**Figure 3.30A**) considering the standard deviation values inherent in the grain size results, it is difficult to accurately predict the effect of different particle size powders on sintered microstructure. However, regarding activation energy of grain growth for binary and ternary phase composites in **Figure 3.16 A-D** the finer powders in the range of 100 nm have lower energy values than the bigger particle sized powders. Overall, for a given ceramic composites, powder size of respective ceramic powders can affect the sintering behavior.

### **3.9 Discussion: Sintering of ceramic oxides of two different powder sizes**

A fundamental conclusion from sintering results of ceramic oxide samples with two different particle sizes is obtained using empirical data presented in **Figure 3.29 & 3.30**. We concluded the following sintering behavior, as the sintering temperature increases, *i.e.*, powders with larger particle size distribution give rise microstructures with higher average grain sizes, while samples with smaller particle sizes tend to have a faster grain growth rate during sintering. We can concur that this phenomenon is well defined in single phase 8Y-ZrO<sub>2</sub>, MgAl<sub>2</sub>O<sub>4</sub>, and Al<sub>2</sub>O<sub>3</sub> from the graphs (**Figure 3.18**). High grain growth rate has been observed and described

previously by Chaim et al.<sup>70</sup> and Mamedov et al.<sup>105</sup> because smaller uniform particles result in faster kinetics of surface diffusion, *i.e.*, grain coarsening that leads to rapid necking at the particle surface during sintering thereby the particle fuse together into homogenous deagglomerated grains. However, beyond the post densification zone (**Figure 3.12** & **Figure 3.13**), the resulting growth kinetics at high temperatures during sintering are found to be limited in nature as observed by the average grain size results. Thus, we believe that the initial higher particle sizes govern the final grain size, as pointed out by the lower final average grain size (*e.g.*, (8Y-ZrO<sub>2</sub>)<sub>3</sub> at 1300°C has finer grain size as compared to (8Y-ZrO<sub>2</sub>)<sub>2</sub>). These trends developed from experimental results in the present study thus achieve a unique nature and can potentially be applied to study the effects of micron-sized powders on resulting grain sizes of the sintered composite. It was observed that these trends in case of multiphase ceramics (Figure 3.23) however were less clear as compared to single phase specimens. Factors affecting grain growth in multiphase oxide ceramics were found to be more complicated. Apart from sintering parameter of temperature and individual powder size, variations in grain growth tendency of individual phases during sintering can also affect the homogeneous arrangement of grains in the microstructure.

Thus, we believe that the initial higher particle sizes govern the final grain size. These resulting particle trends developed from experimental results in the present study thus emphasize the role played by the particle size of powders on grain growth tendency of respective sintered specimens. The trends can also be potentially applied to model grain growth of commercially available larger micron particle based powders.

**Table 3.6 Bulk density of the sintered composites of single phase powders in Figure 3.22 as obtained from Archimedes method.**

Sintering Temperature °C	% Bulk density (Archimedes method)	
	(8Y-ZrO <sub>2</sub> ) <sub>2</sub>	(8Y-ZrO <sub>2</sub> ) <sub>3</sub>
950	88.1 ± 0.8	93.0 ± 0.6
1010	96.9 ± 0.2	98.6 ± 0.4
1100	99.2 ± 0.5	98.7 ± 0.7
1200	98.3 ± 0.3	97.9 ± 0.2
1300	99.2 ± 0.3	98.5 ± 0.2
Sintering Temperature °C	% Bulk density (Archimedes method)	
	(MgAl <sub>2</sub> O <sub>4</sub> ) <sub>1</sub>	(MgAl <sub>2</sub> O <sub>4</sub> ) <sub>2</sub>
940	88.8 ± 0.4	81.8 ± 0.1
960	97.5 ± 0.6	91.1 ± 0.2
1030	98.7 ± 0.6	97.9 ± 0.5
1150	98.3 ± 0.4 @ 1075°C	99.9 ± 0.4
1200	98.2 ± 0.4	98.97 ± 0.2
1300	99.9 ± 0.6	99.3 ± 0.2
Sintering Temperature °C	% Bulk density (Archimedes method)	
	(Al <sub>2</sub> O <sub>3</sub> ) <sub>3</sub>	(Al <sub>2</sub> O <sub>3</sub> ) <sub>2</sub>
900	78.8 ± 5.8	68.7 ± 7.3
1000	98.5 ± 0.2	92.5 ± 0.3
1150	99.3 ± 0.1	99.3 ± 0.7
1200	99.1 ± 0.3	97.8 ± 0.2
1300	98.4 ± 0.4	99.0 ± 0.2

**Table 3.7 Bulk density of the sintered composites of binary and ternary-phase powders in Figure 3.19, as obtained from Archimedes method.**

Sintering Temperature °C	% Bulk density (Archimedes method)	
	$(8Y-ZrO_2)_1/(MgAl_2O_4)_1$	$(8Y-ZrO_2)_2/(MgAl_2O_4)_1$
1000	90.9 ± 0.4	91.3 ± 0.1
1100	98.3 ± 0.6	99.1 ± 0.8
1150	98.8 ± 0.2	99.3 ± 0.3
1200	98.1 ± 0.4	97.8 ± 0.2
1300	99.2 ± 0.7	98.0 ± 0.2
	$(Al_2O_3)_3/(MgAl_2O_4)_1$	$(Al_2O_3)_2/(MgAl_2O_4)_1$
1000	97.9 ± 1.3	94.4 ± 0.6
1100	98.4 ± 0.6	98.1 ± 1.0
1150	98.8 ± 0.1	98.4 ± 0.2
1200	98.9 ± 0.4	98.4 ± 0.3
1300	97.9 ± 0.3	99.1 ± 0.2
	$(8Y-ZrO_2)_1/(Al_2O_3)_1$	$(8Y-ZrO_2)_2/(Al_2O_3)_2$
1000	80.4 ± 1.3	69.2 ± 1.6
1100	92.5 ± 0.2	88.0 ± 0.8
1150	98.1 ± 0.3	98.1 ± 0.1
1200	98.3 ± 0.1	98.6 ± 0.3
1300	98.7 ± 0.2	99.3 ± 0.2
	$(8Y-ZrO_2)_1/(MgAl_2O_4)_1/(Al_2O_3)_3$	$(8Y-ZrO_2)_2/(MgAl_2O_4)_1/(Al_2O_3)_2$
950	80.9 ± 0.9	73.6 ± 0.2
1000	91.4 ± 0.9 @ 1030°C	80.1 ± 0.3
1150	98.7 ± 0.7	97.1 ± 0.5
1200	97.8 ± 0.6	99.0 ± 0.4
1300	98.1 ± 0.4	98.0 ± 0.6



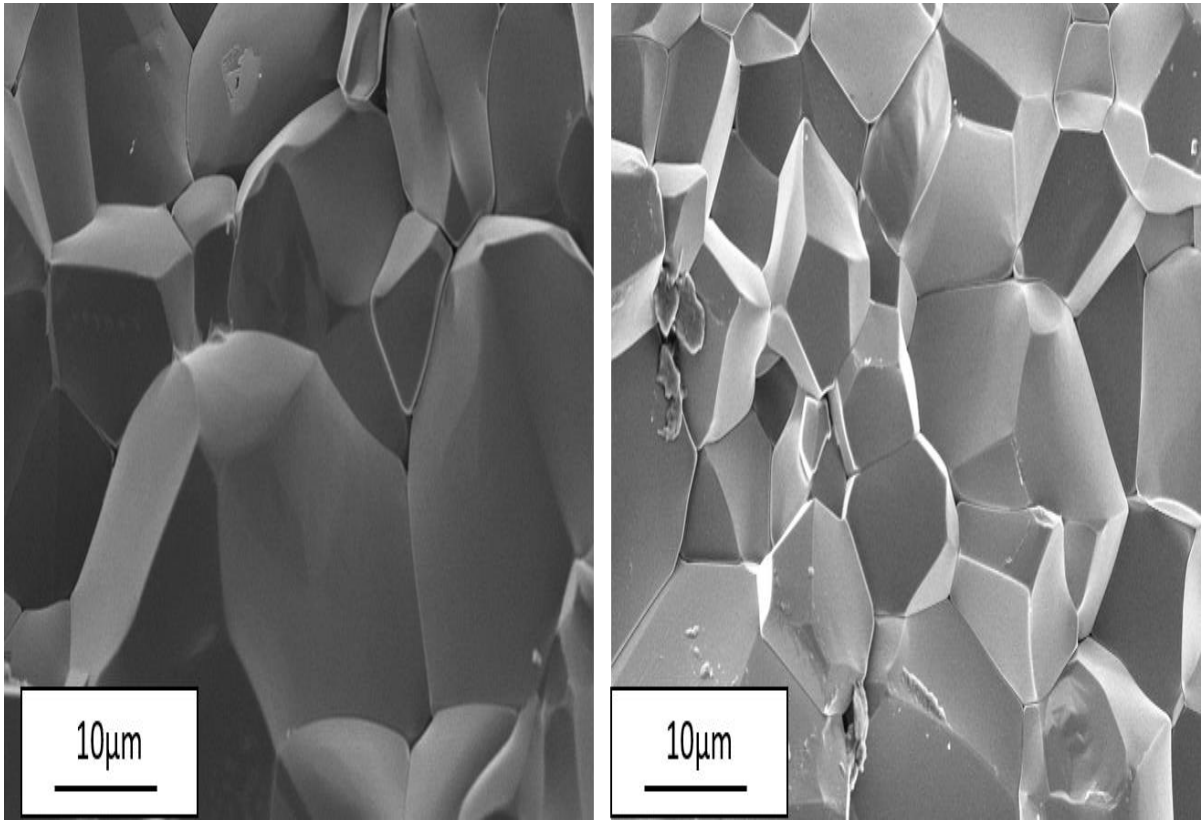


**Figure 3.24 SEM micrographs of alumina sintered specimens fabricated from two different particles sized powders  $(\text{Al}_2\text{O}_3)_2$  (left) and  $(\text{Al}_2\text{O}_3)_3$  (right) sintered at  $1300^\circ\text{C}$ . This representative image highlights the effect of individual powder size on final grain size as discussed in Figure 3.22.**

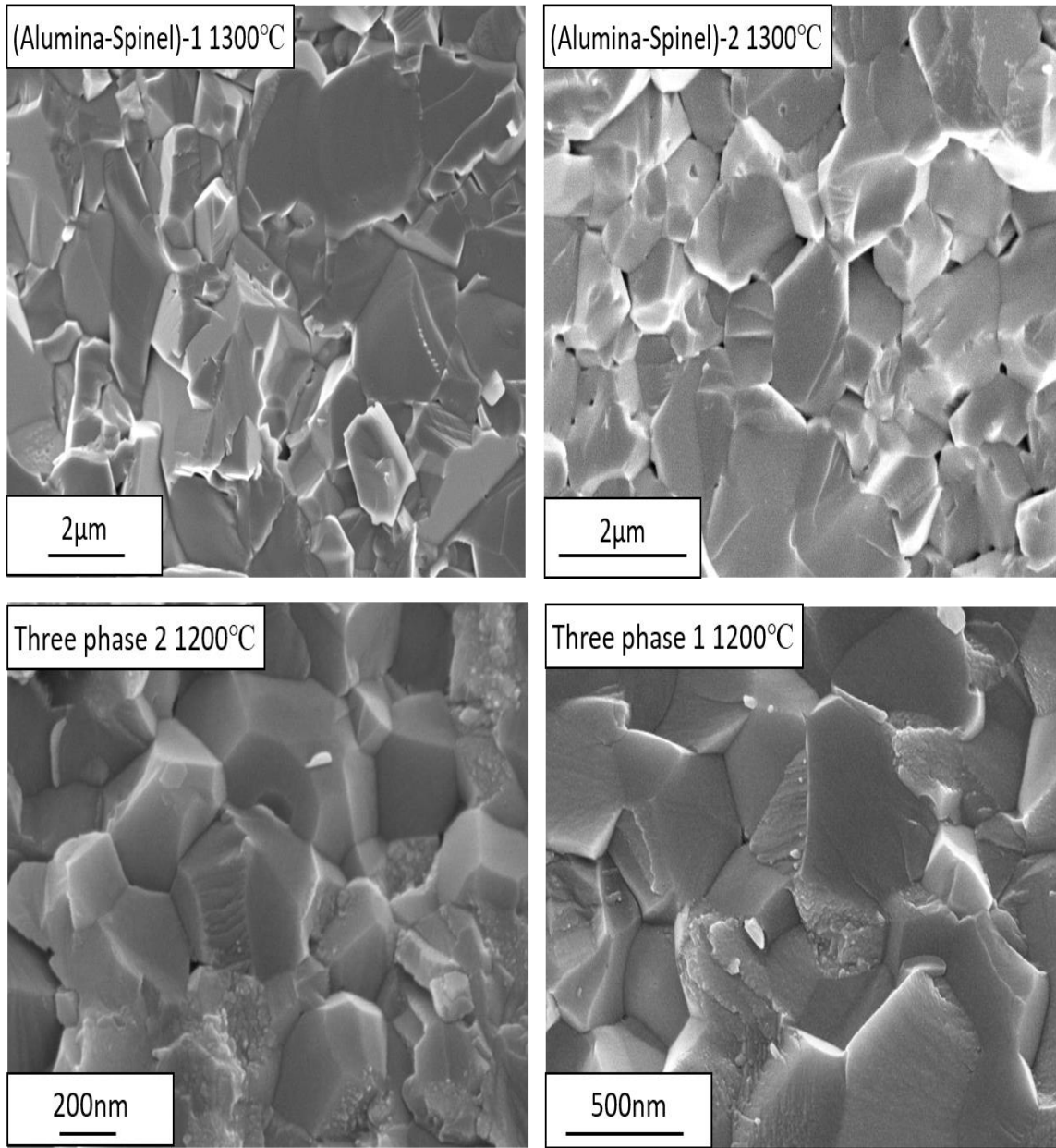


**Figure 3.25** SEM micrographs of alumina-spinel binary composite (top) and three phase 8Y-ZrO<sub>2</sub>/MgAl<sub>2</sub>O<sub>4</sub>/Al<sub>2</sub>O<sub>3</sub> composite. The ceramic oxides are fabricated from two different particles sized powders sintered i.e. (Al<sub>2</sub>O<sub>3</sub>)<sub>3</sub>/(MgAl<sub>2</sub>O<sub>4</sub>)<sub>1</sub> (Top left) and (Al<sub>2</sub>O<sub>3</sub>)<sub>2</sub>/(MgAl<sub>2</sub>O<sub>4</sub>)<sub>1</sub> (Top right) at 1300°C while (8Y-ZrO<sub>2</sub>)<sub>2</sub>/(MgAl<sub>2</sub>O<sub>4</sub>)<sub>1</sub>/(Al<sub>2</sub>O<sub>3</sub>)<sub>2</sub> (Bottom left) and (8Y-ZrO<sub>2</sub>)<sub>1</sub>/(MgAl<sub>2</sub>O<sub>4</sub>)<sub>1</sub>/(Al<sub>2</sub>O<sub>3</sub>)<sub>3</sub> (Bottom right) at 1200°C respectively. The representative image highlights the effect of individual powder size on final grain size as discussed in Figure 3.19.

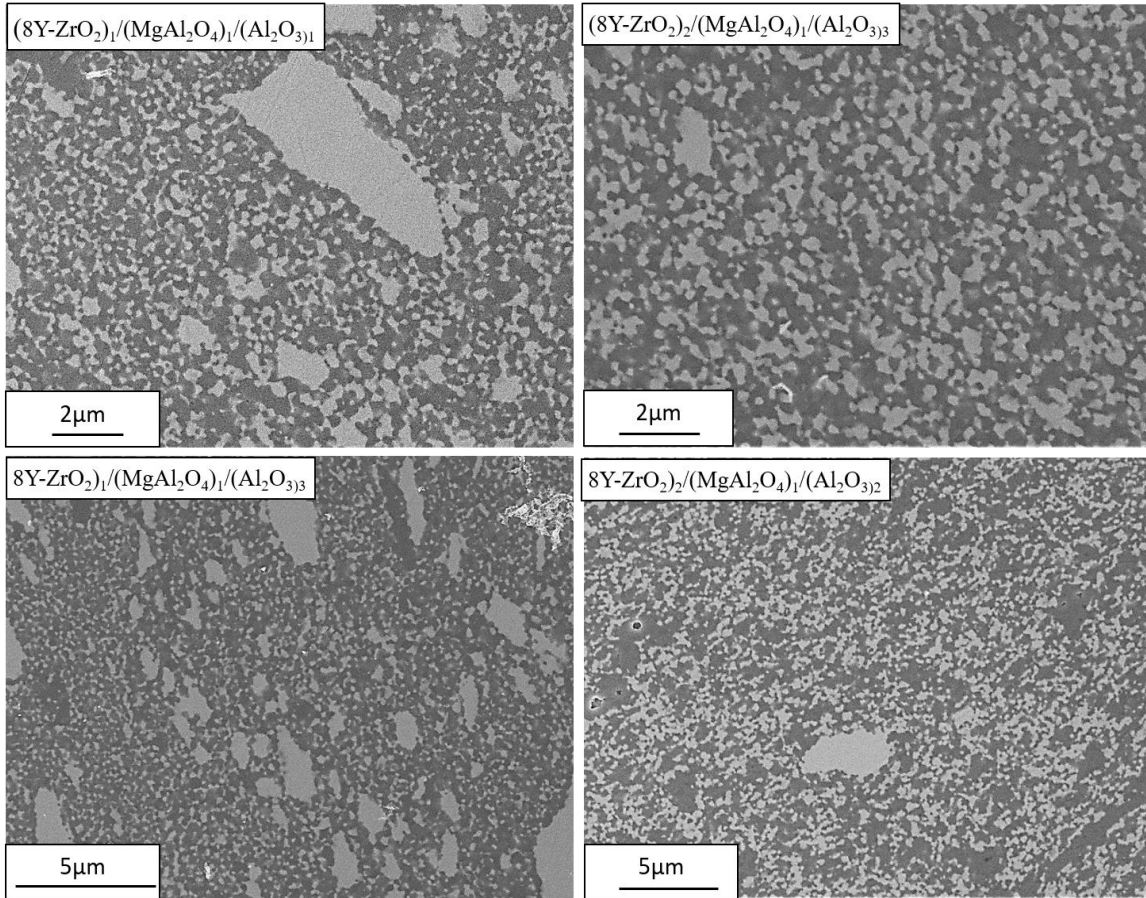


**Figure 3.26** SEM micrographs of polished surfaces of three-phase composites obtained by sintering of various powder mixtures at 1150°C. The different powder mixture used are labeled according to their designations and information concerning the particle size of the can be obtained from table 3.3 and chapter 3. The micrographs on the left side show large clusters of 8Y-ZrO<sub>2</sub> as compared to the micrographs on the right. The spinel and alumina are indicated by the darker regions.

Two reasons can be assumed to be behind the non-uniform clustered microstructure in 8Y-ZrO<sub>2</sub>)<sub>1</sub>/(MgAl<sub>2</sub>O<sub>4</sub>)<sub>1</sub>/(Al<sub>2</sub>O<sub>3</sub>)<sub>3</sub> and (8Y-ZrO<sub>2</sub>)<sub>1</sub>/(MgAl<sub>2</sub>O<sub>4</sub>)<sub>1</sub>/(Al<sub>2</sub>O<sub>3</sub>)<sub>1</sub>. Firstly, each phase ceramic oxide has different grain growth tendency, and furthermore, this tendency is also dependent on the ceramic powder size. Thus, either (8Y-ZrO<sub>2</sub>)<sub>1</sub> and (Al<sub>2</sub>O<sub>3</sub>)<sub>1</sub> or (Al<sub>2</sub>O<sub>3</sub>)<sub>3</sub> achieve higher grain growth than the spinel leading to larger grains as indicated by the clusters. Secondly, milling of individual ceramic powders could be assumed to affect the particle size of the mixture and thereby to cause the ceramic oxide single particles together, which result in large clusters of grains after sintering. Thus, for example, in case of (8Y-ZrO<sub>2</sub>)<sub>2</sub>/(MgAl<sub>2</sub>O<sub>4</sub>)<sub>1</sub>/(Al<sub>2</sub>O<sub>3</sub>)<sub>3</sub>, (8Y-ZrO<sub>2</sub>)<sub>2</sub> and (Al<sub>2</sub>O<sub>3</sub>)<sub>2</sub> powders have higher particle sizes, and hence the rate of densification/grain growth is slower at sintering temperatures of 1150°C; while spinel itself is a hard to sinter ceramic.

Thus, the overall microstructure looks more homogenous and uniform as compared to the ternary phase specimens on the left. To conclude, the knowledge of particle size of individual ceramic powders, grain growth tendency among ceramic oxides and the role played by the particle size on grain growth affects the homogeneity of the ternary phase composites.

### 3.10 Significance of current study as compared to previous literature

**Table 3.8 Summary of studies performed on grain growth of single phase ceramic oxides. Information is provided regarding powder sizes, grain sizes of sintered specimens, sintering parameters, and key observations for comparisons with the present study.**

Author/ year	Particle/ Crystallite Size	Range of Average Grain Sizes	Significant Sintering Parameters	Key points of the study
<b>8Y-ZrO<sub>2</sub></b>				
Tamburini (2004) <sup>106</sup>	Crystallite size: 21 nm (Vendor)	<50 nm to 700 nm	Heating rate: 50-300°C/min Pressure: 15-141 MPa Temperature: 1000-1400°C	Effect of sintering parameters on final density and grain size.
Dahl (2007) <sup>104</sup>	Particle size: <50 nm (BET)	0.21 µm to 3.3 µm	Temperature: 1150-1300°C	Effect of different sintering methods (HP, SPS) on grain growth of 8Y- ZrO <sub>2</sub>
Maca (2010) <sup>107</sup>	Particle size: 140 nm (BET)	3-3.5 µm	Temperature: 1530°C (SSS), 1440°/1290°C (TSS)	Particle size variations on microstructure from Two-Step (TSS) and Single-Step(SSS) Sintering
Takeuchi (2002) <sup>108</sup>	Particle size: 100 nm (Vendor)	170 - >1µm	Temperature: 1100°C-1300°C	Density, grain size, mechanical and electrical properties of 8Y- ZrO <sub>2</sub> powder
Zhang (2011) <sup>109</sup>	Particle size: N/A	100 - 300 nm	Temperature: 1100°C-1200°C	Optical properties of translucent 8Y- ZrO <sub>2</sub> at high pressure and variable temperature
<i>Present study</i>	<i>Particle size: 80-200 nm</i>	<i>90 - 6000 nm</i>	<i>Temperature: 950°C-1300°C</i>	<i>Grain size-particle size correlation</i>

**Table 3.8 Continued**

<b>Author/ year</b>	<b>Particle/Cryst allite</b>	<b>Range of Average Grain Sizes</b>	<b>Significant Sintering Parameters</b>	<b>Key points of the study</b>
<b>Spinel (MgAl<sub>2</sub>O<sub>4</sub>)</b>				
Krell (2009) <sup>110</sup>	Particle size: 50-100 nm, (BET)	0.4-5 μm	Temperature: 1100-1400°C	Grain size effects on hardness of spinel compacts processed by sol- gel, slip casting
Morita (2008, 2009) <sup>84, 85</sup>	Particle size: 360 nm (SEM)	400-500 nm	Heating rate: 2-100°C/min Temperature: 1300°C	Effect of transparency of different spinel composites by changing heating rates
Wollmers hauser (2014) <sup>111</sup>	Particle size: 25.8-33.6, 200 nm (Vendor)	28-52.3 nm, >200 nm	Temperature: 740-845°C	Pressure sintering of ultrafine spinel for evaluating Hall- Petch relation
Wang (2009) <sup>112</sup>	Powder: 60 nm (Vendor)	600-700 nm	Pressure: 5-100 MPa	Two-step pressure profile sintering results in improved transparency in spinel
<i>Present study</i>	<i>Powder: 80-150 nm</i>	<i>100-2280 nm</i>	<i>Temperature: 950°C-1300°C</i>	<i>Grain size-particle size correlations</i>

**Table 3.8 continued**

<b>Author/ year</b>	<b>Particle/Cryst allite</b>	<b>Range of Average Grain Sizes</b>	<b>Significant Sintering Parameters</b>	<b>Key points of the study</b>
<b>Alumina (Al<sub>2</sub>O<sub>3</sub>)</b>				
Aman (2009, 2011) <sup>113, 114</sup>	170 nm (vendor)	360 nm-5 μm	Heating rate: 8-600°C/min Temperature: 1100-1350°C	SPS parameters affect density, grain size, optical properties and grain growth kinetics
Jin (2010) <sup>115</sup>	Bimodal: 0.36-1.1 μm (vendor)  Milled: 800 nm	1.8-2.2, 5.2 μm	Heating rate: 100°C/min Temperature: 700°C	Effect of chemical HF treatment to improve particle deagglomeration for improved sintering
Shen (2002) <sup>89</sup>	0.4 μm (Vendor)	0.8 - 27.5 μm	Temperature 1175 - 1600°C  Pressure: 50-200 MPa Heating rate: 50-600°C/min	Effect of holding time, sintering temperature, pressure on densification and grain growth
Wang (2000) <sup>116</sup>	0.3-0.4, 3.5, 21.4 μm (vendor)	N/A	Heating: 20-300C°/min	Role of particle size on densification during sintering
Santanach (2011) <sup>117</sup>	140 nm (SEM)	0.2 - 9 μm	Heating rate 100-150°C/min Temperature 600-1500°C  Pressure: 10-100 MPa	Influence of pressure, pulse pattern, temperature and hold time on grain size
<i>Present study</i>	<i>Powder: 150-275 nm</i>	<i>160-16000 nm</i>	<i>Temperature: 950°C-1300°C</i>	<i>Grain size-particle size correlation</i>

The results and experimental parameters of the present study for single phase composites were contrasted with relevant literature data as shown in **Table 3.8**. We conclude that the present study involved fabrication of 8Y- ZrO<sub>2</sub> composites with a wide range of grain sizes as compared to most of the past experimental work (Dahl *et al.*<sup>104</sup> fabricated 8Y- ZrO<sub>2</sub> from 0.2nm to >3μm grain size). A similar trend can also be observed in case of polycrystalline spinel specimens where the current study has different microstructures with 100nm to 2.28um grain sizes. On the other hand, Al<sub>2</sub>O<sub>3</sub> has been extensively studied by various researchers, especially for its grain growth tendency. Thus, the significance of the current study lies in its large sampling of sintered microstructures varying from nano-, submicron to micron-sized grains. This extensive nature of the data helps to understand the response of ceramic oxides to temperature more accurately.

Another observation that was highlighted particle size column in **Table 3.8** was that current study is one of few where the DLS method was used to characterize the commercial powders. Most of the literature studies use particle size information that either obtained from the vendor or performs BET, SEM imaging of the commercial powders. As described in chapter 2 the use of the DLS results in an accurate characterization of the commercial ceramic oxide powders than the conventional methods. Hence the current study uses powders that are accurately characterized as compared to past research.

Lastly, to the extent of our knowledge, the current study was one of the very few studies that qualitatively compare the grain growth behavior amongst 8Y- ZrO<sub>2</sub>, Al<sub>2</sub>O<sub>3</sub>, and MgAl<sub>2</sub>O<sub>4</sub> ceramic oxides. This comparison was expected to advance the knowledge regarding the sintering behavior of these commonly researched ceramic oxides.

**Table 3.9 Summary of literature studies performed on grain growth of binary/ternary phase ceramic oxides. Information is provided regarding powder sizes with mixture proportions, respective grain sizes, significant sintering parameters to achieve respective grain sizes and key observations for comparisons with the present study.**

Author/year and material	Particle / Crystallite Size	Grain Size Range	Sintering Parameters	Key Conclusions
Kwon (2001) <sup>118</sup> 8Y-ZrO <sub>2</sub> /Al <sub>2</sub> O <sub>3</sub> (2-5wt%)	Al <sub>2</sub> O <sub>3</sub> : 0.3 μm (8Y-ZrO <sub>2</sub> ): N/A (DLS)	8Y-ZrO <sub>2</sub> : 1.67-4μm Al <sub>2</sub> O <sub>3</sub> : 0.3 μm	Temperature: 1400°C Heating rate: 10°C/min	Thermal analysis, sintering behavior, and microstructure of mechanically alloyed compacts
Tekeli (2005) <sup>119</sup> 8Y-ZrO <sub>2</sub> /Al <sub>2</sub> O <sub>3</sub> (0-10wt%)	8Y-ZrO <sub>2</sub> : 0.3 μm Al <sub>2</sub> O <sub>3</sub> : 0.4 μm (Vendor)	Average size 1.5-7 μm	Temperature: 1400-1600°C Heating rate: 200°C/min	Al <sub>2</sub> O <sub>3</sub> inhibits grain growth behavior and improves fracture toughness/hardness in (8Y-ZrO <sub>2</sub> )
Meng (2012) <sup>98</sup> 16 at% Y-ZrO <sub>2</sub> /Al <sub>2</sub> O <sub>3</sub> (0-10wt.%)	Al <sub>2</sub> O <sub>3</sub> : 600 nm 16at% Y-ZrO <sub>2</sub> : 40 nm (Vendor)	Al <sub>2</sub> O <sub>3</sub> : 0.6-0.8um 16 at% Y-ZrO <sub>2</sub> : 150nm	Temperature: 1200-1400°C Pressure: 100MPa	Densification and hardness of alumina matrix affected due to zirconia loading
Pulgarin (2014) <sup>120</sup> 3Y-ZrO <sub>2</sub> /Al <sub>2</sub> O <sub>3</sub> (50 vol%)-(50 vol%)	Al <sub>2</sub> O <sub>3</sub> : 0.1-0.75μm 3Y-ZrO <sub>2</sub> : 0.37-0.6μm (SediGraph)	Al <sub>2</sub> O <sub>3</sub> : 0.3-0.9 μm 3Y-ZrO <sub>2</sub> 0.5-1.0 μm	Temperature: 1150-1600°C	Effect of different particle sizes of Al-doped, Al-(3Y-ZrO <sub>2</sub> ) on sintered microstructure/hardness
Morita (2005) <sup>92</sup> 3Y-ZrO <sub>2</sub> /MgAl <sub>2</sub> O <sub>4</sub> (30 vol.%)	3Y-ZrO <sub>2</sub> : 270nm Spinel: 360nm (Vendor)	Average Size: 100-300nm	Temperature 1300°C Pressure: 70MPa	Nanocrystalline ultra-fine grained composite fabricated by SPS with improved strength by factor of 2.0-2.5



**Table 3.9 continued**

<b>Author/year and material</b>	<b>Particle / Crystallite</b>	<b>Grain Size Range</b>	<b>Sintering Parameters</b>	<b>Key Conclusions</b>
Zhou (2006) <sup>121</sup> 3Y-ZrO <sub>2</sub> /MgAl <sub>2</sub> O <sub>4</sub> (30 vol.%)	3Y-ZrO <sub>2</sub> : 40nm Spinel: 30nm (Vendor)	Average Size: ~100 nm	Temperature: 1200-1300°C Pressure: 70-100MPa	Spark plasma sintering of fully-dense and nanostructured composite exhibiting superplasticity
Yalamac (2014) <sup>96</sup> Al <sub>2</sub> O <sub>3</sub> /MgAl <sub>2</sub> O <sub>4</sub> (10-20wt.%)	Average size: 0.15-0.2µm (Vendor)	Average size: 3.3 µm	Temperature: 1500-1600°C Heating rate: 10°C/min	Effect of MgAl <sub>2</sub> O <sub>4</sub> addition on classical sintering behavior and microstructure
<i>Present Study</i> 8Y-ZrO <sub>2</sub> /MgAl <sub>2</sub> O <sub>4</sub> (50 vol%)-(50 vol%)	<i>Average</i> <i>size:</i> <i>91-204 nm</i>	<i>Average</i> <i>size:</i> <i>140 nm-1µm</i>	<i>Temperature</i> <i>1000-1300°C</i>	<i>Grain size-particle size correlation</i>
<i>Present Study</i> 8Y-ZrO <sub>2</sub> /Al <sub>2</sub> O <sub>3</sub> (50 vol%)-(50 vol%)	<i>Average</i> <i>size:</i> <i>98-219 nm</i>	<i>Average</i> <i>size:</i> <i>216 nm-723 nm</i>		
<i>Present Study</i> Al <sub>2</sub> O <sub>3</sub> /MgAl <sub>2</sub> O <sub>4</sub> (50 vol%)-(50 vol%)	<i>Average</i> <i>size:</i> <i>143-201 nm</i>	<i>Average</i> <i>size:</i> <i>183 nm-2.2 µm</i>		
Gao (1999) <sup>16</sup> SiC/3Y-ZrO <sub>2</sub> /Al <sub>2</sub> O <sub>3</sub> 5wt% -15wt%-	Average size: 13 m <sup>2</sup> /g (BET)	Average size: N/A	Temperature: 1350-1600°C Heating rate: 600°C/min	Mechanical properties and microstructure of Densified ceramics by SPS of heterogenous precipitated powders
<i>Present Study</i> 8Y-ZrO <sub>2</sub> /Al <sub>2</sub> O <sub>3</sub> / MgAl <sub>2</sub> O <sub>4</sub> (33-33-33 vol%)	<i>Average</i> <i>size:</i> <i>117-214 nm</i>	<i>Average</i> <i>size:</i> <i>130nm-1.09µm</i>	<i>Temperature</i> <i>1000-1300°C</i>	<i>Grain size-particle size correlation</i>

Literature information regarding sintering of binary/ternary phase composites of ceramic oxides has been provided in **Table 3.9** for comparative purposes with present study similar to that performed for single phase oxides. 8Y-ZrO<sub>2</sub>/Al<sub>2</sub>O<sub>3</sub> has been researched extensively, and the current specimens exhibit a similar range of grain sizes (0.14-1μm) to those obtained by Pulgarin et al. with similar individual phase composition (50-50 volume%). However, on the other hand, it was observed that primarily, for multiphase oxides, limited information is obtained specifically for 8Y-ZrO<sub>2</sub>/MgAl<sub>2</sub>O<sub>4</sub> and Al<sub>2</sub>O<sub>3</sub>/MgAl<sub>2</sub>O<sub>4</sub> composites. The different experiments performed for the given binary oxides are studied for tetragonal 3Y-ZrO<sub>2</sub> based system. Furthermore, the amounts of secondary phase added in Al<sub>2</sub>O<sub>3</sub>/MgAl<sub>2</sub>O<sub>4</sub>(<20 wt%) and 3Y-ZrO<sub>2</sub>/MgAl<sub>2</sub>O<sub>4</sub>(30vol%) is less than the present sintered (50-50 vol%) composites. Additionally, in few studies (Kwon (2001), Meng (2012)) there exists a large variation in individual particle sizes of two phases, *i.e.*, secondary phases are nanopowders. It is concluded that these nano-sized powders restrict primary grains to lower the binary grain size effectively. On the other hand, the current study particle size is kept similar ~150 nm to effectively quantify the respective changes in grain size amongst different ceramic oxides. The three-phase composite 8Y-ZrO<sub>2</sub>/MgAl<sub>2</sub>O<sub>4</sub>/Al<sub>2</sub>O<sub>3</sub> in present study is a novel sintered material with the average grain size varying between ~120nm to ~1μm. One of the few relevant studies related to ternary ceramics is by Gao *et al.*, who fabricated zirconia-alumina mullite composites using heating rate of 600°C via SPS from non-commercial chemically synthesized powders. Lastly, similar to the previous discussion on single phase ceramics, size information related of the binary/ternary powder mixtures in most of the studies in **Table 3.9** is either obtained from vendors or from characterization techniques (SEM, sedigraph, BET) which can be less reliable than that obtained by the present method.

Thus, from the literature results provided in **Table 3.8** and **Table 3.9**, It was concluded that the sintering studies performed for single/multiphase ceramic oxides had two primary objectives. Firstly, to show the effect of SPS parameters and addition of secondary phases on grain growth and mechanical/optical properties; secondly analyzing the densification and microstructure of the ceramic composites sintered by different processing techniques like two-step sintering, colloidal processing, hot isostatic pressing along with SPS.

To the best of our knowledge, there have been very few studies on this concept. Wang *et al.*<sup>116</sup> loosely mention it as “growth ratio” to prove grain growth reduction in Al<sub>2</sub>O<sub>3</sub> (with 5% 3Y-ZrO<sub>2</sub>) from 9.5 to 4.1 to highlight advantages offered by the two-step sintering process. Similarly, Maca *et al.*<sup>107</sup> used the grain size to particle size comparison to differentiate the efficiency of single step and two step sintering of alumina and tetragonal zirconia. Jin *et al.*<sup>115</sup> stress the effect of chemical treatment of commercial Al<sub>2</sub>O<sub>3</sub> powder to remove soft agglomerates, thereby reducing overall particle size and resulting in transparent, homogenous, and finer grained specimens. On the other hand, Bardakhanov *et al.*<sup>122</sup> performed studies that dealt with the preparation of dense high-strength ceramics of fine grain sizes from several commercial powders of SiO<sub>2</sub>, Al<sub>2</sub>O<sub>3</sub>, TiO<sub>2</sub>, Y<sub>2</sub>O<sub>3</sub>, SiC, and GdO<sub>3</sub>. Particle size distribution for each of the individual ceramics was determined, and effects on sintering process were observed. However, the nature of this study was found to be broader with few samples, as compared to the current study, although it does concur with the conclusion of the present study that is the size and shape of powder particles affect the resulting ceramic microstructure. A more detailed study was performed by Chaiyabutr *et al.*<sup>123</sup> who evaluated the effect of variable powder sizes of the individual as well as resin/glass infused Al<sub>2</sub>O<sub>3</sub> by slip casting. The results obtained for given composites highlighted the impact of finer particle size on mechanical properties of

biaxial strength, fracture toughness as well as processing parameters of sintering temperature, and particle packing. Tian et al. also established the effect of narrow sized distribution powders of  $\text{Al}_2\text{O}_3$  (0.05-1.24  $\mu\text{m}$ ) led to sintered specimens with reduced grain size by almost 15% at 1600°C than as-received samples

In contrast, the current study involves the more extensive use of the size ratio to describe grain growth tendencies among commercial ceramic oxide powders quantitatively. These ratio values are calculated at different sintering temperatures, and hence they give a quantitative idea regarding the grain growth kinetics of the respective single/multiphase ceramic oxide. This summary highlights the unique and novel nature of the current research which aims at a deeper understanding of the sintering behavior and grain growth phenomenon in ceramic oxides regarding fundamental particle sizes of the powders. Thus, not only do we study the effect of finer particle sizes of individual powders but also compare the tendencies of respective 8Y-ZrO<sub>2</sub>, MgAl<sub>2</sub>O<sub>4</sub> and Al<sub>2</sub>O<sub>3</sub> system during sintering. For this purpose, the present study has formulated a dimensionless ratio called “size ratio,” i.e., a quantity that can correlate the two relevant fundamental distributions involved in powder processing as shown in **Table 3.4 & 3.5**. The necessary information can be useful to study densification and grain growth quantitatively due to sintering parameters (in our case temperature) and powder parameters, i.e., particle size. Thereby, advanced empirical models can be made available in the future for optimizing the spark plasma sintering technique used for processing fine ceramic oxides.

### 3.11 Conclusion

In this chapter, the use of spark plasma sintering has enabled the production of highly dense fine-grained commercial ceramic oxides with grain sizes varying from 150 nm to 10  $\mu\text{m}$ . Grain growth studies concerning changes in sintering temperatures as well as comparisons among different ceramic oxide composites have been carried out. Through curve fitting, exponential Arrhenius based grain growth versus sintering temperatures has been obtained, and resulting activation energy of grain growth values have been calculated for single/multiphase composites.

In single-phase samples,  $\text{MgAl}_2\text{O}_4$  samples were found to grow slowly amongst the single-phase ceramics with a activation energy of 118.4 kJ/mol, while  $(\text{Al}_2\text{O}_3)_3$  at high temperature resulted in anisotropic grains at the size of 15.9  $\mu\text{m}$  with a size ratio of  $\sim 70$  and activation energy of 202.8 kJ/mol. It was also found that the individual grain growth tendency of ceramic oxides affects the resulting multiphase composites. Hence 8Y-ZrO<sub>2</sub>-Al<sub>2</sub>O<sub>3</sub> based samples with a grain size < 1  $\mu\text{m}$  exhibited more uniform and limited growth compared to other binary compositions involving  $\text{MgAl}_2\text{O}_4$  phase. These multiphase composites also result in reduced grain growth (in some cases size ratio lower by a factor of 10) as compared to individual ceramic oxides. Furthermore, powders with different initial particle sizes were sintered between 950°C and 1300°C to obtain different phase composites and compared for grain sizes. It was concluded that the powders with lower particle size achieved faster grain growth indicated by high size ratio and activation energy values, while at higher temperatures large-sized powders sintered into bigger grains or larger average grain size.

Thus, in the present study, several empirical results are analyzed that summarize the role played by particle size distribution of powders to grain size distribution of sintered composites and to obtain a correlation between them empirically. In contrast to the majority of sintering literature, which focused mainly on the effects of sintering parameters on microstructural grain sizes, the present study emphasized the notion that the particle size of powders should also be considered to be an essential element in affecting the given microstructure after sintering.

Chapters 3, in part, is currently being prepared for submission for publication of the material. Karandikar, Keyur; Graeve, Olivia A.; Mecartney, Martha L.; Ohtaki Kenta; Travis, Austin; Evokodimiko Ekaterina; Cummings, Kira. The dissertation/thesis author was the primary investigator and author of this material under the title “Correlation between powder particle size and sintered grain size distributions in ceramic oxides: A spark plasma sintering study.” The thesis author was responsible for extensive particle characterization, ball milling, sintering, and grain growth analysis of ceramic oxide single/multiphase composites.

## **CHAPTER 4: MECHANICAL PROPERTIES AND MICROSTRUCTURAL CHARACTERIZATION**

### **4.1 Motivation and Background**

The use of advanced fabrication technique of spark plasma sintering method to obtain different grain sized compacts of 8Y-ZrO<sub>2</sub>, MgAl<sub>2</sub>O<sub>4</sub>, and Al<sub>2</sub>O<sub>3</sub>-based ceramic composites were discussed in previous chapter 3. This was primarily possible with variations in sintering parameter of temperature and powder particle sizes. Grain size has been known to be an important parameter affecting the mechanical property of strength of sintered ceramic materials<sup>124-126</sup>. Hence the subsequent characterization of all the given ceramic oxides compacts fabricated in the current study regarding microstructure and mechanical strength assumed key importance.

Knowledge of the given material properties was considered to be important as since this study was a part of a project that explores the use of ceramic oxides as potential surrogates in a novel multiphase ceramic oxide fuel that has better efficiency, safety, and transport properties specifically advantageous to a nuclear application. 8Y-ZrO<sub>2</sub> being isostructural with UO<sub>2</sub> is one phase being investigated as a candidate material. Al<sub>2</sub>O<sub>3</sub> and MgAl<sub>2</sub>O<sub>4</sub> are additional ceramic oxides considered since they can provide mechanical strength, thermal conductivity, and other material properties as secondary phases. The submicron and fine grain size microstructure (<200nm grain size) is expected to improve mechanical strength and enhance the material properties of the resulting sintered compacts. Thus, the resulting strength, microstructure and grain sizes of ceramic oxides provided adequate data which was expected to play an important role in choosing appropriate single or multiphase composites for a multiphase nuclear fuel

project, which was further tested for radiation damage/thermal flash studies by our project collaborators.

The current chapter focusses on three key points. Firstly, micro-mechanical properties from microhardness (“hardness”) and fracture toughness tests of these ceramic oxides were analyzed for single/multiphase ceramic specimen. The results are then plotted as a function of grain size using a well-defined Hall-Petch relationship<sup>127</sup>. Secondly, a comprehensive discussion is presented highlighting the extensive nature of current results of mechanical properties in comparison with sintering experiments performed previously. Lastly, a characterization study to determine the modes failures of these sintered oxides was carried out via fractography studies using analysis of SEM micrographs of ceramic’s fracture surfaces. These single/multiphase ceramics characterized by different fracture modes, i.e., inter-, trans-, or mixed- granular and to provide a significant comparison between single/binary and ternary phased microstructures.

There have been numerous individual studies on mechanical properties of single phase 8Y-ZrO<sub>2</sub>, Al<sub>2</sub>O<sub>3</sub>, and MgAl<sub>2</sub>O<sub>4</sub> composites (tabulated in detail in the discussion section (**Table 4.3 and 4.4**) of varying grain size (as small as 50nm). However, their binary/ternary phase mixtures have not been fully explored in the literature. Generally due to rule of mixtures, the hardness properties of binary/ternary composites can be assumed to be function of hardness of individual ceramic oxide phases Thus, the present Hall-Petch (hardness) and toughness/grain size graphs provide novel experimental data regarding the influence of grain size on properties of individual phases. Furthermore, the study aims to observe any possible deviations in the actual results exhibited by the spark plasma sintered multiphase ceramic oxides than the predicted properties due to rule of mixtures. The overall study is expected to expand the use of



these available ceramics obtained from commercial powders to advanced engineering applications. For example, a popular drawback of 8Y-ZrO<sub>2</sub>, which is a common optical ceramic, is its weaker mechanical strength<sup>128</sup>. On the other hand, sintering 8Y-ZrO<sub>2</sub> with other transparent spinel/alumina of fine grain size can potentially result in a better composite material without affecting its transparency.

## 4.2 Experimental Setup

Commercial powders of 8Y-ZrO<sub>2</sub>, Al<sub>2</sub>O<sub>3</sub>, and MgAl<sub>2</sub>O<sub>4</sub> were sintered using spark plasma sintering to obtain single, binary, and ternary composites with varying densities and grain sizes as described in previous chapters. For the purpose of this micromechanical study, sintered specimens with bulk density measurements >95% obtained from Archimedes method were primarily considered. This was done mainly to reduce the role played by porosity on micro-mechanical property results. The sintered SPS sample pellets obtained were 19mm in diameter and 5mm in thickness with most of the sample densities (>95%) depending on sintering parameters. The resulting sample information is provided below in **Table 4.1**.

**Table 4.1** Information regarding the range of sintering temperatures used to obtain variable grain sized single/multiphase composites with density values of the samples calculated by Archimedes' method are tabulated.

Sample Details	Sintering temperatures °C/min	Range of average grain size		Bulk Density
		Smallest (nm)	Largest (nm)	
8Y-ZrO <sub>2</sub>	1000 °C – 1300 °C	219 ± 54	6440	>97%
MgAl <sub>2</sub> O <sub>4</sub>	980 °C – 1300 °C	170 ± 41	2280	>98%
Al <sub>2</sub> O <sub>3</sub>	960 °C – 1300 °C	160 ± 33	16000	>96%
8Y-ZrO <sub>2</sub> /Al <sub>2</sub> O <sub>3</sub>	1150 °C – 1300 °C	300 ± 35	1300	>98%
8Y-ZrO <sub>2</sub> /MgAl <sub>2</sub> O <sub>4</sub>	1100 °C – 1300 °C	150 ± 40	1080	>98%
Al <sub>2</sub> O <sub>3</sub> /MgAl <sub>2</sub> O <sub>4</sub>	1100 °C – 1300 °C	357 ± 53	2200	>98%
8Y-ZrO <sub>2</sub> /MgAl <sub>2</sub> O <sub>4</sub> /Al <sub>2</sub> O <sub>3</sub>	1100 °C – 1300 °C	160 ± 21	1100	>98%

For sample preparation, the samples were fractured into small pieces by the impact of the application of sudden point load. The resulting cross section of fracture surfaces was further embedded in epoxy using a fast-cure resin and hardener (TED Pella, USA). Lapping and polishing were performed using silicon carbide (SiC) lapping discs in steps from 60 - 800 grit. The polishing was performed till 0.2µm surface roughness using water-based diamond suspensions in A-4 alpha polishing cloths (TED Pella) to obtain a finer surface roughness and smooth finish of the fracture surface. Water-based suspensions were preferred rather than oil-based ones to avoid contamination due to organic impurities.

The polished samples were tested for Vickers micro-hardness and fracture toughness testing using indentation fracture method (IF).<sup>129, 130</sup> Hardness testing was performed using diamond indenter on micro-indentation tester (LM-810, LECO Corporation, MI, USA) on a microscopic level with the high precision instrument and clean surfaces (metallographic finish)<sup>131</sup>. Loads of 500-1000gf were used with a dwell time of 15 seconds to obtain coherent diamond shaped indents. Diagonal lengths of the indent (D1, D2) were measured using 50X magnification lens (see Fig. 1B&C). Minimum of 5 readings was obtained across the entire thickness of the polished ceramic oxide cross-sectional surface. The resulting average hardness values (HV number) obtained were converted to GPa (multiplying by a conversion factor of 0.0098). A similar number of readings were also obtained for fracture toughness measurements; the Anstis equation is used with higher indentation loads (1000-2000gf) to obtain coherent indents as well as longer cracks mainly around the corners of the diamond indents.<sup>129, 132, 133</sup> Additional measurement of dimensions namely length of the cracks (D3, D4) was carried out apart from diagonal indent lengths (see Fig. 1 B&C). Modulus (E) values for single phase composites were taken from literature and had been stated in the table of chapter 1 and

theoretically calculated in case of multiphase composites.<sup>134</sup> Refer to ASTM E384 for information on hardness and JIS R1607/IF, ASTM C1421 – 16 for further information on fracture toughness.<sup>130</sup>

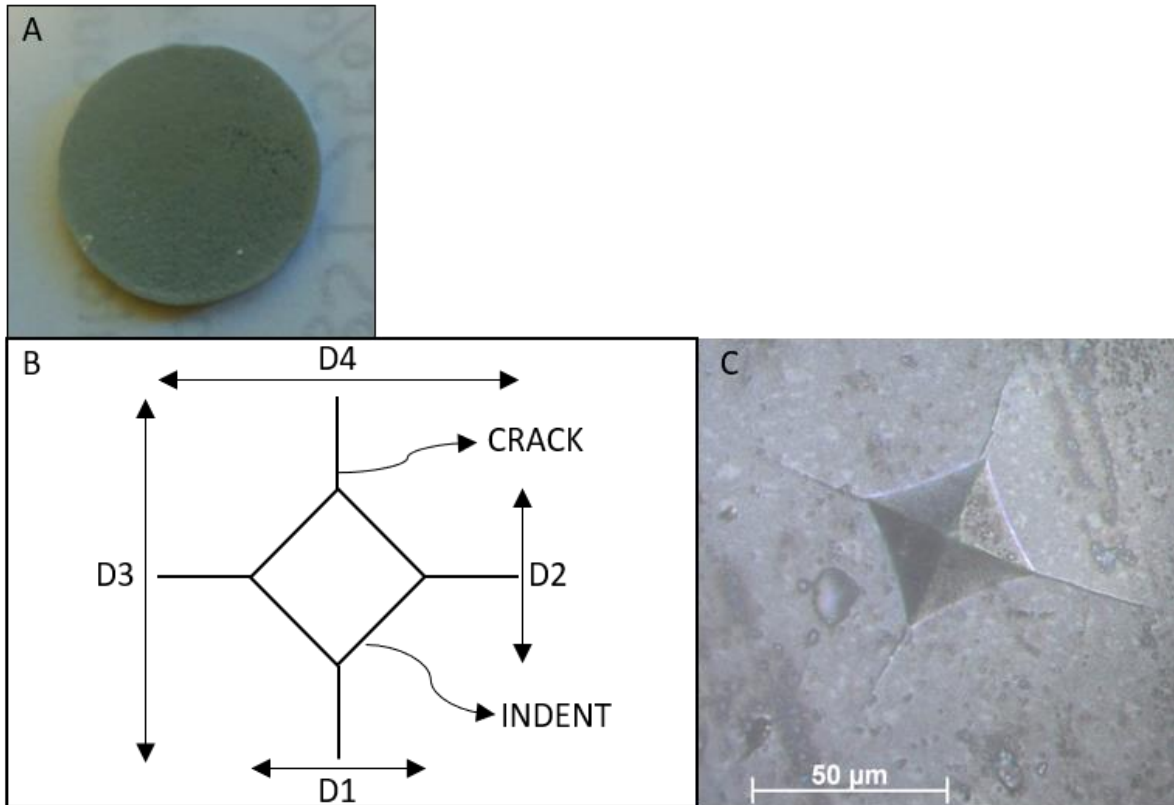


**Figure 4.1** Fig.A shows respective densified SPS pellet (19mm Ø) before fracture. Fig.1B shows sketch depicting hardness and fracture toughness measurements using Vickers indentation method. D1&D2 diagonal measurements for hardness. Fracture toughness involves the use of both indent (D1&D2) and cracks lengths (D3&D4). Fig.1C shows an optical image of indent on a three-phase composite at 50X magnification.



**Figure 4.2 Hardness tester LM 810-AT model manufactured by LECO Corporation<sup>135</sup>.**

The primary method indentation used for testing of hardness and fracture toughness is Vickers indentation hardness method. This method is defined as a nontraditional method as it does not require pre-cracked specimen as compared to that in Charpy test. Other advantages include higher sensitivity and accuracy, the smaller size of indent and so on. While the accuracy of this method for hardness studies has been well established, scientists still debate it to be inaccurate for fracture toughness measurements, but overall, most of the researchers still extensively use the IF method to obtain bulk fracture toughness readings because of its ease of use<sup>136, 137</sup>. The following equations were used by the tester in calculating hardness and fracture toughness (Antsis equation)<sup>132</sup>.

$$\text{Hardness (HV)} = \frac{F}{A} = \frac{0.01819F}{d^2}$$

$$\text{Fracture toughness } K_C = 0.016 \left( \frac{E}{H} \right)^{0.5} \left( \frac{P}{C^{1.5}} \right)$$

Where, d = diagonal indent length measured in m (function of D1&D2), E = Young's modulus (GPa), H = hardness (GPa), P or F = indentation load (N) and c = crack length or size of median cracks (function of D3 and D4)

### 4.3 Results: Hardness of single/multiphase composites

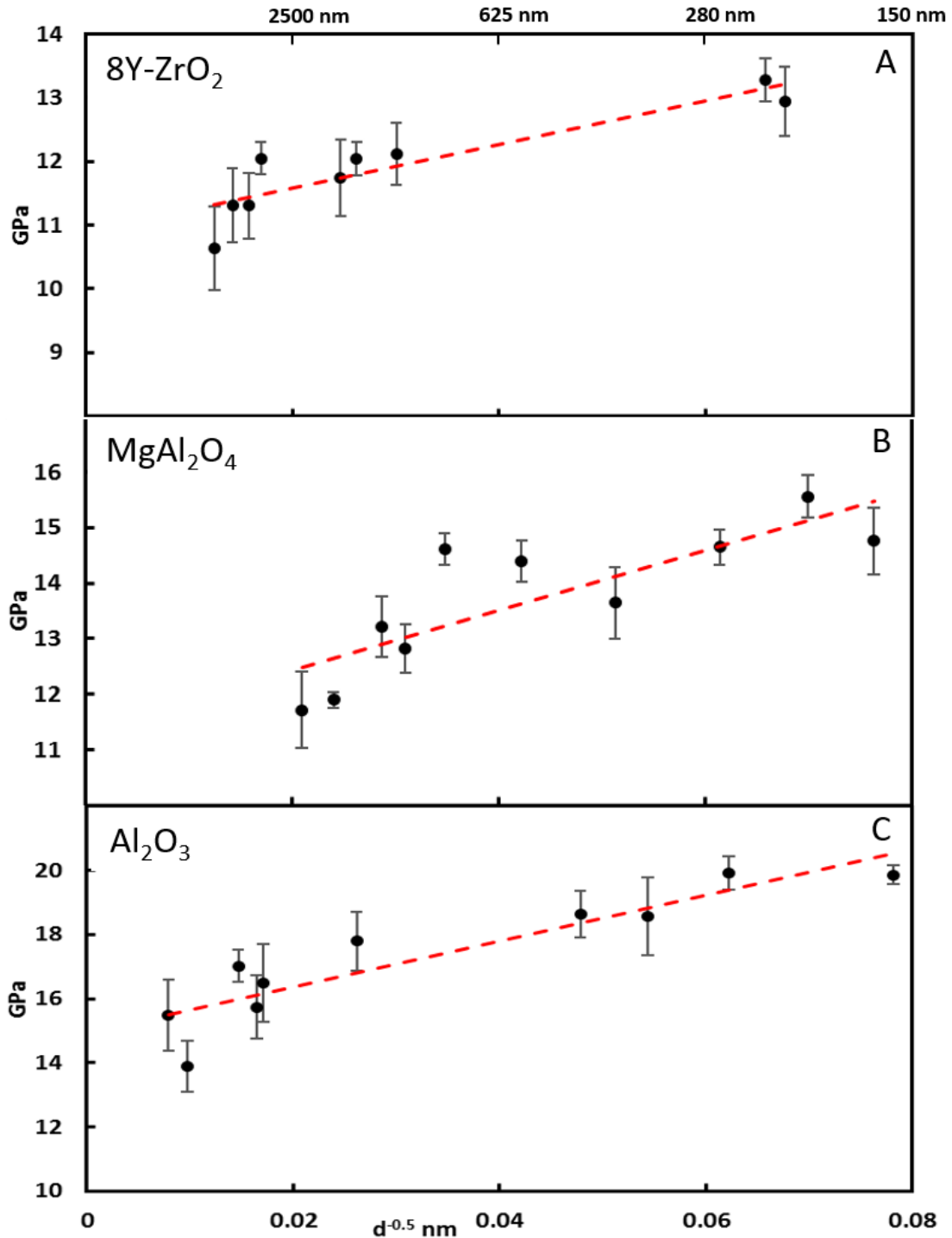
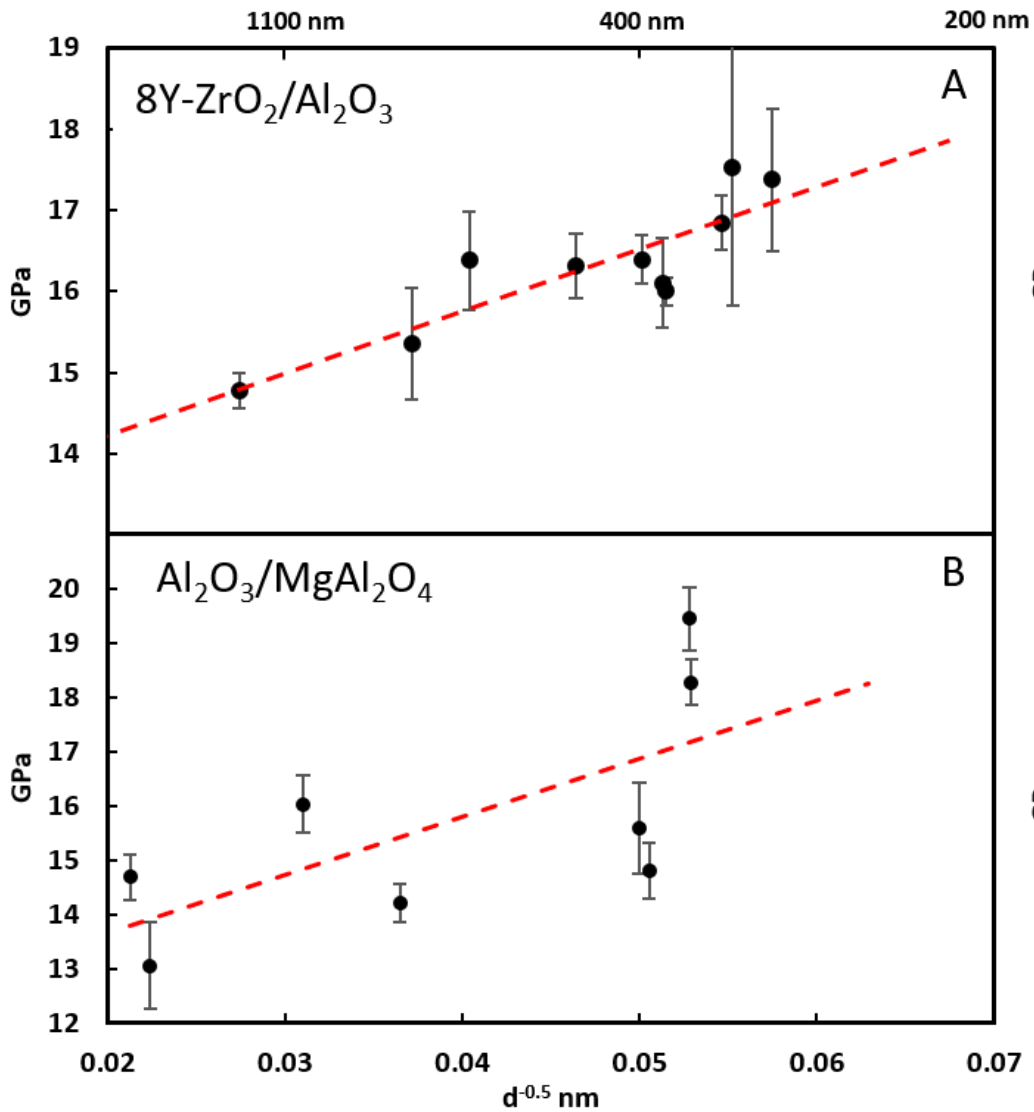


Figure 4.3 Microhardness of single-phase ceramics (3A-3C) plotted as inversely proportional to the square root of grain size to validate the Hall-Petch relationship. The linear intercept (red dashed line) indicates this relationship. The secondary horizontal axis at the top corresponds to the respective size measurements in nanometers



**Figure 4.4 A-B Microhardness of binary phase  $8Y-ZrO_2/Al_2O_3$  (A) and  $Al_2O_3/MgAl_2O_4$  (B) ceramic oxides plotted as inversely proportional to the square root of grain size to evaluate Hall-Petch relationship. The linear intercept (red dashed line) indicates this relationship. The secondary horizontal axis at the top corresponds to the respective size measurements in nanometers**

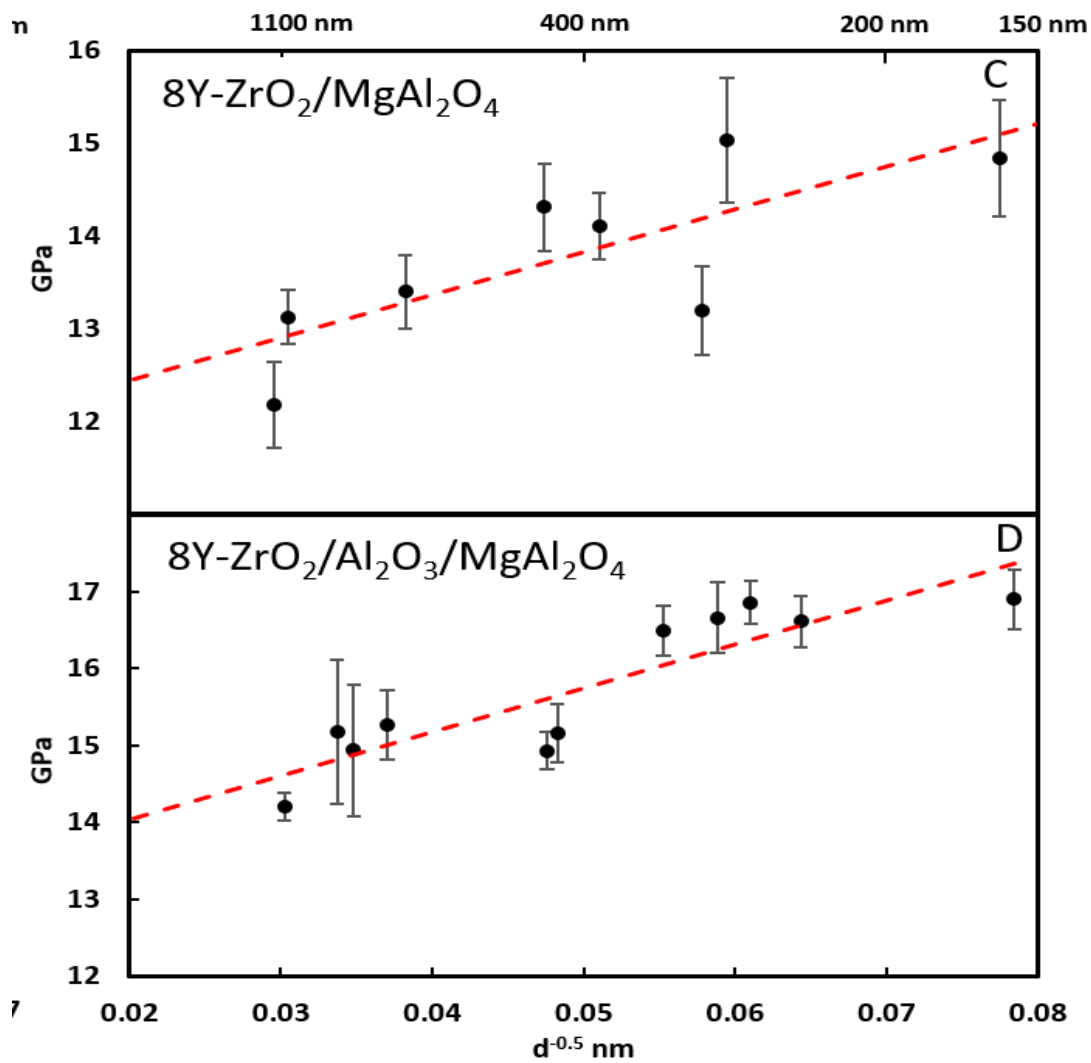


Figure 4.4 C-D Microhardness of binary phase 8Y-ZrO<sub>2</sub>/MgAl<sub>2</sub>O<sub>4</sub> (C) and 8Y-ZrO<sub>2</sub>/MgAl<sub>2</sub>O<sub>4</sub>/Al<sub>2</sub>O<sub>3</sub> (D) ceramic oxides plotted as inversely proportional to the square root of grain size to evaluate Hall-Petch relationship. The linear intercept (red dashed line) indicates this relationship. The secondary horizontal axis at the top corresponds to the respective size measurements in nanometers.

The hardness results are plotted samples for 8Y-ZrO<sub>2</sub>, MgAl<sub>2</sub>O<sub>4</sub>, and Al<sub>2</sub>O<sub>3</sub>-based composites of variable grain sizes. **Figure 4.3** shows plots results in related corresponding to individual oxides of the given ceramics while **Figure 4.4(A-D)** portrays respective binary and ternary phase composites. The hardness vs. grain size data is plotted in a way that is based on Hall-Petch relationship that is commonly used to portray the effect of mechanical strengthening over grain sizes in ceramics and metals<sup>127, 138, 139</sup> (Hall, 1954). The given power law relationship also called “grain boundary strengthening” was first developed primarily a is a linear relation of tensile strength of a given material over different grain sizes and it follows following equation

$$\sigma_y = \sigma_0 + K_H d^{-1/2}$$

where  $\sigma_a$  is applied stress in GPa, d is a grain size of polycrystals;  $\sigma_0$  and  $K_H$  are constants that depend on material properties.

Over the period, various ceramic researchers have also used the Hall-petch relation originally developed for yielding/cleavage has been extended to study the effect of grain sizes on stress-strain behavior (to study strain hardening, strain rate sensitivity) in materials and other mechanical properties.<sup>140</sup> Extension of the Hall-Petch relationship to micro-hardness has been investigated by many researchers in different metals like Al, Cu,<sup>141, 142</sup> Titanium<sup>143</sup> apart from ceramic materials<sup>144</sup>(check **Table 4.4 & 4.3** for further reference information). Thus, in the current study, we have investigated if the current ceramic oxide materials as single and multiphase composites observe the linear hall-petch relation (Hardness  $\propto$  1/ $\sqrt{\text{grain size}}$ ). Furthermore, this allowed us to compare the impact of grain sizes on mechanical properties amongst single-phase ceramics, multiphase ceramics and lastly between single and multiphase composites of 8Y-ZrO<sub>2</sub>/MgAl<sub>2</sub>O<sub>4</sub> and Al<sub>2</sub>O<sub>3</sub> ceramic oxide system. Lastly, for the current study,



coefficient ( $R^2$ ) values were also obtained by regression analysis are used which indicates scatter of data in the given plots that served helpful in the given comparative study

Results summarized in **Figure 4.3** indicate that single-phase ceramic oxides in current study showed the linear hardness-grain size where the finer submicron size samples are exhibiting higher hardness as compared to those consisting of larger grain microstructure. Additionally, this can also be seen from the high correlation ( $R^2 > 0.8$ ) or less scatter of data around the linear fit (indicated by the red dashed line) for each of the sample. Comparison of parameters among single-phase ceramics indicated that for finer grain size, the hardness of fine sized  $\text{Al}_2\text{O}_3$  (**Figure 4.3C**) increased strongly by as much 40% to reach ~20GPa for grain sizes of 150 nm as compared to grain sizes  $>2.5\mu\text{m}$ . This is also indicated by the higher value of slope or  $K_H$ . Similarly, polycrystalline spinel (**Figure 4.3B**) ceramic was found to be harder in nature with the net difference being ~4GPa between the largest and the smallest grain sized ( $<200$  nm) specimen. On the other hand, cubic 8Y-ZrO<sub>2</sub> (**Figure 4.3A**) has the least value of  $K_H$  of Hall-Petch relationship with the hardness values ranging between 11-13 GPa for all the sintered compacts.

Hardness studies were also performed for binary composites, as shown in **Figure 4.4**, for the overall range of sample grain sizes (from 200 nm to  $< 2\mu\text{m}$ ) and  $>95\%$  theoretical density. In general, comparing the  $R^2$  values in **Table 4.2**, multiphase composites ( $R^2 \sim 0.6$  to 0.73) show a non-linear change in hardness versus average grain size as compared their single phase ceramic oxides ( $R^2 > 0.8$ ). This indicates that the effect of sintered microstructure on respective mechanical properties in ceramic composites with additional phases is more complicated as the rule of mixtures for composites applies to along with the traditional Hall-Petch behavior. Additionally, among the binary composites, 8Y-ZrO<sub>2</sub>/Al<sub>2</sub>O<sub>3</sub> (**Figure 4.4A**),

and  $\text{Al}_2\text{O}_3/\text{MgAl}_2\text{O}_4$  (**Figure 4.4B**) showed a larger response of an increase in hardness between larger  $>1\mu\text{m}$  and finer ( $\sim 200\text{nm}$ ) grain size of about 3.5GPa and 5GPa as compared to  $8\text{Y-ZrO}_2/\text{MgAl}_2\text{O}_4$ . Additionally,  $\text{Al}_2\text{O}_3/\text{MgAl}_2\text{O}_4$  has the highest variation in hardness between large-grained ( $> 1\mu\text{m}$ ) and fine-grained ( $\sim 200\text{nm}$ ) composites, with a net change of about 5 GPa with  $K_H$  of 108.2. The novel three-phase ceramic oxide  $8\text{Y-ZrO}_2/\text{MgAl}_2\text{O}_4/\text{Al}_2\text{O}_3$  sintered in this study exhibits hardness results in the range of 14-17 GPa (**Figure 4.4D**).

**Table 4.2 Equation parameters of the linear fit obtained for the hardness vs. grain size results for individual ceramic oxide specimens as plotted in figure 2-3.**

Ceramic Oxide	Slope ( $K_H$ )	$H_0$ (Material parameter)	$R^2$ of linear fit
$8\text{Y-ZrO}_2$	34.508	10.88	0.81
$\text{MgAl}_2\text{O}_4$	58.62	10.94	0.82
$\text{Al}_2\text{O}_3$	71.57	14.95	0.82
$8\text{Y-ZrO}_2/\text{Al}_2\text{O}_3$	69.468	12.96	0.76
$8\text{Y-ZrO}_2/\text{MgAl}_2\text{O}_4$	42.68	11.58	0.60
$\text{Al}_2\text{O}_3/\text{MgAl}_2\text{O}_4$	101.82	11.67	0.49
$8\text{Y-ZrO}_2/\text{MgAl}_2\text{O}_4/\text{Al}_2\text{O}_3$	52.5	13.95	0.73

#### 4.4 Results: Fracture toughness of single/multiphase composites

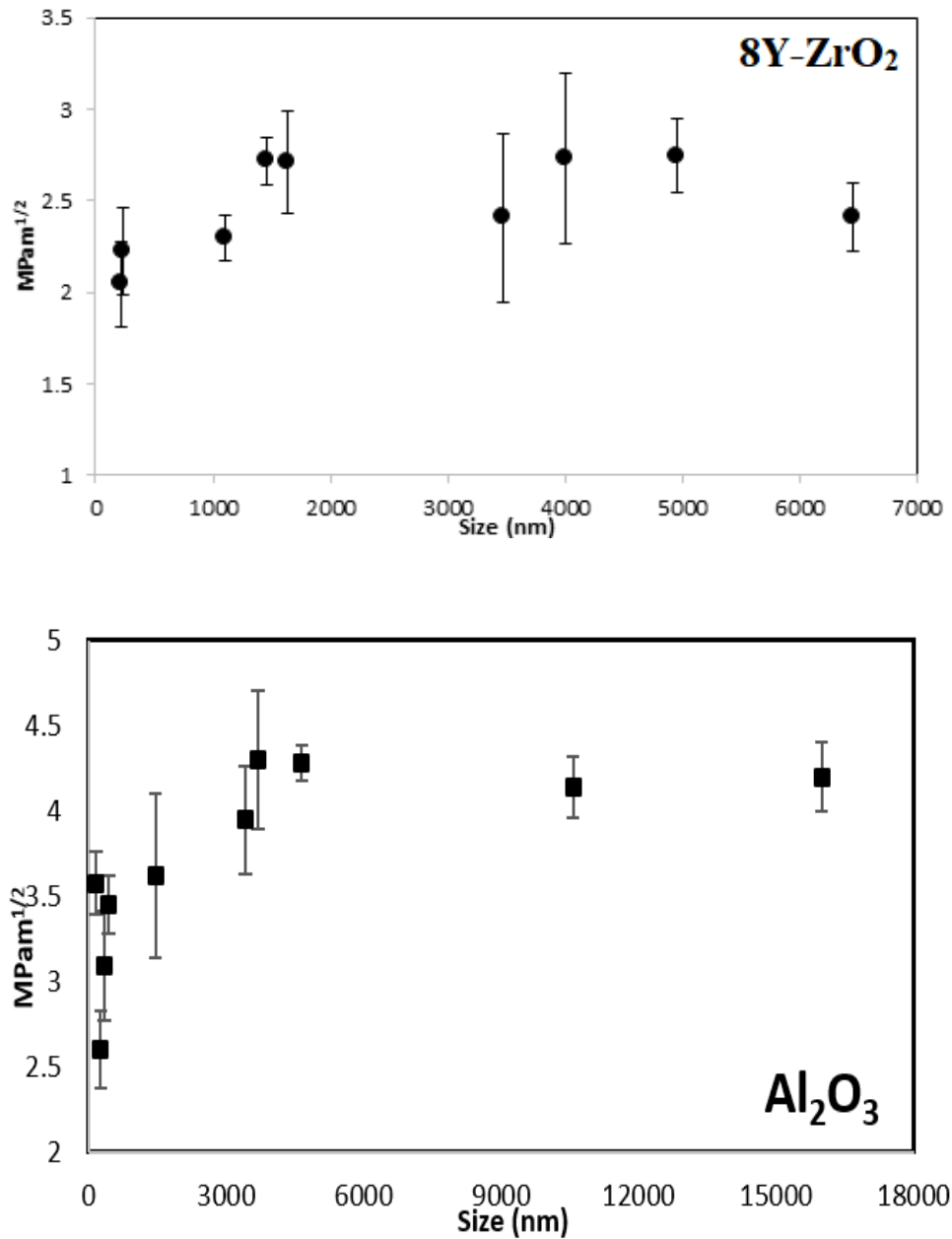


Figure 4.5 Fracture toughness of single phase 8Y-ZrO<sub>2</sub>, Al<sub>2</sub>O<sub>3</sub> and MgAl<sub>2</sub>O<sub>4</sub> ceramic oxides plotted against various grain sizes of the given composites.

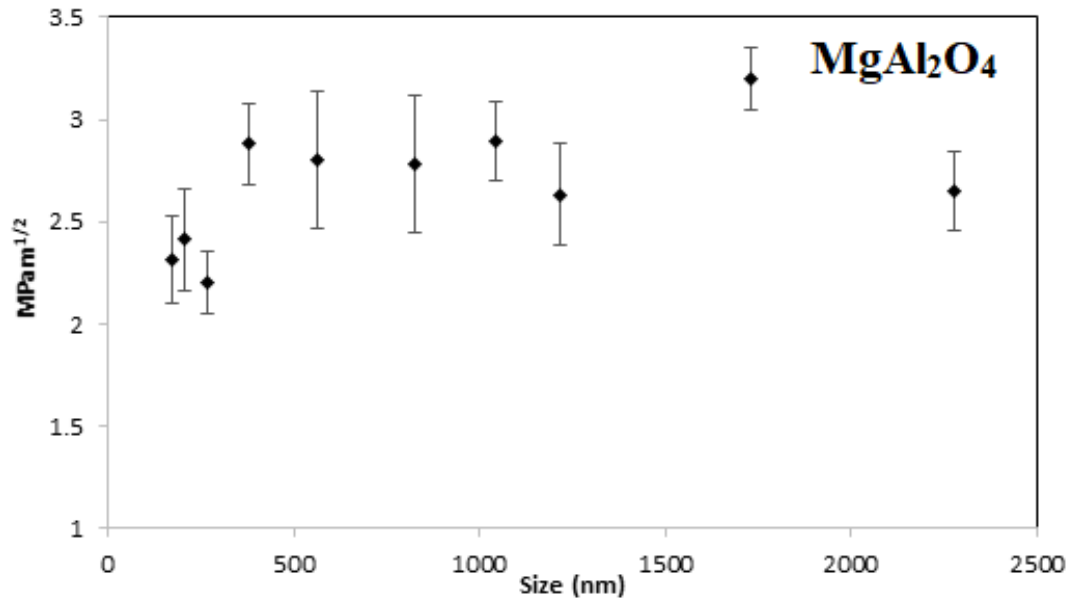


Figure 4.5 Continued.

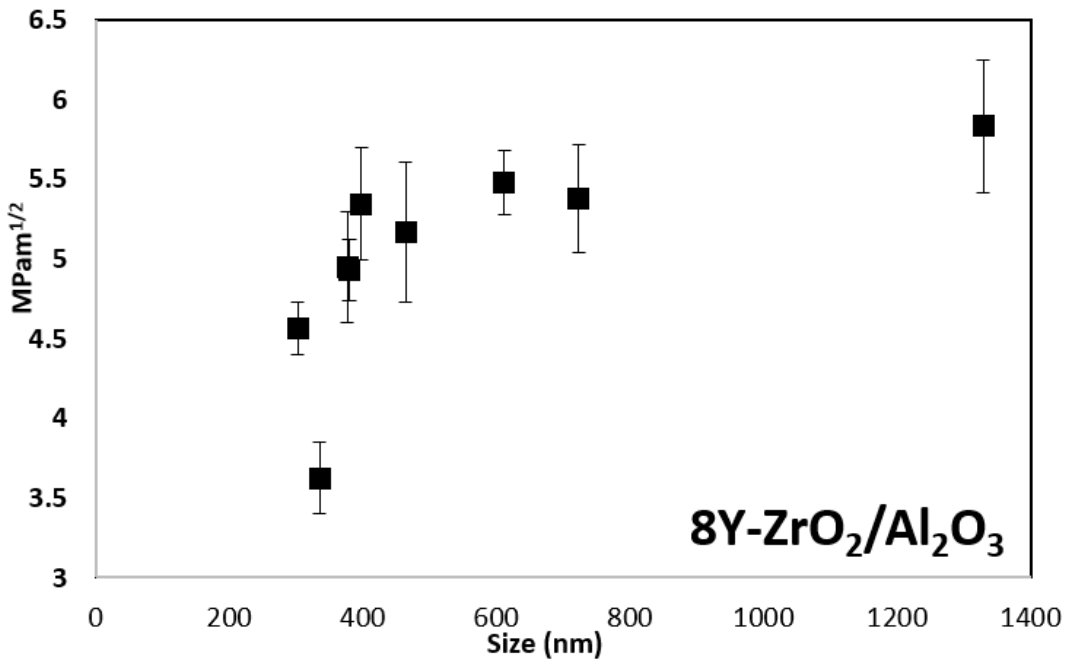


Figure 4.6 Fracture toughness results for the different types of binary and ternary composites of 8Y-ZrO<sub>2</sub>, Al<sub>2</sub>O<sub>3</sub>, and MgAl<sub>2</sub>O<sub>4</sub> ceramic oxides have been plotted against various grain sizes of the given composites.

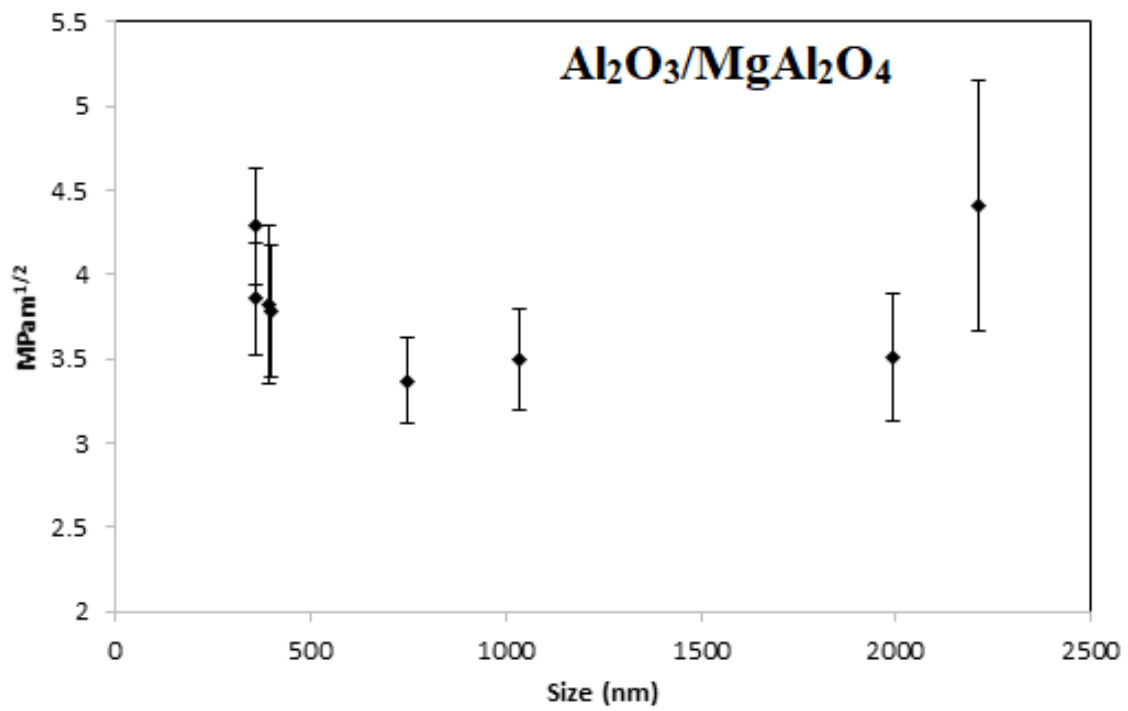
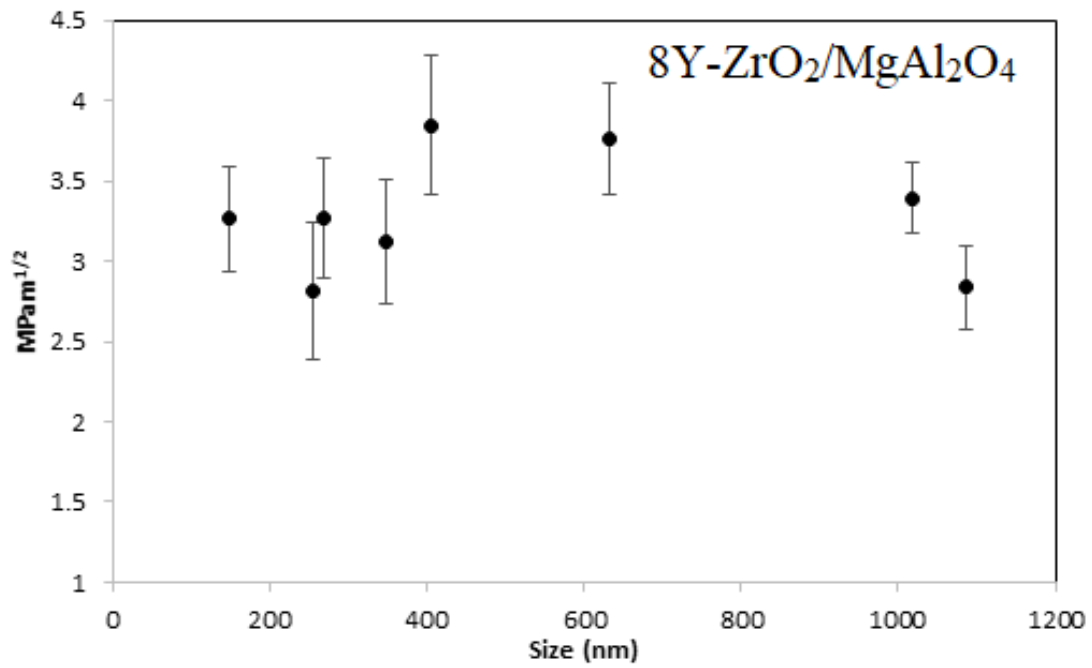
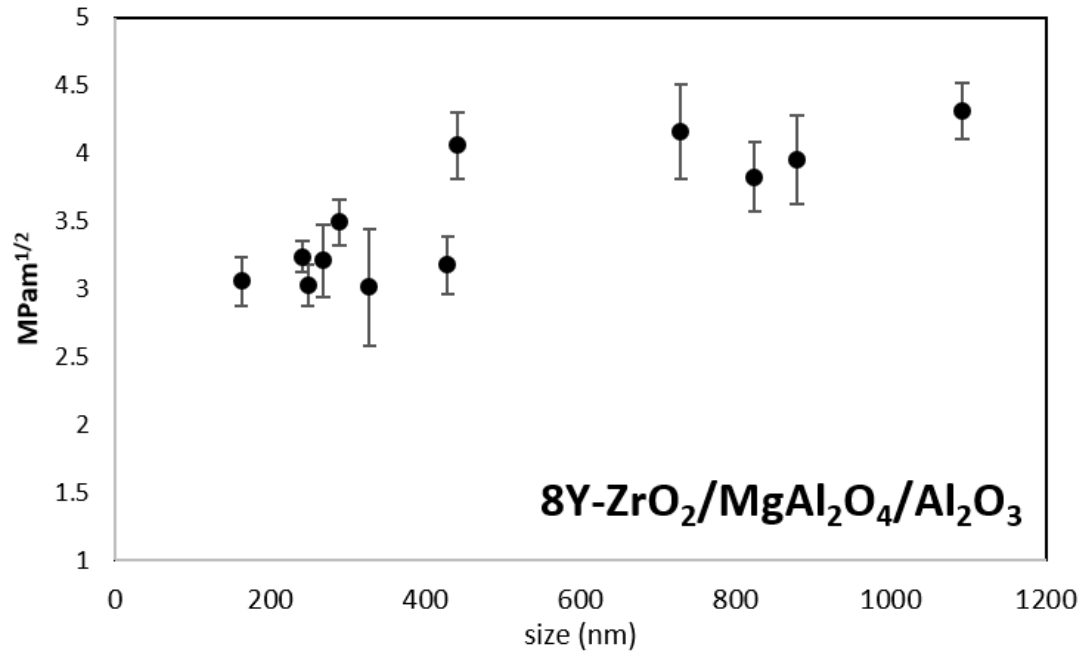


Figure 4.6 Continued.



**Figure 4.7** Fracture toughness results for the ternary composites of 8Y-ZrO<sub>2</sub>, Al<sub>2</sub>O<sub>3</sub>, and MgAl<sub>2</sub>O<sub>4</sub> ceramic oxides have been plotted against various grain sizes of the given composites.

The fracture toughness values exhibited by single-phase Al<sub>2</sub>O<sub>3</sub>, binary 8Y-ZrO<sub>2</sub>/Al<sub>2</sub>O<sub>3</sub>, and three-phase 8Y-ZrO<sub>2</sub>/MgAl<sub>2</sub>O<sub>4</sub>/Al<sub>2</sub>O<sub>3</sub> with varying grain sizes are exhibited in **4.6** and **4.7**. In general, for these ceramic oxides, a sharp change in toughness values was exhibited by composites characterized by fine average grain size. However, the variations in toughness results were insignificant larger grained microstructures. The fracture toughness of 4.3 MPa·m<sup>1/2</sup> measured for the 4 μm-grained Al<sub>2</sub>O<sub>3</sub> sample is almost 70% higher than the 2.5 MPa·m<sup>1/2</sup> fracture toughness exhibited by the 150nm average grain size sample. The binary phase 8Y-ZrO<sub>2</sub>/Al<sub>2</sub>O<sub>3</sub> (**4.7**), exhibited the highest fracture toughness value amongst all the present ceramic oxides at ~6 MPa·m<sup>1/2</sup> for an average grain size of 1.3 μm. The novel ternary phase 8Y-ZrO<sub>2</sub>/Al<sub>2</sub>O<sub>3</sub>/MgAl<sub>2</sub>O<sub>4</sub> composit (**4.7**) exhibited a fracture toughness ranging between 3 and 4.3 MPa·m<sup>1/2</sup> for different grain sized sintered compacts.

The toughness values for single phase 8Y-ZrO<sub>2</sub> and MgAl<sub>2</sub>O<sub>4</sub> were found to be in the range of 2-3 MPa·m<sup>1/2</sup>, but results also had significant standard deviations as high as ±0.5

MPa.m<sup>1/2</sup>. Similarly, the specimens of 8Y-ZrO<sub>2</sub>/MgAl<sub>2</sub>O<sub>4</sub> and Al<sub>2</sub>O<sub>3</sub>/MgAl<sub>2</sub>O<sub>4</sub> were found to exhibit toughness results mostly in the range of 3-4 MPa.m<sup>1/2</sup>. Overall, no correlation was observed between the toughness and grain size for these four ceramic oxides, and hence no further significant conclusions were obtained.

#### 4.5 Results: Fracture surface characterization of single/multiphase oxides

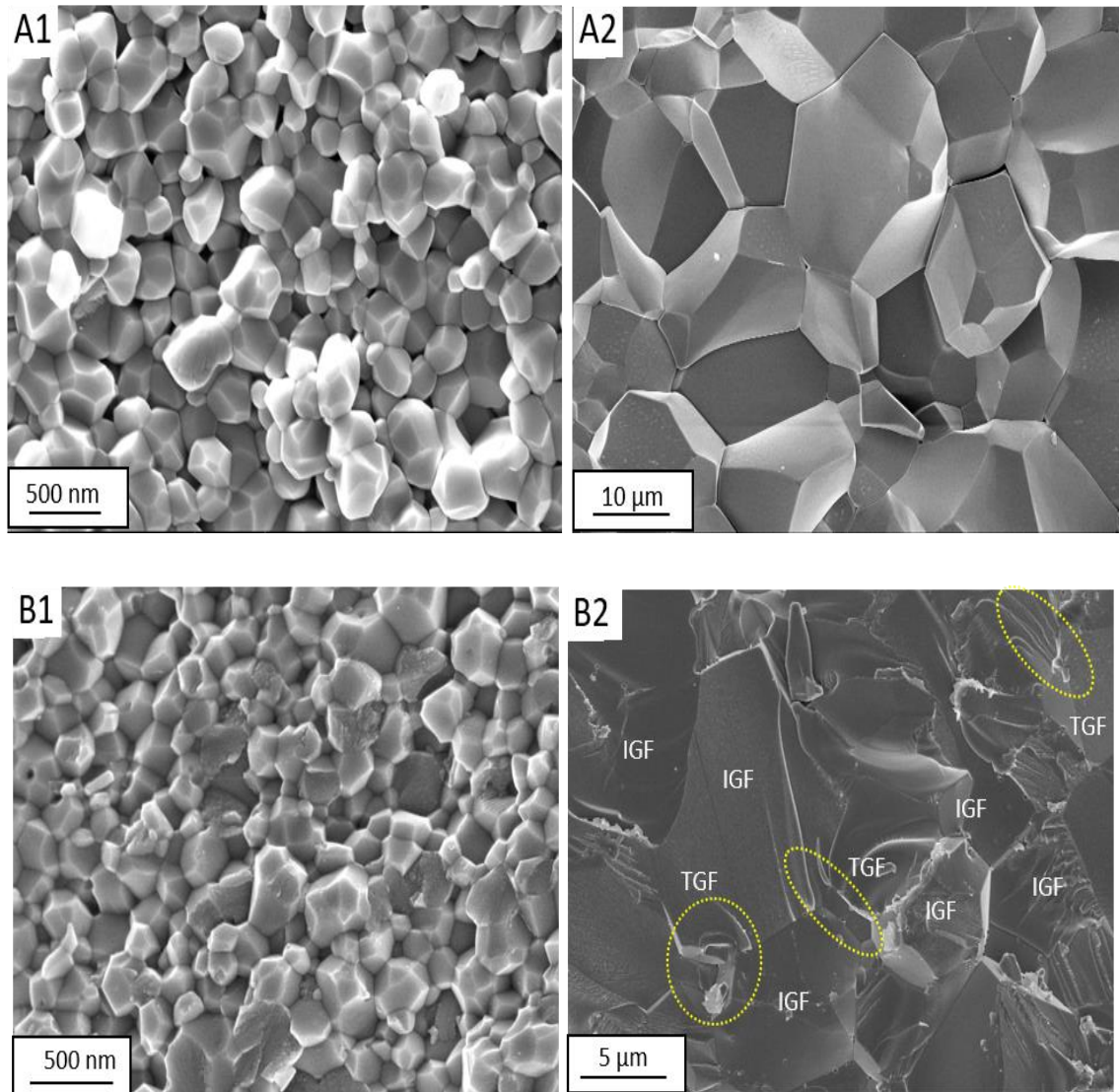


**Figure 4.8** SEM micrographs of fracture surfaces of single phase ceramics of Al<sub>2</sub>O<sub>3</sub> (A), 8Y-ZrO<sub>2</sub> (B) and MgAl<sub>2</sub>O<sub>4</sub> (C). Two different modes of fracture Intergranular (IGF) and Transgranular (TGF) are highlighted in the microstructures at different areas. Areas undergoing TGF are highlighted by circles. Fig. A1, B1, C1 are ceramic microstructures sintered at lower temperature (<1000 °C) while fig. A2, B2, and C2 are surfaces of composites sintered at higher temperatures (>1200 °C).

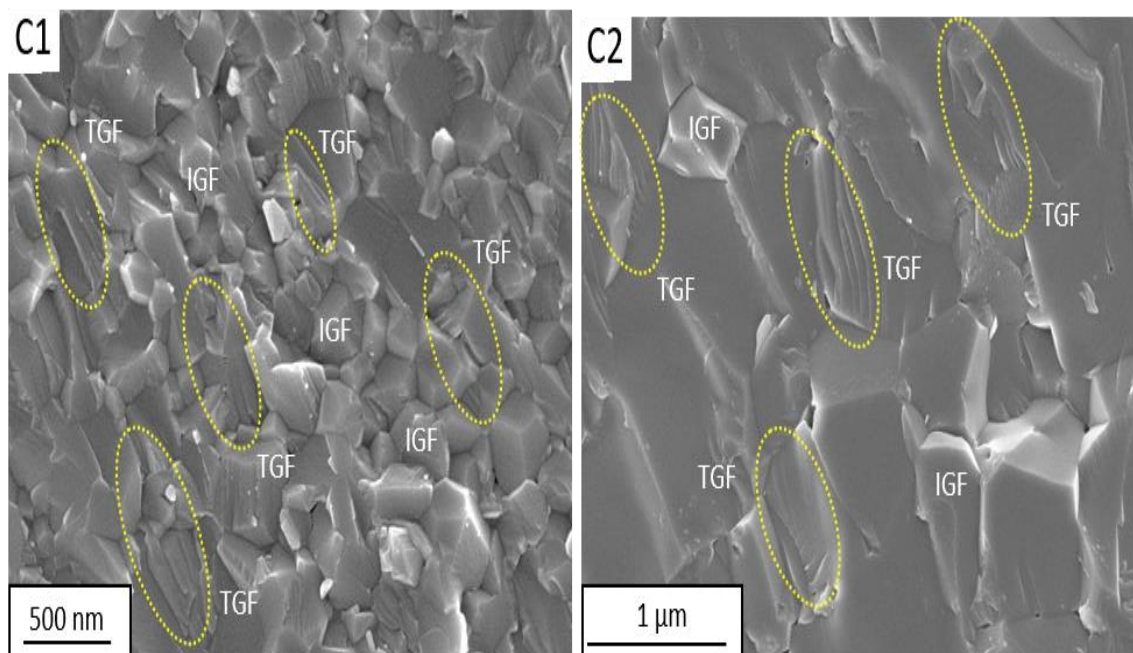


**Figure 4.8 Continued.**

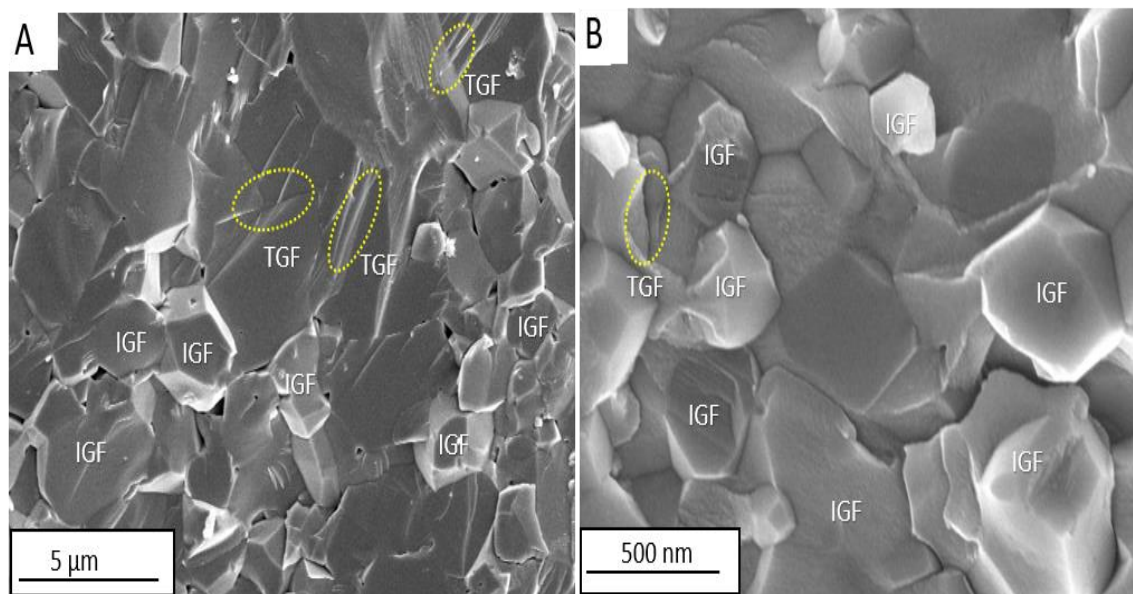


**Figure 4.9 SEM micrographs of fracture surfaces in binary phase ceramics of  $\text{Al}_2\text{O}_3/\text{MgAl}_2\text{O}_4$  (A),  $8\text{Y-ZrO}_2/\text{Al}_2\text{O}_3$  (B),  $8\text{Y-ZrO}_2/\text{MgAl}_2\text{O}_4$  (C) and ternary phase composite (D). Intergranular (IGF) and Transgranular (TGF) modes are highlighted in the microstructures at different areas by circles. All the samples sintered at sintering temperatures  $>1150^\circ\text{C}$ .**



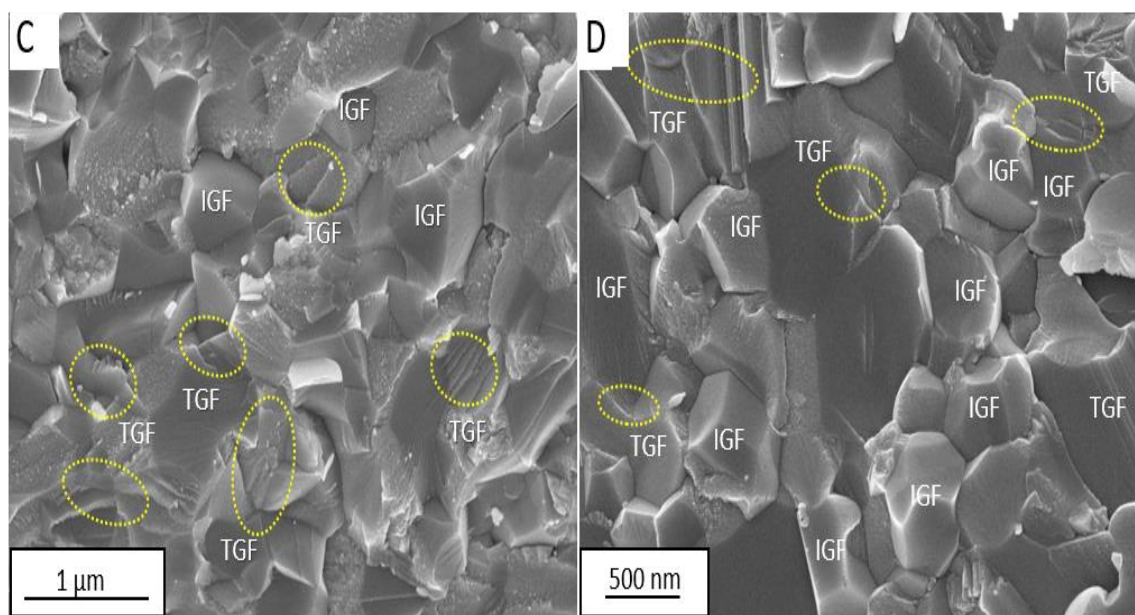


**Figure 4.9 Continued**

The cross-sectional fracture surface was imaged using scanning electron microscopy imaging. Different modes of fracture, i.e., intergranular(IGF), transgranular (TGF) and mixed mode are identified in these ceramic oxide microstructures in these figures at various places highlighted by circular are. The SEM micrographs **Figure 4.8** portray differences in microstructures of fracture surfaces for single phase oxides of 8Y-ZrO<sub>2</sub>, MgAl<sub>2</sub>O<sub>4</sub>, and Al<sub>2</sub>O<sub>3</sub>. The micrographs **A1**, **B1**, and **C1** in **Figure 4.8** show fracture surfaces of single phase composites having fine grain sizes (< 300nm), i.e., sintered at lower temperatures around 1000°C. Correspondingly, **A2**, **B2**, and **C2** images show the respective microstructures at the higher sintering temperatures (< 1200°C), thereby containing larger micron-sized grains. It was observed that complete intergranular cleavage is found in both smaller and larger grain sized samples of Al<sub>2</sub>O<sub>3</sub> (**Figure 4.8 A1-2**). In the case of 8Y-ZrO<sub>2</sub>, IGF is still a primary mode of fracture at different grain sizes, but few grains did exhibit TGF especially in higher grain sized samples (**Figure 4.8 B2**). On the other hand, crack propagation on fracture in MgAl<sub>2</sub>O<sub>4</sub> (**Figure**

**4.8C)** grains preceded primarily via transgranular mode irrespective of sintering temperature and this effect was more clearly observed in micron-sized grains as seen in **Figure 4.8C**.

**Figure 4.9** depicts micrographs of fracture surfaces of binary ceramic composites and the respective ternary composites that were obtained by sintering of powders mixed in equal proportions by volume as explained previously. The failure mode of these novel composites was more complicated as compared to their phase ceramic oxides. Mixed mode of fracture (IGF + TGF) was exhibited in ternary phase 8Y-ZrO<sub>2</sub>/MgAl<sub>2</sub>O<sub>4</sub> /Al<sub>2</sub>O<sub>3</sub> (**Figure 4.9D**) and spinel-based binary (**Figure 4.9 A&C**) composites. However, the microstructure of 8Y-ZrO<sub>2</sub>/Al<sub>2</sub>O<sub>3</sub> (**Figure 4.9B**) showed numerous areas of intergranular failure with well-defined grain boundaries.

#### **4.6 Discussion of hardness results in Single phase ceramic oxides**

The results shown in **Figure 4.3**, **Figure 4.4**, and **Figure 4**. indicate that hall-petch relationship (indicated by red regression line) was observed more prominently in single/three phase ceramic oxides ( $R^2 > 0.8$ ). The relationship is generally used to exhibit the change in hardness with a reduction in grain size. For example, the hardness values of alumina sample changed from 14 GPa to ~20GPa for a respective reduction in average grain size from 2.5 $\mu$ m to <150nm with minimal difference in theoretical density of the sample. A clear justification of this Hall-Petch explanation for the present results is proposed using previously published data by Tekeli *et al.*<sup>119</sup> During the measurement of hardness by the indentation process, the surface of sintered ceramic undergoes deformation due to Vickers indent resulting in a diamond-shaped impression (from the Vickers indenter) is generated along with on the ceramic microstructure. The size of this indent which is measure of deformation varies in microstructures having variable average grain sizes. This is because the deformation impression

and resulting dislocations due to it interact with the grain boundaries between different grains in the microstructure. A large number of these grains are individually oriented in different directions than the adjacent grain, and thereby the resulting surface energy associated with the grain boundary is different throughout the microstructure giving rise of high/low angle grain boundaries (of different energy). With the reduction in grain size, i.e., from  $>2\mu\text{m}$  to  $<200\text{nm}$ , the number of resulting individually oriented grains increase and as a result more grain boundaries are obtained. This results in higher crack-grain boundary interactions, and therefore, the resulting crack profile propagates in complex paths instead of going simply straight across the grains. As a result, higher fracture energy is needed for this complex crack propagation; Thus, a finer microstructure results in higher fracture energy thereby, improved strength or hardness values. For further clarity of the explanation, **Figure 4.10** is provided a pictorial representation of the phenomena described for given ceramics.

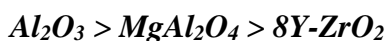
As described in the previous paragraph, the number of grain boundaries affect the resulting hardness property of present ceramic oxides as observed for single-phase ceramics. However, in case of multiphase composites (**Figure 4.4 and 4.5**) the respective Hall-Petch dependence of hardness grain size results was found in  $8\text{Y-ZrO}_2/\text{Al}_2\text{O}_3$  and  $8\text{Y-ZrO}_2/\text{MgAl}_2\text{O}_4/\text{Al}_2\text{O}_3$  binary composite as indicated by correlation factors  $R^2 > 0.7$  (although not as strong as single phase oxides). The other two compositions namely  $8\text{Y-ZrO}_2/\text{MgAl}_2\text{O}_4$  and  $\text{Al}_2\text{O}_3/\text{MgAl}_2\text{O}_4$ , showed significant scatter in data over grain size with  $R^2$  as low as 0.5. Thus, it can be proposed that in case of binary composites. It is well known in literature that the hardness properties of multiphase composites are function of their single phases due to rule of mixtures. However, the nature of the grain boundary can be also possible to be different according to the type of ceramic oxides used to sinter the respective compact Thus, for example

for a finer <200nm 8Y-ZrO<sub>2</sub>/MgAl<sub>2</sub>O<sub>4</sub> microstructure, some of the grain boundaries involved which are either made up of 8Y-ZrO<sub>2</sub>/MgAl<sub>2</sub>O<sub>4</sub> or 8Y-ZrO<sub>2</sub>/8Y-ZrO<sub>2</sub> or MgAl<sub>2</sub>O<sub>4</sub>/MgAl<sub>2</sub>O<sub>4</sub> grains might have a weaker nature or lower energy thereby promoting crack propagation and eventually affecting the bulk hardness value of given binary specimen. It is important to note that grain size also varied depending on the variability of the size of the individual grains and thus on the homogeneity of microstructure as described in the discussion section of previous chapter 3. Thus the given inherent material hardness and grain boundary effects affect the H<sub>0</sub> and K<sub>H</sub> terms of Hall-Petch relationship. Thus, Hardness vs. grain size relation in binary composites is proposed to be more complicated which is the function of grain boundaries as well as inherent material hardness of the single phases. The given conclusion can also be applied for explaining the hardness-grain size relation in ternary grain sized specimens (**Figure 4.10**). The grain growth between individual phases was found to be more uniform, with finer microstructure number of grain boundaries superseding the effect due to varying individual grain boundary nature. The resulting crack deflection helped in higher hardness (17GPa for an average grain size of <150 nm as compared to 14 GPa for >1μm sized grained composite).

#### **4.7 Comparisons of mechanical properties among single phase materials**

The extensive results allow us to compare the individual response of hardness versus grain size among single phase oxides of 8Y-ZrO<sub>2</sub>, MgAl<sub>2</sub>O<sub>4</sub>, and Al<sub>2</sub>O<sub>3</sub>. The result was achieved by comparing the slopes or K<sub>H</sub> and H<sub>0</sub> values of the linear fits tabulated in **Table 2**.

The extent of the given ceramic oxides adherence to the Hall-Petch relationship is different,



Although there are very few theories to explain this concept, experiments performed by Krell et. al.<sup>145</sup> help to assume that the intrinsic properties of Al<sub>2</sub>O<sub>3</sub>, MgAl<sub>2</sub>O<sub>4</sub>, and 8Y-ZrO<sub>2</sub> are responsible for this variation in maximum hardness values exhibited by the respective ceramic.

It is known that dislocations, i.e., defects are generated from surface deformation due to indentation forces during hardness testing. Depending on the material property, the mobility of these dislocations affects the hardness property of the resulting ceramic oxide; this phenomenon is used to describe hardness grain size tendency in the previous section. In case of  $\text{Al}_2\text{O}_3$ , due to higher dislocation mobility, the resulting hardness values are high, while in case of while in the crystal lattice structure of  $\text{MgAl}_2\text{O}_4$  limits this mobility of dislocation reduction and thereby resulted in lower performance or hardness.

Similarly, the hardness response of binary phase ceramics as indicated by the slope  $K_H$  values in **Table 2** exhibited the following trend:

$$\text{Al}_2\text{O}_3/\text{MgAl}_2\text{O}_4 > 8\text{Y-ZrO}_2/\text{Al}_2\text{O}_3 > 8\text{Y-ZrO}_2/\text{MgAl}_2\text{O}_4$$

Since all the composites contain equal individual phases of ceramic oxides, the resulting trend can be quantitatively explained to be dependent on to the respective hardness values/trend of the individually sintered  $8\text{Y-ZrO}_2$ , alumina and spinel composites themselves.  $8\text{Y-ZrO}_2$ ,  $\text{Al}_2\text{O}_3$  and  $\text{MgAl}_2\text{O}_4$  composites.  $\text{Al}_2\text{O}_3$  was found to exhibit the highest hardness of all three single-phase oxides of  $\sim 19$  GPa, followed by  $\text{MgAl}_2\text{O}_4$  then  $8\text{Y-ZrO}_2$ . As such, it imparted higher hardness to its binary-phase composites of  $\text{Al}_2\text{O}_3/\text{MgAl}_2\text{O}_4$  and  $8\text{Y-ZrO}_2/\text{Al}_2\text{O}_3$  as compared to  $8\text{Y-ZrO}_2/\text{MgAl}_2\text{O}_4$  composite.

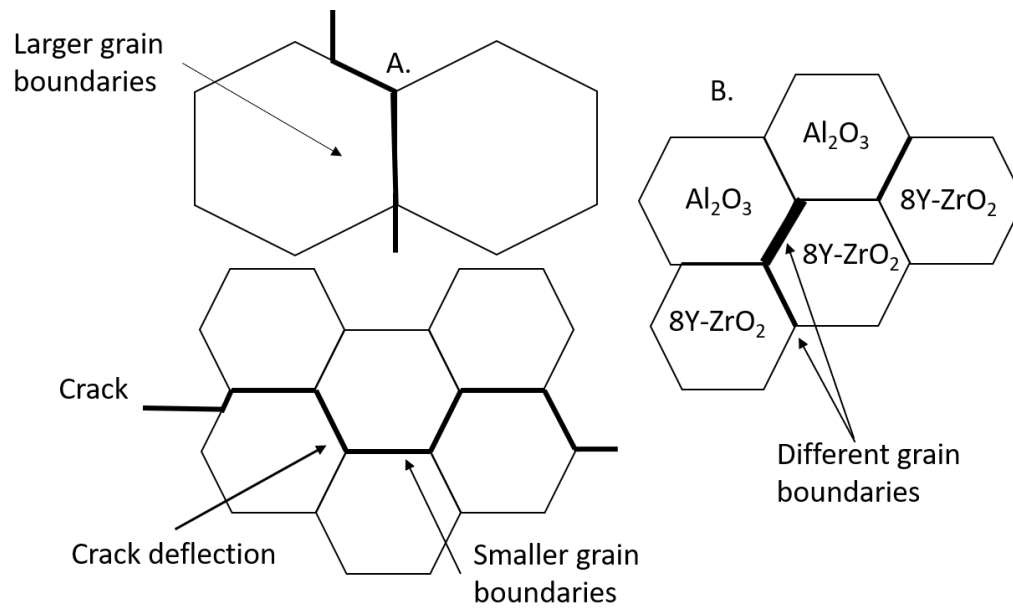


**Figure 4.10 Crack interaction and the resulting mobility due to microstructural grains. In case of single-phase ceramics (A), the crack can either propagate or deflect thereby affecting according to their interactions with grain boundaries between larger or finer grains. This affects the resulting mechanical strength or hardness of the material. In case of multiphase oxides (B) along with the grain size, the grain boundary energy or nature also varies according to the type of neighboring grains (i.e., 8Y-ZrO<sub>2</sub>/8Y-ZrO<sub>2</sub> OR 8Y-ZrO<sub>2</sub>/ Al<sub>2</sub>O<sub>3</sub>). Hence dependence of hardness only on grain size is more complicated than a hall-petch relationship. This can also result in higher strength values for multiphase composites than their respective single-phase ceramics.**

#### 4.8 Fracture toughness vs. grain size tendency

Fracture toughness values have been obtained for single-phase ceramic oxides at different grain sizes obtained by varying sintering temperatures in the figure. It is well known in the literature, that due to their brittle nature, ceramic oxides are well known for their low toughness values<sup>137, 146</sup>; the current data for most of the ceramic oxides fall well within the range of values ( $<5\text{MPam}^{1/2}$  for present oxides). Al<sub>2</sub>O<sub>3</sub> portrays the highest toughest amongst them ( $4.3\text{MPam}^{1/2}$ ) as compared to 8Y-ZrO<sub>2</sub> or MgAl<sub>2</sub>O<sub>4</sub> (maximum value =  $\sim 3\text{MPam}^{1/2}$ ). Among the binary composites, alumina-based binaries, i.e., 8Y-ZrO<sub>2</sub>/Al<sub>2</sub>O<sub>3</sub> ( $6\text{MPam}^{1/2}$ ) and Al<sub>2</sub>O<sub>3</sub>/MgAl<sub>2</sub>O<sub>4</sub> ( $4.5\text{MPam}^{1/2}$ ) show a higher value than 8Y-ZrO<sub>2</sub>/MgAl<sub>2</sub>O<sub>4</sub>. Comparing the results for the single-phase ceramic oxides, we can conclude that the tougher alumina phase imparts responsible for the overall increase in its respective binary composite. The resulting

$\text{Al}_2\text{O}_3$  phase is expected to play a part in case of ternary ceramic oxide of 8Y- $\text{ZrO}_2/\text{MgAl}_2\text{O}_4/\text{Al}_2\text{O}_3$  which show a maximum value of  $\sim 4.3\text{MPam}^{1/2}$ .

In contrast to hardness, it is hard to predict toughness trends among individual single/multiphase ceramics as the scatter and deviation of toughness values over grain size is high. These tendencies concur with the ones observed in previously published data by other researchers<sup>84, 102</sup> where bulk toughness results have a low/negligible dependence on average grain sizes for 8Y- $\text{ZrO}_2$  and  $\text{MgAl}_2\text{O}_4$  ceramic materials. However, the initial increment in some of the toughness results can be attributed to grain growth. As the grains grow larger, the overall number of grains and grain boundaries in the microstructure gets affected. The mobility of indentation crack is not affected due to the reduced crack-boundary interactions. This increases the material ability to withstand fracture by crack propagation before it ruptures, which defines its respective fracture toughness property. However, it is difficult to explain the cause of insignificant changes in the results in larger grain-sized composites. This becomes more complicated in case of binary/ternary phase oxides as along with grain size, the inherent properties of respective 8Y- $\text{ZrO}_2$ ,  $\text{MgAl}_2\text{O}_4$ , and  $\text{Al}_2\text{O}_3$  grains also can be a factor in affecting the resulting mechanical property.

It is important to note that this scatter of toughness values can be related to the inaccuracies of indentation method itself. Compared to the standard deviation values hardness results the resulting variations in fracture toughness measurements were found to be higher (indicated by longer Y-error bars in the toughness - grain size plots). One of the probable causes could be that toughness equations involved the measurement of crack lengths (as explained in procedure section) along with the hardness indent diagonals. Since these are obtained from optical measurements at 50X magnification, error values in measuring edges between diagonal

indent and crack lengths can get propagated into the final resulting toughness value. Furthermore, in case of toughness, the crack profile are measured in a straight line away from the indents, Thus any deflections or non-linear path of crack propagation could not be measured accurately, thereby adding more unreliability in the measurement. The given problem due to the optical measurements leading to inaccurate results is also pointed out by Trunec *et al.*<sup>144</sup>. Irrespective of the errors, the given fracture toughness values for single phase and multiphase composites for a range of grain sizes are still significant. This is mainly due to a large number of data points obtained in the given study as there is the lack of literature data regarding the toughness properties of currently ceramic oxides, specifically binary and ternary phase ceramic oxides. This is further reiterated in the subsequent significance section.

#### **4.9 Fractal Micrography discussion studies**

To understand the failure modes in the ceramic oxides that are used in the current research, micrographs of fracture surfaces were characterized as shown in **Figure 4.8** and **Figure 4.9**. According to previous literature related to fracture mechanics, three primary modes of brittle fracture or cleavage are common, namely, intergranular fracture (IGF), transgranular fracture (TGF) mix mode of inter- and trans-granular fracture. Intergranular fracture generally when the crack grows through weak grain boundaries surrounding sintered ceramic grains while transgranular fracture occurs across the grain itself which is weaker than the corresponding boundaries.<sup>147–150</sup>

The fracture surface results of present single-phase composites have been compared with previous literature studies to observe any contrasting results. In case of 8Y-ZrO<sub>2</sub>, IGF was found to be the primary mode of fracture, and small presence transgranular fracture surfaces, especially in larger micron, sized granular microstructure (**Figure 4.8B**). Ghosh<sup>151</sup> found



similar microstructural features for 8Y-ZrO<sub>2</sub>, i.e., intergranular fracture at lower sintering temperatures (and hence smaller grain size); while a failure at the higher sintering temperatures (>1200°C) was found to be a combination of inter- and transgranular modes which is in agreement with our SEM analysis. One of the reasons for can be assumed to be related to the change in bond energy of 8Y-ZrO<sub>2</sub> grains boundaries as the grains grow with temperature thereby affecting yield strength and mode of fracture. The transgranular nature of crack growth in MgAl<sub>2</sub>O<sub>4</sub> that is independent of grain size, has also been highlighted by other researchers.<sup>152, 153</sup> The intrinsic property of cubic structured spinel (MgAl<sub>2</sub>O<sub>4</sub>) consisting of high number of slip systems or cleavage planes is an important factor for the transgranular mode of failure. In case of alumina, researchers have found both intergranular<sup>154</sup> and transgranular<sup>155</sup> fracture modes; however current study only exhibits the first mode. In case of binary and multiphase mixtures mix mode (IGF & TGF) of fractures is observed in most of the microstructures as observed in **Figure 4.9**. However, in case of 8Y-ZrO<sub>2</sub>/Al<sub>2</sub>O<sub>3</sub> (**Figure 4.9(B)**), the microstructural grains exhibit mainly intergranular fracture with few outliers areas undergoing TGF. This can be related to the individual grains of 8Y-ZrO<sub>2</sub> and Al<sub>2</sub>O<sub>3</sub> themselves favoring to fail in an intergranular manner. Thus, it can be concluded that the presence of polycrystalline MgAl<sub>2</sub>O<sub>4</sub> results in mix mode of fracture among binary composites of 8Y-ZrO<sub>2</sub>/MgAl<sub>2</sub>O<sub>4</sub> and Al<sub>2</sub>O<sub>3</sub>/MgAl<sub>2</sub>O<sub>4</sub> and the novel three-phase composite.

The intergranular type of microstructure with consisting of microcracks from indentation can also contribute to the increase of fracture toughness; this was observed from current SPS alumina results. The complex nature of crack propagation supposedly improves the hardness and toughness values as the multiphase ceramics undergo failure. Furthermore, polycrystalline commercial powders used in the study give rise to sintered grains having

multiple crystal planes; these planes which can either reduce or promote crack growth, thereby influence strength and failure mechanisms of the corresponding materials. Thus, the type of failure mode of present ceramic oxide microstructures were assumed to play an important factor their mechanical strength. However, key features in these advanced microstructures were still needed to be completely understood, which required further comprehending and modeling of failure behavior of the current ceramic oxides.

#### 4.10 Comparative studies between single and multiphase composites

**Table 4.3 Performance matrix of multiphase composites versus single phase ceramic oxides in terms of % change (%Δ) in hardness and fracture toughness**

Multiphase composites	With respect to Single phase Al <sub>2</sub> O <sub>3</sub>		With respect to Single phase MgAl <sub>2</sub> O <sub>4</sub>		With respect to single phase 8Y-ZrO <sub>2</sub>	
	Hardness	Toughness	Hardness	Toughness	Hardness	Toughness
	%Δ	%Δ	%Δ	%Δ	%Δ	%Δ
8Y-ZrO <sub>2</sub> /Al <sub>2</sub> O <sub>3</sub>	- 13	36			31	110
Al <sub>2</sub> O <sub>3</sub> /MgAl <sub>2</sub> O <sub>4</sub>	- 2.5	2.6	25	38		
8Y-ZrO <sub>2</sub> /MgAl <sub>2</sub> O <sub>4</sub>			- 3	20	13	40
8Y-ZrO <sub>2</sub> /MgAl <sub>2</sub> O <sub>4</sub> / Al <sub>2</sub> O <sub>3</sub>	- 14	<1	8	35	30	57

The results of mechanical properties of multiphase composites are compared against the values exhibited by their phase ceramic oxide. The maximum hardness and toughness values for a particular single phase ceramic oxide are obtained from **Figure 4.3Error! Reference source not found.**, and the % change in the difference of results (%Δ) when compared to their binary/ternary phase composites are calculated and tabulated in **Table 4.3**.

Overall, the majority of results showed that the addition of secondary phase improves hardness and fracture toughness of individual ceramics, specifically of 8Y-ZrO<sub>2</sub> and MgAl<sub>2</sub>O<sub>4</sub>.

For example, the maximum hardness (13GPa) and toughness ( $2\text{-}3\text{MPam}^{1/2}$ ) values of 8Y-ZrO<sub>2</sub> are lower by almost 110% when compared to binary phase 8Y-ZrO<sub>2</sub>/ Al<sub>2</sub>O<sub>3</sub> (50%-50% volume mixture). Similar improvements in mechanical properties of Al<sub>2</sub>O<sub>3</sub>/MgAl<sub>2</sub>O<sub>4</sub> (Hardness % $\Delta$  =25, Toughness % $\Delta$ = 38) are higher than individual spinel.

On the other hand, few negative points in performance matrix **Table 4.3** are obtained, specifically when binary and ternary based alumina composites are compared with respect to single phase Al<sub>2</sub>O<sub>3</sub>. Thus, it can be concluded that addition of either or both secondary phase MgAl<sub>2</sub>O<sub>4</sub> and 8Y-ZrO<sub>2</sub> (in equal proportion) results in potentially weaker sintered specimens. However, the magnitude of this reduction in properties is significantly lower, when overall advantages of using multiphase ceramics over single phase ceramic oxides are compared (maximum negative % $\Delta$  in hardness **Table 4.3** is 13 while maximum positive change is 31%). In fact, binary composites 8Y-ZrO<sub>2</sub>/Al<sub>2</sub>O<sub>3</sub> portrayed superior toughness values  $\sim 5.8\text{MPam}^{1/2}$  which is 36% tougher as compared to a single-phase Al<sub>2</sub>O<sub>3</sub> ( $4.3\text{MPam}^{1/2}$ ) even though it showed 13% lower hardness than the respective single phase. Lastly, it can be concluded that the novel three-phase 8Y-ZrO<sub>2</sub>/MgAl<sub>2</sub>O<sub>4</sub> /Al<sub>2</sub>O<sub>3</sub> composite was found to exhibit a better combination of both fracture toughness and microhardness when compared to the majority of binary and single phase composites (except for the single-phase alumina and alumina-spinel).

This improvement in mechanical properties in multiphase composites can be attributed to several possible reasons. As discussed previously finer grain size and individual grain orientation gave rise to improved microstructures exhibiting better strength (**Figure 4.10**). Additionally, multiphase ceramics also posed complex grain boundaries due to different individual ceramic oxide grain, which interacts with resulting indentation cracks<sup>98</sup>. These grain boundaries are complex in nature due to the difference in inherent properties of the individual

grain itself. For example, mismatch of lattice parameters or thermal expansion coefficients of individual grains itself. For example, Kwon *et al.*<sup>156</sup> concluded that difference in thermal expansion coefficients of cubic 8Y-ZrO<sub>2</sub> matrix ( $10.5 \times 10^{-6} \text{K}^{-1}$ ) and Al<sub>2</sub>O<sub>3</sub> ( $8.8 \times 10^{-6} \text{K}^{-1}$ ) particles, lead to residual stresses being introduced in the composite during cooling from the sintering temperatures. In fact, in the cubic 8Y-ZrO<sub>2</sub> matrix, both tangential tensile and radial compressive stress were developed. These pre-stressed conditions are assumed to make the resulting 8Y-ZrO<sub>2</sub>/Al<sub>2</sub>O<sub>3</sub> binary composite stronger. The retention of mechanical properties with additional phases was considered important because these secondary/ternary phases were considered to be potential candidates in the fabrication of multiphase ceramic oxide for fuel application as described previously. Thus, the performance matrix described in **Table 4.3** provides valuable empirical information regarding the mechanical properties of 8Y-ZrO<sub>2</sub>, MgAl<sub>2</sub>O<sub>4</sub> and Al<sub>2</sub>O<sub>3</sub> based composites. This information can benefit in the selection of suitable candidate amongst these ceramic oxides materials for a given engineering application.

#### 4.11 Significance of the present study

**Table 4.4 Summary of relevant studies performed regarding mechanical properties of sintered single-phase ceramic oxides in past literature. Information is provided regarding hardness, and fracture toughness for respective grain sizes for making coherent comparisons with the present study.**

Author/year	Sample Composition	Range of average grain size	Range of Hardness(GPa)	Range of toughness (MPam <sup>1/2</sup> )
Tamburini <i>et al.</i> , (2011) <sup>102</sup>	8Y-ZrO <sub>2</sub>	< 100 nm to > 700 nm	14.0 - 15.3	3.1
Mazaheri <i>et al.</i> (2008) <sup>157</sup>		0.3 μm to 2.35 μm	12.8 -13.5	~ 3.2
Tekeli. S (2005) <sup>119</sup>		5 μm to 7 μm	~12.9	~ 1.5
<i>Present study</i>		200 nm – 6.4 μm	11-13	2.0 - 2.7
Morita <i>et al.</i> (2008) <sup>84</sup>	Spinel (MgAl <sub>2</sub> O <sub>4</sub> )	0.5 μm – 100 nm	14.5 – 13.0	1.5 – 2.0
Rothman <i>et al.</i> (2014) <sup>158</sup>		0.3 μm –10 μm	16 – 13	1.0 - 2.5
Wollmershauser <i>et al.</i> (2014) <sup>111</sup>		28 nm - <200nm	17 – 20	1.1-2.2
<i>Present study</i>		170nm – 2280nm	12 - 16	2.2-3.2

**Table 4.4 continued**

Author/year	Sample Composition	Range of average grain size	Range of Hardness(GPa)	Range of toughness (MPam <sup>1/2</sup> )
Pulgarin <i>et al.</i> (2014) <sup>120</sup>	Alumina (Al <sub>2</sub> O <sub>3</sub> )	0.5 μm-4.5 μm	10 - 18	N/A
Krell <i>et al.</i> (2011) <sup>145</sup>		0.2 μm-3 μm	18 - 23	N/A
Shen <i>et al.</i> (2002) <sup>89</sup>		0.8 - 28 μm	21 - 16	3.0 - 4.3
Teng <i>et al.</i> (2007) <sup>159</sup>		1.5μm- >10μm	20	4.1
<i>Present study</i>		160 nm – 16 μm	13.9 - 19.9	3.1 - 4.3

**Table 4.4** shows a summary of the relevant literature studies carried out by ceramic scientists with the primary focus on the influence of grain size on micro-mechanical properties of 8Y-ZrO<sub>2</sub>, MgAl<sub>2</sub>O<sub>4</sub> and Al<sub>2</sub>O<sub>3</sub> based composites sintered by SPS. These results are compared with the results obtained from the current study.

Overall, in the case of single phase composites, the present hardness values lay between 16-20GPa for MgAl<sub>2</sub>O<sub>4</sub> and 14~20GPa for Al<sub>2</sub>O<sub>3</sub> which was well within the values obtained by other research studies for given ceramics summarized in **Table 4.4**. Regarding MgAl<sub>2</sub>O<sub>4</sub>, it can be concluded that our hardness values for submicron to micron size grains is an extension of a similar Hall-Petch correlation, which is also plotted by Wollmershauser *et al.*<sup>111</sup> in the nano-scale regime (28-100nm). Similarly, the fracture toughness values also concur

with previous literature for respective grain sizes as seen in **Table 4.4**. However, the current 8Y-ZrO<sub>2</sub> specimens (~13GPa) were found to exhibit results at the lower range of hardness values as compared to data obtained by Tamburini<sup>102</sup> and Mazahari<sup>157</sup> but similar toughness values compared to other studies for specific grain size range (3-7% lower). The small difference could be attributed to either different types of powder, i.e., due to variation in impurities in synthesized (Mazahari) and commercially obtained powder or the hardness testing technique, i.e., variations in indent loads (0.5-1kgf in present studies, while 500gf in Tamburini and 5kgf in Mazahari).

Overall, the discussion and primary conclusions from current research related to changes in hardness and fracture toughness due to variations in grain sizes of sintered composite agreed with the literature presented in **Table 4.4**. To further illustrate this observation, a strong hardening tendency with smaller grain size was observed in Al<sub>2</sub>O<sub>3</sub> (~40% increase in hardness for finest grains) for present study which concurs with the studies performed on alumina in **Table 4.4**. For example, Pulgarin et al.<sup>20</sup> achieved an increase of 8GPa in hardness property for a submicron sized Al<sub>2</sub>O<sub>3</sub> as compared to the higher 4.5µm average grain sized microstructure. Lastly, the present conclusion regarding the limited improvements in hardness property of 8Y-ZrO<sub>2</sub> at finer grain sizes is supported by the fact that an only small difference is obtained between the hardness results (~1.5GPa) in the last column for all the experimental studies concerning the individual ceramic oxide.

Thus, the unique nature of the current research is that it is among the few studies that analyze the grain size behavior on mechanical properties with the use of Hall-Petch relationships (usually used in metals). In case of single phase materials, few researchers<sup>111, 145</sup> did emphasis on this linear relationship while explaining hardness/toughness of Al<sub>2</sub>O<sub>3</sub> and



spinel ceramic oxides, but offered less in-depth and extensive analysis regarding the present research.

**Table 4.5 Summary of literature studies performed regarding mechanical properties of sintered multiphase ceramic oxides. Information is provided regarding the sample composition, hardness, and fracture toughness for respective grain sizes for coherent comparisons with present study**

Author/year	Sample Composition	Range of average grain size	Range of Hardness (GPa)	Range of toughness MPam <sup>1/2</sup>
Kwon <i>et al.</i> (2011) <sup>156</sup>	8Y-ZrO <sub>2</sub> /Al <sub>2</sub> O <sub>3</sub> ↑ (2-5wt %)	8Y-ZrO <sub>2</sub> : 1.67-2.73μm Al <sub>2</sub> O <sub>3</sub> : 0.3μm	12.5 - 13.0	1.5 – 1.7
Meng <i>et al.</i> (2012) <sup>98</sup>	16at% Y-ZrO <sub>2</sub> /Al <sub>2</sub> O <sub>3</sub> ↑ (5-10wt%)	Al <sub>2</sub> O <sub>3</sub> : 0.6-0.8μm	18.0 - 20.0	3.5 - 4.1
Tekeli. S (2005) <sup>119</sup>	8Y-ZrO <sub>2</sub> /Al <sub>2</sub> O <sub>3</sub> ↑ (0-10wt%)	1 - 7μm	12.7 - 14.2	1.5 - 2.4
<i>Present study</i>	8Y-ZrO <sub>2</sub> /Al <sub>2</sub> O <sub>3</sub> ↑↑ (50Vol%)	300nm – 1.3μm	14.8 - 17.3	3.6 - 5.8
Yalamac <i>et al.</i> (2014) <sup>96</sup>	Al <sub>2</sub> O <sub>3</sub> /MgAl <sub>2</sub> O <sub>4</sub> (10- ↑ 20wt%)	3.3μm	17.5 - 18.5	N/A
<i>Present study</i>	Al <sub>2</sub> O <sub>3</sub> /MgAl <sub>2</sub> O <sub>4</sub> ↑↑ (50Vol%)	350nm - 2.2μm	13.0 – 19.4	3.4 - 4.8
Quenard <i>et al.</i> (2000) <sup>160, 161</sup>	3Y-ZrO <sub>2</sub> /MgAl <sub>2</sub> O <sub>4</sub> ↑ (1-30wt%)	0.2 - 0.8μm	14.4-16.3	2.3 - 6.6

**Table 4.5 continued**

Author/year	Sample Composition	Range of average grain size	Range of Hardness (GPa)	Range of toughness MPam <sup>1/2</sup>
Present study	8Y-ZrO <sub>2</sub> /MgAl <sub>2</sub> O <sub>4</sub> (50Vol%)	150nm -1.08μm	12.1 - 14.8	2.8 - 3.8
Chen <i>et al.</i> (2005) <sup>33</sup>	3Y-ZrO <sub>2</sub> /Al <sub>2</sub> O <sub>3</sub> / mullite (/30/30 wt%)	0.43μm	15.0	N/A
Khoshkalam. (2013) <sup>97</sup>	3Y-ZrO <sub>2</sub> /Al <sub>2</sub> O <sub>3</sub> / MgAl <sub>2</sub> O <sub>4</sub> (10-20/10-20)wt%	1 - 2μm	12.0-18.0	6.0-7.0
<i>Present study</i>	8Y-ZrO <sub>2</sub> /Al <sub>2</sub> O <sub>3</sub> / MgAl <sub>2</sub> O <sub>4</sub>	160 nm- 1.1μm	14.2 – 16.9	3.0-4.3

The extensive and novel nature of the current empirical study is highlighted by the fact that there is limited information on most of the binary/three phase ceramic oxide composites as shown in **Table 4.5**. The current multiphase composites had an equal proportion of secondary and ternary phases whereas literature studies for given ceramics had lower concentrations of respective phase addition. In some experiments like for 8Y-ZrO<sub>2</sub>/Al<sub>2</sub>O<sub>3</sub> performed Kwon *et al.*<sup>156</sup>, the percentage secondary phase alumina was more equivalent to the level of dopant additions(1-3wt%) than phase additions. Furthermore, the number of samples with variable grain sizes was found to be low in most of the studies performed for 8Y-ZrO<sub>2</sub>/Al<sub>2</sub>O<sub>3</sub> and Al<sub>2</sub>O<sub>3</sub>/MgAl<sub>2</sub>O<sub>4</sub> sintered oxides. Thus, it is hard to make concrete comparisons between the hardness and toughness values of present results of binary composites with literature.

Nevertheless, the range of current results reported for 8Y-ZrO<sub>2</sub>/Al<sub>2</sub>O<sub>3</sub> were on the higher side than those reported in the literature (see **Table 4.5**). Two explanations were possible for the present experimental observations in these binary composites. Firstly, the average grain sizes of the samples used in the present study vary from 300 nm to <2 μm compared to micron-sized samples in the literature; thereby according to the hall-petch relationship the hardness values are much higher in present 8Y-ZrO<sub>2</sub>/Al<sub>2</sub>O<sub>3</sub> samples, but this did not explain the improvement in fracture toughness results. Secondly, the higher concentration of alumina (50% volume) can be responsible for higher mechanical properties of toughness and hardness by rule of mixtures. This effect of phase additions on the improvement in mechanical properties is well known as demonstrated by researchers with respect to increasing concentration of Al<sub>2</sub>O<sub>3</sub> or 8Y-ZrO<sub>2</sub> as respective secondary phases<sup>96, 98, 119</sup>. Similar explanations can be offered for higher mechanical properties of the present Alumina-Spinel composites as compared to the data in the literature. Lastly, as to author's best knowledge, novel grain size – hardness relations for binary 8Y-ZrO<sub>2</sub>/MgAl<sub>2</sub>O<sub>4</sub> and ternary phase have been established. Most of the literature study in **Table 4.5** is focused on tetragonal Ytria-stabilized zirconia-based 3Y-ZrO<sub>2</sub>/MgAl<sub>2</sub>O<sub>4</sub> and 3Y-ZrO<sub>2</sub>/MgAl<sub>2</sub>O<sub>4</sub>/ Al<sub>2</sub>O<sub>3</sub> composites. It is well known that 3Y-ZrO<sub>2</sub> has better mechanical properties<sup>162-164</sup> than its cubic 8Y-ZrO<sub>2</sub> counterpart and hence this could explain the lower hardness and fracture toughness values exhibited by the current ceramic oxide specimens.

#### **4.12 Conclusion**

An extensive analysis of the influence of grain size on hardness and fracture toughness of different ceramic composites sinter from 8Y-ZrO<sub>2</sub>, MgAl<sub>2</sub>O<sub>4</sub> and Al<sub>2</sub>O<sub>3</sub> commercial powders was presented in the current chapter of the dissertation. Comparing the present results with literature indicate that apart from most of the single-phase oxides, current study adds novel

results regarding Hall-Petch correlation for most of binary and ternary phase sintered specimens. A strong correlation of Hall-Petch relationship was observed for single phase ceramic oxides and ternary composite ( $R^2 \sim 0.8$ ). On the other hand, fracture toughness values of these ceramics contained scatter of results for different grain sizes; thereby no correlation could be obtained. These studies quantitatively analyzed changes in mechanical strength due to submicron-, nano-sized over larger grain microstructures. Furthermore, amongst all studied ceramic composites, single phase alumina and its binary composites with equal proportionate of 8Y-ZrO<sub>2</sub> attained the highest hardness and toughness values of 20 GPa and 5.8 MPam<sup>1/2</sup> respectively. Also, it was observed that in general, multiphase composites have both superior hardness (up to 30%) and fracture toughness (as far as >100%) when compared to 8Y-ZrO<sub>2</sub>, and MgAl<sub>2</sub>O<sub>4</sub> separately. This proves that it is advantageous to obtain multifunctional fine-grained composites that offer various engineering applications, without a significant compromise of the initial mechanical properties of their single phased constituents. Lastly, the micrographic study of fracture surfaces highlighted the presence of primary inter-granular/trans-granular or mix modes of failure in single/multiphase composites.

Chapter 4, in part, is currently being prepared for submission for publication of the material. Karandikar, Keyur; Graeve, Olivia A.; Mecartney, Martha L.; Ohtaki Kenta; Travis, Austin; Evokodimiko Ekaterina; Cummings, Kira. The thesis author was the primary investigator and author of this material under the title “Mechanical properties of 8Y-ZrO<sub>2</sub>, MgAl<sub>2</sub>O<sub>4</sub>, and Al<sub>2</sub>O<sub>3</sub> based single/multiphase ceramic composites produced by spark plasma sintering.” The thesis author was responsible for testing hardness and toughness mechanical properties and fractography of the single/multiphase phase composites.

## CHAPTER 5: HEATING RATE AND MASTER SINTERING CURVE

### 5.1 Experimental Set-up, Results and Discussion

Table 5.1 Results highlighting grain size values for single phase 8Y-ZrO<sub>2</sub>, MgAl<sub>2</sub>O<sub>4</sub> and Al<sub>2</sub>O<sub>3</sub> powders at different heating rates at a sintering temperature. Density % is the bulk density of the samples calculated by Archimedes principle. Respective ceramic oxide specimen designations used in the current research are provided accordingly.

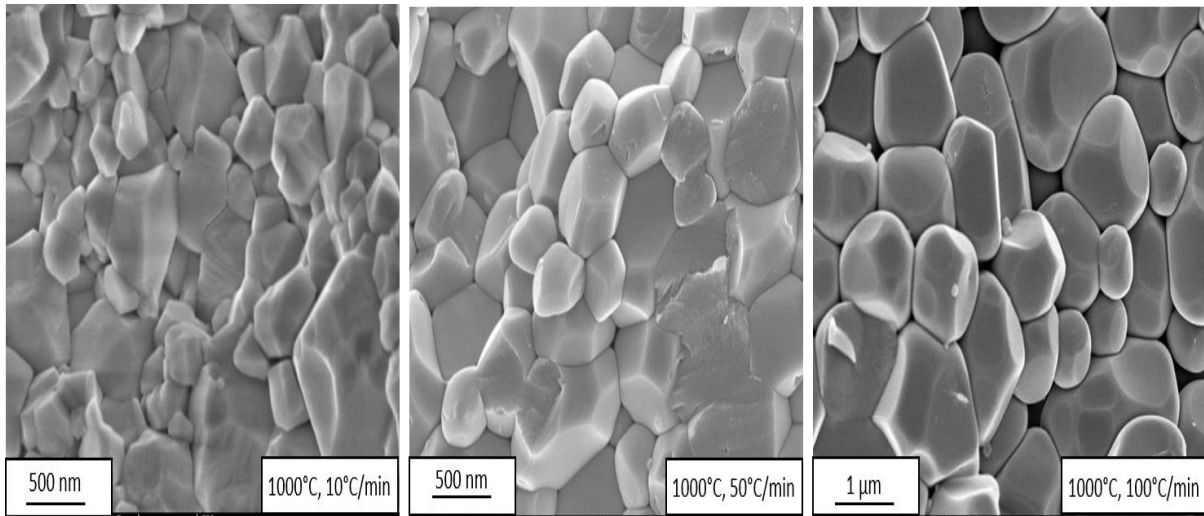
Specimen	Temperature °C	Heat. rate °C/min	Grain size nm	Density %
(8Y-ZrO <sub>2</sub> ) <sub>2</sub>	1000	100	280 ± 80 nm	97.8 ± 0.9
	1000	50	284 ± 63 nm	97.9 ± 0.8
	1000	10	219 ± 54 nm	96.9 ± 1.0
(8Y-ZrO <sub>2</sub> ) <sub>3</sub>	1100	100	1.72 ± 0.21 um	98.4 ± 0.5
	1100	10	1.58 ± 0.17 um	98.7 ± 0.2
(MgAl <sub>2</sub> O <sub>4</sub> ) <sub>1</sub>	1030	100	241.3 ± 43.2	98.1 ± 0.4
	1030	50	245.3 ± 63.6	98.6 ± 0.6
	1030	10	265.3 ± 55.2	98.7 ± 0.6
(MgAl <sub>2</sub> O <sub>4</sub> ) <sub>2</sub>	1030	100	338.8 ± 99.3	99.1 ± 0.2
	1030	50	324.3 ± 116.2	98.7 ± 0.4
	1030	10	265.3 ± 55.2	98.9 ± 0.5
(Al <sub>2</sub> O <sub>3</sub> ) <sub>2</sub>	1080	100	472.5 ± 140.5	99.1 ± 0.4
	1080	10	409.2 ± 54.5	99.5 ± 0.9
(Al <sub>2</sub> O <sub>3</sub> ) <sub>3</sub>	1000	100	307.8 ± 66.2	98.6 ± 0.8
	1000	50	355.9 ± 143.5	98.9 ± 0.3
	1000	10	258.5 ± 63.9	98.4 ± 0.2

**Table 5.2 Results highlighting grain size values for multiphase 8Y-ZrO<sub>2</sub>, MgAl<sub>2</sub>O<sub>4</sub> and Al<sub>2</sub>O<sub>3</sub> powders at different heating rates at a particular sintering temperature. Density % is the bulk density of the samples calculated by Archimedes principle. Respective ceramic oxide specimen designations used in the current research are provided accordingly.**

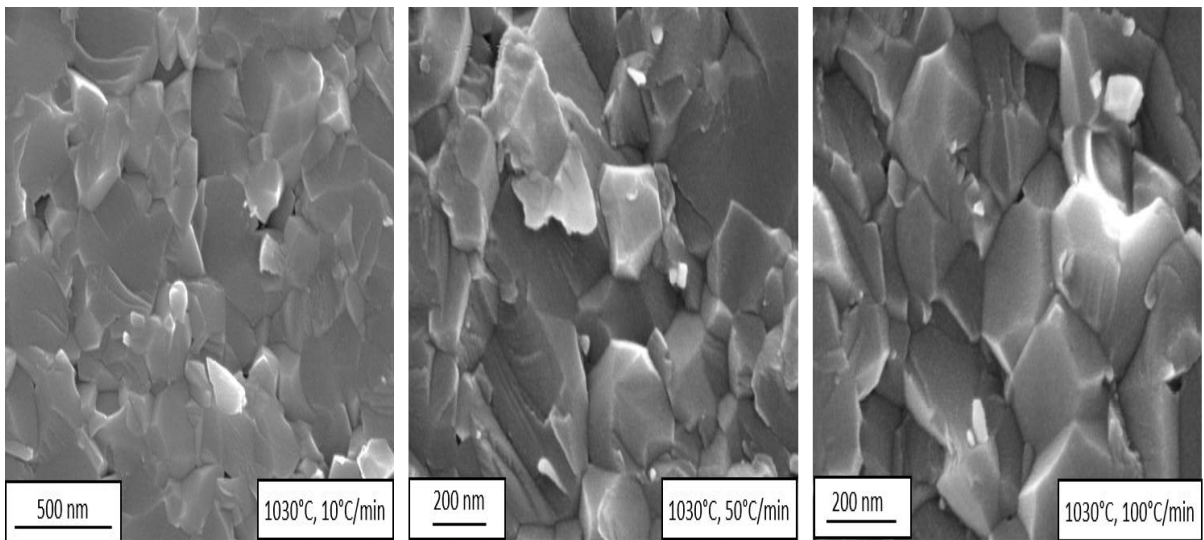
<b>Specimen</b>	<b>Temperature °C</b>	<b>Heat. rate °C/min</b>	<b>Grain size nm</b>	<b>Density %</b>
<b>(Al<sub>2</sub>O<sub>3</sub>)<sub>3</sub>/ (MgAl<sub>2</sub>O<sub>4</sub>)<sub>1</sub></b>	1100	100	370.0 ± 67.5	98.1 ± 1.0
	1100	10	528.3 ± 102.6	98.9 ± 0.6
<b>(Al<sub>2</sub>O<sub>3</sub>)<sub>2</sub>/ (MgAl<sub>2</sub>O<sub>4</sub>)<sub>1</sub></b>	1100	100	408.8 ± 81.8	98.3 ± 0.3
	1100	50	577.0 ± 102.1	98.7 ± 0.6
	1100	10	619.8 ± 129.3	98.9 ± 0.6
<b>Specimen</b>	<b>Temperature °C</b>	<b>Heat. rate °C/min</b>	<b>Grain size nm</b>	<b>Density %</b>
<b>(8Y-ZrO<sub>2</sub>)<sub>2</sub>/ (Al<sub>2</sub>O<sub>3</sub>)<sub>1</sub></b>	1100	100	257.5 ± 55	92.4 ± 0.1
	1100	50	279.5 ± 54	93.9 ± 0.6
	1100	10	342.2 ± 76.8	99.7 ± 0.6
<b>(8Y-ZrO<sub>2</sub>)<sub>2</sub>/ (Al<sub>2</sub>O<sub>3</sub>)<sub>3</sub></b>	1100	100	281.3 ± 60.9	98.4 ± 0.7
	1100	10	581.9 ± 143.6	98.9 ± 0.3

Table 5.2 continued

<b>Specimen</b>	<b>Temperature °C</b>	<b>Heat. rate °C/min</b>	<b>Grain size nm</b>	<b>Density %</b>
<b>(8Y-ZrO<sub>2</sub>)<sub>1</sub>/ (MgAl<sub>2</sub>O<sub>4</sub>)<sub>1</sub></b>	1100	100	284.8 ± 46.7	99.0 ± 0.7
	1100	50	412.9 ± 78.5	99.6 ± 0.6
	1100	10	N/A	99.7 ± 0.1
<b>(8Y-ZrO<sub>2</sub>)<sub>2</sub>/ (MgAl<sub>2</sub>O<sub>4</sub>)<sub>1</sub></b>	1000	100	142.0 ± 27.1	91.2 ± 0.3
	1000	50	110.3 ± 46.1	84.0 ± 0.2
<b>Specimen</b>	<b>Temperature °C</b>	<b>Heat. rate °C/min</b>	<b>Grain size nm</b>	<b>Density %</b>
<b>(8Y-ZrO<sub>2</sub>)<sub>2</sub> /(MgAl<sub>2</sub>O<sub>4</sub>)<sub>1</sub> /(Al<sub>2</sub>O<sub>3</sub>)<sub>3</sub></b>	1030	100	134.1 +/- 35.4	92.0± 0.6
	1030	50	142.7 +/- 28.4	90.5 ± 0.5
	1030	10	115.9 +/- 21	80.4 ± 0.6
<b>(8Y-ZrO<sub>2</sub>)<sub>2</sub> /(MgAl<sub>2</sub>O<sub>4</sub>)<sub>1</sub>- /(Al<sub>2</sub>O<sub>3</sub>)<sub>2</sub></b>	1100	100	288.8 +/- 49.7	98.7 ± 0.4
	1100	50	341 +/- 86	98.9 ± 0.6
	1100	10	367.1 +/- 99.5	98.3 ± 0.5



**Figure 5.1 SEM micrographs of the fracture surface of the  $(8Y-ZrO_2)_1$  sintered composite at different heating rates of 10, 50, and 100°C/min. The sintering temperature at 1000°C while other parameters were kept constant. Powder particle size was  $82\pm 31$ nm.**



**Figure 5.2 SEM micrographs of the fracture surface of the  $(MgAl_2O_4)_1$  sintered composite at different heating rates of 10, 50, and 100 °C/min. The sintering temperature was constant at 1030 °C. The powder particle size was measured as  $84\pm 15$  nm**



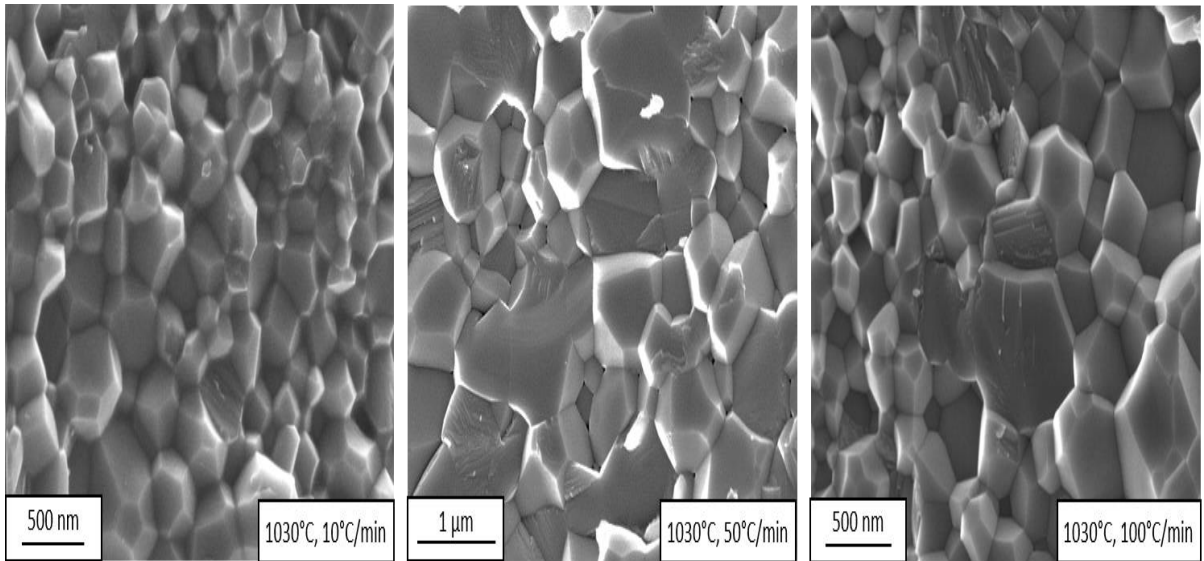


**Figure 5.3 SEM micrographs of the fracture surface of  $(\text{Al}_2\text{O}_3)_3$  sintered composite at different heating rates of 10, 50, and 100 °C/min. The sintering temperature was constant at 1030°C. The powder particle size was measured as  $149\pm 28$  nm.**

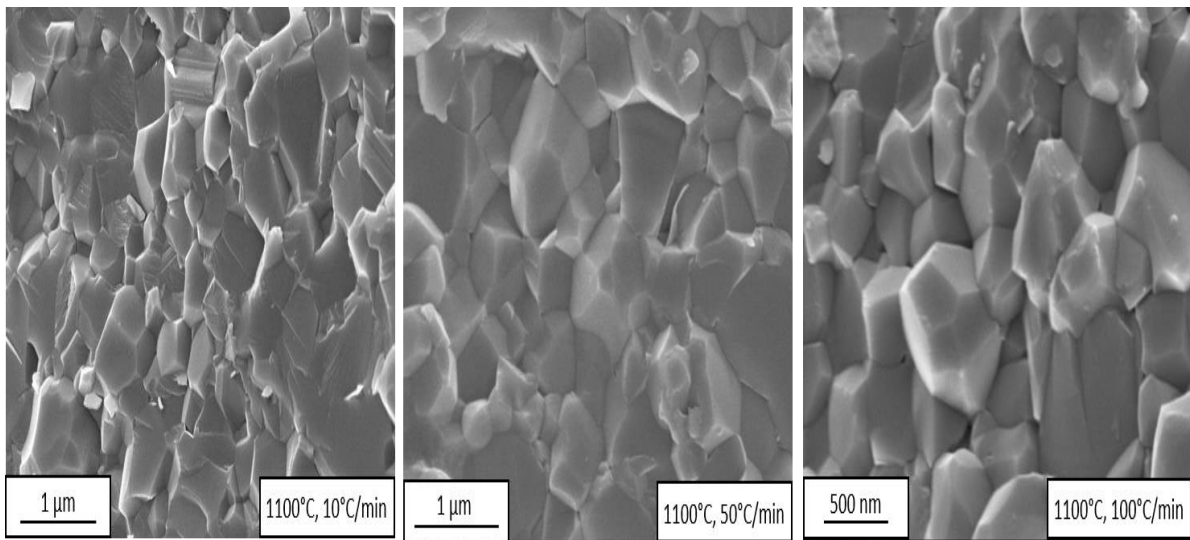


**Figure 5.4 SEM micrographs of the fracture surface of  $(\text{Al}_2\text{O}_3)_3/(\text{MgAl}_2\text{O}_4)_1$  sintered composite at different heating rates of 10, 50 and 100 °C/min. The sintering temperature was constant at 1100°C. The powder particle size was measured as  $147\pm 22$  nm.**

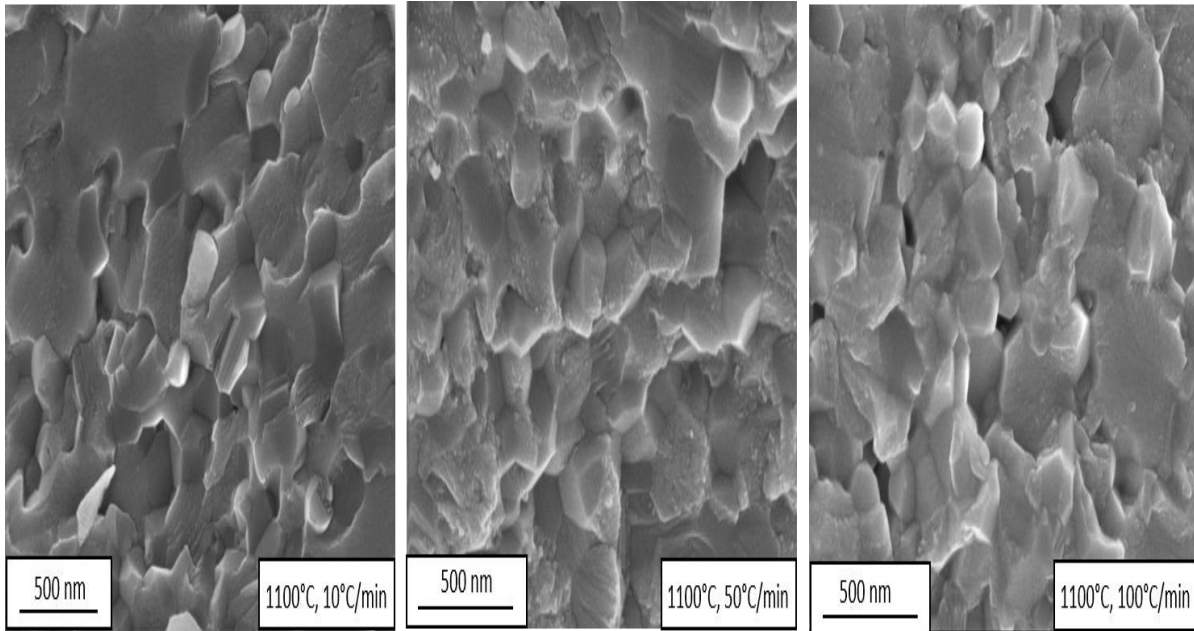


**Figure 5.5 SEM micrographs of the fracture surface of the  $(8Y-ZrO_2)_2/(Al_2O_3)_1$  sintered composite at different heating rates of 10,50 and 100°C/min. The sintering temperature was constant at 1100°C. The powder particle size was measured as  $197\pm 31$  nm.**

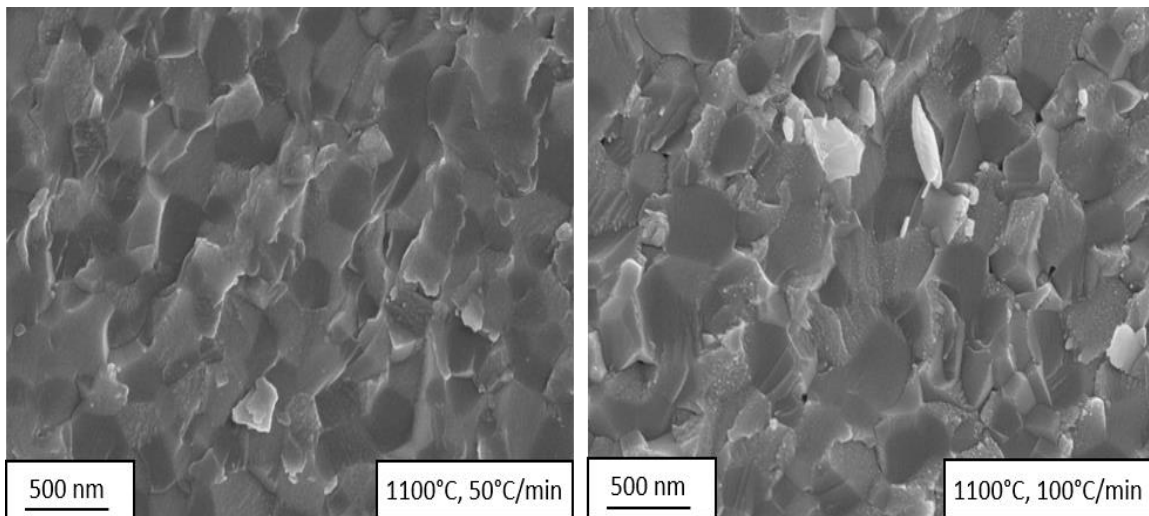


**Figure 5.6 SEM micrographs of the fracture surface of the  $(8Y-ZrO_2)_2/(MgAl_2O_4)_1$  sintered composite at different heating rates of 10 and 100°C/min. The sintering temperature was constant at 1100°C. The powder particle size was measured as  $91\pm 15$ nm.**

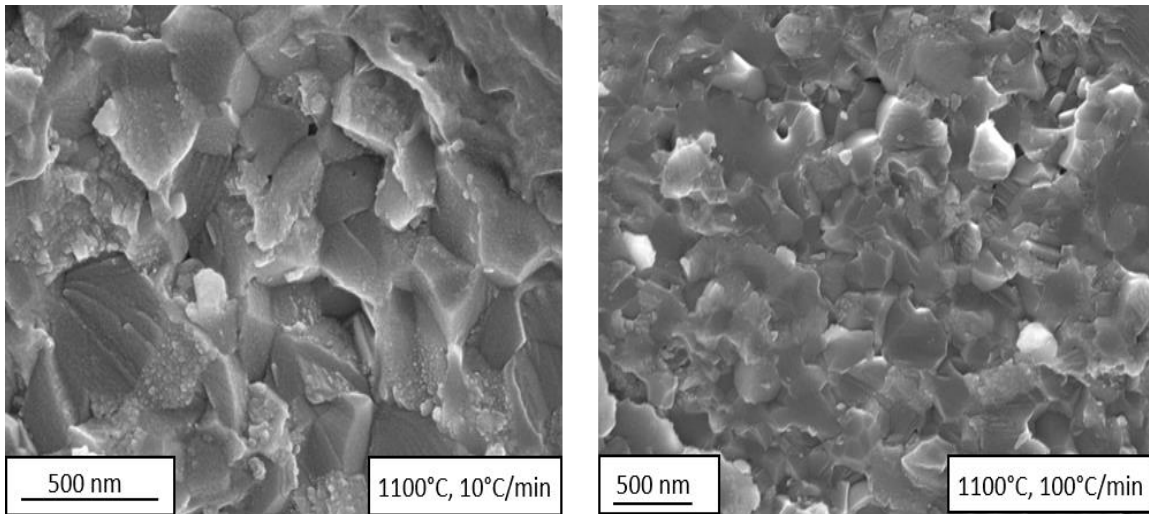


**Figure 5.7 SEM micrographs of the fracture surface of the  $(8Y-ZrO_2)_2/(MgAl_2O_4)_1/(Al_2O_3)_2$  sintered composite at different heating rates of 10 and 100°C/min. The sintering temperature was constant at 1100°C. The powder particle size was measured as  $214\pm 30$ nm.**

**Table 5.1 and 5.2** highlights respective data of the average grain size (nm) for two different specimens of binary and ternary phase  $8Y-ZrO_2$ ,  $Al_2O_3$  and  $MgAl_2O_4$  based composites versus heating rates (nm). Overall, in case of  $Al_2O_3/MgAl_2O_4$ , higher heating rates resulted creating finer grain sized microstructures. This observation is highlighted by the lower average grain size of  $(Al_2O_3)_2/(MgAl_2O_4)_1$  by  $\sim 200$  nm i.e.  $408.8 \pm 81.8$  nm at 100°C/min heating rate as compared to  $619.8 \pm 129.3$  when heated at 10°C/min (Sintering temperature=1100°C). Similar grain size-heating rate effect is also exhibited for other binary composites i.e. both  $(8Y-ZrO_2)/(Al_2O_3)$  specimens and  $(8Y-ZrO_2)_1/(MgAl_2O_4)_1$  at a constant value of sintering temperature. Lastly, results also indicate that for novel three phase composites, 100 °C/min heating rate is responsible for the least grain size values, irrespective of different sintering temperature and different particle sized samples. However, it is difficult to accurately confirm this trend because of the average grain size values of the given composites. For example, in case of the  $[(8Y-ZrO_2)_2/(MgAl_2O_4)_1/(Al_2O_3)_2]$  sample, sintering at

10 °C/min to 100 °C/min caused overall change in grain sizes by 80nm, while the standard deviation of the results lies between 40 to 99.5 nm.

Correspondingly, **Table 5.2** highlights the relative % density results for the given novel sintered multiphase ceramic oxides. In case of Alumina-Spinel, the changes in heating rate from 10-100°C/min was found to result in less than 1% difference in the density values which are well within the standard deviation of the results in a table. In case of multiphase composites of  $(8Y-ZrO_2)_1/(MgAl_2O_4)_1$  and  $(8Y-ZrO_2)_2/(MgAl_2O_4)_1/(Al_2O_3)$ , for specimens sintered at lower temperatures of 1000 °C, lower heating rates resulted in denser microstructures, while samples with sintering temperature of 1100 °C achieved almost complete densification independent of the heating profile. SEM images of respective multiphase microstructures are provided in **Figure 5.1-5.7** for further clarification.

**Table 5.1** highlights the relative % density results and grain size of single phase 8Y-ZrO<sub>2</sub>, Al<sub>2</sub>O<sub>3</sub> and MgAl<sub>2</sub>O<sub>4</sub> composites versus heating rates. Out of all the single-phase samples, the average grain size of (8Y-ZrO<sub>2</sub>)<sub>2</sub> sample (table and figure) was affected by the variations in heating rate. This average grain size of (8Y-ZrO<sub>2</sub>)<sub>1</sub> sintered at 100 °C/min was  $1.72 \pm 0.21$  μm as compared to  $1.58 \pm 0.17$  μm when sintered at 100 °C/min. Overall, the average changes in grain sizes in MgAl<sub>2</sub>O<sub>4</sub>, Al<sub>2</sub>O<sub>3</sub>, 8Y-ZrO<sub>2</sub> specimens were found to be well within the standard deviation values. For examples the grain sizes changed by 42nm from 300 to 258 nm in (Al<sub>2</sub>O<sub>3</sub>)<sub>1</sub> sample as shown in **Table 5.1** when the heating rate was reduced from 100°C/min to 10°C/min which is in a similar range as the standard deviation results ( $307.8 \pm 66.2$  nm and  $258.5 \pm 63.9$  nm respectively). Lastly, the respective relative density values were also obtained for given composites, and they were constant for the given specimens sintered at 10 - 100 °C/min. As a result, trends between heating rates and grain size and density are not clear, and it can be

concluded that heating rate is not primary factor driving the sintering of respective single phase ceramic oxide composites.

In case of present study, average grain size and relative density of the sintered specimens have been considered as a criterion to observe the influence of heating rate on microstructures of novel multiphase ceramic oxides. Based on results in **Table 5.1 and Figure 5.1**, faster heating rates led to finer grain sizes for binary and ternary ceramic oxides in general. Thus the grain size results of novel binary and ternary ceramic oxides sintered in the present study agree the heating rate trends found in past literature for  $\text{Al}_2\text{O}_3$ ,  $\text{BaTiO}_3$ . As the heating rates increase from 10 to 100 °C/min, the effective sintering cycle time to reach the desired temperature is shorter. The initial stage of sintering, that occurs at lower temperatures and is governed by grain growth due to surface diffusion and other grain coarsening mechanisms, is smaller. Hence powder compacts under faster heating rates tend to skip these dominant mechanisms while simultaneously densifying through grain boundary diffusion thereby exhibiting limited grain growth.

On the other hand, the results from relative density versus heating rates are contrasting in nature amongst the multiphase composites. Density value for  $(8\text{Y-ZrO}_2)_2/(\text{Al}_2\text{O}_3)_1$  powder compact is lower at higher heating rate of 100°C/min. A possible explanation of this result is that higher heating rates to thermal gradients during sample densification process, causing porosity thereby affecting the bulk density value which is also observed for 3Y-  $\text{ZrO}_2$ . Furthermore, the present results corroborate with sintering of single phase alumina by Aman (2009), which helps us to explain that the thermal gradients enhance local surface diffusion across the sample similar to Soret effect thereby affecting overall densification process. However, in case of  $(8\text{Y-ZrO}_2)_2/(\text{MgAl}_2\text{O}_4)_1$  and  $(8\text{Y-ZrO}_2)_2/(\text{MgAl}_2\text{O}_4)_1/(\text{Al}_2\text{O}_3)_3$  increase in

heating rate led to higher densification values. These results on the other hand are unique as they do not follow the regular densification mechanism in nature and have not been explored in literature. One assumption that can be obtained from these results is that electric field used in SPS delays the thermal based sintering mechanism. This might lead to enhanced densification by affecting the grain boundary energy and powder particle interface kinetics in the die during the actual sintering process [Demuynck]. The pulsed current was also found to influence the conductivity of Zirconia(8Y-ZrO<sub>2</sub>) and Alumina(Al<sub>2</sub>O<sub>3</sub>) which are insulators at room temperatures as studied by [Demuynck (2012)], these material properties potentially resulting particle interface kinetics. Lastly, in case of both (Al<sub>2</sub>O<sub>3</sub>)<sub>3</sub>/(MgAl<sub>2</sub>O<sub>4</sub>) samples the densification was not affected by respective heating rate, this can be possibly because the high sintering temperature of 1100°C/min could be enough for samples to densify irrespective of the heating rates. We can potentially expect the effects of heating rate expected to be more profound at samples held at lower sintering temperatures i.e. possibly between 900-1000°C.

Previous experimental studies performed by Tamburini *et al.* for cubic zirconia(8Y-ZrO<sub>2</sub>) observed no changes in density but the reduction in grain sizes by only 20nm when for a range of heating rates between 50-380°C/min. The densification effects obtained in the present study for 8Y-ZrO<sub>2</sub> concurs the literature findings, although the respective grain size tendency was found to be variable among different research studies. Kim *et al.* suggest that low heating rate leads to small grain size (0.21µm) for low heating rate and less porosity with sintering temperature. Low heating rate densification of Al<sub>2</sub>O<sub>3</sub>. Similarly, Morita *et al.* in MgAl<sub>2</sub>O<sub>4</sub> observed that at higher sintering temperatures with respect the relative density remains same >99% independent of heating rate. However, the densification is faster at lower densification

rates  $<10^{\circ}\text{C}/\text{min}$ . Thus the present results of spinel fall are obtained for samples sintered at higher sintering temperatures i.e. in the post densification zone.

In short, it can be concluded that heating rate effects are more significant at lower sintering temperatures, i.e.,  $<1100^{\circ}\text{C}$  in case of present study. Higher heating rates lead to finer grain sizes in multiphase composites attributed to homogenous grain growth of individual phases. On the other hand, change in heating rates were found to not significantly affect density or grain sizes for single phase composites, these observation is also found from results in previous literature studies<sup>4, 22–24</sup>. Furthermore, it was difficult to establish the relation between heating-rate/densification as other factors like the effective sintering time, the powder/material properties, and the type of sintering parameters used can play a part in defining the sintered microstructure.

## **5.2 Master Sintering Curve: Theory and Procedure**

The research presented in the present doctoral thesis was mainly of empirical nature. Hence it involved sintering and observation of the microstructures of the resulting different single/multiphase ceramic oxides by varying parameters of sintering temperature (Chapters 3) and heating rate (Chapter 5). To complement the empirical findings and predict the kinetics of sintering of 8Y-ZrO<sub>2</sub>, MgAl<sub>2</sub>O<sub>4</sub> and Al<sub>2</sub>O<sub>3</sub>-based oxides, we have used a basic simple theoretical model from past literature. Specifically, the Master Sintering Curves (MSC) have been plotted for each of the sintered composites from the previous empirical heating rate experiments as described in section 5.1.

Master sintering curve is a widely used concept used to measure the sinterability of a ceramic powder based composite<sup>179–183</sup>. This technique was proposed by Su and Johnson<sup>184</sup> to model the sintering and densification of a green body compact from empirical data independent

of the thermal profile/path used (iso-thermal, heating time, temperature, and so on). MSC model is based on combined stage sintering study carried out by Hansen *et al.*<sup>185</sup> that combines the three stages (initial particle surface necking, intermediate and final grain growth) in a single continuous sintering process. This phenomenon is achieved by developing an equation that separates and links the geometric parameters related to the actual microstructure of the fabricated specimen to the time-temperature profile used during the manufacturing process. The MSC model in case of isotropic linear shrinkage of the green compact accounts for various diffusion mechanisms involved and is described by the following equation:

$$\int_{\rho_0}^{\rho} \frac{(G(\rho))^n}{3\rho(\Gamma(\rho))} d\rho = \int_0^t \frac{\gamma\Omega D_0}{kT} \exp\left(-\frac{Q}{RT}\right) dt \quad (5.1)$$

Where n is 3 for volume diffusion, and n is 4 for grain boundary diffusion. The other symbols of the equation are as follows:

$\gamma$  is the surface energy,  $\Omega$  is the atomic volume, k is the Boltzmann's constant,  $\Gamma$  is the lumped scaling factor containing density-dependent geometric terms ( $\Gamma$  represents geometric factors as the driving force in sintering), T is the absolute temperature, G is the mean grain size, t is the time, L is the sample length,  $D_0$  is the diffusivity pre-exponent, Q is apparent activation energy for densification, R is universal constant. The equation 5.1 assumes that grain growth can be described as a function of density  $\rho$ , and sintering process is dominated by only one diffusion mechanism i.e., volume or grain boundary.

Rearrangement and integration of equation **5.1** to account for the heating history of the SPS process result in a single density based parameter  $\Pi$  on the left-hand side, while R.H.S of the same equation results in parameters namely work of sintering  $\Theta$ . These are elaborated in equations 5.2 and 5.3 below.



$$\text{L.H.S} = \Pi(\rho) = \frac{k}{\gamma\Omega D_0} \int_{\rho_0}^{\rho} \frac{(G(\rho))^n}{3\rho(\Gamma(\rho))} d\rho \quad (5.2)$$

$$\text{R.H.S} = \Theta(t, T(t)) = \int_0^t \exp\left(\frac{1}{T} \left(-\frac{Q}{RT}\right)\right) dt \quad (5.3)$$

The current study was focused on using the MSC curves to model densification tendency in SPS sintering of ceramic oxide composites. Thus, MSC curves were used to find the apparent activation energy Q empirically based on a set of sintering experiments with three different constant heating rates of 10°C/min, 50°C/min and 100°C/min for given single/multiphase ceramic oxide composite. For this purpose, the popularly used technique of linearization of equation 5.1 using sigmoid model<sup>186, 187</sup> was applied to obtain the linear relation between the two most important parameters, i.e., the natural log of work of sintering  $\Theta$  and relative density  $\rho$ . This further led to two different sub-parameters of density namely densification parameter  $\psi$  and densification ratio  $\Phi$

$$\text{Where relative density, } \rho = \rho_0 + \frac{1-\rho_0}{1+\exp\left(-\frac{\ln\Theta-a}{b}\right)} \quad (5.3)$$

$$\text{And densification parameter, } \psi = \frac{\rho-\rho_0}{1-\rho_0} = \frac{1}{1+\exp\left(-\frac{\ln\Theta-a}{b}\right)} \quad (5.4)$$

$$\text{Moreover, power law-based densification ratio, } \Phi = \frac{\rho-\rho_0}{1-\rho} = \left(\frac{\Theta}{\Theta_{ref}}\right)^n \quad (5.5)$$

Few of the key terms in the equations 5.3, 5.4 and 5.5 are  $\rho_0$ = initial green body relative density before the actual sintering, a, b = mathematical constants for sigomoidal curve,  $\Theta_{ref}$  is work of sintering in the middle of densification cycle i.e.,  $\rho = (\rho_0+1)*0.5$ , and n is the power-law exponent.

The linearized form of master sintering curve equation 5.2 using sigmoidal function is obtained by taking the log of equation 5.5 below:

$$\text{Ln } \phi = n(\text{ln}\Theta - \Theta_{ref}) \quad (5.6)$$

The mathematical constants a and b can be calculated by treating equation 5.6 as a straight line, and hence x-intercept  $a = \text{Ln}\Theta_{ref}$  and slope  $b = 1/n$ .

Thus, the first step involved in this study was to import the temperature (T), time(t) and displacement of the ram(mm) of the actual sintering cycle during SPS of the given ceramic oxide composites. For a given material, the three individual data sets were obtained related to the heating rates of 10°C/min, 50°C/min, and 100°C/min used for sintering. For MSC curves, the starting temperatures were considered to be the point where primary work of densification proceeds, i.e., the piston displacement and velocity values started to increase from 0. Minimum 25 readings of temperature were selected to plot the sintering curves. The loading diagrams in chapter 3 can be revisited for further clarification of the terms. The green density of the compacts was calculated previously by volumetric analysis using the mass of the powder loaded into the die. The piston displacement was normalized and converted to relative densities accordingly over the range of the temperatures.

Equations 5.3 was now used to plot  $\text{ln } \Theta$  values by continuously empirically assuming a value of Q (200, 500, 1000kJ/mol, and so on) in equation 5.3. Equation 5.5 was used to find  $\rho$  or calculated density at a given temperature T for a given sintering cycle. The difference between calculated density at a given temperature and the final maximum density was squared which is given by the following parameter  $\Delta$ . Thus, this difference  $\Delta = (\text{final density} - \text{calculated density})^2$  where the final density was the bulk density of ceramic composite obtained by Archimedes method. The resulting values of Q gave range of results for difference  $\Delta$  out of

which smallest value is considered. The resulting  $\Theta$  that gave the minimum value which was then as L.H.S of equation 5.3 thereby giving use the empirical value of apparent activation energy for a specific SPS sintered ceramic oxide composite. Thus, the linearized MSC model from literature was used to find out apparent activation energy of the given ceramic process<sup>187</sup>. As an example, the data set for plotting master sintering curve of the single-phase  $\text{Al}_2\text{O}_3$  along with resulting plots at different activation energies are shown in **Table 5.3 & Figure 5.8**. The respective sigmoid MSC obtained for different values of Q ranging from 200-1000kJ/mol are show in **figure 5.8**. Further calculations using linearization model of master sintering curves as described below is performed to obtain  $\ln \Theta_{\text{ref}}$  and n for the respective sintering process of alumina as shown in **figure 5.8**. Apparent activation energy of 960.6kJ/mol was obtained from the calculations using MSC equations described previously for single phase  $\text{Al}_2\text{O}_3$ .

**Table 5.3 Dataset for one of the three heating rates (10°C/min) used for generation of master sintering curve of single phase Al<sub>2</sub>O<sub>3</sub> composite. Density was obtained using green density, final density from Archimedes principle and ram displacement. Note that the temperature was converted to Kelvin(K) for calculations of lnΘ.**

Time(s)	Temp (°C)	Density	-Q/RT	Exp(-Q/RT)	Exp(-Q/RT) *t/T	lnΘ
2693	840	0.52144	-54.0337	3.41551E-24	8.26413E-24	-53.1501
2754	850	0.52144	-53.5526	5.52611E-24	1.3552E-23	-52.6555
2814	860	0.52144	-53.0799	8.8653E-24	2.20185E-23	-52.1702
2873	870	0.524515	-52.6155	1.41051E-23	3.5454E-23	-51.6938
2933	880	0.52759	-52.1592	2.22618E-23	5.66295E-23	-51.2255
2993	890	0.53374	-51.7107	3.48607E-23	8.97146E-23	-50.7654
3054	900	0.542965	-51.2698	5.4174E-23	1.41046E-22	-50.313
3114	910	0.552191	-50.8365	8.3562E-23	2.1996E-22	-49.8686
3174	920	0.561416	-50.4103	1.27959E-22	3.40438E-22	-49.4318
3233	930	0.573716	-49.9913	1.94562E-22	5.22875E-22	-49.0027
3294	940	0.589091	-49.5792	2.93794E-22	7.97822E-22	-48.5802
3356	950	0.604467	-49.1738	4.40658E-22	1.2092E-21	-48.1643
3414	960	0.619842	-48.775	6.56606E-22	1.81805E-21	-47.7565
3474	970	0.638292	-48.3826	9.72122E-22	2.71694E-21	-47.3548
3533	980	0.656743	-47.9964	1.43026E-21	4.03282E-21	-46.9598
3595	990	0.675193	-47.6164	2.09149E-21	5.95322E-21	-46.5704
3652	1000	0.693644	-47.2424	3.04021E-21	8.7218E-21	-46.1885
3714	1010	0.718244	-46.8741	4.39358E-21	1.27185E-20	-45.8112
3774	1020	0.73977	-46.5116	6.31336E-21	1.84274E-20	-45.4404
3835	1030	0.767445	-46.1547	9.02164E-21	2.65525E-20	-45.0752
3894	1040	0.795121	-45.8031	1.28218E-20	3.80259E-20	-44.716
3955	1050	0.825871	-45.4569	1.81261E-20	5.41865E-20	-44.3619
4015	1060	0.859697	-45.1159	2.5492E-20	7.6782E-20	-44.0133
4058	1070	0.884298	-44.78	3.56696E-20	1.07779E-19	-43.6742
4075	1080	0.89967	-44.449	4.96633E-20	1.49577E-19	-43.3465

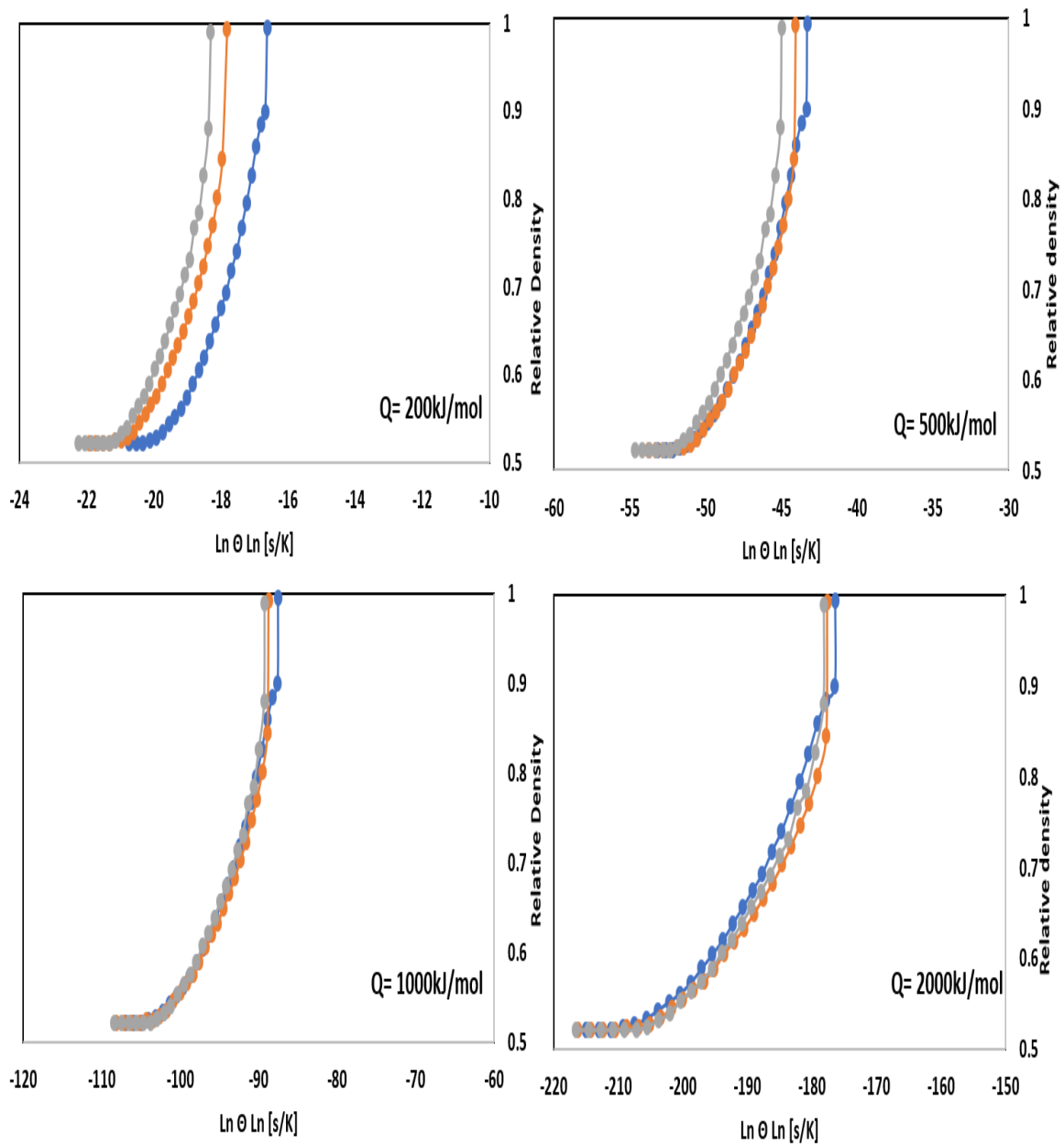


**Figure 5.8 Master sintering curves of relative density vs work of sintering calculations for single phase  $\text{Al}_2\text{O}_3$  at different empirical values of activation energy. Data sets of sintering profile at three different heating rates is used for this purpose. The minimum value of activation energy at which all the three curves converge is the apparent activation energy of the process. The respective linearization curves are shown in the next figure.**

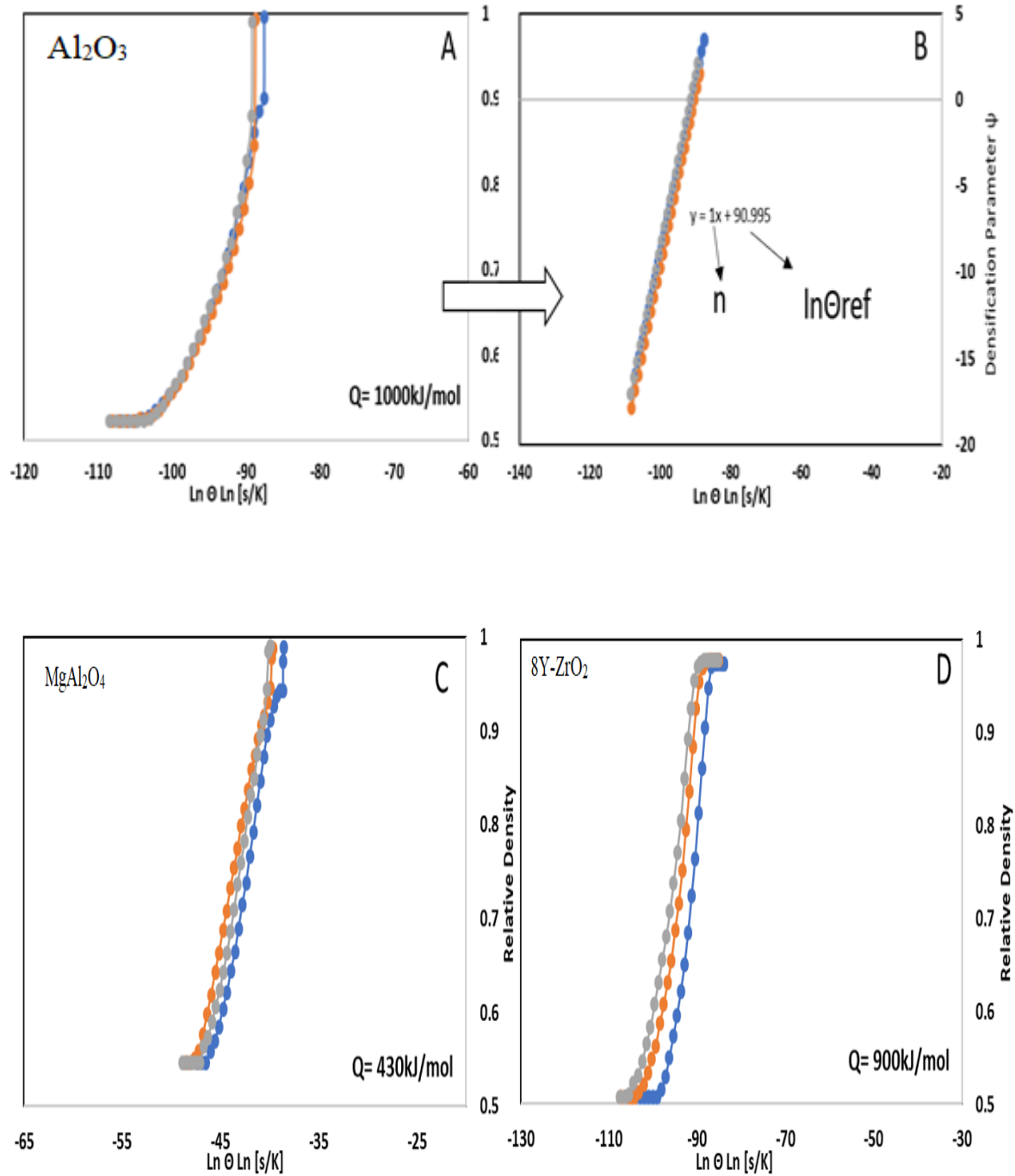


**Figure 5.9** Fig.B portrays Linearization of master sintering curve model for calculation of activation energy for  $\text{Al}_2\text{O}_3$ . The linearization is performed using an initial estimate of  $Q=1000 \text{ kJ/mol}$  that is used to plot the sigmoid curves in Figure A. Figures C and D show respective sigmoid curves with apparent activation energy values found out for  $\text{MgAl}_2\text{O}_4$  and  $8\text{Y-ZrO}_2$  respectively.

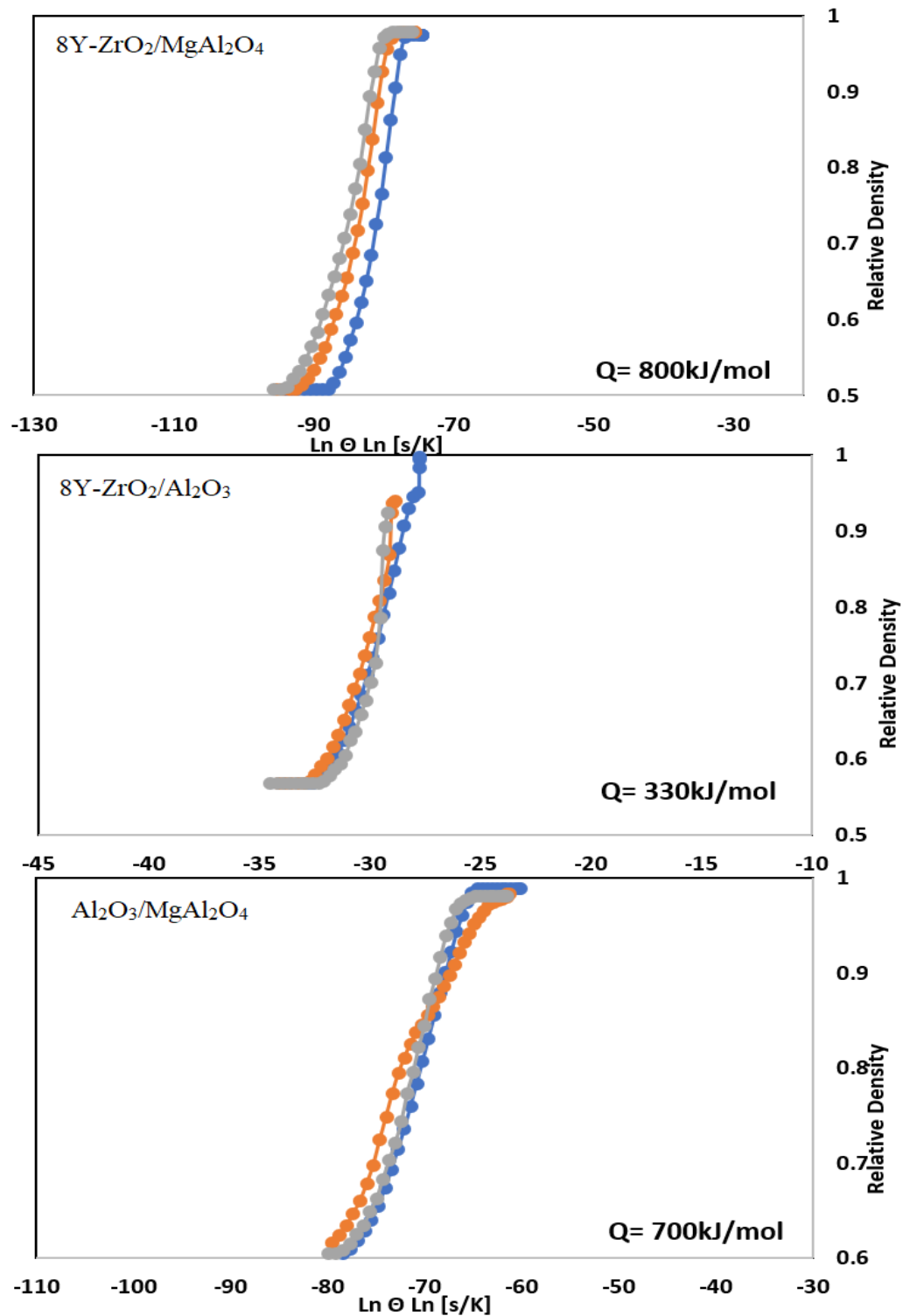


Figure 5.10 Master sintering curves of relative density vs. work of sintering plotted for binary phase composites of 8Y-ZrO<sub>2</sub>, Al<sub>2</sub>O<sub>3</sub>, and MgAl<sub>2</sub>O<sub>4</sub>. The resulting apparent activation energy of the sintering process for each ceramic is provided. Three sintering rates are used for plotting of MSC curves.

The resulting sintering curves for single phase ceramic oxides have been plotted in **Figure 5.8** using experimental data from three different heating rates. The activation energies were calculated from these curves, and it was found out that  $\text{MgAl}_2\text{O}_4$  had the least activation  $\sim 430\text{kJ/mol}$  while  $\text{Al}_2\text{O}_3$  exhibited the highest activation energy of about  $\sim 960.6\text{kJ/mol}$ <sup>171, 188–190</sup>. These values were well within the data from the previous SPS literature studies that have been performed which concluded the average values of  $480\text{kJ/mol}$  and  $1030\text{kJ/mol}$ . On the other hand, the current apparent activation energy for  $8\text{Y-ZrO}_2$  was found to be higher than the past experimental results (ranging from  $873\text{kJ/mol}$  to  $607\text{kJ/mol}$  in literature<sup>187, 191–194</sup>). However, it is important to know that the given activation energy is called “apparent” or only an empirical indication of the thermal sintering process. During sintering ceramic oxides densify through volume or surface grain boundary diffusion accompanied by grain growth and grain boundary sliding. Since all of these factors may occur simultaneously, the results obtained in the current study could vary drastically than previous research. Green density, sintering parameters, particle size and packing, final density measurements can thus affect the empirical calculations of MSC curves, and these might have resulted in a higher energy value in the current  $8\text{Y-ZrO}_2$  specimens.

Based on the experiments in chapter 3 and current MSC data we hypothesized that a correlation exists between grain growth and activation energy. The low grain growth ( $<1\mu\text{m}$  at high sintering temperatures) that was highlighted in chapter 3 can be corroborated by the low activation energy values during the sintering process. This growth was slow as compared to  $8\text{Y-ZrO}_2$  and  $\text{Al}_2\text{O}_3$  where the grains grew exponentially at temperatures  $>1100^\circ\text{C}$ , and this can be attributed to the resulting high apparent activation energies during the sintering process. The



high activation energy can affect the thermal response of the ceramic oxides concerning sintering temperature is thereby affecting the microstructure of the fabricated specimen.

The master sintering curves for binary composites of 8Y-ZrO<sub>2</sub>, MgAl<sub>2</sub>O<sub>4</sub>, and Al<sub>2</sub>O<sub>3</sub> were plotted with the resulting apparent activation energy values in **Figure 5.9**. All of the binary phase composites have activation energies less than 1000kJ/mol with 8Y-ZrO<sub>2</sub>/Al<sub>2</sub>O<sub>3</sub> SPS process being the lowest at 330 kJ/mol. The resulting values are new and to the best of our knowledge, no 50-50 volume% mixed binary composites have been studied for their activation energies by other researchers. It is well known that in case of multiphase composites sintering kinetics more complicated due to the presence of different properties of individual phases. Hence the binary empirical results from these MSC curves that can only be considered as an estimate for the sake of comparison with each other. However, we observed that the presence of secondary phases of zirconia and Spinel reduced the activation energy of alumina-based composites than single phase pure alumina. Thus, the sintering process of Al<sub>2</sub>O<sub>3</sub>/MgAl<sub>2</sub>O<sub>4</sub>(700kJ/mol) and Al<sub>2</sub>O<sub>3</sub>/MgAl<sub>2</sub>O<sub>4</sub>((330kJ/mol) resulted in lower activation energy as compared to single phase Al<sub>2</sub>O<sub>3</sub>(1000 kJ/mol). The resulting low values can be related to the limited grain growth tendency of the binary composites which was also observed in chapter 3 (size ratio of multiphase ceramics is less than its phases by almost a factor of 10). In fact, amongst binary phase composite themselves, 8Y-ZrO<sub>2</sub>/Al<sub>2</sub>O<sub>3</sub> showed the lowest grain size (~1µm) at the highest sintering temperature (1300°C) which can be correlated by the fact that it possessed the lowest activation energy value. This reduction in activation energies due to phase additions can further be validated via results obtained by other ceramic researchers. For example, Rozenburg<sup>195</sup> determined that LiF-doped spinel values exhibit lower activation energy of ≤300kJ/mol as compared to undoped spinel(480kJ/mol). Lastly, master sintering curves

failed to converge sufficiently in case of three phase composites that were sintered at similar heating rates of 10, 50 and 100°C/min. It was assumed that one of the reasons for this limitation was that the model was less reliable in predicting complicated sintering mechanisms of ternary phased powders at a fundamental level.

### **5.3 Conclusion**

The primary object of this chapter was to fabricate and observe the effects of different heating rates on the microstructure and sintering kinetics of single, binary and ternary phase composites. All the specimens were processed at three different rates of 10,50 and 100°C and average grain sizes, bulk densities and SEM micrographs of the fracture surface were analyzed.. On the other hand, significant reductions in average grain sizes were observed in binary and ternary phase systems at higher sintering temperatures. The latter half of the chapter dealt with plotting sintering curves for all the single, binary and ternary phase composites of 8Y-ZrO<sub>2</sub>, MgAl<sub>2</sub>O<sub>4</sub>, and Al<sub>2</sub>O<sub>3</sub>. The resulting apparent activation energies were found out for spinel and alumina and they concurred with the previous experimental data obtained by other ceramic scientists. The knowledge of these activation energy values helped to validate further the grain growth tendencies that were described in chapter 3 among the respective ceramic oxide specimens.

Chapter 5, in part, is currently being prepared for submission for publication of the material. Karandikar, Keyur; Graeve, Olivia A.; Mecartney, Martha L.; Ohtaki Kenta; Travis, Austin. The thesis author was the primary investigator and author of this material under the title “Effect of heating rate on microstructure and properties of spark plasma sintered ceramic oxides.” The thesis author was responsible for heating rate effects on sintering condition of ceramic oxide composites.

## REFERENCES

- 1 D.A.Taylor, “Advanced Ceramics – The Evolution , Classification , Properties , Production , Firing , Finishing and Design of Advanced Ceramics,” *Mater. Aust.*, **33** [1] 20–22 (2001).
- 2 D. Galusek and K. Ghillányová, “Ceramic Oxides;” pp. 1–58 in *Ceram. Sci. Technol.* Edited by R. Riedel and I.-W. Chen. Wiley-VCH Verlag GmbH & Co. KGaA, Weinheim, Germany, 2010.
- 3 E.S. Lukin, N.A. Makarov, A.I. Kozlov, N.A. Popova, E. V Anufrieva, M.A. Vartanyan, I.A. Kozlov, M.N. Safina, et al., “Oxide Ceramics of the New Generation and areas of application,” *Glas. Ceram.*, 65 [9–10] 348–353 (2008).
- 4 A. Balakrishnan, *Nanostructured Ceramic Oxides for Supercapacitor Applications*. CRC Press, Boca Rosa, 2014.
- 5 X.Q. Cao, R. Vassen, and D. Stoeber, “Ceramic materials for thermal barrier coatings,” *J. Eur. Ceram. Soc.*, **24** [1] 1–10 (2004).
- 6 W.J. Lackey, D.P. Stinton, G.A. Cerny, A.C. Schaffhauser, and L. Fehrenbacher, *Ceramic Coatings for Advanced Heat Engines—A Review an Projection*. 1987.
- 7 W.E. Lee, E. Giorgi, R. Harrison, A. Maître, and O. Rapaud, “Nuclear Applications for Ultra-High Temperature Ceramics and Max Phases;” pp. 391–415 in *Ultra-High Temp. Ceram. Mater. Extrem. Environ. Appl. First Ed.*, 1st ed. John Wiley & Sons, Inc., 2014.
- 8 M. Mecartney, *Multiphase Nanocrystalline Ceramic Concept for Nuclear Fuel, Project No.13-4818*. 2017.
- 9 A.H. Chokshi, “Superplasticity in fine grained ceramics and ceramic composites: current understanding and future prospects,” *Mater. Sci. Eng.*, **A166** 119–133 (1993).
- 10 W.E. Lee, M. Gilbert, S.T. Murphy, and R.W. Grimes, “Opportunities for Advanced Ceramics and Composites in the Nuclear Sector,” *J. Am. Ceram. Soc.*, **97** [7] 2005–2030 (2013).
- 11 J. Maier, “Nano-Ionics : Trivial and Non-Trivial Size Effects on Ion Conduction in Solids,” *Zeitschrift für Phys. Chemie*, **217** [4] 415–436 (2009).

- <sup>12</sup> Anselmi-Tamburini, Umberto, and I.G. Tredici, “Nanocrystalline Functional Materials in Bulk Form with Grain Size Below 50 nm;” pp. 2337–2350 in *Encycl. Nanotechnol.* Edited by B. Bhushan. Springer Netherlands, Dordrecht, 2016.
- <sup>13</sup> E.D. Bofjesen, M. Søndergaard, M. Christensen, and B.B. Iversen, “Particle size effects on the thermal conductivity of ZnO;” pp. 335–338 in *9th Eur. Conf. Thermoelectr.* 2012.
- <sup>14</sup> Y.L. Huang, Z.W. Liu, X.C. Zhong, H.Y. Yu, and D.C. Zeng, “NdFeB based magnets prepared from nanocrystalline powders with various compositions and particle sizes by spark plasma sintering,” *Powder Metall.*, **55** [2] 124–129 (2012).
- <sup>15</sup> H. Eilers, “Effect of particle / grain size on the optical properties of Y<sub>2</sub>O<sub>3</sub>: Er ,Yb,” *J. Alloys Compd.*, **474** 569–572 (2009).
- <sup>16</sup> L. Gao, “SiC-ZrO<sub>2</sub>(3Y)-Al<sub>2</sub>O<sub>3</sub> Nanocomposites superfast densified by SPS,” *NanoStructured Mater.*, **11** [1] 43–49 (1999).
- <sup>17</sup> N.Y. Wu, T.C. Holgate, N. Nong, N. Pryds, and S. Linderoth, “Effects of Synthesis and Spark Plasma Sintering Conditions on the Thermoelectric Properties of Ca<sub>3</sub>Co<sub>4</sub>O<sub>9+δ</sub>,” *J. Electron. Mater.*, **42** [7] 2134–2142 (2013).
- <sup>18</sup> L. An, A. Ito, and T. Goto, “Effect of sintering temperature on the transparency and mechanical properties of lutetium aluminum garnet fabricated by spark plasma sintering,” *J. Eur. Ceram. Soc.*, **32** [12] 3097–3102 (2012).
- <sup>19</sup> E. Matijevic, H. Giesche, and Y.-S. Her, “Effects of Particle uniformity on the Sinterability of Powders,” *Sci. Sinter.*, **28** [1] 3–17 (1996).
- <sup>20</sup> J.S. Chappell, T.A. Ring, and J.D. Birchall, “Particle size distribution effects on sintering rates,” *J. Appl. Phys.*, **60** 383 (2014).
- <sup>21</sup> D.-M. Liu, “Influence of Solid loading and Particle Size distribution on the Porosity development of Green Alumina Ceramic mouldings,” *Ceram. Int.*, **23** 513–520 (1997).
- <sup>22</sup> F. Shiau, T. Fang, and T. Leu, “Effect of Particle-Size Distribution on the Microstructural Evolution in the Intermediate Stage of Sintering,” *J. Am. Ceram. Soc.*, **80** [2] 286–290 (1997).

- 23 M.N. Rahaman, *Ceramic processing and sintering*, 2nd ed. Marcel Dekker, New York, 2003.
- 24 B.K. Datta, “Raw Materials: Their production and characteristics;” pp. 59–67 in *Powder Metall. An Adv. Tech. Process. Eng. Mater.*, Second Edi. PHI Learning private limited, Delhi, India, 2012.
- 25 C.A. Handwerker, J.E. Blendell, and R.L. Coble, “Sintering of Ceramics;” pp. 3–19 in *Sci. Sinter. New Dir. Mater. Process. Microstruct. Control*. Edited by H. Palmour III, R.M. Spriggs and P.S. Uskokovic. Springer US, 1989.
- 26 M.J. Madou, “Salt-Assisted Spray Pyrolysis;” pp. 572–574 in *Manuf. Tech. Microfabr. Nanotechnol.* CRC Press, 2011.
- 27 R. Rice W., “Preparation of Ceramic Powders;” pp. 60–63 in *Ceram. Fabr. Technol.* CRC Press, 2002.
- 28 E.G. Zemtsova, A. V Monin, V.M. Smirnov, B.N. Semenov, and N. Morozov, “Formation and Mechanical Properties of Alumina Ceramics Based on Al<sub>2</sub>O<sub>3</sub> Micro- and Nanoparticles,” *Phys. Mesomech.*, **18** [2] 134–138 (2015).
- 29 L.B. et al. Kong, “Transparent Ceramic Materials;” pp. 29–91 in *Transparent Ceram.* 2015.
- 30 H.B. Zhang, B. Kim, K. Morita, H. Yoshida, J. Lim, and K. Hiraga, “Optimization of high-pressure sintering of transparent zirconia with nano-sized grains,” *J. Alloys Compd.*, **508** [1] 196–199 (2010).
- 31 K. Morita, B.-N. Kim, K. Hiraga, and H. Yoshida, “Fabrication of high-strength transparent MgAl<sub>2</sub>O<sub>4</sub> spinel polycrystals by optimizing spark-plasma-sintering conditions,” *J. Mater. Res.*, **24** [9] 2863–2872 (2009).
- 32 R.W. Rice, C.C. Wu, and F. Boichelt, “Hardness–Grain-Size Relations in Ceramics.,” *J. Am. Ceram. Soc.*, **77** [10] 2539–2553 (1994).
- 33 T. Chen and M.L. Mecartney, “Superplastic compression , microstructural analysis and mechanical properties of a fine grain three-phase alumina – zirconia – mullite ceramic composite,” *Mater. Sci. Eng. A*, **410–411** 134–139 (2005).

- 34 D. Joseph and A. Kumar, "Static Laser Light Scattering Studies from Red Blood Cells," *Opt. Photonics J.*, **6** 237–260 (2016).
- 35 Wikimedia Commons contributors, *File:DLS.svg*, *Wikimedia Commons, Free media Repos.*, (2014).
- 36 R. Pecora, "Dynamic light scattering measurement of nanometer particles in liquids," 123–131 (2000).
- 37 V. Uskoković, "Dynamic Light Scattering Based Microelectrophoresis: Main Prospects and Limitations," *J. Dispers. Sci. Technol.*, **33** [12] 1762–1786 (2012).
- 38 M.I. Ltd, *Zetasizer Nano Series User Manual-MAN0317*. 2004.
- 39 Microtrac Inc., *Nanotracs Wave II Particle Size And ZetaPotential Analyzer - Operation and Maintenance*. 2015.
- 40 Zeta-meter.Inc, *Zeta Potential : A Complete Course in 5 Minutes*, 1–8 (n.d.).
- 41 H. Kato, A. Nakamura, K. Takahashi, and S. Kinugasa, "Accurate Size and Size-Distribution Determination of Dynamic Light Scattering and Asymmetrical Flow Field Flow," *nanomaterials*, **2** 15–30 (2012).
- 42 R.C. Murdock, L. Braydich-stolle, A.M. Schrand, J.J. Schlager, S.M. Hussain, and M.E.T. Al, "Characterization of Nanomaterial Dispersion in Solution Prior to In Vitro Exposure Using Dynamic Light Scattering Technique," *Toxicol. Sci.*, **101** [2] 239–253 (2008).
- 43 H. Kato, M. Suzuki, K. Fujita, M. Horie, S. Endoh, Y. Yoshida, H. Iwahashi, K. Takahashi, *et al.*, "Reliable size determination of nanoparticles using dynamic light scattering method for in vitro toxicology assessment.," *Toxicol. In Vitro*, **23** [5] 927–34 (2009).
- 44 I. Treviranus and Horiba Ltd., *Trusting your zeta potential results*, (2013).
- 45 J. Jiang, G. Oberdörster, and P. Biswas, "Characterization of size, surface charge, and agglomeration state of nanoparticle dispersions for toxicological studies," *J. Nanoparticle Res.*, **11** [1] 77–89 (2008).

- 46 M. Vecera and J. Pospíšil, “Stability and rheology of aqueous suspensions,” *Procedia Eng.*, **42** 1720–1725 (2012).
- 47 D. Fairhurst and I. Particle sciences, *An Overview of the Zeta Potential Part 3: Uses and Applications*, *Am. Pharm. Rev.*, 139288 (2013).
- 48 D. Hanaor, M. Michelazzi, C. Leonelli, and C.C. Sorrell, “The effects of carboxylic acids on the aqueous dispersion and electrophoretic deposition of ZrO<sub>2</sub>,” *J. Eur. Ceram. Soc.*, **32** [1] 235–244 (2012).
- 49 R.W.O. Brien, B.R. Midmore, A. Lamb, and R.J. Hunter, “Electroacoustic Studies of Moderately Concentrated Colloidal Suspensions,” *Faraday Discuss. Chem. Soc.*, **90** 301–312 (1990).
- 50 ISO/TC 24/SC 4, *ISO 14887:2000(en) Sample preparation — Dispersing procedures for powders in liquids*. n.d.
- 51 N. Mandzy, E. Grulke, and T. Druffel, “Breakage of TiO<sub>2</sub> agglomerates in electrostatically stabilized aqueous dispersions,” *Powder Technol.*, **160** [2] 121–126 (2005).
- 52 Malvin Instruments, *Influence of Concentration Effects and Particle Interactions on DLS Analysis of Bioformulations*, (2014).
- 53 A.M. Herrera, A.A. Martins de Oliveira, A.P. Novaes de Oliveira, and D. Hotza, “Processing and Characterization of Ytria-Stabilized Zirconia Foams for High-Temperature Applications,” *J. Ceram.*, **2013** 1–8 (2013).
- 54 T.G.F. Souza, V.S.T. Ciminelli, and N.D.S. Mohallem, “A comparison of TEM and DLS methods to characterize size distribution of ceramic nanoparticles A comparison of TEM and DLS methods to characterize size distribution of ceramic nanoparticles,” *J. Phys. Conf. Ser.*, **733** 12039 (2016).
- 55 M. Frank, S. Naleway, T. Haroush, C.-H. Liu, S. Siu, J. Ng, I. Torres, A. Ismail, *et al.*, “Stiff, porous scaffolds from magnetized alumina particles aligned by magnetic freeze casting,” *Mater. Sci. Eng. C-Biomimetic Supramol. Syst.*, (2017).

- <sup>56</sup> M. Yavuz, H. Maeda, L. Vance, H.K. Liu, and S.X. Dou, “Effect of ball milling materials and methods on powder processing of Bi2223 superconductors,” *Supercond. Sci. Technol.*, **11** [10] 1153–1159 (1998).
- <sup>57</sup> N.M. Rendtorff, S. Grasso, C. Hu, G. Suarez, E.F. Aglietti, and Y. Sakka, “Dense zircon (ZrSiO<sub>4</sub>) ceramics by high energy ball milling and spark plasma sintering,” *Ceram. Int.*, **38** [3] 1793–1799 (2012).
- <sup>58</sup> J. Peng, C. Wang, L. Li, F. Wang, Q. Shen, and L. Zhang, “Improvement of sinterability of barium dititanate powders by ball-milling,” *J. Mater. Sci. Mater. Electron.*, **23** [3] 706–711 (2011).
- <sup>59</sup> Z. Yunfeng, W. Kaijun, and H. Jin, “Effect of Ball Milling on the Properties of Zirconia Powder Prepared by Alcohol-aqueous Coprecipitation Method,” *Key Eng. Mater.*, **544** 34–37 (2013).
- <sup>60</sup> N.Z.F. Mukhtar, M.Z. Borhan, M. Rusop, and S. Abdullah, “Effect of Milling Time on Particle Size and Surface Morphology of Commercial Zeolite by Planetary Ball Mill,” *Adv. Mater. Res.*, **795** 711–715 (2013).
- <sup>61</sup> R. Orru, R. Licheri, A. Mario, A. Cincotti, and G. Cao, “Consolidation / synthesis of materials by electric current activated / assisted sintering,” *Mater. Sci. Eng. R*, **63** 127–287 (2009).
- <sup>62</sup> S. Grasso, Y. Sakka, and G. Maizza, “Electric current activated / assisted sintering ( ECAS ): a review of patents 1906 – 2008,” *Sci. Technol. Adv. Mater.*, **10** [53001] 24 (2009).
- <sup>63</sup> M. Suárez, A. Fernández, J.L. Menéndez, R. Torrecillas, H.U. Kessel, J. Hennicke, R. Kirchner, and T. Kessel, “Challenges and Opportunities for Spark Plasma Sintering : A Key Technology for a New Generation of Materials,” (2013).
- <sup>64</sup> J.T. Cahill, V.R. Vasquez, S.T. Mixture, D. Edwards, and O.A. Graeve, “Effect of Current on Diffusivity in Metal Hexaborides : A Spark Plasma Sintering Study,” *ACS Appl. Mater. Interfaces*, **9** 37357–37363 (2017).
- <sup>65</sup> J.P. Kelly and O.A. Graeve, “Mechanisms of pore formation in high-temperature carbides: Case study of TaC prepared by spark plasma sintering,” *Acta Mater.*, **84** [Supplement C] 472–483 (2015).



- <sup>66</sup> K. Sinha, B. Pearson, S.R. Casolco, J.E. Garay, and O.A. Graeve, “Synthesis and Consolidation of BaAl<sub>2</sub>Si<sub>2</sub>O<sub>8</sub>:Eu: Development of an Integrated Process for Luminescent Smart Ceramic Materials,” *J. Am. Ceram. Soc.*, **92** [11] 2504–2511 (2009).
- <sup>67</sup> O.A. Graeve, R. Kanakala, L. Kaufman, K. Sinha, E. Wang, B. Pearson, G. Rojas-George, and J.C. Farmer, “Spark plasma sintering of Fe-based structural amorphous metals (SAM) with Y<sub>2</sub>O<sub>3</sub> nanoparticle additions,” *Mater. Lett.*, **62** [17] 2988–2991 (2008).
- <sup>68</sup> O.A. Graeve, M.S. Saterlie, R. Kanakala, S.D. de la Torre, and J.C. Farmer, “The kinetics of devitrification of amorphous alloys: The time–temperature–crystallinity diagram describing the spark plasma sintering of Fe-based metallic glasses,” *Scr. Mater.*, **69** [2] 143–148 (2013).
- <sup>69</sup> J. Kelly, S. Fuller, K. Seo, E. Novitskaya, V. Eliasson, A. M. Hodge, and O. A. Graeve, “Designing in situ and ex situ bulk metallic glass composites via spark plasma sintering in the super cooled liquid state,” *Mater. Des.*, **93** (2015).
- <sup>70</sup> R. Chaim, M. Levin, A. Shlayer, and C. Estournes, “Sintering and densification of nanocrystalline ceramic oxide powders: a review,” *Adv. Appl. Ceram.*, **107** [3] 159–169 (2008).
- <sup>71</sup> K. Inoue, Electric-discharge sintering US 3241956 A; 1966.
- <sup>72</sup> K. Lu, “Sintering of nanoceramics,” *Int. Mater. Rev.*, **53** [1] 20–38 (2017).
- <sup>73</sup> Z. Zhang, Z. Liu, J. Lu, X. Shen, and F. Wang, “ScienceDirect The sintering mechanism in spark plasma sintering – Proof of the occurrence of spark discharge,” *Scr. Mater.*, **81** 56–59 (2014).
- <sup>74</sup> R. Chaim, “Superfast densification of nanocrystalline oxide powders by spark plasma sintering,” *J Mater Sci* (, **41** 7862–7871 (2006).
- <sup>75</sup> ASTM International, *ASTM C373-88(2006) Standard Test Method for Water Absorption, Bulk Density, Apparent Porosity, and Apparent Specific Gravity of Fired Whiteware Products*. West Conshohocken, PA, 2006.
- <sup>76</sup> ASTM International, *ASTM E112-12 Standard Test Methods for Determining Average Grain Size*. West Conshohocken, PA, 2012.

- 77 R.E. Chinn, “Grinding and Polishing;” in *Ceramography Prep. Anal. Ceram. Microstruct.* ASM International, Materials Park, Ohio, USA, 2002.
- 78 B.B. Bokhonov, A. V Ukhina, D. V Dudina, A.G. Anisimov, V.I. Mali, and I.S. Batraev, “Carbon uptake during Spark Plasma Sintering : investigation through the analysis of the carbide ‘ footprint ’ in a Ni – W alloy,” *RSC Adv.*, **5** 80228–80237 (2015).
- 79 H. Naceur, A. Megriche, and M. El Maaoui, “Effect of sintering temperature on microstructure and electrical properties of Sr<sub>1-x</sub>(Na<sub>0.5</sub>Bi<sub>0.5</sub>)<sub>x</sub> Bi<sub>2</sub>Nb<sub>2</sub>O<sub>9</sub> solid solutions,” *J. Adv. Ceram.*, **3** [1] 17–30 (2014).
- 80 A. Ferna, J.L. Mene, R. Torrecillas, and M. Sua, “Grain growth control and transparency in spark plasma sintered self-doped alumina materials,” *Scr. Mater.*, **61** 931–934 (2009).
- 81 D. Quach, C. Faconti, J.R. Groza, and F. Raether, “Initial Stages of Sintering of Alumina by Thermo-Optical Measurements,” *J. Am. Ceram. Soc.*, **90** [9] 2716–2722 (2007).
- 82 R.J. BRATTON, “Sintering and Grain-Growth Kinetics of MgAl<sub>2</sub>O<sub>4</sub>,” *J. Am. Ceram. Soc.*, **54** [3] 141–143 (1971).
- 83 S. Shukla, S. Seal, R. Vij, and S. Bandyopadhyay, “Reduced activation energy for grain growth in nanocrystalline yttria-stabilized zirconia,” *Nano Lett.*, **3** [3] 397–401 (2003).
- 84 K. Morita, B.-N. Kim, K. Hiraga, and H. Yoshida, “Fabrication of transparent MgAl<sub>2</sub>O<sub>4</sub> spinel polycrystal by spark plasma sintering processing,” *Scr. Mater.*, **58** [12] 1114–1117 (2008).
- 85 K. Morita, B.-N. Kim, H. Yoshida, and K. Hiraga, “Spark-Plasma-Sintering Condition Optimization for Producing Transparent MgAl<sub>2</sub>O<sub>4</sub> Spinel Polycrystal,” *J. Am. Ceram. Soc.*, **92** [6] 1208–1216 (2009).
- 86 D.M. Saylor, B. El Dasher, Y. Pang, H.M. Miller, P. Wynblatt, A.D. Rollett, and G.S. Rohrer, “Habits of Grains in Dense Polycrystalline Solids,” *J. Am. Ceram. Soc.*, **26** 724–726 (2004).
- 87 I. Chen, “Mobility control of ceramic grain boundaries and interfaces,” *Mater. Sci. Eng. A*, **166** [1–2] 51–58 (1993).

- 88 D.A. Molodov, L.A. Barrales-mora, and J. Brandenburg, "Grain boundary motion and grain rotation in aluminum bicrystals: recent experiments and simulations Grain boundary motion and grain rotation in aluminum bicrystals: recent experiments and simulations," *IOP Conf. Ser. Mater. Sci. Eng.*, **89** 12008 (2015).
- 89 Z. Shen, M. Johnsson, Z. Zhao, and M. Nygren, "Spark plasma sintering of Alumina," *J. Am. Ceram.*, **85** [8] 1921–27 (2002).
- 90 D. Pravarthana, D. Chateigner, L. Lutterotti, M. Lacotte, S. Marinel, P. a. Dubos, I. Hervas, E. Hug, *et al.*, "Growth and texture of spark plasma sintered Al<sub>2</sub>O<sub>3</sub> ceramics: A combined analysis of X-rays and electron back scatter diffraction," *J. Appl. Phys.*, **113** [15] 153510 (2013).
- 91 O. Al, Q. Tian, J. Dai, Z. Lv, and T. Zhai, "Processing Research Effect of characteristics of submicrometer powder on the sintering behaviors of," **17** [7] 676–680 (2016).
- 92 K. Morita, K. Hiraga, B.-N. Kim, H. Yoshida, and Y. Sakka, "Synthesis of dense nanocrystalline ZrO<sub>2</sub>–MgAl<sub>2</sub>O<sub>4</sub> spinel composite," *Scr. Mater.*, **53** [9] 1007–1012 (2005).
- 93 P. Palmero, "Structural Ceramic Nanocomposites: A Review of Properties and Powders ' Synthesis Methods," *Nanomaterials*, **5** 656–696 (2015).
- 94 N. Nafsin and R.H.R. Castro, "Direct measurements of quasi -zero grain boundary energies in ceramics," *J. Mater. Res.*, **32** [1] 166–173 (2017).
- 95 X. Zhou, D.M. Hulbert, J.D. Kuntz, J.E. Garay, and A.K. Mukherjee, "Superplasticity of the nanostructured binary systems of Zirconia-Alumina-Spinel ceramics by spark plasma sintering;" pp. 155–164 in *Adv. Ceram. matrix Compos. X*. Edited by J.P. Singh, N. P.Bansal and M.K. Waltraud. The American ceramic society, 2004.
- 96 E. Yalamaç, "Effect of spinel addition on the sintering behavior and microstructure of alumina-spinel ceramics," *Ceram. - Silikaty*, **58** [4] 314–319 (2014).
- 97 M. Khoshkalam, "Materials Science & Engineering A An investigation on mechanical properties of Alumina – Zirconia – Magnesia spinel composite ceramics fabricated by gel-casting using solution combustion synthesized powder," *Mater. Sci. Eng. A*, **587** 336–343 (2013).

- <sup>98</sup> F. Meng, C. Liu, F. Zhang, Z. Tian, and W. Huang, “Densification and mechanical properties of fine-grained Al<sub>2</sub>O<sub>3</sub>–ZrO<sub>2</sub> composites consolidated by spark plasma sintering,” *J. Alloys Compd.*, **512** [1] 63–67 (2012).
- <sup>99</sup> Z.Z. Fang and H. Wang, “Densification and grain growth during sintering of nanosized particles,” *Int. Mater. Rev.*, **53** [6] 326–352 (2008).
- <sup>100</sup> C.B. Carter and M.G. Norton, “Sintering and Grain Growth,” pp. 439–456 in *Ceram. Mater. Sci. Eng.* Springer New York, New York, NY, 2013.
- <sup>101</sup> D.S. Smith and A. Smith, “The effect of differential shrinkage in ceramic bonding,” *J. Mater. Sci. Lett.*, **5** 349–352 (1986).
- <sup>102</sup> U. Anselmi-Tamburini, J.E. Garay, Z. a. Munir, a. Tacca, F. Maglia, G. Chiodelli, and G. Spinolo, “Spark plasma sintering and characterization of bulk nanostructured fully stabilized zirconia: Part II. Characterization studies,” *J. Mater. Res.*, **19** [11] 3263–3269 (2011).
- <sup>103</sup> D.V. Quach, S. Kim, R. a. De Souza, M. Martin, and Z. a. Munir, “Grain Size Effect in the Electrical Properties of Nanostructured Functional Oxides through Pressure Modification of the Spark Plasma Sintering Method,” *Key Eng. Mater.*, **484** 107–116 (2011).
- <sup>104</sup> D. V. Quach, H. Avila-Paredes, S. Kim, M. Martin, and Z. a. Munir, “Pressure effects and grain growth kinetics in the consolidation of nanostructured fully stabilized zirconia by pulsed electric current sintering,” *Acta Mater.*, **58** [15] 5022–5030 (2010).
- <sup>105</sup> V. Mamedov, “Spark plasma sintering as advanced PM sintering method,” *Powder Metall.*, **45** [4] 322 (2002).
- <sup>106</sup> U. Anselmi-Tamburini, J.E. Garay, Z. a. Munir, a. Tacca, F. Maglia, and G. Spinolo, “Spark plasma sintering and characterization of bulk nanostructured fully stabilized zirconia: Part I. Densification studies,” *J. Mater. Res.*, **19** [11] 3255–3262 (2011).
- <sup>107</sup> K. Maca, V. Pouchly, and P. Zalud, “Two-Step Sintering of oxide ceramics with various crystal structures,” *J. Eur. Ceram. Soc.*, **30** 583–589 (2010).
- <sup>108</sup> T. Takeuchi, I. Kondoh, N. Tamari, N. Balakrishnan, K. Nomura, H. Kageyama, and Y. Takeda, “Improvement of Mechanical Strength of 8 mol % Ytria-Stabilized Zirconia

- Ceramics by Spark-Plasma Sintering,” *J. Electrochem. Soc.*, **149** [4] A455 (2002).
- 109 H. Zhang, B.-N. Kim, K. Morita, H.Y. Keijiuro Hiraga, and Y. Sakka, “Effect of sintering temperature on optical properties and microstructure of translucent zirconia prepared by high-pressure spark plasma sintering,” *Sci. Technol. Adv. Mater.*, **12** [5] 55003 (2011).
- 110 A. Krell, J. Klimke, and T. Hutzler, “Advanced spinel and sub um Al<sub>2</sub>O<sub>3</sub> for transparent armour applications,” *J. Eur. Ceram. Soc.*, **29** [2] 275–281 (2009).
- 111 J.A. Wollmershauser, B.N. Feigelson, E.P. Gorzkowski, C.T. Ellis, R. Goswami, S.B. Qadri, J.G. Tischler, F.J. Kub, *et al.*, “An extended hardness limit in bulk nanoceramics,” *Acta Mater.*, **69** 9–16 (2014).
- 112 C. Wang and Z. Zhao, “Transparent MgAl<sub>2</sub>O<sub>4</sub> ceramic produced by spark plasma sintering,” *Scr. Mater.*, **61** [2] 193–196 (2009).
- 113 Y. Aman, V. Garnier, and E. Djurado, “Spark plasma sintering kinetics of pure  $\alpha$ -alumina,” *J. Am. Ceram. Soc.*, **94** [9] 2825–2833 (2011).
- 114 Y. Aman, V. Garnier, and E. Djurado, “A Screening Design Approach for the Understanding of Spark Plasma Sintering Parameters: A Case of Translucent Polycrystalline Undoped Alumina,” *Int. J. Appl. Ceram. Technol.*, **7** [5] 574–586 (2009).
- 115 X. Jin, L. Gao, and J. Sun, “Highly Transparent Alumina Spark Plasma Sintered from Common-Grade Commercial Powder: The Effect of Powder Treatment,” *J. Am. Ceram. Soc.*, **93** [5] 1232–1237 (2010).
- 116 S.W. Wang, L.D. Chen, and T. Hirai, “Densification of Al<sub>2</sub>O<sub>3</sub> powder using spark plasma sintering,” *J. Mater. Res.*, **15** [4] 982–987 (2000).
- 117 J.G. Santanach, A. Weibel, C. Estourns, Q. Yang, C. Laurent, and A. Peigney, “Spark plasma sintering of alumina: Study of parameters, formal sintering analysis and hypotheses on the mechanism(s) involved in densification and grain growth,” *Acta Mater.*, **59** [4] 1400–1408 (2011).
- 118 N. Kwon, G. Kim, H.S. Song, and H. Lee, “Synthesis and properties of cubic zirconia – alumina composite by mechanical alloying,” *Mater. Sci. Eng. A*, **299** 185–194 (2001).

- 119 S. Tekeli, "Fracture toughness (K<sub>1C</sub>), hardness, sintering and grain growth behaviour of 8YSCZ/Al<sub>2</sub>O<sub>3</sub> composites produced by colloidal processing," *J. Alloys Compd.*, **391** [1–2] 217–224 (2005).
- 120 H.L. Calambás Pulgarin and M.P. Albano, "Sintering, microstructure and hardness of different alumina-zirconia composites," *Ceram. Int.*, **40** [4] 5289–5298 (2014).
- 121 X. Zhou, D.M. Hulbert, J.D. Kuntz, J.E. Garay, and A.K. Mukherjee, "Superplasticity of the nanostructured binary systems of Zirconia-Alumina-Spinel ceramics by spark plasma sintering;" pp. 155–164 in *Adv. Ceram. Matrix Compos. X, Vol. 165*. Edited by J. P. Singh, N.P. Bansal and M.K. Waltraud. John Wiley & Sons, Inc., Hoboken, NJ, USA, 2006.
- 122 S. Bardakhanov and V. Lysenko, "Ceramic Preparation of Nanopowders and Experimental Investigation of Its Properties;" in *Adv. Ceram. - Synth. Charact. Process. Specif. Appl.* Edited by P.C.S. (Ed.). Intertech, 2011.
- 123 Y. Chaiyabutr, R. Giordano, and R. Pober, "The Effect of Different Powder Particle Size on Mechanical Properties of Sintered Alumina, Resin- and Glass-Infused Alumina," *J. Biomed. Mater. Res. Part B Appl. Biomater.*, [June] 502–508 (2008).
- 124 J.P. Singh, A.P. Virkar, D.K. Shetty, and R.S. Gordow, "Strength-Grain Size Relations in Polycrystalline Ceramics," *J. Am. Ceram. Soc.*, **62** [3–4] 179–183 (1979).
- 125 W.M. Rainforth, P. Zeng, and L. Ma, "Controlling grain size in oxide ceramics for optimization of strength and wear resistance," *Mater. Sci. Forum*, **715–716** 703–710 (2012).
- 126 C. Koch, "Bulk Behavior of Nanostructured Materials;" pp. 93–111 in *Nanostructure Sci. Technol.* Edited by R.W. Siegel, E. Hu, D.M. Cox, H. Goronkin, L. Jelinski, C.C. Koch, J. Mendel, M.C. Roco, et al. Springer Netherlands, Dordrecht, 1999.
- 127 E.O. HALL, "Variation of Hardness of Metals with Grain Size," *Nature*, **173** [4411] 948–949 (1954).
- 128 K. Tsukuma, I. Yamashita, and T. Kusunose, "Transparent 8 mol% Y<sub>2</sub>O<sub>3</sub> –ZrO<sub>2</sub> (8Y) Ceramics," *J. Am. Ceram. Soc.*, **91** [3] 813–818 (2008).
- 129 Č. Danko, M. Maji, and Č. Lidija, "Int. Journal of Refractory Metals and Hard Materials

- Vickers indentation fracture toughness of Y-TZP dental ceramics,” *Int. J. Refract. Met. Hard Mater.*, **64** 14–19 (2017).
- 130 ASTM International, *ASTM E384-16 Standard Test Method for Microindentation Hardness of Materials*. 2016.
- 131 L. Corporation, *LM Series Digital Microindentation Tester Instruction Manual; Part number 200-740*. St. Joseph, Mi, USA, 2016.
- 132 G.R. Astsis, P. Chantikul, B.R. Lawn, and D.B. Marshall, “A Critical Evaluation of Indentation Techniques for Measuring Fracture Toughness: I, Direct Crack Measurements,” *J. Am. Ceram. Soc.*, **64** [9] 533–538 (1981).
- 133 G.D. Quinn, “Fracture Toughness of Ceramics by the Vickers Indentation Crack Length Method: A Critical Review;” pp. 45–62 in *Mech. Prop. Perform. Eng. Ceram. II Ceram. Eng. Sci. Proc.* John Wiley & Sons, Inc., 2006.
- 134 R.G. Munro, *Elastic Moduli Data for Polycrystalline Ceramics, NISTIR 6853*. Gaithersburg, 2002.
- 135 L. Corporation, *LV Series: Macro-Vickers Hardness Testing System*, (n.d.).
- 136 G.D. Quinn, “FRACTURE TOUGHNESS OF CERAMICS BY THE VICKERS INDENTATION CRACK,” (2006).
- 137 G. D. Quinn, R. Gettings, and L. K. Ives, *A standard reference material for vickers hardness of ceramics and Hardmetals*. 2004.
- 138 T. Akatsu, S. Numata, M. Yoshida, Y. Shinoda, and F. Wakai, “Indentation Size Effect on the Hardness of Zirconia Polycrystals;” pp. 13–20 in *Fract. Mech. Ceram. Act. Mater. Nanoscale Mater. Compos. Glas. Fundam.* 2005.
- 139 M. Furukawa, Z. Horita, M. Nemoto, R.Z. Valiev, and T.G. Langdon, “Microhardness measurements and the hall-petch relationship in an Al-Mg alloy with submicrometer grain size,” *Acta Mater.*, **44** [11] 4619–4629 (1996).
- 140 R.W. Armstrong, “Engineering science aspects of the Hall – Petch relation,” *Acta Mech*, **225** 1013–1028 (2014).

- 141 A.S. Taha and F.. H. Hammad, “Application of the Hall-Petch Relation to Microhardness measurements on Al, Cu, Al-MD 105, and Al-Cu Alloys,” *phys. stat. sol.*, **119** 455–462 (1990).
- 142 Z.C. Cordero, B.E. Knight, and C.A. Schuh, “Six decades of the Hall – Petch effect – a survey of grain-size strengthening studies on pure metals,” *Int. Mater. Rev.*, **61** [8] 495–512 (2017).
- 143 K.Y. Wang, T.D. Shen, M.X. Quan, and W.D. Wei, “Hall-Petch relationship in nanocrystalline titanium produced by ball-milling,” *J. Mater. Sci. Lett.*, **12** 1818–1820 (1993).
- 144 M. Trunec, “Effect of grain size on mechanical properties of 3Y-TZP ceramics,” *Ceramics-Silikaty*, **52** [3] 165–171 (2008).
- 145 A. Krell and A. Bales, “Grain size-Dependent hardness of transparent magnesium aluminate spinel,” *Int. J. Appl. Ceram. Technol.*, **8** [5] 1108–1114 (2011).
- 146 K. Maiti and A. Sil, *Preparation of Nano and Micron Sized ZrO<sub>2</sub> Dispersed Al<sub>2</sub>O<sub>3</sub> Ceramic Composites and Study Their Hardness and Fracture Toughnesses*. 2011.
- 147 A.F. Liu, “Deformations and fracture mechanisms and static strength of metals;” pp. 47–119 in *Mech. Mech. Fract. An Introd.* ASTM International, Materials Park, Ohio, USA, 2005.
- 148 M. Yamada, K. Sekine, T. Kumazawa, and Y. Tanabe, “Relationship between the cone crack and fracture mode in ceramics under high-velocity-projectile impact,” *JCS-Japan*, **118** [10] 903–908 (2010).
- 149 A.H. Heuer, “Transgranular and Intergranular Fracture in Polycrystalline Alumina,” *J. Am. Ceram. Soc.*, **52** [9] 510–511 (1969).
- 150 W. Yang, “SEM Quantification of Transgranular vs Intergranular Fracture,” *J. Am. Ceram.*, **95** [2] 290–295 (1991).
- 151 A. Ghosh and A. Suri, K., “Low-Temperature Sintering and Mechanical Property Evaluation of Nanocrystalline 8 mol% Yttria Fully Stabilized Zirconia,” *J. Am. Ceram. Soc.*, **90** [7] 2015–2023 (2007).



- 152 I.E. Reimanis, K. Rozenburg, H.-J. Kleebe, and R.L. Cook, "Fabrication of transparent spinel: the role of impurities," *Wind. Dome Technol. Mater. IX, Proc. SPIE*, **5786** [May 2005] 48–55 (2005).
- 153 J.M. Perkins, "Microstructure and properties of (rare earth) doped oxide ceramics.;" University of Warwick., 2006.
- 154 L. Gao, H.Z. Wang, J.S. Hong, H. Miyamoto, K. Miyamoto, Y. Nishikawa, and S.D.D.L. Torre, "Mechanical Properties and Microstructure of Nano-SiC-Al<sub>2</sub>O<sub>3</sub> Composites Densified by Spark Plasma Sintering," *J. Eur. Ceram. Soc.*, **19** 609–613 (1999).
- 155 R. Rice W., "Grain Dependence of Hardness, Compressive Strength, Wear, and Related Behavior at Elevated Temperatures;" pp. 428–456 in *Mech. Prop. Ceram. Compos.* CRC Press, 2000.
- 156 N.. Kwon, G.H. Kim, H.S. Song, and H.L. Lee, "Synthesis and properties of cubic zirconia-alumina composites by mechanical alloying.," *Mater. Sci. Eng. A*, **299** [1–2] 185–194 (2001).
- 157 M. Mazaheri, A.M. Zahedi, and M.M. Hejazi, "Processing of nanocrystalline 8 mol % yttria-stabilized zirconia by conventional , microwave-assisted and two-step sintering," *Mater. Sci. Eng. A*, **492** 261–267 (2008).
- 158 A. Rothman, S. Kalabukhov, N. Sverdlov, M.P. Dariel, and N. Frage, "The effect of grain size on the mechanical and optical properties of spark plasma sintering-processed magnesium aluminate spinel MgAl<sub>2</sub>O<sub>4</sub>," *Int. J. Appl. Ceram. Technol.*, **11** [1] 146–153 (2014).
- 159 X. Teng, H. Liu, and C. Huang, "Effect of Al<sub>2</sub>O<sub>3</sub> particle size on the mechanical properties of alumina-based ceramics," *Mater. Sci. Eng. A*, **452–453** 545–551 (2007).
- 160 O. Quenard, C. Laurent, A. Peigney, and A. Rousset, "Zirconia-spinel composites. Part I: Synthesis of powders and dense materials," *Mater. Res. Bull.* -, **35** [12] 1967–1977 (2000).
- 161 O. Quenard, C. Laurent, A. Peigney, and A. Rousset, "Zirconia – spinel composites . Part II : mechanical properties," *Mater. Res. Bull.*, **35** [12] 1979–1987 (2000).
- 162 A. Krell, T. Hutzler, and J. Klimke, "Transmission physics and consequences for

- materials selection, manufacturing, and applications,” *J. Eur. Ceram. Soc.*, **29** [2] 207–221 (2009).
- <sup>163</sup> A. Maerten, C. Fleck, and W. Mueller, “Tetragonal and Cubic Zirconia Multilayered Ceramic Constructs Created by EPD,” *J. Phys. Chem. B*, **117** 1694–1701 (2013).
- <sup>164</sup> C. Wang, X. Mao, Y.-P. Peng, B. Jiang, J. Fan, Y. Xu, L. Zhang, and J. Zhao, “Preparation and Optical Properties of Infrared Transparent 3Y-TZP Ceramics,” *Materials (Basel)*, **10** [4] 390 (2017).
- <sup>165</sup> E. a. Olevsky, S. Kandukuri, and L. Froyen, “Consolidation enhancement in spark-plasma sintering: Impact of high heating rates,” *J. Appl. Phys.*, **102** [11] 114913 (2007).
- <sup>166</sup> P. Hermanek and S. Carmignato, “Reference object for evaluating the accuracy of porosity measurements by X-ray computed tomography,” *Case Stud. Nondestruct. Test. Eval.*, **6** 122–127 (2016).
- <sup>167</sup> X.. Chen, K.. Khor, S.. Chan, and L.. Yu, “Preparation yttria-stabilized zirconia electrolyte by spark-plasma sintering,” *Mater. Sci. Eng. A*, **341** [1–2] 43–48 (2003).
- <sup>168</sup> P. Dahl, I. Kaus, Z. Zhao, M. Johnsson, and M. Nygren, “Densification and properties of zirconia prepared by three different sintering techniques,” *Ceram. Int.*, **33** 1603–1610 (2007).
- <sup>169</sup> B. Kim, A. Dash, Y. Kim, K. Morita, H. Yoshida, J. Li, and Y. Sakka, “Low-temperature spark plasma sintering of alumina by using SiC molding set,” 1141–1145 (2016).
- <sup>170</sup> X. Zhou, D.M. Hulbert, J.D. Kuntz, R.K. Sadangi, V. Shukla, B.H. Kear, A.K. Mukherjee, S.W. Wang, *et al.*, “Microstructure and mechanical effects of spark plasma sintering in alumina monolithic ceramics,” *Scr. Mater.*, **58** [1] 603–606 (2008).
- <sup>171</sup> W.Q. Shao, S.O. Chen, D. Li, H.S. Cao, Y.C. Zhang, and S.S. Zhang, “Prediction and control of microstructure evolution for sub-microscale alpha-Al<sub>2</sub>O<sub>3</sub> during low-heating-rate sintering based on the master sintering curve theory,” *J. Eur. Ceram. Soc.*, **29** 201–204 (2009).
- <sup>172</sup> Z. Shen, M. Johnsson, Z. Zhao, and M. Nygren, “Spark Plasma Sintering of Alumina,” **27** [187381] 1921–1927 (2002).

- 173 A.K. Mukherjee, “Optically Transparent Polycrystalline Al<sub>2</sub>O<sub>3</sub> Produced by Spark Plasma Sintering,” **154** [22668] 151–154 (2008).
- 174 H. Zhang, Y. Xu, B. Wang, X. Zhang, J. Yang, and K. Niihara, “Effects of heating rate on the microstructure and mechanical properties of rapid vacuum sintered translucent alumina,” *Ceram. Int.*, **41** [9] 12499–12503 (2015).
- 175 G. Bonnefont, G. Fantozzi, S. Trombert, and L. Bonneau, “Fine-grained transparent MgAl<sub>2</sub>O<sub>4</sub> spinel obtained by spark plasma sintering of commercially available nanopowders,” *Ceram. Int.*, **38** [1] 131–140 (2012).
- 176 T.V. Minh, “Densification and Characterization of Transparent Polycrystalline Spinel Produced by Spark Plasma Sintering,” Rutgers, The State University of New Jersey, 2014.
- 177 J.E. Garay, “Current-Activated, Pressure-Assisted Densification of Materials,” *Annu. Rev. Mater. Res.*, **40** [1] 445–468 (2010).
- 178 L. Wang, J. Zhang, and W. Jiang, “Recent development in reactive synthesis of nanostructured bulk materials by spark plasma sintering,” *Int. J. Refract. Met. Hard Mater.*, **39** 103–112 (2013).
- 179 D.C. Blaine, S.J. Park, P. Suri, and R.M. German, “Application of Work-of-Sintering Concepts in Powder Metals,” *Metall. Mater. Trans. A*, **37A** 2006–2827 (2006).
- 180 D. Choron, S. Marinel, B. Pintault, S. Beaudet-savignat, and R. Macaigne, “Construction of master sintering curves to understand the effect of Na addition on ZnO-based varistors,” *J. Eur. Ceram. Soc.*, **35** [15] 4195–4202 (2015).
- 181 R.K. Enneti, M.G. Bothara, S. Park, and S. V Atre, “Development of master sintering curve for field-assisted sintering of HfB<sub>2</sub> – 20SiC,” *Ceram. Int.*, **38** [5] 4369–4372 (2012).
- 182 I.M. Robertson and G.B. Schaffer, “Some Effects of Particle Size on the Sintering of Titanium and a Master Sintering Curve Model,” *Metall. Mater. Trans. A*, **40A** 1968–1979 (2009).
- 183 R.R. Thridandapani, D.E. Clark, R.W. Hendricks, G. Lu, and G.R. Pickrell, “The Effect of Microwave Energy on Sintering The Effect of Microwave Energy on Sintering;” 2011.

- 184 H. Su and D.L. Johnson, "Master Sintering Curve A Practical Approach to sintering," *J. Am. Ceram. Soc.*, **79** [12] 3211–17 (1996).
- 185 J.D. Hansen, R.P. Rusin, M. H. Teng, and D.L. Johnson, "Combined-Stage Sintering Model," *J. Am. Ceram. Soc.*, **75** [5] 1129–1135 (1992).
- 186 D.C. Blaine, S. Park, and R.M. German, "Linearization of Master Sintering Curve," **1409** 1403–1409 (2009).
- 187 S. Qiao, "Master Sintering Curve and bimodal sintering of Zirconia, Order No. 1557614," San Diego State University, 2014.
- 188 W. Shao, S.O. Chen, D. Li, S.S. Zhang, and M. Science-poland, "Construction of the master sintering curve for submicron size  $\alpha$ -Al<sub>2</sub>O<sub>3</sub> based on non-isothermal sintering containing lower heating rates only," *Mater. Sci.*, **27** [1] 97–107 (2009).
- 189 Q. Yang, C. Laurent, A. Peigney, J.G. Santanach, A. Weibel, and C. Estourne, "Spark plasma sintering of alumina: Study of parameters, formal sintering analysis and hypotheses on the mechanism(s) involved in densification and grain growth," *Acta Mater.*, **59** 1400–1408 (2011).
- 190 M. Demuyck, J. Erauw, O. Van Der Biest, F. Delannay, and F. Cambier, "Densification of alumina by SPS and HP : A comparative study," **32** 1957–1964 (2012).
- 191 R. Caruso, N. Mamana, and E. Benavidez, "Densification kinetics of ZrO<sub>2</sub>-based ceramics using a master sintering curve," *J. Alloys Compd.*, **495** [2] 570–573 (2010).
- 192 T.A. Lee and A. Navrotsky, "Enthalpy of formation of cubic yttria-stabilized zirconia," *J. Mater. Res.*, **18** [4] 908–918 (2003).
- 193 S.J. Park, S.H. Chung, D. Blaine, P. Suri, and R.M. German, *Master Sintering Curve Construction Software and Its Applications*. 2004.
- 194 V. Pouchly and K. Maca, "Master sintering curve - A practical approach to its construction," *Sci. Sinter.*, **42** [1] 25–32 (2010).